

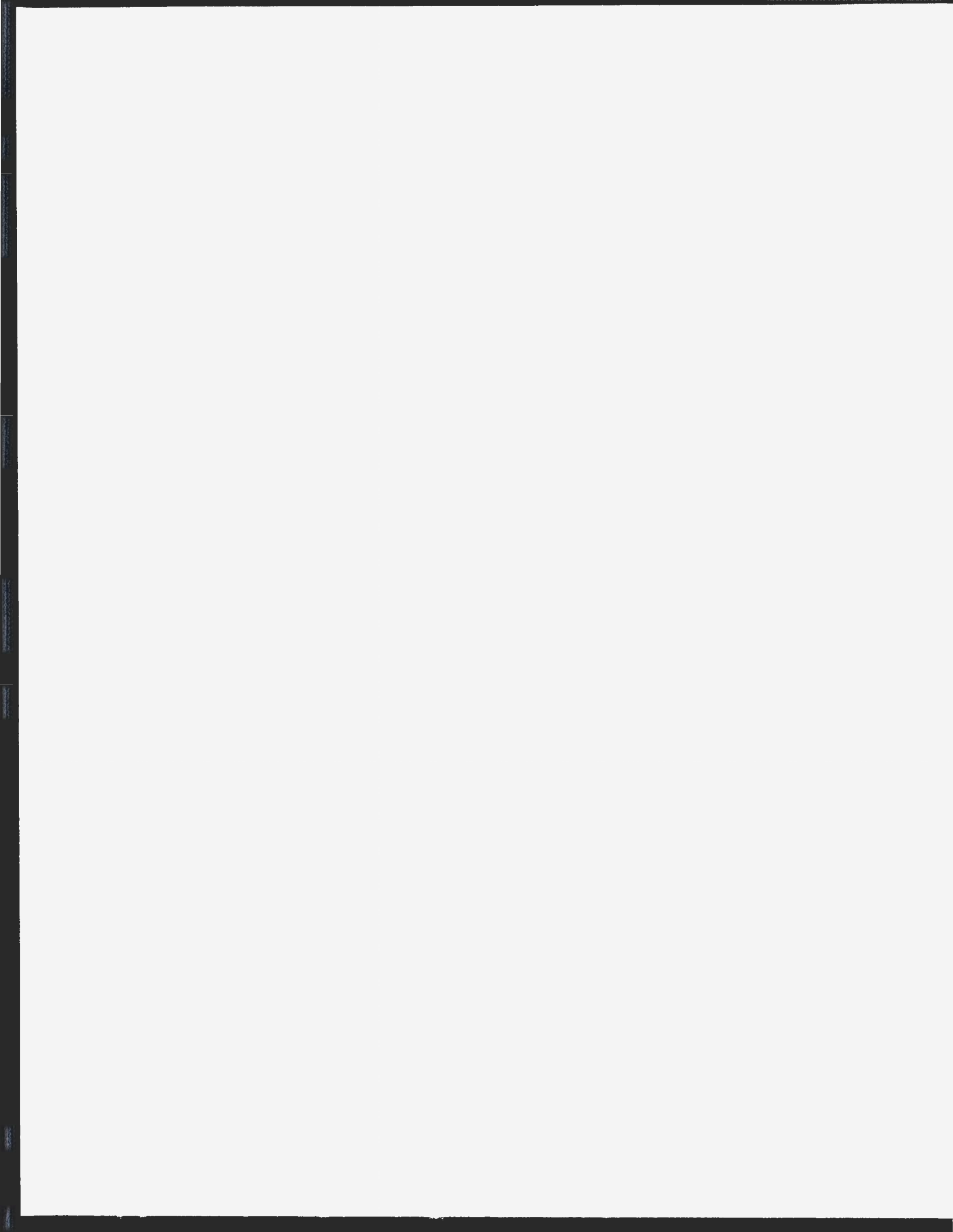
APPLICATION OF A GENERAL CFD CODE
TO PLANING CRAFT PERFORMANCE

CENTRE FOR NEWFOUNDLAND STUDIES

**TOTAL OF 10 PAGES ONLY
MAY BE XEROXED**

(Without Author's Permission)

ERIC THORNHILL



National Library
of Canada

Bibliothèque nationale
du Canada

Acquisitions and
Bibliographic Services

Acquisitions et
services bibliographiques

395 Wellington Street
Ottawa ON K1A 0N4
Canada

395, rue Wellington
Ottawa ON K1A 0N4
Canada

Your file *Votre référence*

ISBN: 0-612-84073-5

Our file *Notre référence*

ISBN: 0-612-84073-5

The author has granted a non-exclusive licence allowing the National Library of Canada to reproduce, loan, distribute or sell copies of this thesis in microform, paper or electronic formats.

L'auteur a accordé une licence non exclusive permettant à la Bibliothèque nationale du Canada de reproduire, prêter, distribuer ou vendre des copies de cette thèse sous la forme de microfiche/film, de reproduction sur papier ou sur format électronique.

The author retains ownership of the copyright in this thesis. Neither the thesis nor substantial extracts from it may be printed or otherwise reproduced without the author's permission.

L'auteur conserve la propriété du droit d'auteur qui protège cette thèse. Ni la thèse ni des extraits substantiels de celle-ci ne doivent être imprimés ou autrement reproduits sans son autorisation.

Canada

APPLICATION OF A GENERAL CFD CODE TO PLANING CRAFT PERFORMANCE

by

©Eric Thornhill, B. Eng., M. Eng.

A Thesis Submitted to the School of Graduate Studies
in Partial Fulfillment of the Requirements for the Degree of
Doctor of Philosophy in Engineering

Faculty of Engineering and Applied Science
Memorial University of Newfoundland

June 2002

St. John's, Newfoundland, Canada

Abstract

Performance prediction is an important part of vessel design. Common methods for predicting planing hull performance include the use of empirical equations and model testing. Empirical equations are often only applicable to similar hull types over a small range of parameters, while model testing is often prohibitively expensive, particularly for small craft. Ever increasing computer power is making the use of computational fluid dynamics (CFD) as a performance prediction tool a practical alternative. This work presents the results of a study involving CFD to evaluate the performance of a high-speed planing vessel moving at steady speed through calm water.

After a review of the state-of-the-art in CFD methods, it was decided that an unstructured, multiphase, finite volume code employing the volume-of-fluid (VOF) method for free surface capturing would be best suited for the study. The use of a commercial CFD code was found to be the best alternative as they are publicly available, generally undergo extensive validation, have a wide user-base, and receive periodic upgrades and improvements. The code chosen was Fluent (v5.3).

Fluent could not, however, be used directly to simulate the behaviour of a planing vessel. The performance of high-speed craft is intimately linked to the orientation of the hull at speed, which cannot be known *a priori*. Planing hulls rise and change trim angle in response to the pressure field generated by the flow. In order to solve for these changes in

hull position, the simulation method had to ensure that dynamic equilibrium was achieved in terms of lift and trimming moment. This was accomplished with an iterative scheme wherein the flow field was solved for discrete hull orientations that were then adjusted based on force and moment results until the conditions of equilibrium were met.

The work began with a set of physical model experiments used to provide the baseline from which the numerical results would be evaluated. Three sets of simulations were then performed to evaluate the prediction method. The first set fixed the hull orientation to match those measured in the physical experiments. This enabled a direct comparison of the numerical results to the physical results. A second set of simulations was then performed where only the equilibrium condition of lift was satisfied; trim angles remained fixed at the experimental values. The last set of simulations solved for equilibrium in both lift and trimming moment and represent the results of predictions that would be produced without the benefit of physical experiments.

It was found that the CFD simulations produced high hull pressure forces compared with the experimental results. In the first set of simulations, this meant high drag forces. When the model was permitted to move vertically (with a fixed trim angle) in the second set of simulations, the numerical model lifted higher in the water. This reduced the pressure drag results, but decreased the wetted area and hence the frictional drag. During the last set of simulations, which permitted the model to trim and heave to achieve dynamic equilibrium, trim angle and sinkage were found to decrease relative to the previous simulation set. As a result, pressure drag was found to decrease, but frictional drag predictions improved. Values for total resistance were found to be low when compared

with experimental results. The under predicted resistance results from the second and third set of simulations were a direct consequence of the over predicted hull pressures identified during the first set of simulations. Despite these high pressure values, the results of the predictions still followed experimental trends, and the procedure for solving dynamic equilibrium was successful.

ACKNOWLEDGEMENTS

I would like to thank my supervisors Dr. Neil Bose, Dr. Brian Veitch, Dr. Don Bass and Dr. Pengfei Liu for their advice and consultation throughout the tenure of this degree program. I would also like to thank the Institute for Marine Dynamics (IMD) and Oceanic Consulting Corporation for providing the facilities and resources needed for this project. I am grateful for the financial support provided by the Natural Sciences and Engineering Research Council (NSERC), and Memorial University of Newfoundland (MUN).

TABLE OF CONTENTS

Abstract	i
Acknowledgements	iv
Table of Contents	v
List of Figures	viii
List of Tables	xii
1 Introduction	1
1.1 Problem Discussion	3
1.2 Planing Hulls	5
1.3 Numerical Considerations	8
1.3.1 <i>Grid Definition – Meshing</i>	8
1.3.2 <i>Solution Techniques</i>	13
1.3.2.1 <i>Segregated vs. Coupled Solvers</i>	16
1.3.2.2 <i>Implicit vs. Expicit Methods</i>	17
1.3.2.3 <i>Convection and Diffusion</i>	17
1.3.2.4 <i>Pressure-Velocity Coupling</i>	18
1.3.2.5 <i>Relaxation and Multigrid Methods</i>	19
1.3.2.6 <i>Boundary Conditions</i>	21
1.3.3 <i>Turbulence Modeling</i>	22
1.3.4 <i>Free Surface Treatment</i>	26
1.3 Summary.....	28
2 Physical Experiments	30
2.1 Model & Tow Arrangement	31
2.1.1 <i>Planing Boat Model</i>	32
2.1.2 <i>Tow Arrangement</i>	33
2.2 Test Program.....	34
2.3 Test Results.....	36
2.3.1 <i>Resistance</i>	36
2.3.2 <i>Running Trim</i>	37

2.3.3	<i>Sinkage Results</i>	39
2.3.4	<i>Hull Pressures</i>	40
2.3.5	<i>Wave Profiles</i>	49
2.3.6	<i>Boundary Layer Velocity Profiles</i>	51
2.4	Uncertainty Analysis.....	60
2.5	Summary.....	64
3	Numerical Simulations	65
3.1	Problem Set-Up and Description.....	69
3.1.1	<i>Flow Domain & Mesh</i>	70
3.1.2.1	<i>Turbulence</i>	77
3.1.2	<i>Solver Parameters</i>	80
3.1.3	<i>Initialization</i>	80
3.1.4	<i>Determination of Measured Quantities</i>	83
3.1.5	<i>Grid Dependence Study</i>	87
3.2	Method of Analysis	90
3.3	Results from Initial Simulations	95
3.3.1	<i>Hull Pressures</i>	95
3.3.2	<i>Flow Velocities</i>	97
3.3.3	<i>Free Surface</i>	101
3.4	Discussion.....	105
4	Equilibrium Simulations	106
4.1	Literature Review.....	107
4.2	Procedure.....	110
4.3	0 - Degrees of Freedom.....	113
4.4	1 – Degree of Freedom.....	123
4.5	2 – Degrees of Freedom.....	132
4.6	Discussion.....	144
5	Conclusions	147
5.1	Physical Experiments.....	147
5.2	Numerical Simulations	150

5.3 Equilibrium Simulations.....152
5.4 Recommendations for Future Work155
References157

APPENDIX A: Results from Physical Model Tests: Phase I

A.1 Results from Physical Model Tests: Phase I..... A-1

APPENDIX B: Results from Boundary Layer Measurements

B.1 Results from Boundary Layer Measurements.....B-1

APPENDIX C: Results from Physical Model Tests: Phase II

C.1 Results from Physical Model Tests: Phase II.....C-1

APPENDIX C: Results from Numerical Simulations

LIST OF FIGURES

Figure 1.1 – Typical Pressure and Velocity Distribution on Flat Plate	6
Figure 1.2 – Forces on a 2D Planing Surface	7
Figure 1.3 – Structured and Unstructured Meshes.....	10
Figure 1.4 – Mesh Refinement.....	11
Figure 2.1 – Plan View of Towing Tank	31
Figure 2.2 – Model Hull (LOA = 1.475m)	32
Figure 2.3 – Model Hull Cross Section	33
Figure 2.4 – Gimbal	33
Figure 2.5 – Tow Arrangement.....	34
Figure 2.6 – Instrument Positions in Model.....	35
Figure 2.7 – Model Scale Resistance	37
Figure 2.8 – Running Trim	38
Figure 2.9 – Change in Trim.....	39
Figure 2.10 – Sinkage and Trim Results.....	40
Figure 2.11 – Wave Probe Array in Tank.....	41
Figure 2.12 – Example Wave Probe Traces.....	41
Figure 2.13 – Example Wave Profile.....	42
Figure 2.14 – Wave Trends.....	43
Figure 2.15 – Dimensions of Sample Slice.....	45
Figure 2.16 – Typical Wave.....	47
Figure 2.17 – Resistance Components.....	48
Figure 2.18 – Model at Speed (6.0 m/s).....	49
Figure 2.19 – Pressure Results: P1, P3, P6, P9.....	50
Figure 2.20 – LDV Mount	53
Figure 2.21 – Typical LDV Data	54
Figure 2.22 – Boundary Layer Velocities (Model Speed = 4.0 m/s).....	54
Figure 2.23 – Vessel Attitude (4.0 m/s).....	55
Figure 2.24 – Velocity Change vs. Trim Angle.....	56
Figure 2.25 – Flat Plate Analysis.....	57

Figure 2.26 – Pressure Change on Hull	58
Figure 2.27 – Standard Deviations from LDV Data	60
Figure 2.28 – Typical Instrument Histogram.....	62
Figure 3.1 – Planing Hull Model Domain	71
Figure 3.2 – Model Surfaces and Lines	72
Figure 3.3 – Base Domain Mesh.....	73
Figure 3.4 – Element Refinement	75
Figure 3.5 – Hull Surface of Refined Mesh.....	76
Figure 3.6 – Refined Domain Mesh.....	76
Figure 3.7 – Trimming Moment History	78
Figure 3.8 – Initialization with Predefined Free Surface	82
Figure 3.9 – Initialization with and without UDF.....	83
Figure 3.10 – Water Volume Fraction Along Chine.....	86
Figure 3.11 – Sample of Commands Used Each Time-Step	86
Figure 3.12 – Trimming Moment (Refinement Envelope).....	88
Figure 3.13 – Lift Force History (Hull Surface Refinement)	89
Figure 3.14 – Forces on Model	91
Figure 3.15 – Friction Lines.....	92
Figure 3.16 – Hull Pressures (Elevation Plot)	96
Figure 3.17 – Pressure Profiles on Two Transverse Cuts.....	97
Figure 3.18 – Pathlines of Particles Released Below The Waterline	98
Figure 3.19 – Pathlines of Particles Released Above The Waterline	99
Figure 3.20 – Velocity Vectors Near Transom.....	100
Figure 3.21 – Pressure Contours at Centerline Plane	100
Figure 3.22 – Velocity Vectors Near Pressure Peak Location.....	101
Figure 3.23 – Free Surface at Centerline Plane	102
Figure 3.24 – Free Surface Contours	103
Figure 3.25 – Wave Profiles from Physical Experiments.....	103
Figure 3.26 – Wetted Surface Area from CFD	104
Figure 3.27 – Wetted Surface Area from Experiments.....	104

Figure 4.1 – Flowchart for Equilibrium Program	112
Figure 4.2 – Total Resistance: 0-DOF	114
Figure 4.3 – Pressure Resistance: 0-DOF	115
Figure 4.4 – Frictional Resistance: 0-DOF	116
Figure 4.5 – Wetted Area: 0-DOF	116
Figure 4.6 – Hull Pressures	118
Figure 4.7 – Pressure Distributions on Hull Centerline	119
Figure 4.8 – Boundary Layer Velocity Profiles	120
Figure 4.9 – Velocity Change vs. Trim Angle	121
Figure 4.10 – Pressure and Velocity Profiles on Hull Centerline	122
Figure 4.11 – Expanded Flow Chart for 1-Degree of Freedom	124
Figure 4.12 – Total Resistance: 1-DOF	125
Figure 4.13 – Frictional Resistance: 1-DOF	126
Figure 4.14 – Wetted Area: 1-DOF	127
Figure 4.15 – Sinkage: 1-DOF	127
Figure 4.16 – Pressure Resistance: 1-DOF	130
Figure 4.17 – Lift and Drag Vectors	131
Figure 4.18 – Wetted Centerline Length: 1-DOF	131
Figure 4.19 – Expanded Flow Chart for 2-Degree of Freedom	133
Figure 4.20 – Lift vs. Sinkage & Trim	135
Figure 4.21 – Moment vs. Sinkage & Trim	135
Figure 4.22 – Running Trim: 2-DOF	137
Figure 4.23 – Sinkage: 2-DOF	137
Figure 4.24 – Hull Orientations	138
Figure 4.25 – Peak Pressure vs. Trim Angle	140
Figure 4.26 – Wetted Area: 2-DOF	140
Figure 4.27 – Frictional Resistance: 2-DOF	141
Figure 4.28 – Pressure Resistance: 2-DOF	142
Figure 4.29 – Total Resistance: 2-DOF	142
Figure 4.30 – Moment Slope vs. Model Speed	143

Figure B.1 – Boundary Layer Velocities (model speed = 4.0 m/s)	B-2
Figure B.2 – Boundary Layer Velocities (model speed = 5.0 m/s)	B-2
Figure B.3 – Boundary Layer Velocities (model speed = 6.0 m/s)	B-3
Figure B.4 – Boundary Layer Velocities (model speed = 6.5 m/s)	B-3
Figure D.1 – Wave Profile: 1.0 m/s	D-1
Figure D.2 – Wave Profile: 1.5 m/s	D-2
Figure D.3 – Wave Profile: 2.0 m/s ($F_n = 0.59$)	D-3
Figure D.4 – Wave Profile: 2.5 m/s ($F_n = 0.79$)	D-4
Figure D.5 – Wave Profile: 3.0 m/s ($F_n = 1.00$)	D-5
Figure D.6 – Wave Profile: 3.5 m/s ($F_n = 1.23$)	D-6
Figure D.7 – Wave Profile: 4.0 m/s ($F_n = 1.47$)	D-7
Figure D.8 – Wave Profile: 4.5 m/s ($F_n = 1.71$)	D-8
Figure D.9 – Wave Profile: 5.0 m/s ($F_n = 1.96$)	D-9
Figure D.10 – Wave Profile: 5.5 m/s ($F_n = 2.21$)	D-10
Figure D.11 – Wave Profile: 6.0 m/s ($F_n = 2.47$)	D-11
Figure D.12 – Wave Profile: 6.5 m/s ($F_n = 2.72$)	D-12
Figure D.13 – Wave Profile: 7.0 m/s ($F_n = 2.98$)	D-13

LIST OF TABLES

Table 2.1 – Particulars for the Niagara Jet Boat	31
Table 2.2 – Static trim angles for ballast conditions.....	36
Table 2.3 – Typical Instrument Variation.....	61
Table 2.4 – Instrument Precisions.....	63
Table 2.5 – Other Model Uncertainties.....	64
Table 3.1 – Solver Parameters	79
Table A.1 – Static trim angles and drafts (at tow point) for ballast conditions	A-1
Table A.2 – Column Descriptions for Result Tables	A-2
Table A.3 – Phase I Results: Model Weight 25.2 kg, Model LCG = 0.528 m.....	A-3
Table A.4 – Phase I Results: Model Weight 29.55 kg, Model LCG = 0.493 m.....	A-4
Table A.5 – Phase I Results: Model Weight 29.55 kg, Model LCG = 0.534 m.....	A-5
Table A.6 – Phase I Results: Model Weight 29.55 kg, Model LCG = 0.572 m.....	A-6
Table A.7 – Phase I Results: Model Weight 33.91 kg, Model LCG = 0.535 m.....	A-7
Table B.1 – LDV Results: Model Speed = 4.0 m/s	B-4
Table B.2 – LDV Results: Model Speed = 5.0 m/s	B-5
Table B.3 – LDV Results: Model Speed = 6.0 m/s	B-6
Table B.4 – LDV Results: Model Speed = 6.5 m/s	B-7
Table C.1 – Phase II: LDV Aft Position, Model Speed = 4.0 m/s.....	C-1
Table C.2 – Phase II: LDV Forward Position, Model Speed = 4.0 m/s (Part 1)	C-2
Table C.3 – Phase II: LDV Forward Position, Model Speed = 4.0 m/s (Part 2)	C-3
Table C.4 – Phase II: LDV Aft Position, Model Speed = 5.0 m/s.....	C-4
Table C.5 – Phase II: LDV Forward Position, Model Speed = 5.0 m/s.....	C-5
Table C.6 – Phase II: LDV Aft Position, Model Speed = 6.0 m/s.....	C-6
Table C.7 – Phase II: LDV Forward Position, Model Speed = 6.0 m/s.....	C-7
Table C.8 – Phase II: LDV Aft Position, Model Speed = 6.5 m/s.....	C-8
Table C.9 – Phase II: LDV Forward Position, Model Speed = 6.5 m/s.....	C-9

Table E.1 – Physical Experimental Results	E-1
Table E.2 – Savitsky’s Method Results (Savitsky, 1964).....	E-2
Table E.3 – Equilibrium Simulation Results: 0-Degree of Freedom.....	E-3
Table E.4 – Equilibrium Simulation Results: 1-Degree of Freedom.....	E-3
Table E.5 – Equilibrium Simulation Results: 2-Degree of Freedom.....	E-4

CHAPTER 1

INTRODUCTION

1 INTRODUCTION

An essential step in ship design is hydrodynamic performance evaluation. It allows the designer to determine whether a design will meet the given requirements. Several methods are commonly used, such as drawing on experience from similar vessels, using empirical data, or performing tests of a scaled-down prototype. For more advanced designs, the latter is preferred since these tests will generally give the best prediction of performance. Model tests, however, are costly, as they require the construction of a model prototype(s) to tight tolerances, as well as the use of a test facility and appropriate electronic instrumentation. An alternative to physical experiments is the use of numerical model tests where performance can be evaluated entirely by computer simulations. Although still being developed and improved, numerical simulations using computational fluid dynamics (CFD) techniques are now frequently used to augment, and occasionally replace, physical experiments. This is

due to the potential of CFD for yielding both accurate and detailed predictions at a lower cost. Some of the strengths of numerical modeling have been summarized in the following excerpt.

“Even though experimentation remains the tool most commonly used by designers to obtain accurate values of the hydrodynamic and aerodynamic forces acting on the boat, numerical simulations have some major advantages. In particular, they are relatively inexpensive and fast to use, so that it is possible to test and select different candidate geometries before setting up models for the towing tank or wind tunnel. Moreover, they allow the visualization of several quantities – such as the flow streamlines, the wave profiles or the pressure distribution – that are difficult to obtain from experiments. This is a very useful aid for the designer to understand the physics of the flow phenomena, at least from a qualitative point of view.” (Caponnetto *et al.*,1998)

Research in the field of computational fluid dynamics (CFD) has progressed greatly over the last three decades as increases in computing power have made it possible to solve the equations governing fluid behavior. These equations, which are generally unsolvable analytically (except for a few special cases), can be approximated using numerical methods processed by a computer. The continuous domain of a problem is sub-divided into a series of discrete points or elements. The governing equations are likewise discretized across these divisions. Complex differential equations are thereby transformed into a series of relatively simple coupled equations that can be solved by any number of numerical methods. This concept is not new, but the complexity of the equations and the enormity of the calculations have made its application impractical without the computational power of today’s computers.

The present research focused on utilizing the latest techniques in CFD to the specific problem of a planing vessel moving at steady speed through calm water. After a review of relevant literature, it was decided that an unstructured, multiphase, finite volume code employing the volume-of-fluid (VOF) method for free surface capturing would be used for the study. The use of a commercial CFD code was found to be the best alternative as they are publicly available, generally undergo extensive validation, have a wide user-base, and receive periodic upgrades and improvements. The code chosen was Fluent (v5.3), which can perform calculations of the discretized Reynolds Averaged Navier-Stokes (RANS) equations including viscous effects, turbulence modeling, and free surface constraints on unstructured adaptive grids. This software was incorporated in an iterative scheme developed by the author that permitted the model to respond to forces induced by the flow, allowing it to achieve dynamic equilibrium. Though not as significant for some vessels, this feature is essential for correctly modeling the behavior of ships moving at or near planing speeds.

1.1 Problem Discussion

The problem addressed by this research was that of evaluating the behaviour of a planing vessel operating at steady speed in calm water through the use of computer simulations. There are two primary aspects to this problem: simulation of the flow field around the vessel, and satisfying dynamic equilibrium.

Simulation of the flow field around a vessel requires software that can solve the discretized Navier-Stokes equations including the effects of gravity, a free surface, and turbulence. The options available for acquiring such a program consisted of

developing the code, using existing research code, or using commercial code.

Development of this type of code was outside the scope and resources of the study,

whereas research codes often have prohibitive restrictions on their use. It was

therefore necessary to rely on a commercial package to meet the CFD needs for this

problem. Commercial software has several advantages over the other alternatives.

These include: technical support, continual upgrades to the software, discounted rates

for universities, independently performed verification and validation studies, a wide

user-base, and the option of unrestricted use (should the full license fee be paid).

The software chosen was Fluent (v5.3), a general purpose CFD solver whose

applications include models such as: pipe flows, mixing processes, thermal systems,

and reacting flows. It employs the finite volume method for the solution of the

governing differential equations for fully unstructured meshes. Free surfaces can be

included in a simulation using the volume-of-fluid method and several choices for

turbulence modeling are available. Fluent comes with its own mesh generation

program, Gambit (v1.2), capable of generating both structured and unstructured

meshes of the flow domain.

A limitation with this software, and with CFD software in general, was that the

problem geometry was fixed for a given simulation. This may not be an obstacle for

many types of models, but planing vessels undergo significant changes in running

trim and vertical position that must also be simulated to produce meaningful results.

In order to overcome this restriction and allow the vessel to respond to the flow field,

a program was developed by the author that expanded the CFD solver, enabling it to

also solve for dynamic equilibrium. The procedure involved altering the position and attitude of the vessel based on the previous flow results, then re-meshing and solving for the new system. Iterations continued until dynamic equilibrium was achieved.

In addition to the numerical work, an extensive program of physical model tests was carried out on the same vessel used in the computer simulations. Performed for several ballast conditions, these tests included the basic measurements of trim, vertical position, wetted area, and resistance, as well as the more detailed measurements of hull pressures, boundary layer velocities, and wave profiles. The data collected from these tests were used to evaluate the results from the CFD/equilibrium computations.

After a general discussion of planing vessels, the remainder of this chapter focuses on some of the major aspects involved with implementing CFD to this type of problem. These include grid definition, solution techniques, turbulence modeling, and free surface boundary conditions.

1.2 Planing Hulls

Planing hulls are built for high speed operation. Their design differs from that of displacement vessels in that they attempt to exploit the flow separation that displacement hulls try to avoid. This results in several characteristic features of planing hull forms, such as flat surfaces, transom sterns, hard chines and corners, and v-shaped transverse sections. All of these features are aimed at developing positive dynamic pressures at high speeds that lift the vessel, allowing it to ride the wave it

generates. At these speeds, this can lead to dramatic decreases in resistance compared with displacement hulls.

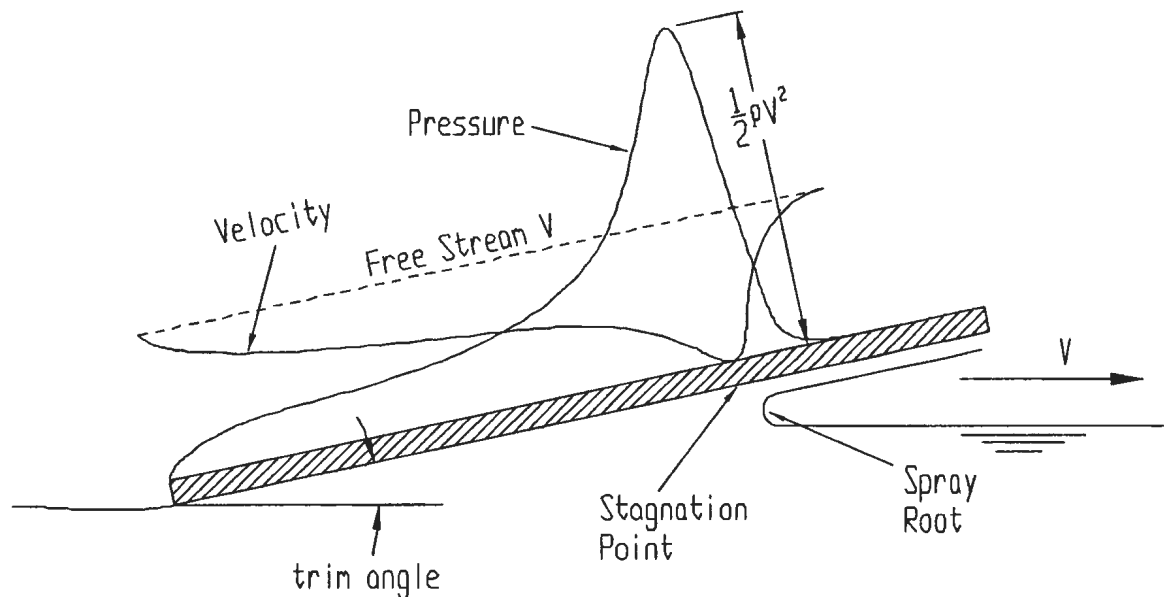


Figure 1.1 – Typical Pressure and Velocity Distribution on Flat Plate

Planing behaviour is often simplified for analysis by considering the two dimensional case of a flat plate moving at a given trim angle. The flow generated by this plate has been considered representative of flows generated in more complex situations. Figure 1.1 shows typical velocity and pressure distributions for a 2D planing flat plate (gravity and viscosity were neglected). When the flow makes contact with the plate, part of it is deflected forward where it rides upward parallel to the plate, and where it is eventually jettisoned as spray. The rest of the flow is directed downward along the length of the plate where it rejoins with the free stream flow. Between these two regions is a stagnation point where the flow has zero velocity relative to the plate. At this point, maximum pressure (equal to the total dynamic pressure) is achieved. This pressure decreases sharply on each side of the stagnation point but levels off

somewhat in the direction of flow toward the aft end of the plate. The velocity distribution is zero at the stagnation point but approaches the free stream velocity at each end of the plate.

This pressure distribution causes a net force normal to the plate. The effect of this force is shown in Figure 1.2 for both frictionless and viscous fluids. For the inviscid case, the vertical component of the pressure force produces lift on the plate. The horizontal component acts to resist the forward motion in the form of induced drag. In the viscous case, induced drag is increased by frictional drag. A component of frictional drag also acts vertically due to the trim angle, causing a slight decrease in the net lift.

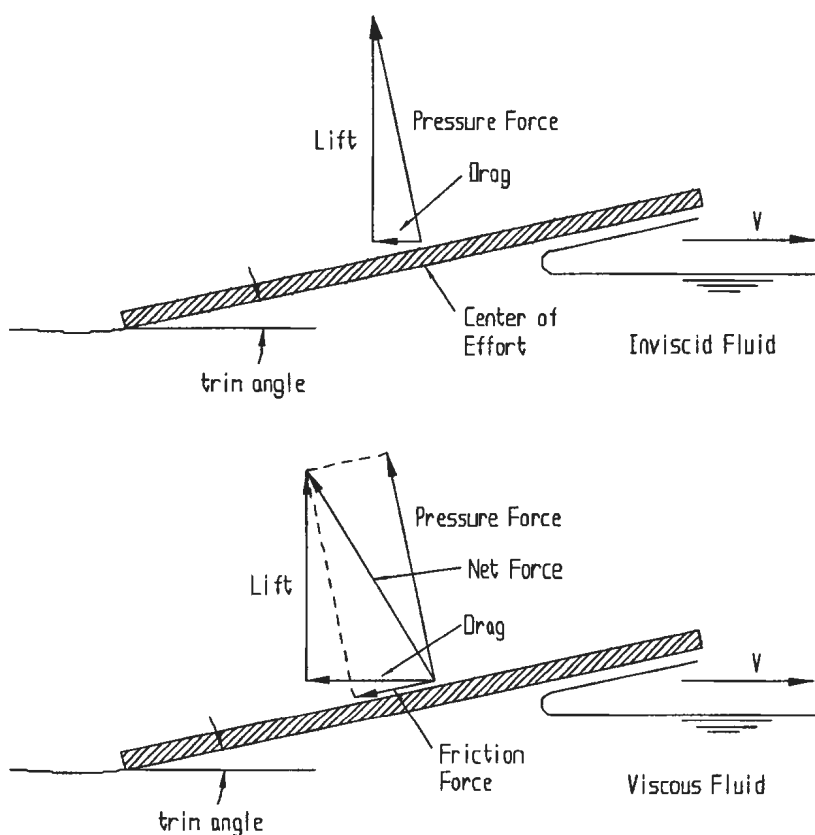


Figure 1.2 – Forces on a 2D Planing Surface

Though simplified, this flat plate demonstrates the primary characteristics common to all planing craft. The vessel approaches the undisturbed surface at a positive trim angle. Some flow is re-directed as spray while the rest is forced aftwards along the hull. A pressure distribution is formed which peaks near the leading edge of the wetted surface area. This pressure, along with frictional effects, creates lift and drag on the vessel. These forces and their associated moments must balance those from the vessel's weight and propulsion to achieve steady state motion.

There is an intrinsic relationship between the vessel's attitude, weight and thrust, and the resulting force distribution along the hull. The sensitive balance of these forces and moments must be satisfied if the performance of a planing vessel is to be evaluated correctly. This is the focus of the present work.

1.3 Numerical Considerations

Computational fluid dynamics is a comprehensive field covering a broad range of related topics. This section is intended to introduce the primary areas of CFD involved in the numerical simulations discussed in this thesis.

1.3.1 *Grid Definition – Meshing*

The numerical methods used to solve the governing equations of fluid flow require that the fluid domain be first discretized into geometrically simple cells or elements. Meshing is an important step in any computational method, since the accuracy of the solution can be directly related to the sizes and shapes of the mesh elements. This solution dependence on grid definition has led to a wide variety of techniques for

their development and improvement. Meshes can take several forms, but are generally identified as being either structured or unstructured.

Structured meshes are currently the most common in CFD applications. This type of mesh requires a systematic scheme of node and element numbering related to the generation of the grid. One of the advantages of structured meshes is that the implicit nature of grid structure means that the mesh connectivity (a map of the grid structure) does not need to be stored, thereby reducing computer memory requirements.

Structured grids also allow the use of more efficient solution methods, which can reduce computer processing time. The primary disadvantage of structured meshes is that they can be difficult, and sometimes impossible, to create for complex geometries. The domain often needs to be segmented into topologically similar regions or blocks, which are then mapped with separate structured grids. This approach can decrease the time needed to build a mesh over fully structured grids, but the solver must have the ability to handle the resulting block interfaces, often resulting in a need for increased computer resources.

Unstructured meshes can be regarded as the extreme case of segmenting a domain into regions, brought to the point where the resulting 'blocks' become so small that the local structured meshes in each block are no longer required. Unlike structured mesh approaches, the elements are not ordered in any regular fashion, although they do conform exactly to the boundaries of the domain. For this type of mesh, the physical locations of the grid points or nodes must be stored along with the

connectivity of the mesh: a listing of which nodes make up each element as well as the identities of their neighbouring elements.

Unstructured grids are flexible, useful for complex geometries, and can be constructed with any type of element or with combinations of different element types (hybrid meshes). Using an unstructured hybrid mesh can greatly accelerate the meshing process of a CFD simulation. The drawbacks of this method are the increased computational resources required, and the fact that solvers have to be designed specifically to handle unstructured meshes. Examples are shown in Figure 1.3 of structured (in the 'C'), unstructured (in the 'F') and hybrid (in the 'D') meshes.

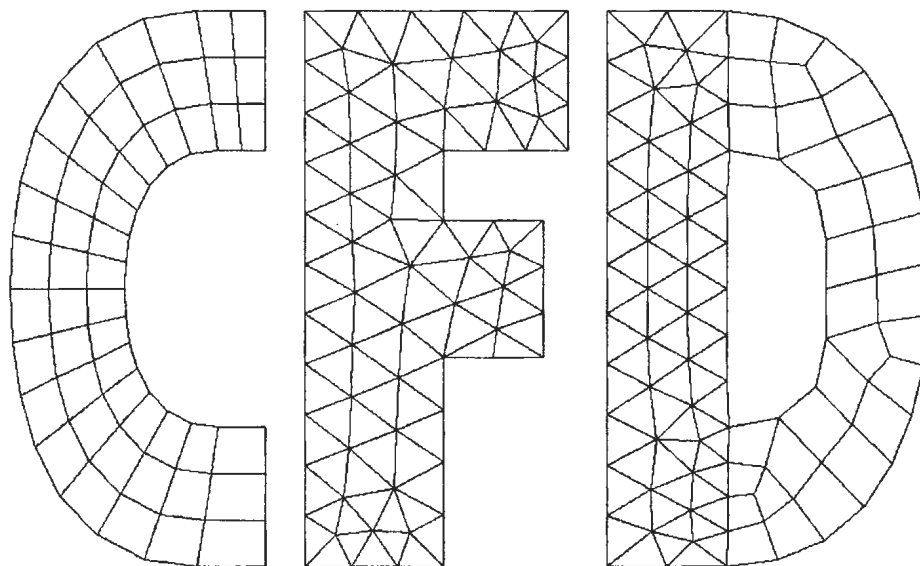


Figure 1.3 – Structured and Unstructured Meshes

An important advantage of unstructured meshes is the ease with which adaptive meshing techniques may be incorporated. These techniques allow the mesh to be altered, either refined or coarsened, based on any given criteria. Since there is no

inherent structure to be preserved, adding or removing mesh elements only results in local updates to the connectivity. Adaptation can take several forms; two common types are hanging node and conformal.

When hanging node adaptation is used, elements in regions to be refined are subdivided into multiple smaller elements. There may be one or more nodes that split the interface between a refined and an unrefined element. These are hanging nodes and require special treatment by the solver. This method of refinement is straightforward and effective. However, after multiple levels of refinement are applied, the mesh connectivity and element shapes may degrade, resulting in highly skewed elements.

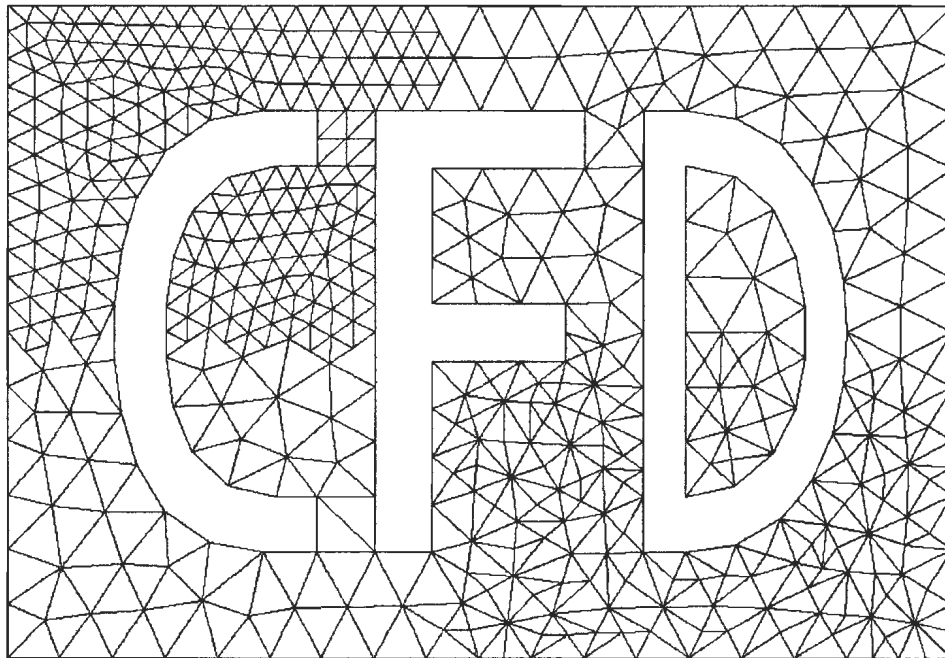


Figure 1.4 – Mesh Refinement

Conformal adaptation implies that there will be no hanging nodes after the refinement process. New nodes are inserted and the local connectivity of the mesh is re-computed in that region. Special techniques such as the Delaunay criteria (Peyret, 1996) are often required to minimize distortions in newly formed elements. This method is generally only used with triangular or tetrahedral meshes. An example of a mesh that has undergone refinement is given in Figure 1.4. Hanging node adaptation was used to refine the upper-left corner while conformal adaptation was used to refine the lower-right corner.

Meshing is an essential part of performing CFD simulations. Choosing the appropriate meshing strategy is therefore an important aspect of any computational work. Structured grids are typically more difficult to implement, but have the advantage that more efficient methods can be used for the solution process.

Unstructured grids are easier to apply and are more versatile in terms of geometrical adaptation, but require greater computational resources by the solver. However, as the speed and memory capacity of computers continues to increase, computational time becomes less of an issue, thereby making unstructured grids the favoured alternative. For the present work, unstructured hybrid adaptive grids (with hanging nodes) were used exclusively in the numerical simulations. The flexibility of this approach meant that the flow domain could be meshed automatically, a requirement for the method used to solve the geometry-dependent problem of dynamic equilibrium.

1.3.2 Solution Techniques

The essential goal of any CFD program is to solve a set of equations with appropriate boundary and/or initial conditions. The Navier-Stokes equations governing the conservation of mass and momentum of fluid are a set of coupled, non-linear, mixed elliptic-parabolic partial differential equations (Versteeg & Malalasekera, 1995).

Although a few exact analytical solutions exist for some simplified cases, such as the laminar flow over an infinitely long plate (Currie, 1974), exact solutions cannot be determined for practical flows. It is therefore necessary to employ numerical methods to develop approximate solutions to these equations. Several techniques have been used to solve the Navier Stokes equations, including finite difference methods, finite element methods, finite volume methods, and spectral methods. The basic steps for each of these methods can be summarized as:

- Using simple functions to approximate unknown flow variables.
- Discretizing the governing flow equations with substitutions of the approximate functions followed by mathematical manipulations.
- Solving the resulting algebraic equations.

Finite difference methods employ approximations of derivatives by truncated Taylor series expansions given in terms of values at a given grid point and its immediate neighbours. Substitution of these discrete approximations in place of continuous derivatives in the governing equations results in algebraic equations for the unknown flow variables at each grid point. This was one of the first methods used to tackle flow problems, but was found to be sensitive to the grid structure.

Finite element methods employ simple piecewise functions to describe the variations of the flow variables on individual elements. When these functions are substituted into the governing equations, an associated error, or residual, is produced. An attempt is then made to minimize the error, often with the use of weighting functions. The result of this operation is a set of algebraic equations defining the values of the coefficients of the original piecewise approximating functions defined for each element. Most commonly employed for structural problems, progress has been made towards improving this method for fluid equations (Baker, 1998).

Spectral methods use functions such as truncated Fourier series or Chebyshev polynomial series to approximate flow variables. However, unlike finite difference and finite element methods, these functions are applied to the entire flow domain instead of being restricted to local grid points or elements. The approximate functions are then substituted into the governing equations resulting in an error, or residual. A similar method as the finite element method can then be used to minimize this error, or the error can be made to vanish on specific grid points. The result is a set of algebraic equations defining the values of the coefficients of the approximating truncated series. Though theoretically sound, relatively few codes are based on this methodology (Peyret, 1983).

The finite volume method (FVM) was originally developed to overcome certain restrictions in finite difference formulations and has since evolved to be a well established and thoroughly validated method for CFD problems (Versteeg & Malalasekera, 1995). The procedure involves integrating the governing equations

over all of the finite control volumes in the domain. Each control volume is associated with a discrete point at which the dependent variables such as velocity, pressure and temperature are to be calculated. Approximations of terms in the integrated governing equations representing such processes as convection, diffusion, and sources, are then made using finite difference type substitutions (various terms in the integration are approximated with grid point values of the dependent variables such as the velocity components). The result is a system of algebraic equations representing the conservation of flow variables for each control volume. Solving a system of algebraic equations, usually by an iterative method, is a step required by all the methods mentioned here.

The finite volume method can take full advantage of an arbitrary or unstructured mesh. Modifying the shape and location of the control volumes as well as varying the rules and accuracy for the evaluation of the flux through the control surfaces gives considerable flexibility to the method. In addition, as the conservation laws are discretized directly, the basic quantities of mass momentum and energy remain conserved at the discrete level. This is called *conservativeness* and is an important property for a numerical method (Hirsch, 1988). For a general flow variable ϕ , the conservation equation for a control volume is expressed in terms of the processes tending to increase or decrease its value as shown below.

$$\left[\begin{array}{l} \text{Rate of change} \\ \text{of } \phi \text{ in the} \\ \text{control volume} \end{array} \right] = \left[\begin{array}{l} \text{Net change of } \phi \\ \text{due to convection} \\ \text{through surfaces} \\ \text{of control volume} \end{array} \right] + \left[\begin{array}{l} \text{Net change of } \phi \\ \text{due to diffusion} \\ \text{through surfaces} \\ \text{of control volume} \end{array} \right] + \left[\begin{array}{l} \text{Net rate of creation} \\ \text{or destruction of } \phi \\ \text{inside of control} \\ \text{volume} \end{array} \right]$$

The Fluent software is a general purpose CFD code and uses the finite volume method for discretization of all the governing equations. There are, however, several options for how the solution method is employed. These include solvers for 2D problems and for 3D problems, or for time-independent problems (steady) and time-dependent problems (unsteady). Further specification of the solution method, particularly with issues related to the finite volume method, can also be made. These options, briefly discussed in the following sections, allow the solution procedure to be optimized for specific problems.

1.3.2.1 Segregated vs. Coupled Solvers

This solution option is related to how the equations are solved once discretized. It consists of “segregated” and “coupled” methods. Both schemes are based on a finite volume technique, but differ in the procedure used to determine the unknown flow variables. The segregated method solves the governing equations sequentially (i.e. segregated from one another). After each governing equation is solved, the code checks for convergence and then iterates stepwise through all the equations until convergence is achieved. In the coupled solver, the governing equations of momentum, continuity, and energy are solved simultaneously (coupled together). Any additional equations for scalars (such as turbulence kinetic energy and dissipation) are then solved sequentially using the procedure of the segregated solver. The choice of which solver to use depends on the type of problem being solved.

1.3.2.2 *Implicit vs. Explicit Methods*

Another aspect of the solution method is how the equations are formulated before they are solved by either the segregated or coupled schemes. The approach can be either “implicit” or “explicit”. For an implicit scheme, the unknown value of a given variable in each cell is computed using a relation that includes both existing and unknown values from neighboring cells. Therefore each unknown appears in more than one equation in the system, and these equations must be solved simultaneously to give the unknown quantities. For the explicit scheme however, the unknown value in each cell for a given variable is computed using a relation that includes only existing values. Therefore, each unknown appears in only one equation in the system, and the equations for the unknown value in each cell can be solved one at a time to give the unknown quantities.

1.3.2.3 *Convection and Diffusion*

An issue that can arise when using the finite volume method concerns the roles of convection and diffusion. It results from the fact that diffusive properties affect a given transported quantity in all directions, while convection spreads influence only in the direction of flow. The discretization scheme must be chosen such that the control volumes are influenced correctly by both of these factors. Several schemes have been developed for this purpose, such as the power law-scheme and the QUICK scheme. Both methods incorporate the effects of simultaneous convection and diffusion by means of weighted contributions in the discretized equations. The power-

law scheme determines the weighting based on the Peclet Number¹ while the QUICK (Quadratic Upstream Interpolation for Convective Kinetics) scheme uses a higher order discretization based on an upstream weighted quadratic interpolation. Higher order schemes like QUICK are generally advantageous as they involve more neighbouring cells, thereby reducing error by bringing in a wider influence.

1.3.2.4 Pressure - Velocity Coupling

Another issue involved in the finite volume method comes from the treatment of pressure in the equations. Shown in equations [1.1] and [1.2] are the equations for conservation of momentum and mass, respectively.

$$\rho \frac{Du_i}{Dt} = \mu \left(\frac{\partial^2 u_i}{\partial x_j \partial x_j} \right) - \frac{\partial p}{\partial x_i} + S_i \quad [1.1]$$

$$\frac{\partial u_i}{\partial x_i} = 0 \quad [1.2]$$

The equations are intimately coupled in velocity but there is no clear transport equation for pressure, an important source term of momentum. This results in an indirect specification because the correct pressure field is needed while solving the momentum equations to ensure that the resulting velocity field will satisfy the continuity equation. Additional considerations and algorithms are therefore needed to perform the flow field calculation. One such method is the SIMPLE (Semi-Implicit Method for Pressure-Linked Equations) algorithm, which uses an iterative approach to overcome the problem. Initial guessed velocity and pressure fields are used to solve

¹ Peclet Number is a measure of the relative strengths of convection and diffusion.

the momentum equations. A pressure correction equation, deduced from the continuity equation, is then used to improve the guessed fields until convergence is achieved (Versteeg & Malalasekera, 1995). Other pressure-velocity coupling techniques, such as SIMPLER (SIMPLE –Revised), SIMPLEC (SIMPLE-Consistent) and PISO (Pressure Implicit with Splitting of Operators), have also been developed (Peyret, 1983).

A special case develops when there exists strong body forces (e.g. gravity or surface tension forces) in multiphase flows. This is the case for the present research problem due to the hydrostatic forces caused by gravity. When large body forces are present in multiphase flows, the body force and pressure gradient terms in the momentum equation are almost in equilibrium, with the contributions of convective and viscous terms small in comparison. Segregated algorithms converge poorly unless partial equilibrium of pressure gradient and body forces is taken into account. An optional “implicit body force” treatment that can account for this effect, was available in Fluent which can make the solution procedure more robust. The basic procedure involves augmenting the correction equation, with an additional term involving corrections to the body force. This results in extra body force correction terms and allows the flow to achieve a realistic pressure field early in the iterative process (Fluent User’s Manual, 1999).

1.3.2.5 Relaxation and Multigrid Methods

Once the equations have been discretized, it does not always follow that successive iterations will lead to a converged solution. At times, the values of an unknown flow

variable, such as pressure, may oscillate or drift away from the true solution of the equations. Avoiding such divergence of the iteration process has resulted in the development of various treatments of the discretization equations. One such approach is to slow down how quickly a given variable is corrected at each cycle. Should, for example, the pressure correction for a given iteration be large, it could result in unstable computations leading to divergence (Patankar *et al.* 1998). This technique of reducing variable corrections is called under-relaxation (over-relaxation is when the variable values change more rapidly than without relaxation, and is sometimes used to accelerate convergence). Proper settings of the relaxation factors for a given problem can increase the efficiency of the solver.

Other numerical problems can also occur during the solution process. Traditional matrix solvers like the implicit Gauss-Seidel method are known to converge rapidly for the first few iterations, but slowly thereafter. These methods are most efficient for smoothing out errors of wavelengths comparable to the mesh size, but are ineffective in annihilating low-frequency components. As the grid is refined, these low-frequency modes dominate the solution error and additional iterations become progressively less productive. One way of improving the convergence of these iterative matrix solvers is by using multigrid methods. These methods solve the equations using a sequence of successively coarser meshes so that all frequency components are reduced at comparable rates (Patankar *et al.* 1998). Depending on the solver (e.g. implicit or explicit) being used, either an algebraic multigrid (AMG) or a full-approximation storage multigrid (FAS-Multigrid) technique can be employed in Fluent.

1.3.2.6 *Boundary Conditions*

The flow in a given problem is controlled by the boundary conditions imposed on the domain. Although many types of boundary conditions are available in a general purpose CFD code, only those related to the present research will be discussed here. These are: wall, velocity inlet, symmetry, and outflow boundary conditions.

Wall boundary conditions are used to define solid boundaries. No flow can pass through a wall boundary condition and in viscous flows the no slip condition is automatically imposed. Tangential wall velocities can, however, be set indirectly by specifying a “moving wall”.

Velocity inlet boundary conditions are used to define the flow velocity, along with all relevant scalar properties of the flow (such as the volume fraction, i.e. inflow is water or air). For incompressible flows, this type of boundary condition produces a constant mass inflow rate.

Symmetry boundary conditions are used when the physical geometry of interest, and the expected pattern of the flow solution, both have mirror symmetry. Flow conditions of all variables at a symmetry boundary condition can be summarized as having zero normal velocity and zero normal gradient.

Outflow boundary conditions are used to model flow exits where the details of the flow velocity and pressure are not known prior to solving the flow problem.

Conditions at outflow boundaries are not defined but extrapolated from the interior

and hence have no impact on the upstream flow. The outflow velocity and pressure are updated in a manner that is consistent with a fully-developed flow assumption².

1.3.3 Turbulence Modeling

Despite advances in computing power and mathematics, full descriptions of practical turbulent flows are unreachable for now and for the foreseeable future. However, useful estimations of the mean turbulent flow characteristics can still be made if some approximations or models are employed in the solution of the Navier-stokes equations of fluid momentum. Reynolds (1895) proposed that for many applications, only the mean flow characteristics are desired. By decomposing the velocity and pressure terms into mean and fluctuating components (based on a long time average), the Navier-Stokes equations can be re-expressed in terms of these decomposed terms. These equations, called the Reynolds-averaged Navier-Stokes (RANS) equations for mean linear fluid momentum, form the basis for many of the methods of turbulence modeling.

The Navier-Stokes equation for linear momentum is given below:

$$\frac{\partial u_i}{\partial t} + u_j \frac{\partial u_i}{\partial x_j} = -\frac{\partial p}{\partial x_i} + \nu \nabla^2 u_i \quad [1.3]$$

Velocity is decomposed into mean, \bar{u}_i , and fluctuating, u'_i , parts as follows:

$$u_i = \bar{u}_i + u'_i \quad [1.4]$$

Similarly for pressure,

$$p = \bar{p} + p' \quad [1.5]$$

² Fully developed flows are flows in which the flow velocity profile (and/or profiles of other properties such as temperature) is unchanging in the flow direction.

Substituting the decomposed velocity and pressure into the momentum equation [1.3] and taking an ensemble mean leads to the RANS equation:

$$\frac{\partial \bar{u}_i}{\partial t} + \bar{u}_j \frac{\partial \bar{u}_i}{\partial x_j} = -\frac{\partial \bar{p}}{\partial x_i} + \nu \nabla^2 \bar{u}_i - \frac{\partial \tau_{ij}}{\partial x_j} \quad [1.6]$$

where,

$$\tau_{ij} = \overline{u'_i u'_j} \quad \text{is the Reynolds-stress tensor.} \quad [1.7]$$

The Reynolds-stress tensor represents an additional set of unknowns to the momentum and continuity equations. These equations cannot be solved in the above form since the number of unknowns is greater than the number of available equations. This is called the Reynolds-stress closure problem (Wilcox, 1983).

There are several methods for obtaining closure to the RANS equations that range in both complexity and the need for computing power. It should be noted that the fundamental nature of these equations prevents them from being able to provide any detailed information about turbulent flow structures. They are instead intended to estimate mean values such as velocities, pressures, and turbulence intensity levels, which can then be used for design purposes. The ability of these equations to produce accurate information about these mean parameters directly depends on the quality of the models used to approximate the unknown terms.

Most common turbulence models are based on what is referred to as “eddy viscosity” and are classed as being; algebraic, one equation, two equation, or second order.

These classifications relate to the level of mathematical sophistication used to derive the model, and also to the level of computational cost to the CFD solver. An algebraic

model, for example, replaces the Reynold's stress terms with an algebraic expression containing the velocity and/or pressure terms. Models like the two equation and second order type models rely on additional Reynold's averaged transport equations such as dissipation or kinetic energy to achieve closure. The unknown terms in these models are also replaced with algebraic expressions, but since they are of a higher order, the errors associated with them tend to be less significant to the lower order terms of interest. Higher order models, though potentially more accurate, do result in a considerable increase in processing and memory demands for the computations (Speziale, 1991).

Due to the nature of the approximations made in turbulence models, different models tend to behave best for different applications. A universally accurate turbulence model is probably unattainable. This is still an area that needs significant improvement (Stern *et al.* 1999). The turbulence models discussed below (Fluent User's Manual, 1999) are available with Fluent. The most commonly used model in ship flows are the one-equation Spalart-Allmaras model (Wilcox, 1993) and the standard k- ϵ model although other models such as the Reynolds stress approach have also been attempted (Deng & Visonneau 1996, 1999).

- *Spalart-Allmaras Model*

The Spalart-Allmaras model is a relatively simple one-equation model that solves a modeled transport equation for the kinematic eddy (turbulent) viscosity. It was designed specifically for aerospace applications involving wall-bounded flows and has been shown to give good results for boundary layers subjected to adverse pressure gradients.

- *Standard k- ϵ Model*

The standard k- ϵ model requires the solution of two separate transport equations (kinetic energy and dissipation) to independently determine the turbulent velocity and length scales. This model is known for its robustness, economy, and has been shown to be reasonably accurate for a wide range of turbulent flows. It is a semi-empirical model; its derivation relies on both phenomenological considerations and empiricism.

- *RNG k- ϵ Model (ReNormalization Group)*

The RNG k- ϵ model was derived using a rigorous statistical technique (called renormalization group theory). It is similar in form to the standard k- ϵ model, but includes certain refinements that make it applicable to a wider range of flows including rapidly strained and swirling flows.

- *Realizable k- ϵ Model*

The realizable k- ϵ model is another improved version of the standard k- ϵ model containing a new formulation for the turbulent viscosity and a new transport equation for the dissipation rate. The term “realizable” means that the model satisfies certain mathematical constraints on the Reynolds stresses, consistent with the physics of turbulent flows (unlike the standard or RNG k- ϵ models). It can generally provide superior performance for flows involving rotation, boundary layers under strong adverse pressure gradients, separation, and recirculation.

- *Reynolds Stress Model (RSM)*

The Reynolds Stress Model achieves closure to the RANS equations by using transport equations for the Reynolds stresses, together with an equation for the dissipation rate (requiring the solution of seven transport equations in 3D flow). The rigorous nature of the RSM means that it has greater potential to give accurate predictions for complex flows. However, the closure assumptions employed to model various terms in the transport equations can degrade its performance in some cases; results may not be better than the simpler models.

However, use of the RSM is necessary when the flow features of interest are the result of anisotropy in the Reynolds stresses.

- *Large Eddy Simulation (LES)*

LES provides an alternative approach in which the large eddies are computed in a time-dependent simulation that uses a set of “filtered” equations. Filtering is a manipulation of the exact Navier-Stokes equations to remove only the eddies that are smaller than the size of the filter, which is usually taken as the mesh size. Like Reynolds averaging, the filtering process creates additional unknown terms that must be modeled in order to achieve closure. Statistics of the mean flow quantities, which are generally of most engineering interest, are calculated during the time-dependent simulation. The attraction of LES is that, by modeling less of the turbulence (and solving more), the error induced by the turbulence model will be reduced. LES models are, however, quite recent and require substantially more computational time and memory than other models.

1.3.4 Free Surface Treatment

A free surface is the interface between water and air in a numerical simulation. It is determined by enforcing both kinematic and dynamic boundary conditions. The kinematic condition ensures that there is no flow across the wave surface. Dynamic conditions ensure that the normal stress at the free surface balances the ambient pressure and surface tension, and that the tangential stress components vanish.

Surface tension forces need not be modeled in ship flow simulations, as their effects are not generally significant (Stern *et al.*, 1999). For the treatment of the free surface in numerical schemes, two main approaches can be distinguished:

- “free-surface fitting” methods in which one boundary of the computational domain coincides with the free surface and the grid is moved, stretched and compressed during the iteration process;
- “free-surface capturing” methods in which the numerical grid is fixed and the free surface is defined by some kind of scalar function. This function divides the domain into grid zones, which are either filled with fluid or not.

In surface fitting methods, the free surface is a sharp interface, the motion of which is followed. This is done by creating a grid in the fluid domain defining the free surface. During the solution process, the grid moves with or tracks the free surface by ensuring that the boundary conditions are always satisfied. Many finite-element methods use this approach. This method does, however, require that the mesh be adapted in the course of the solution process to ensure that it conforms to the changing free surface location. This grid adaptation may be either general or simplified (e.g. grid points sliding along predefined lines or spines). A background grid can also be defined that determines the paths along which grid points may slide.

Free surface fitting techniques are generally accurate and require little change to the RANS solver itself. But they are less suitable for large free surface distortions or topology changes such as breaking waves. Even large amplitude surface motions can be difficult to track without introducing re-gridding techniques such as the Arbitrary-Lagrangian-Eulerian (ALE) method (Hirt, 1999). Unstructured meshes could also be a solution in such cases. The majority of recent methods for steady flow around the hull in ship resistance codes use free surface fitting techniques (Stern *et al.*, 1999).

The alternative approach, surface capturing, solves the RANS equations on a pre-determined grid that is not fitted to the wave surface. The domain mesh extends into the air region, and therefore does not need to be adapted during the calculation process. The method does, however, require an additional algorithm to resolve the free surface within the meshed domain. Surface capturing methods have the potential to handle complicated ship forms (e.g. protruding bulbous bows, barge sterns) and flow phenomena such as breaking waves or spray (Stern *et al.*, 1999). One such method, often used with FVM solvers such as Fluent, is the volume-of-fluid (VOF) method.

The VOF method is based on the concept of a fluid volume fraction. Within each grid cell (control volume) it is customary to retain only one value for each flow quantity (e.g., pressure, velocity, temperature, etc.). The use of a single quantity (the fluid volume fraction in each grid cell) to define the free surface is consistent with the resolution of the other flow quantities. The fluid volume fractions in each cell are used to identify surfaces, as well as surface slopes and surface curvatures. Surfaces are located in cells partially filled with fluid or between cells full of fluid and cells that have no fluid. Slopes and curvatures are computed by using the fluid volume fractions in neighboring cells. The use of a volume tracking as opposed to a surface-tracking function means that the VOF method is robust enough to accommodate severe free surface movements such as sloshing or breaking waves (Hirt, 1999).

1.4 Summary

Computer simulations of ship flows can be used in conjunction with, or as an alternative to, more traditional methods of evaluating designs. CFD offers a designer

the flexibility to test virtually any hull shape and examine its flow field with a resolution unavailable by any other method. However, a restriction with typical CFD codes is that they are unable to solve problems where the geometry of the domain and the flow field are inter-related. High speed planing vessels are an example of such a problem. The orientation of the hull depends on the pressure field of the flow in order to achieve dynamic equilibrium, but the flow's pressure field is itself a function of the orientation of the hull. The current research focuses on augmenting the general purpose CFD code Fluent to solve the geometry-dependent performance of a high speed planing vessel by forcing it to achieve dynamic equilibrium. A description of this problem was given, followed by a brief outline of planing vessel flows. Aspects of relevant numerical concerns related to this type of CFD work were also presented as an introduction to the current work.

The following chapters first describe the physical model experiments used for evaluation of the CFD simulations. The numerical simulations are then described in detail including the development of the grid, the solution process, and typical results. Simulations involving the additional solution of the equations of dynamic equilibrium are described and discussed. The final chapter then summarizes the work and draws conclusions from the available results.

CHAPTER 2

PHYSICAL EXPERIMENTS

2 PHYSICAL EXPERIMENTS

In order to provide a set of physical data to evaluate the results of the numerical simulations discussed in Chapters 3 and 4, a set of bare hull resistance tests were performed on a 1:8 scale model of an 11.8 m long planing hull in the Clearwater Towing Tank at the National Research Council of Canada's Institute for Marine Dynamics (NRC/IMD). The experiments covered a range of speeds and included six different ballast configurations (displacement and longitudinal center of gravity). Measurements were made of tow force, running trim, sinkage, hull pressures, wetted surface area, and wave profiles. Additional tests were done to measure the boundary layer thickness at two locations along the hull using a laser Doppler velocimeter. These were each done at four speeds for the design ballast configuration. This chapter describes the model and test setup, the test program, and provides examples of the measured data.

2.1 Model & Tow Arrangement

The vessel tested was a 1:8 scale model of the *Niagara Jet Boat* by MetalCraft Marine Incorporated. The *Niagara* is a recreational craft that operates in rivers and lakes giving days tours for up to 36 people with 2 crew. There are several *Niagara Jet Boat* type vessels currently in operation. The particulars are given in Table 2.1.

LBP	11.8 m
Beam	4.3 m
Displacement (Design)	18 metric tons
Propulsion	3 x Hamilton 291 Waterjets
Maximum Speed	40 knots

Table 2.1 – Particulars for the Niagara Jet Boat

The experiments were performed over a three week period in November-December 2000 at NRC/IMD's Clearwater Towing Tank (CWT). The tank, shown in Figure 2.1, is 200 m long, 12 m wide, 7 m deep and contains fresh water. Models are attached to a tow carriage, which has a maximum speed of 10.0 m/s with accelerations available in steps of 0.2 m/s^2 up to 1.2 m/s^2 .

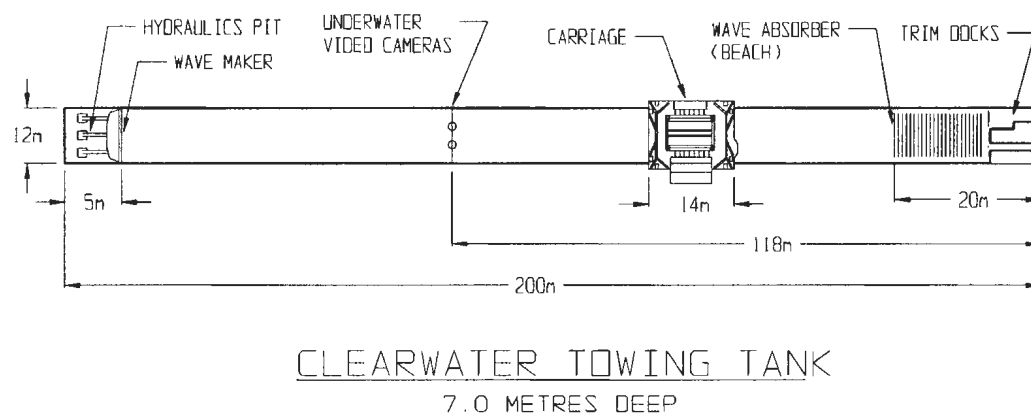


Figure 2.1 – Plan View of Towing Tank

2.1.1 Planing Boat Model

The model hull was constructed out of carbon fiber reinforced plastic strengthened with transverse and longitudinal stiffeners, a watertight bulkhead near the stern, and a shear deck with coaming. A plastic splash guard cover was fitted during tests.

The hull surface, shown in Figure 2.2, was marked with station numbers on the bottom and port side. Knife edges extending 1mm from the hull surface were fitted along the chines to promote flow separation. The hull was not prismatic but did have a simple shape as shown in Figure 2.3. This cross section was constant from the transom for about 2/3 the length of the hull (covering the wetted length of the model when planing at high speed). A small flat bottom area at the centerline turns to a low deadrise of 5.9° . This deadrise then turns sharply to 40.8° near the chine (see Figure 2.3).

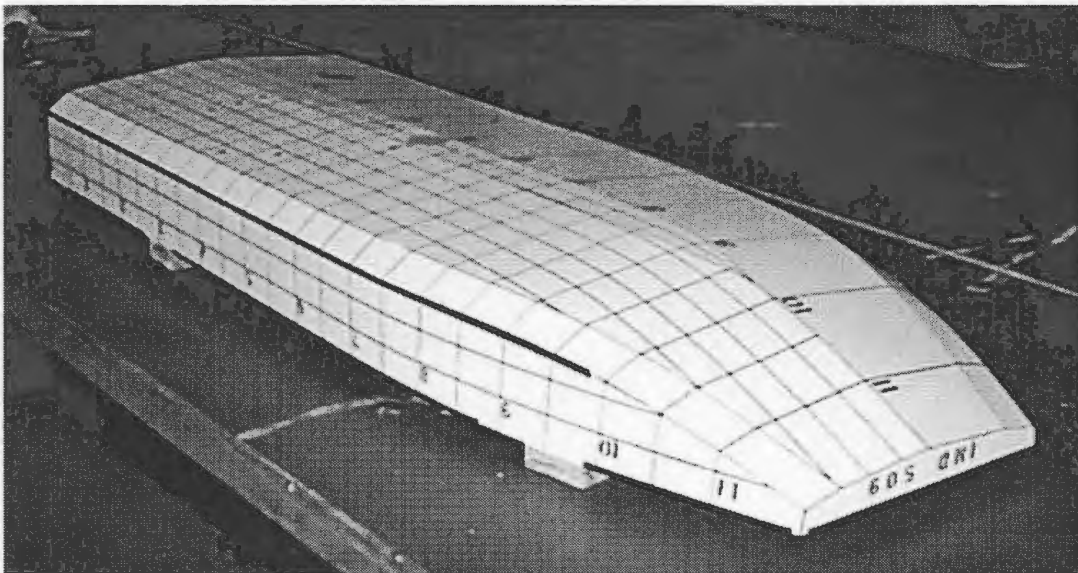


Figure 2.2 – Model Hull (LOA = 1.475m)

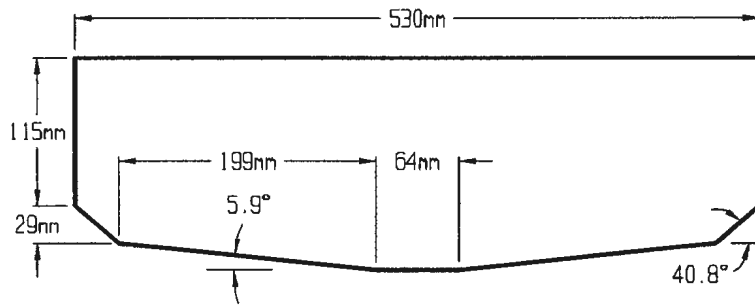


Figure 2.3 – Model Hull Cross Section

2.1.2 Tow Arrangement

The model was fitted to the tow carriage using a gimbal and yaw restraint. Tow force was transmitted from the heave post through a linear bearing to an ‘S’-shaped load cell (max. load = 50 lb.) and then through a universal joint to the model (see Figure 2.4). The universal joint allowed the model to pitch and roll freely and the heave post was free to move vertically in the tow post arrangement. The model was prohibited from rotating about the heave post by a yaw restraint, which was counterbalanced so that it did not affect the ballast. The tow arrangement is shown in Figure 2.5.

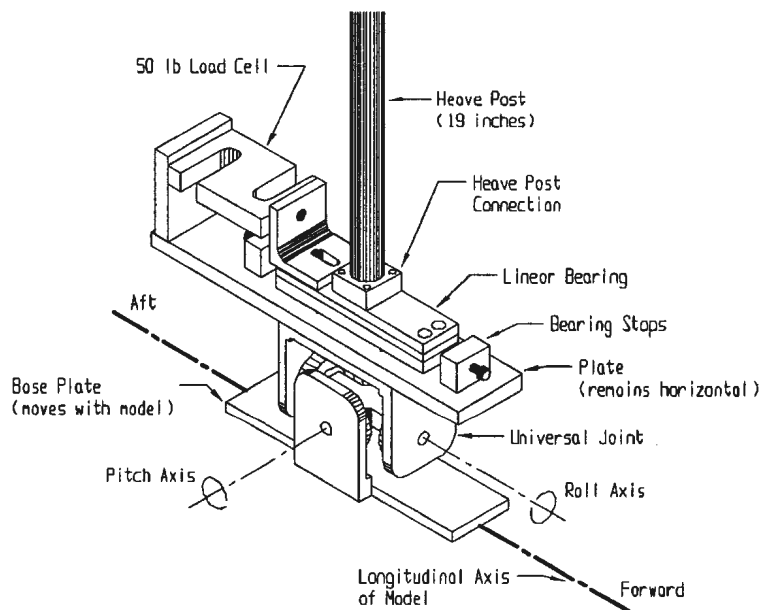


Figure 2.4 – Gimbal

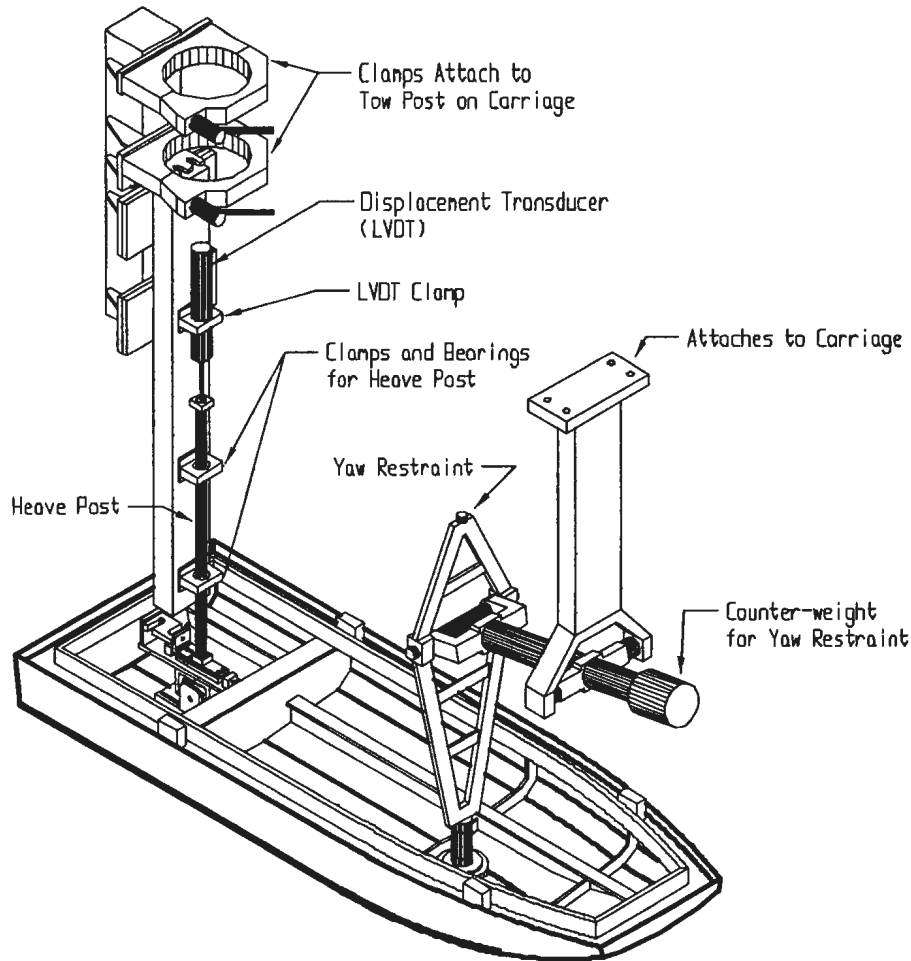


Figure 2.5 – Tow Arrangement

2.2 Test Program

The test program consisted of two phases. The first phase focused on testing the effects of different ballast conditions over a range of speeds. Measurements were made of tow force, running trim, sinkage, hull pressures, wetted surface areas, and wave profiles. The second phase was performed solely at the design ballast condition, and was used to measure boundary layer velocity profiles below the hull surface using a laser Doppler velocimeter (LDV).

Planing craft performance is sensitive to ballast condition, so tests were performed over a range of displacements and locations of the longitudinal center of gravity (LCG). These conditions are given in Table 2.2, which also shows the static trim angles of the model. The first column lists the three displacements (design displacement $\pm 15\%$) and the first row lists the three LCG positions (design LCG $\pm 7\%$). LCG position was referenced from the transom base.

A plan view of the model hull bottom is given in Figure 2.6 showing the relative locations of the LDV windows, pressure transducers (labeled P1 through P9), tow point, and LCGs.

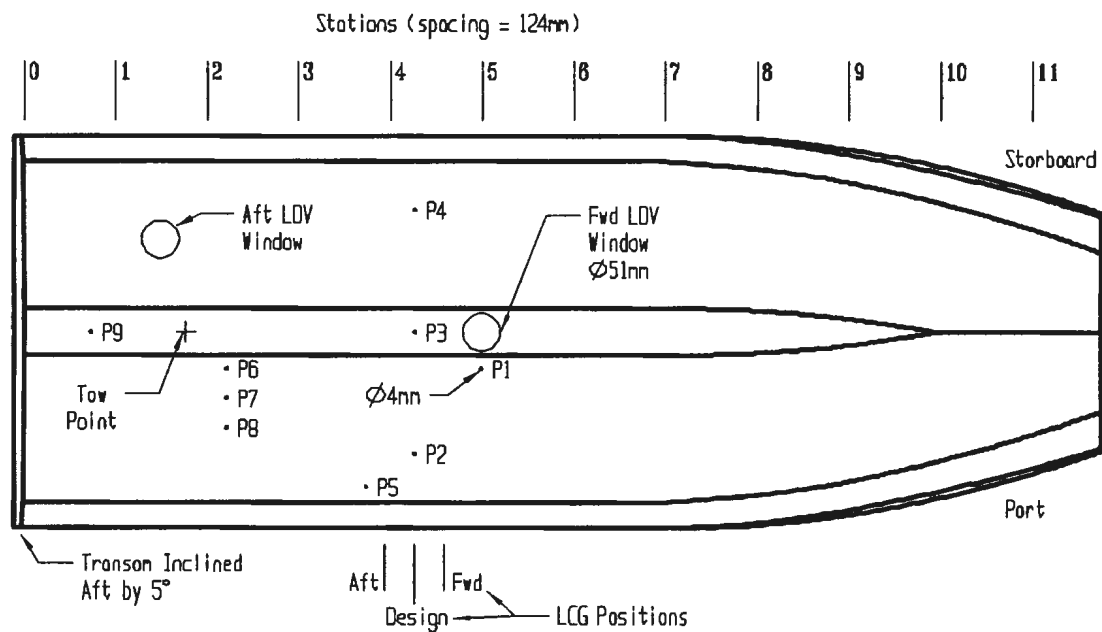


Figure 2.6 – Instrument Positions in Model

Displacement	LCG = 0.49 m	LCG = 0.53 m	LCG = 0.57 m
25.2 kg	-	1.0°	-
29.6 kg	2.0°	1.1°	0.4°
33.9 kg	-	1.3°	-

Table 2.2 – Static trim angles for ballast conditions

2.3 Test Results

The following sections present examples, with discussion, of the experimental data that was collected during testing. For reference purposes, complete tabulated sets of the data is included in Appendices A and B, with the exception of the wave profile data which was too large a set to be represented in this way.¹ Unless otherwise stated, data was sampled at 100 Hz for all instruments.

2.3.1 Resistance

The resistance curves for the model were typical for a planing vessel and had the characteristic ‘hump’ speed at the onset of planing. Figure 2.7 shows the resistance results for the various ballast conditions. Only the design condition was tested over the full speed range. The curves closest to the design condition show the effect of a 7% change of LCG (both fore and aft) on resistance, while the two more distant curves show the effect of a 15% change in displacement.

¹ Wave elevations were collected from 23 probes, acquiring data at 100 samples/second. Given approximately 200 runs, averaging 50 seconds of acquisition per run, the data set consisted of roughly 23,000,000 data points.

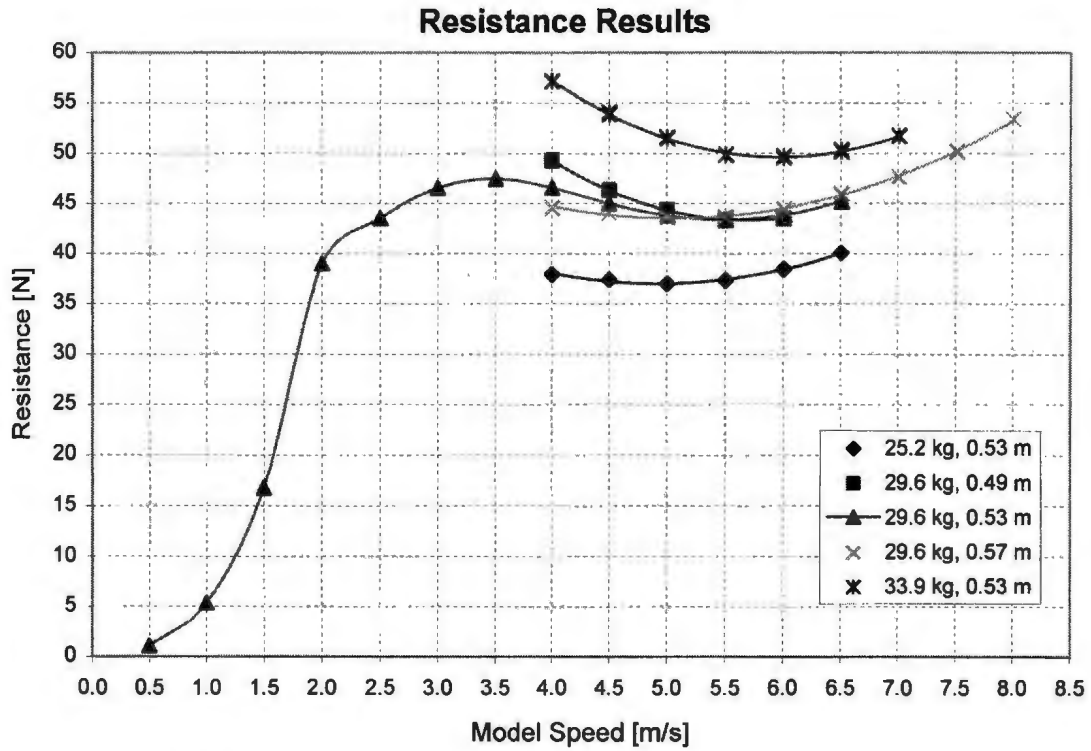


Figure 2.7 – Model Scale Resistance

2.3.2 Running Trim

Trim angle is an important factor in planing craft performance as it changes the geometry of the hull relative to the water. The running trim angles for this model followed similar trends as the resistance curves, clearly identifying the ‘hump’ speed at which planing begins. Shown in Figure 2.8 are the running trims for the various ballast conditions.

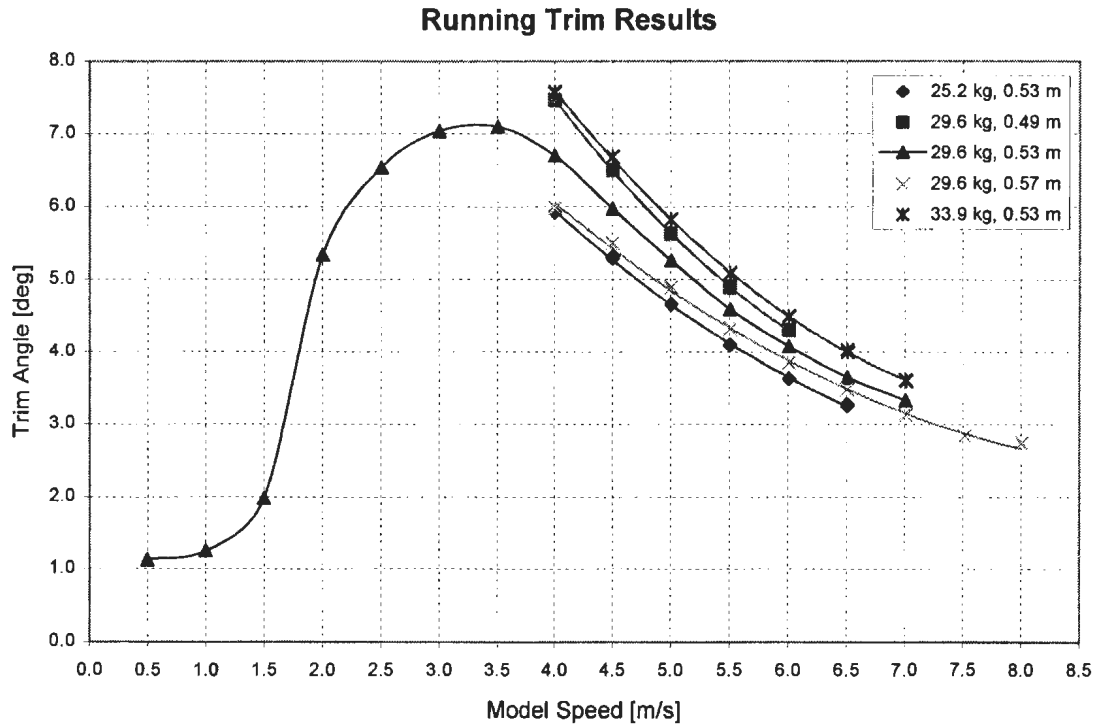


Figure 2.8 – Running Trim

It can be seen from the plots that the different ballast conditions were not tested to the same maximum speeds. For instance, the aft LCG ballast condition was only tested to 6.0 m/s while the forward LCG condition was tested to 8.0 m/s. This occurred because the model was prone to dynamic instability, or porpoising, at high speeds. The aft LCG position made the model susceptible to this instability at speeds above 6.0 m/s and was therefore not tested beyond that limit.

Another way of presenting the running trim results is to plot the change in trim angle developed at speed from the static trim angle at rest (see Table 2.2). This plot, given in Figure 2.9, shows that when in the planing regime, the threshold above which porpoising occurred was when the change in trim angle dropped below approximately 2.1°. More details of the porpoising characteristics of this model can be found in Thornhill *et al.*

(2000). This form of dynamic instability can be hazardous to a vessel and its crew and should be avoided.

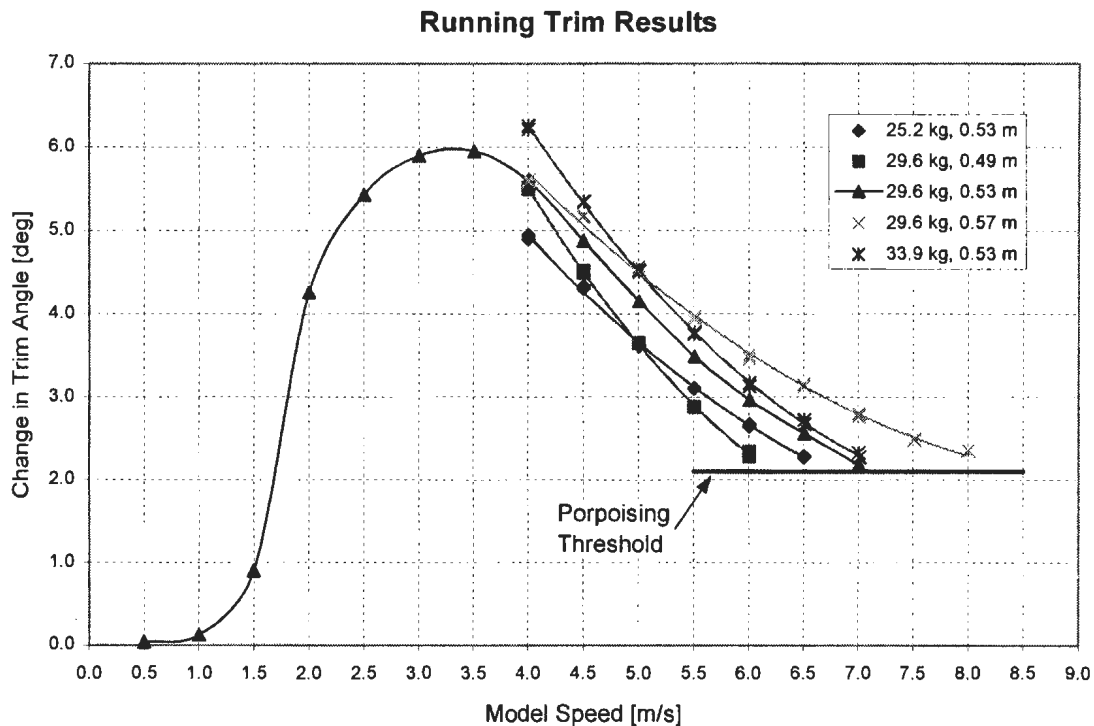


Figure 2.9 – Change in Trim

2.3.3 Sinkage Results

Sinkage refers to the change in the vertical position of the model at speed and was measured using an LVDT (linear voltage differential transducer) mounted on top of the heave post (see Figure 2.5). Shown below in Figure 2.10 is the sinkage profile for the design ballast condition. Also given in the figure is the trim profile for this condition. These are presented together because sinkage is related to trim angle (the model did not rotate about the tow point where sinkage was measured). At low speeds, the model began to trim by the stern and sank downwards in the water. As it climbed its bow wave, trim peaked and then began to decrease while the model continued to rise upwards. At high

speeds, trim angle continued to decrease while the vertical position leveled off to approximately 3.5cm above its original position.

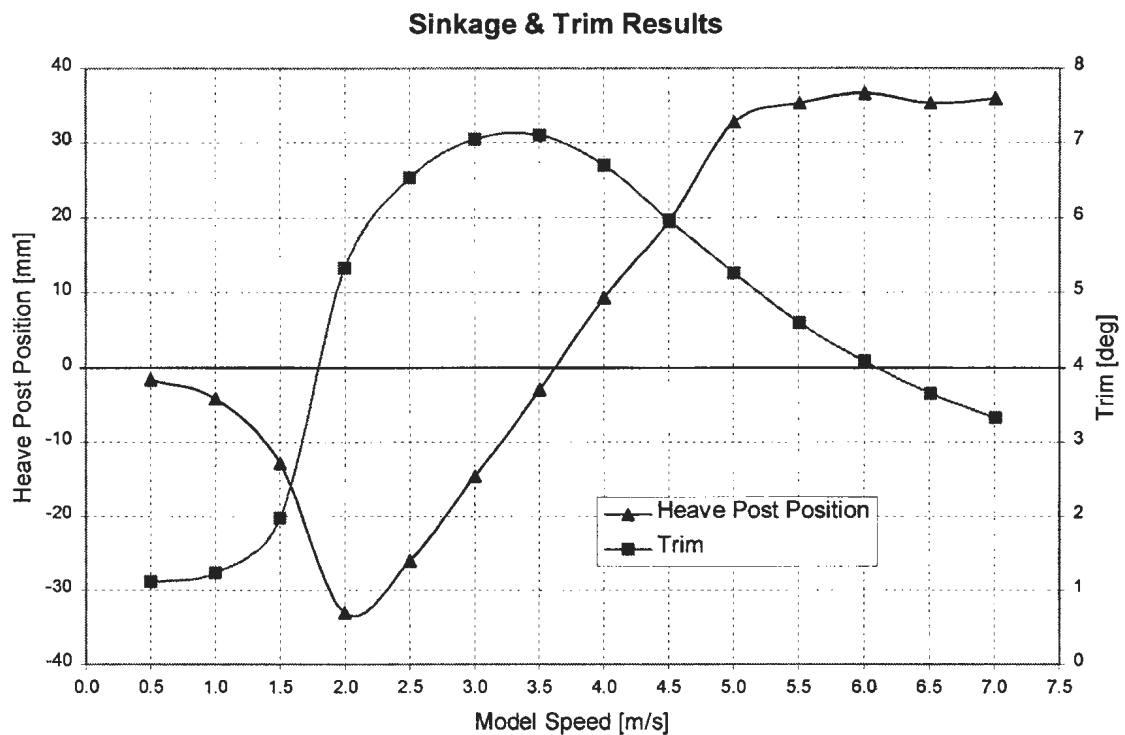


Figure 2.10 – Sinkage and Trim Results

2.3.4 Wave Profiles

The surface wave profiles produced by the model at speed were captured by a transverse array of capacitance probes located midway along the tow tank. The set contained 23 probes spaced 177.8 mm (7 inches) apart, the first being 177.8 mm from the side of the model. Sampled at 100 Hz, the time traces from the probes show the wave elevations at the various longitudinal cuts. A proximity switch was used to correlate the position of the model with the probe data; the tow carriage would trigger the switch when the model's bow was in line with the probe array. The probe array is shown in Figure 2.11 attached to

a beam fixed to the tank wall. An example of the data collected from the first three probes is shown in Figure 2.12.

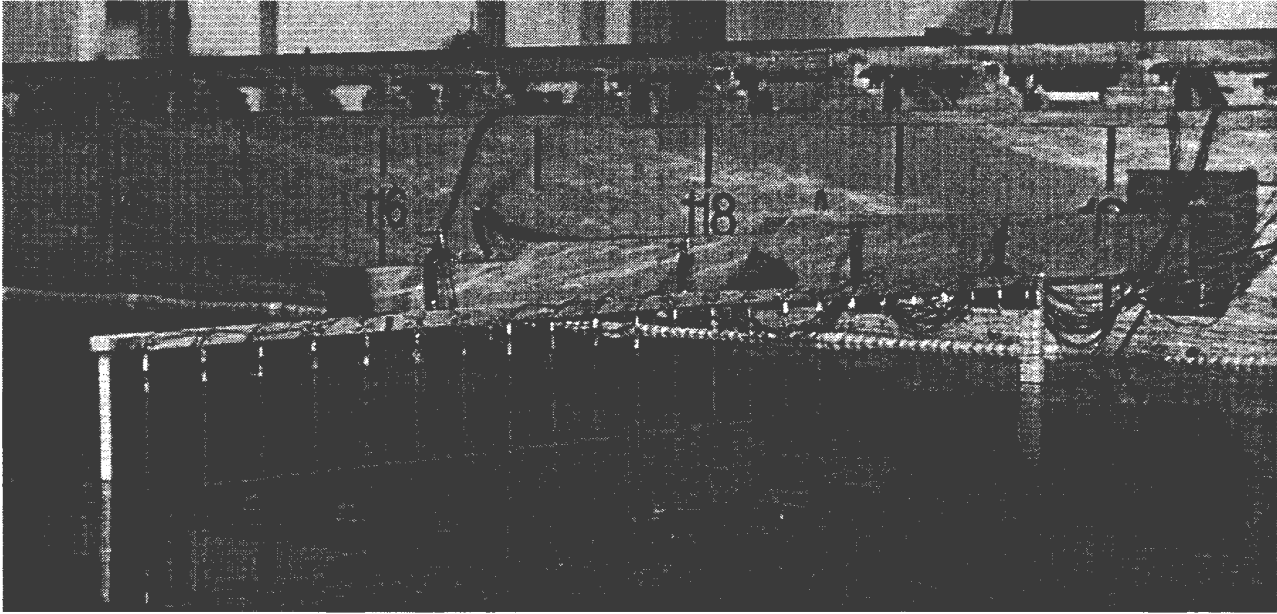


Figure 2.11 – Wave Probe Array in Tank

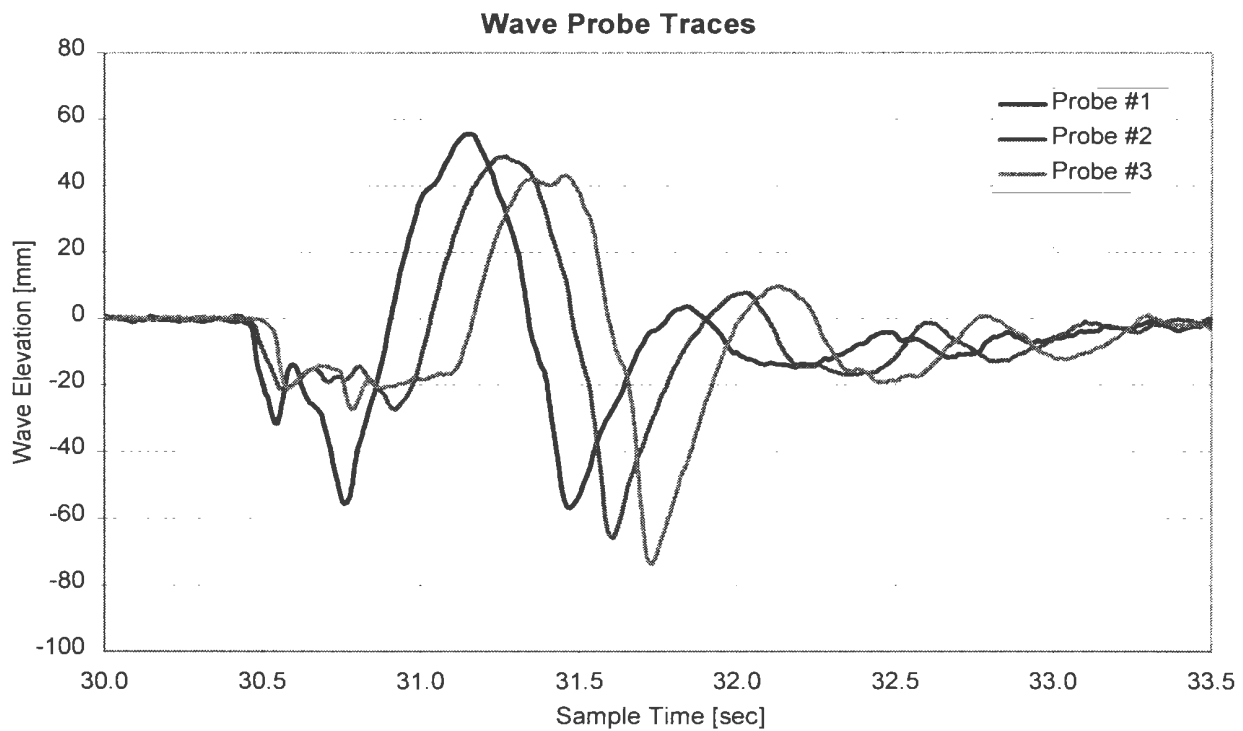


Figure 2.12 – Example Wave Probe Traces

The wave probe data was measured in terms of wave elevation verses sample time. It was converted to sets of data of wave elevation verses longitudinal position relative to the model by multiplying the sample time by the model speed and correcting for relative position using the proximity switch time. Once this was done, the data could be plotted as a surface allowing visualization of the wave profiles for each test. Shown in Figure 2.13 is an example wave profile from the probe data (using Matlab® version 6, release 12). Similar plots for the design ballast condition for model speeds from 1.0 to 7.0 m/s are given in Appendix D.

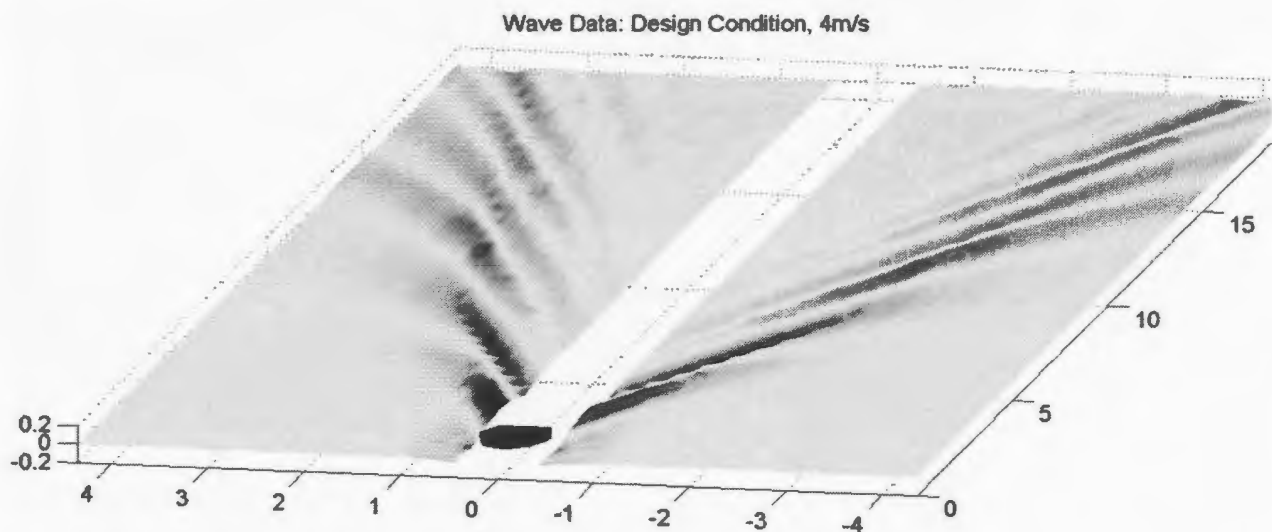


Figure 2.13 – Example Wave Profile

The wave profiles at lower speeds were in the form of the characteristic Kelvin wedge pattern (Lewis, 1988) with well-defined divergent and transverse waves. As speed increased, the waves grew in size and wavelength. At about 3.0 m/s, the transverse waves had lost most of their amplitude with nearly all of the wave energy moving in the divergent waves. Past this speed, the transverse waves virtually disappeared and the

divergent waves became smaller in height and traveled at ever decreasing angles relative to the path of the model, effectively closing the wedge shape of the wave pattern.

Further analysis of the data was conducted by isolating the crests and troughs of the waves as local maxima and minima on the individual probe traces. Wave angles and wave heights could then be determined for each test. Given in Figure 2.14 are the maximum wave heights and average wave angles (of the divergent waves relative to the path of the model) plotted against model speed. The wave heights show a clear rise with increasing model speed and reach a maximum at the “hump” speed of approximately 3.0 m/s which was also identified by the resistance (Figure 2.7) and running trim (Figure 2.8) plots. Past this point, maximum wave height was observed to decrease with further increase in speed. The average angle of the divergent waves decreased considerably with increasing speed (by nearly 40 degrees). This was evident by a narrower wave pattern at the highest speeds (see Appendix D).

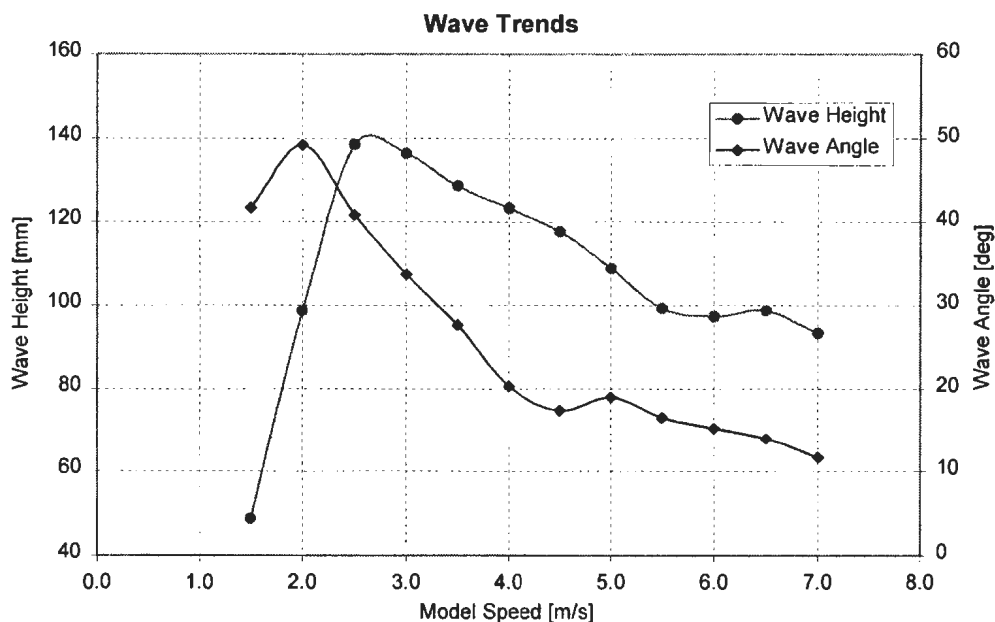


Figure 2.14 – Wave Trends

The wave data was also used to help quantify the components of resistance for a planing hull through measurement of the energy in the model's wave field. As a vessel moves forward at steady speed through calm water, it performs work on the water, partly in the form of waves. By calculating the energy in the waves, the component of resistance associated with wave making can therefore be determined.

A force F , multiplied by a distance d , is the work done for a system and is equal to the total change in kinetic and potential energy, ΔE , of that system.

$$F \cdot d = \Delta E \quad [2.1]$$

and can be re-expressed as:

$$F = \Delta E/d \quad [2.2]$$

For the present case, the force is the wave-making resistance on the hull, and ΔE is the energy of the wave system. By choosing the distance, d , to be 1 unit, the above equation becomes:

$$R_w = E'_w \quad [2.3]$$

where,

R_w is the wave-making resistance on the hull

E'_w is the energy of the wave system per unit length in the direction of vessel motion (referred to as energy density)

The energy density of the wave system should therefore equal the resistance of the hull due to wave generation. Wave energy was calculated by integrating the wave elevations

in a transverse slice of the wave field. Energy density was then determined by dividing the wave energy in the slice, by the length of the slice. Given that the vessel travels at steady speed through calm water, it was assumed that the energy density in the wave field was constant; any infinitely wide transverse slice should yield the same value. In terms of the experimental measurements, a slice to be sampled must be wide enough to traverse the entire wave field, and be made as long as possible in order to minimize error in the averaging step. As the width of the slice was set by the geometry of the wave probe array, the length of the slice was set to the point at which the width of the wave profile approached the width of the probe array. Shown in Figure 2.15 are the dimensions of a slice of a typical wave profile used for calculation of the wave energy density.

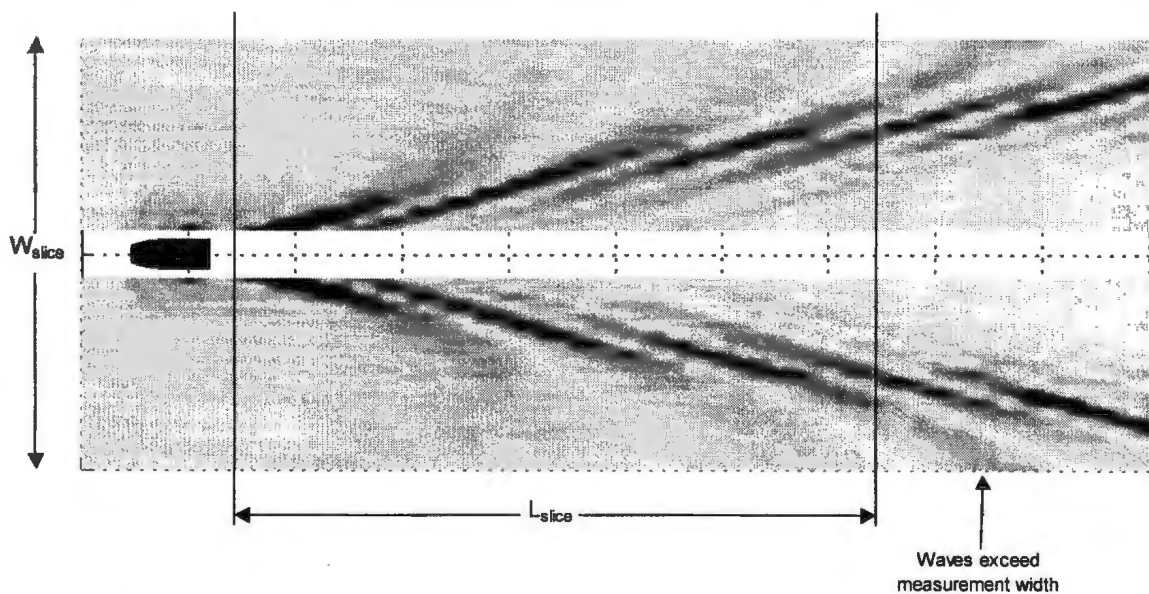


Figure 2.15 – Dimensions of Sample Slice

Using notation defined in Figure 2.16, the potential energy $d(\text{PE})$ in a small column of water is given by (Lighthill, 1978):

$$d(\text{PE}) = m \cdot g \cdot \bar{z} \quad [2.4]$$

Where \bar{z} is the distance from the baseline to the center of gravity of the column of water defined by:

$$\bar{z} = \frac{h + \eta}{2} \quad [2.5]$$

The mass m , is given by:

$$m = \rho \cdot (h + \eta) \cdot dx \cdot dy \quad [2.6]$$

The total potential energy of a wave of length L , and width W is therefore:

$$PE_T = \int_x^{(x+L)} \int_y^{(y+W)} d(PE) = \int_x^{(x+L)} \int_y^{(y+W)} \rho \cdot g \cdot \frac{(h + \eta)^2}{2} \cdot dydx \quad [2.7]$$

The potential energy due to the wave only can be determined by letting h equal zero, yielding:

$$PE_w = \int_x^{(x+L)} \int_y^{(y+W)} \frac{1}{2} \cdot \rho \cdot g \cdot \eta^2 \cdot dydx \quad [2.8]$$

Discretizing this for the sampled experimental data gives:

$$PE_w = 2 \cdot \sum_i \sum_j \frac{1}{2} \cdot \rho \cdot g \cdot \eta_{(i,j)}^2 \cdot \Delta y \cdot \Delta x \quad [2.9]$$

where,

- $\eta_{(i,j)}$ is the elevation at a given longitudinal position i , at a given probe j
- Δx is the longitudinal distance between samples in the x direction
(defined by the model velocity divided by the sampling rate)
- Δy is the transverse distance between the probes (177.8 mm). Δy for the probe closest to the model was extended to cover the distance to the center of the tank.

The limits on the summations depend on the size of the portion of the wave field being analyzed. An additional factor of two was included in the equation to account for both sides of the tank (wave probes were only placed on the starboard side of the model).

For conservative non-dissipative waves, only half of the total energy is potential energy, with the other half existing as kinetic energy (Dean, 1984). The total wave energy is therefore twice the potential energy.

$$E_w = 2 \cdot PE_w \quad [2.10]$$

The energy density of the wave per unit length in the longitudinal direction is then determined by dividing the total energy by the length of the slice.

$$E'_w = \frac{E_w}{L} \quad [2.11]$$

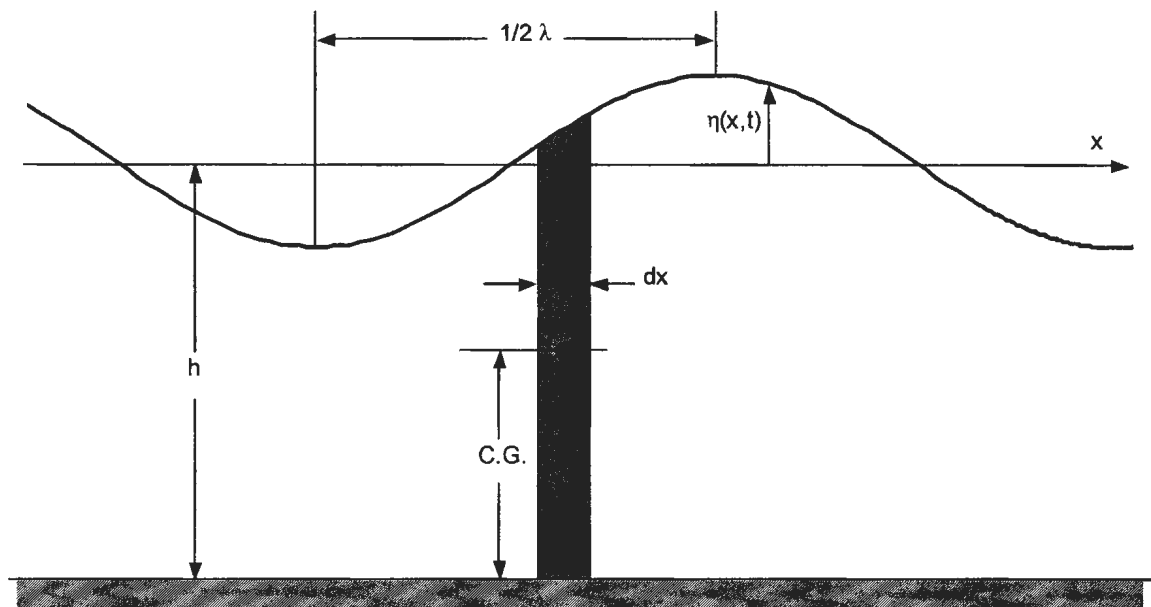


Figure 2.16 – Typical Wave

Shown below in Figure 2.17, is a plot of the resistance components of the planing hull model in the design ballast condition. The total resistance values are the results from the tow force measurement. The frictional resistance was calculated using the ATTC friction line (discussed in Section 3.2). The pressure resistance was determined by subtracting the frictional resistance from the total resistance, while the wave energy density was calculated by the method described above. The wave energy density was considerably lower than the pressure resistance, although it did follow the same trend of increasing to the hump speed then decreasing afterwards. This suggests that only about half the work done by the pressure forces on the hull was going into producing waves. The remainder would be used for spray production and other influences such as turbulence generation. The percentage of total energy going into spray seemed high, as the spray was not overly pronounced as shown in Figure 2.18

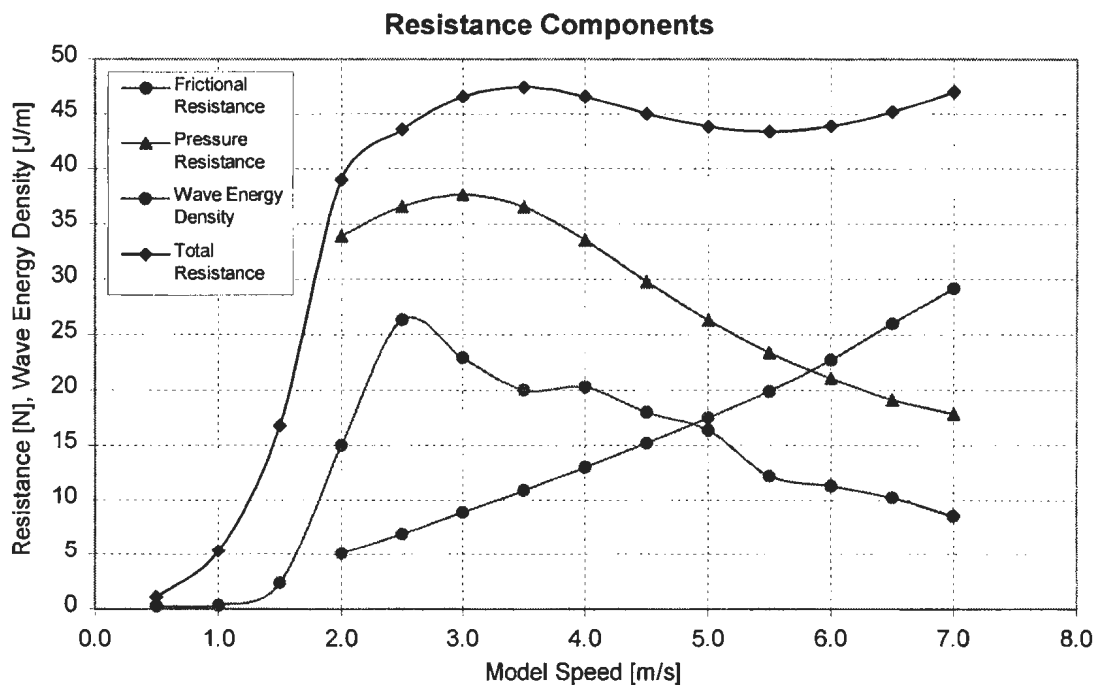


Figure 2.17 – Resistance Components

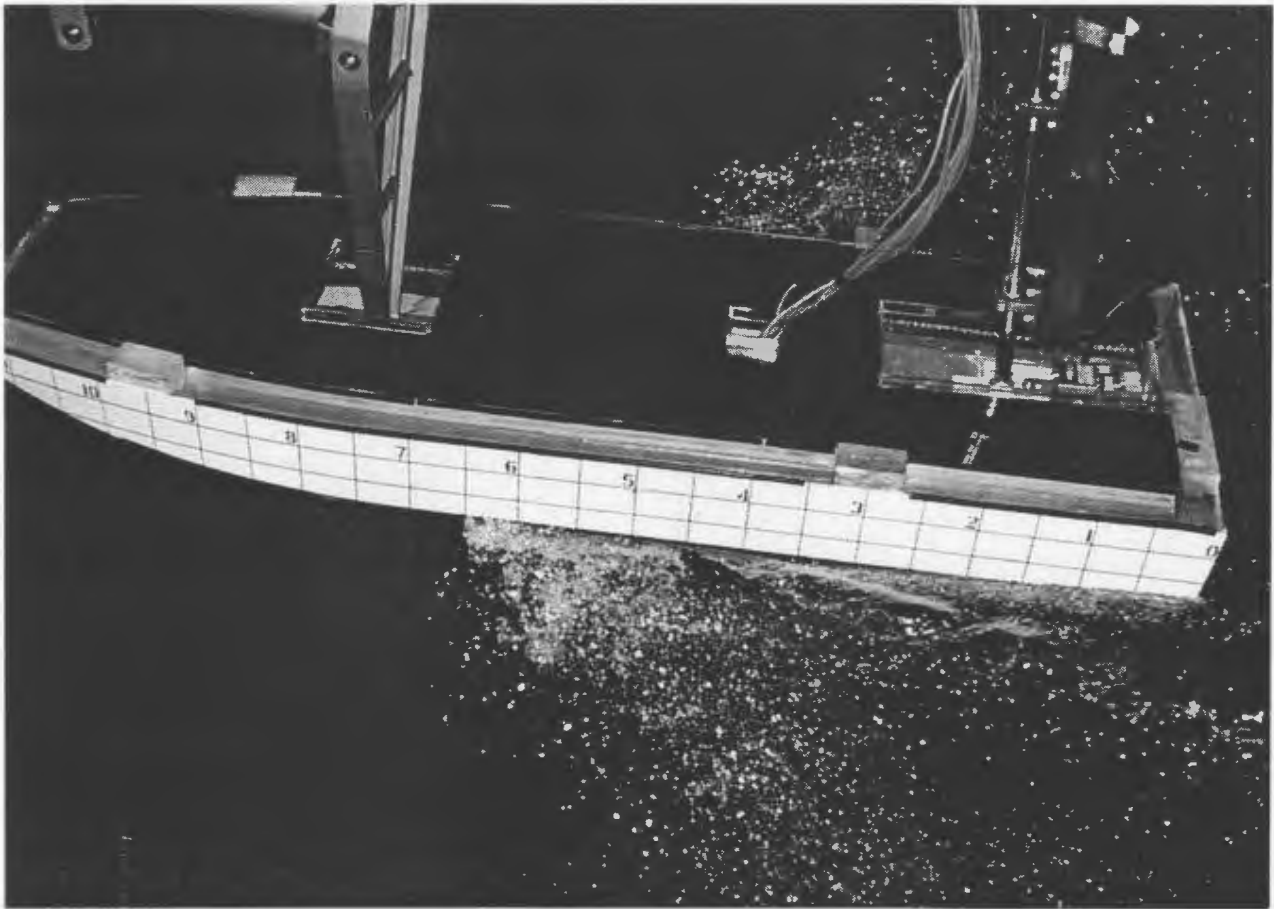


Figure 2.18 – Model at Speed (6.0 m/s)

2.3.5 Hull Pressures

Hull pressures on the model were measured using nine pressure taps mounted flush to the hull bottom at various locations (see Figure 2.6). Several of these pressure taps malfunctioned during tests while others encountered relatively high levels of noise (see Table 2.4). The results could not therefore be relied upon for specific quantitative information of the pressure distribution on the hull. They can, however, be used to identify certain trends that developed with increasing model speed. The most notable of these are shown in the Figure 2.19.

Figure 2.19 shows the pressure results for taps located on or near the centerline of the hull. The results at low speeds primarily represent hydrostatic influence until about 3.0 m/s, corresponding to the onset of planing, after which dynamic pressures became increasingly significant. Forward pressures were seen to grow with increasing speed, a result consistent with simple 2D planing theory. As the model velocity increased, the wetted length shortened, bringing the peak pressure region closer to the forward pressure taps. The aft pressure taps, however, show decreasing trends with increasing velocity. At the highest speeds, gauge pressure was even found to be negative. This result was not expected or supported by classical planing theory, which predicts positive pressures approaching a minimum of zero at the transom. Though an unusual result, references to experimentally measured negative pressures on model planing hulls have been made in both Du Cane (1974) and Hirano *et al.* (1990).

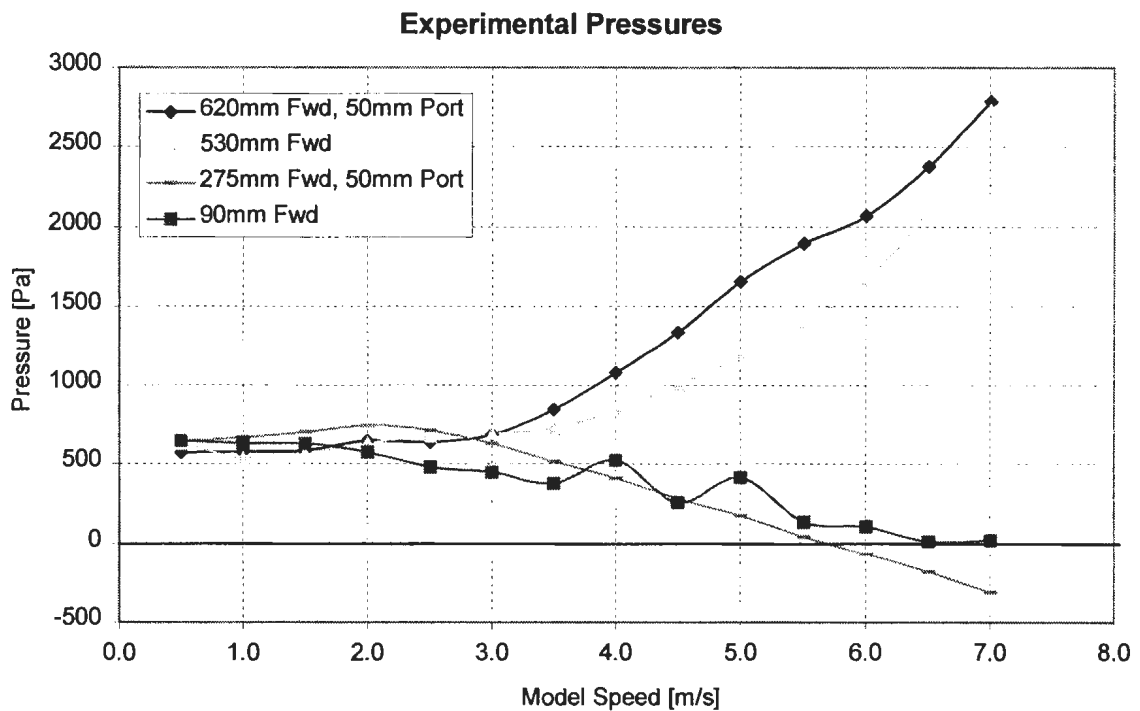


Figure 2.19 – Pressure Results: P1, P3, P6, P9

2.3.6 Boundary Layer Velocity Profiles

The second phase of the experimental program was dedicated to determining velocity profiles in the boundary layer at two locations for four different model speeds in the design ballast condition. The measurements were made using a laser Doppler velocimeter (LDV) fitted in the model. This instrument has several advantages over other more common techniques for velocity measurements such as pitot tubes and hot-film anemometry. Primarily, the LDV is non-intrusive; only laser light enters the water, so it has no influence on the thin layer of fluid where the measurements are made.

The LDV uses intersecting laser beams to make velocity measurements. Strictly speaking, the LDV measures the velocity of particles in the flow and not the flow itself. A particle, when traveling through the volume of intersection of the beams, reflects light as it passes through an interference pattern of light and dark bands caused by the lasers of matching wavelength. Processors in the LDV determine the frequency of this pulsating reflected light picked up by sensors in the probe. As the distance between the interference bands is known, the processor can then calculate the velocity of the particle. Numerous particle measurements are averaged to determine the mean flow velocity. Particles are added as “seed” to the flow and are generally in the size range of 0.5 – 5.0 microns. The measurement volume of the LDV depends on both the beam diameter and the angle of intersection. For these experiments the volume was an ellipsoid 0.64 mm in height (perpendicular to the hull) and 76 μm in diameter.

Seeding is an important part of LDV testing as it controls both the data rate (the number of particles passing through the intersection volume per second) and validation (the

percentage of particles that could be processed into velocity measurements). For these experiments, seed was added for each test by aiming a small stream of a concentrated water/seed mix into the path of the model. Several types of seed were used, including silver-coated glass micro-balloons (average diameter 10 μm) and pre-sifted all-purpose flour. Both of these seed types behaved well, though the flour presented a considerable cost savings. Data rates for the experiments ranged from 30 to 3000 Hz with validation between 60-95%. Typical values for most tests were data rates around 500 Hz with 75% validation.

The set-up for the experiments had the LDV probe mounted inside the model on a set of micrometer tables used to position the probe for each measurement. The probe faced downward and projected the lasers through a small acrylic window in the hull. The beams intersected at a point just below the window where a measurement was taken (see Figure 2.20). The micrometer tables were used to precisely position the probe at different locations within the boundary layer. A single run of the carriage was used to measure the velocity of each point in the boundary layer at each model speed. Successive runs were needed to resolve the velocity profile for a given model speed.

Raw data from a typical test is given in Figure 2.21. It shows the acceleration, constant speed, and deceleration portions of the run. The figure also shows that the raw velocity data fell onto equally spaced discrete values (seen as bands of points). This feature is an artifact of the LDV's internal processors that determine the particle velocities. The width between these bands can be changed, but doing so also alters the range of velocities that

can be measured. A smaller bandwidth results in a smaller velocity range. These experiments used a bandwidth of approximately 0.1 m/s.

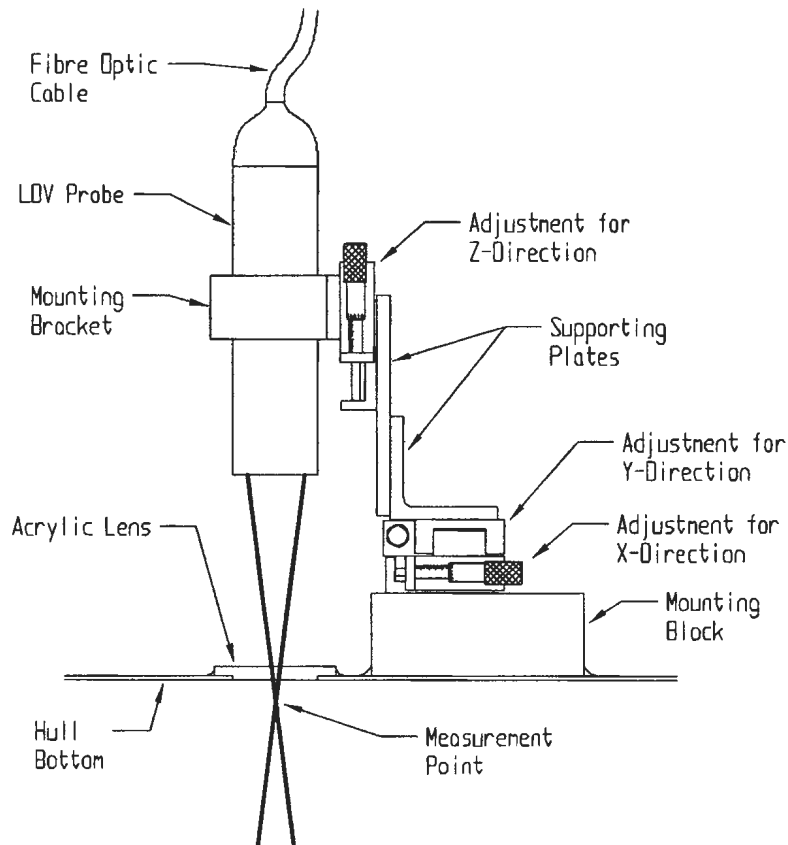


Figure 2.20 – LDV Mount

Boundary layer velocity profiles for two positions on the hull for each of four model speeds (4.0 m/s, 5.0 m/s, 6.0 m/s and 6.5 m/s) were measured. Results for the model speed of 4.0 m/s are given below in Figure 2.22; a complete set of results is given in Appendix B.

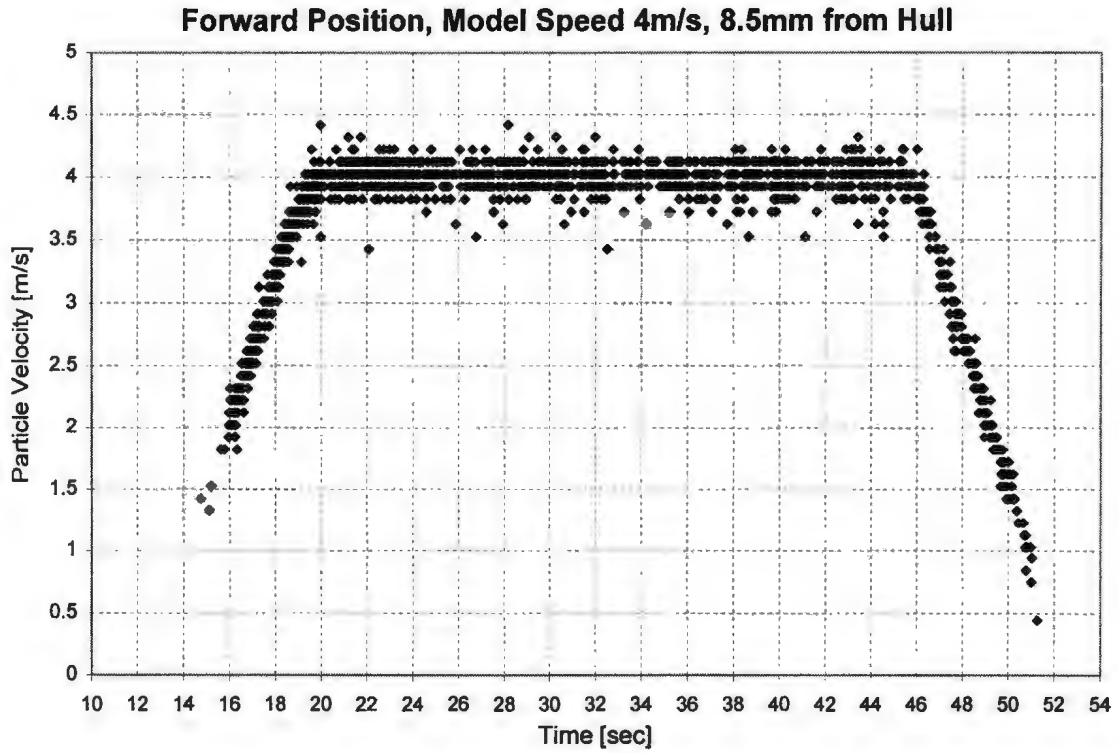


Figure 2.21 – Typical LDV Data

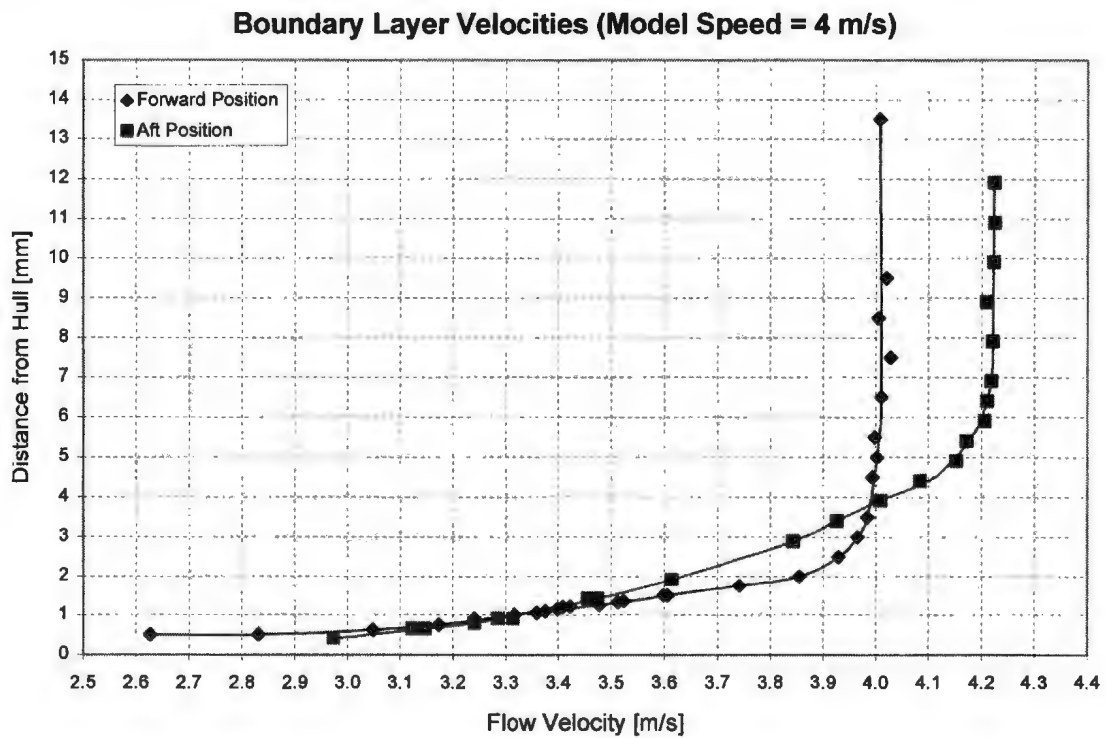


Figure 2.22 – Boundary Layer Velocities (Model Speed = 4.0 m/s)

The results from these measurements clearly show the boundary layer velocity form, thickness, and the free stream velocity for both of the two locations at each speed tested (for a total of 8 profiles). In the figure, the forward position shows a boundary layer thickness of about 4 mm with a free stream velocity equal to the model velocity. The aft position shows that the boundary layer had grown thicker and that the flow achieved a greater free stream velocity, exceeding that of the model speed. The positions of the forward and aft measurement positions relative to the leading edge of the wetted hull area for a given model speed are shown below in Figure 2.23.

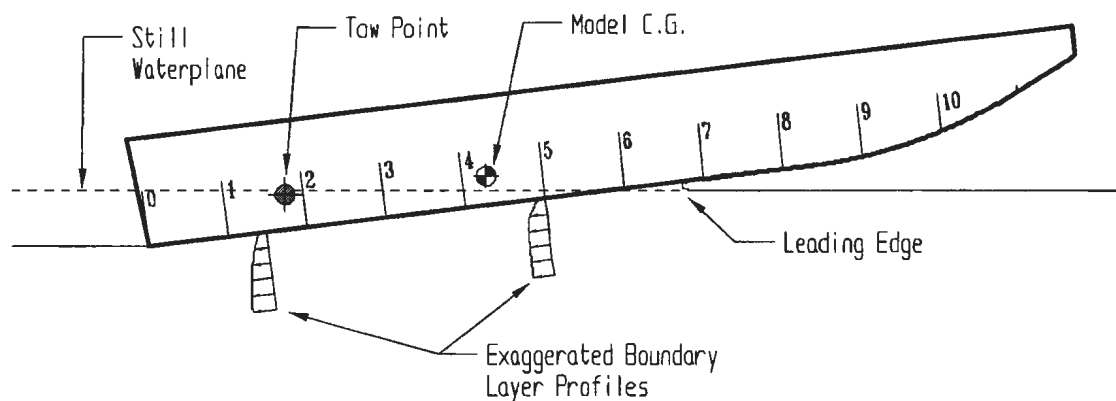


Figure 2.23 – Vessel Attitude (4.0 m/s)

In general, boundary layer thickness decreased with increasing model speed as expected. It was also observed that the percentage increase in free stream velocity from the forward to the aft position tended to decrease as the model speed increased (trim angle also decreased). A linear relationship was found between the velocity change of the flow between the forward and aft locations and trim angle. This velocity change was used in a non-dimensional form given by equation [2.12] and is shown plotted in Figure 2.24. This was an unexpected result. According to planing theory, the free stream velocity should

not exceed the model speed below the hull. It is possible that a slight bias error caused by imperfect hull windows could be responsible. However, it was not possible to check for such an error with the equipment available.

$$\Delta V = \frac{V_{Aft} - V_{Fwd}}{V_M} \quad [2.12]$$

where,

ΔV is the change in velocity from the aft to fwd position

V_{Aft} is the free stream velocity at the aft LDV window

V_{Fwd} is the free stream velocity at the forward LDV window

V_M is the model speed

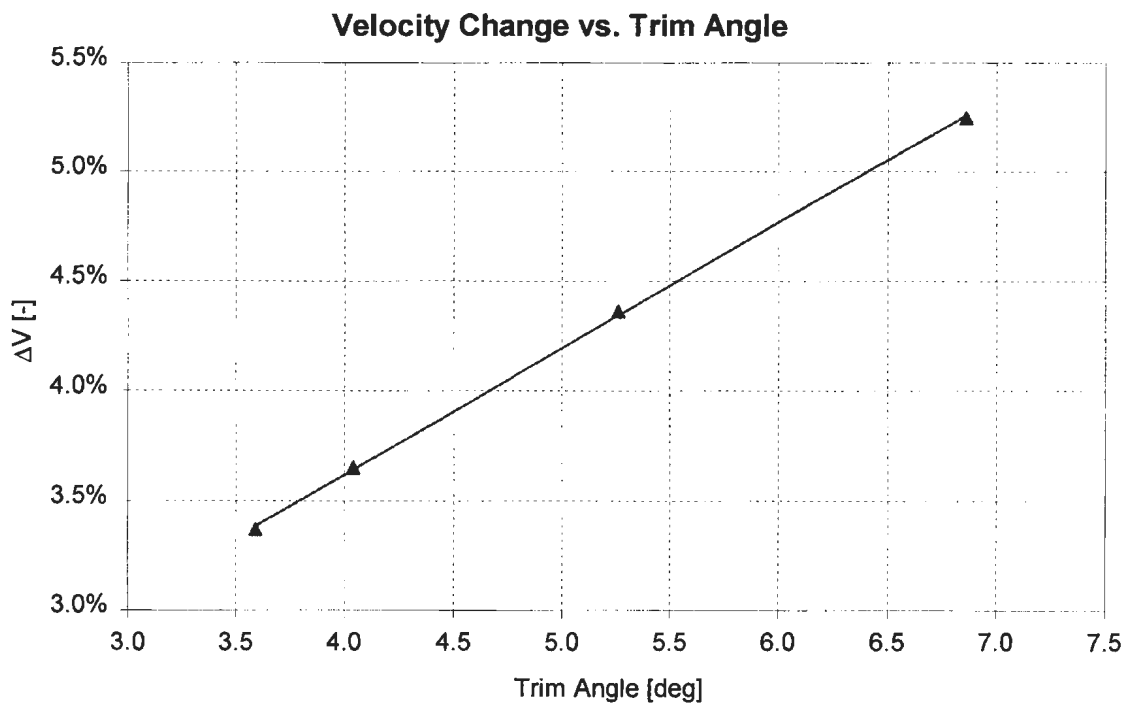


Figure 2.24 – Velocity Change vs. Trim Angle

A simple analysis of the pressure/velocity relationship on the hull can be performed using Bernoulli's equation at two positions on the hull, as shown in equation [2.13] and Figure 2.25.

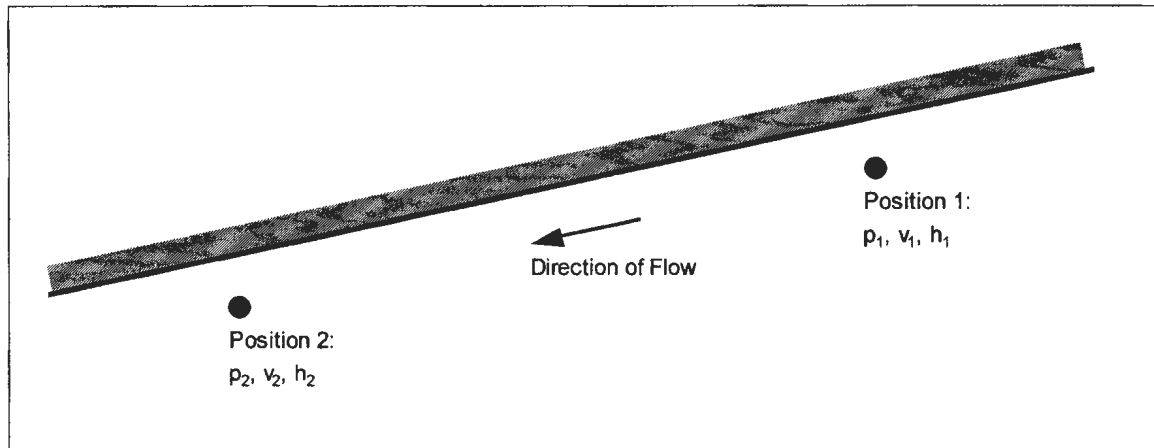


Figure 2.25 – Flat Plate Analysis

$$\frac{p_1}{\rho} + \frac{v_1^2}{2} + gh_1 = \frac{p_2}{\rho} + \frac{v_2^2}{2} + gh_2 \quad [2.13]$$

where,

p_1, p_2 are the pressures at positions 1 and 2 respectively

v_1, v_2 are the free stream velocities at positions 1 and 2 respectively

h_1, h_2 are the elevations at positions 1 and 2 respectively

Re-arranging this equation gives:

$$\Delta p = \Delta p_D + \Delta p_H \quad [2.14]$$

where,

Δp is the total change in pressure: $(p_2 - p_1)$

Δp_D is the change in dynamic pressure (due to velocity): $\frac{1}{2}\rho(v_1^2 - v_2^2)$

Δp_H is the change in hydrostatic pressure (due to elevation): $\rho g(h_1 - h_2)$

Using these equations, the following figure was created. The experimental pressure change was determined from the pressure tap results. The hydrostatic pressure change was calculated as above using the difference in height between the two positions (which varied with trim angle). The dynamic pressure change was calculated using the free stream velocities measured with the LDV. The total pressure change was the sum of the hydrostatic and dynamic pressure changes.

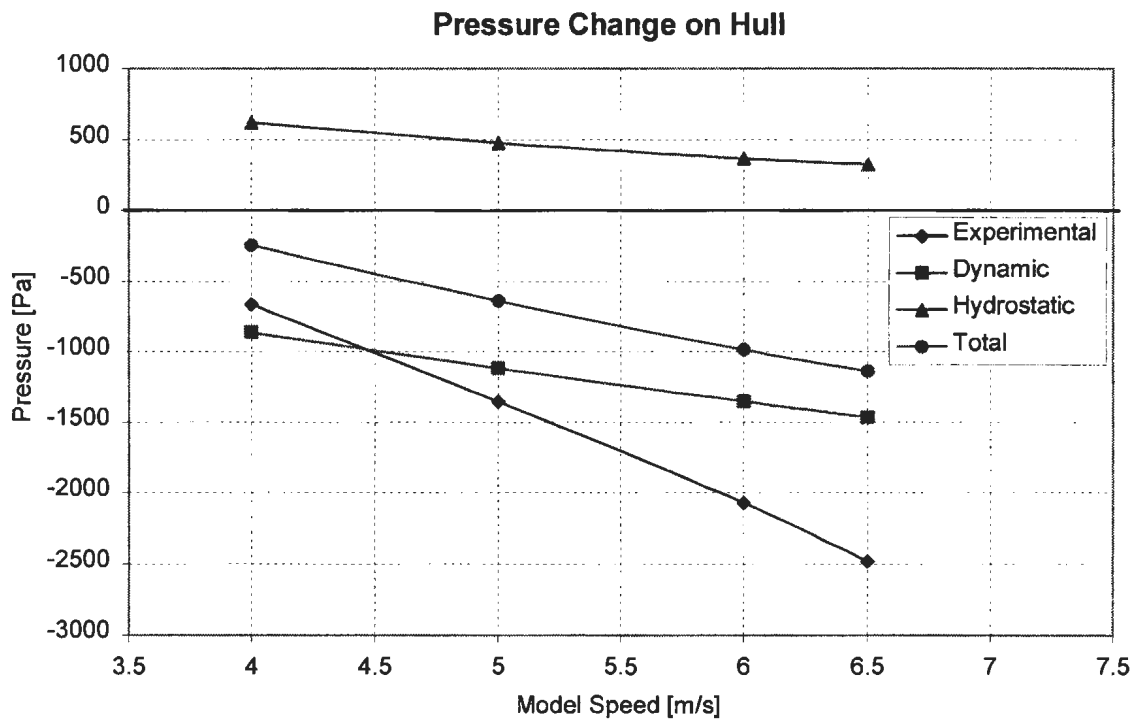


Figure 2.26 – Pressure Change on Hull

The results in the figure calculated with Bernoulli's equation using the LDV measurements show decreasing trends, as do the experimental pressure measurements. The magnitudes and slopes of the two curves, however, were not in good agreement. The measured pressure change on the hull was more pronounced and decreased more rapidly with increasing speed than indicated by the free stream velocity results. The flow

dynamics were therefore not modeled well by irrotational flow analysis, perhaps due to the presence of significant levels of turbulence and vorticity.

One difficulty with the LDV measurement technique was the determination of the reference or zero position of the hull surface. The procedure for finding this zero position consisted of systematically moving the measurement point closer to the lens until the photo-detectors gave an overload error. This meant that the measurement volume was inside the lens, and that the beams were reflecting directly back to the detectors. It was, however, possible that measurements could be taken with a small portion of the measurement volume inside of the lens, without overloading the photo-detectors. The size of this overlap could not be determined. The orientation of the probe meant that the largest dimension of the measurement volume (0.64 mm) was perpendicular to the hull. It was assumed that measurements could not be made if more than half of the measurement volume was inside the lens. This gives an uncertainty in the hull zero position for the LDV measurements of approximately 0.32 mm. The shape of the profiles is not affected by this bias, which would shift the entire curve up or down.

Another result from the analysis of the raw LDV data came from the standard deviations of the samples used to calculate the mean flow velocities. Shown in Figure 2.27, the standard deviations followed a similar trend as the velocities. High standard deviations were measured close to the hull, while in the free stream they leveled off. The higher values close to the hull can be attributed to two primary factors: turbulence and velocity gradient. Wall bounded turbulence in the boundary layer can cause fluctuations in velocity that would result in increased standard deviation. The large velocity gradient

close to the hull would also result in increased standard deviation since a broader range of velocities spanning from the bottom to the top of the measurement volume would have been captured.

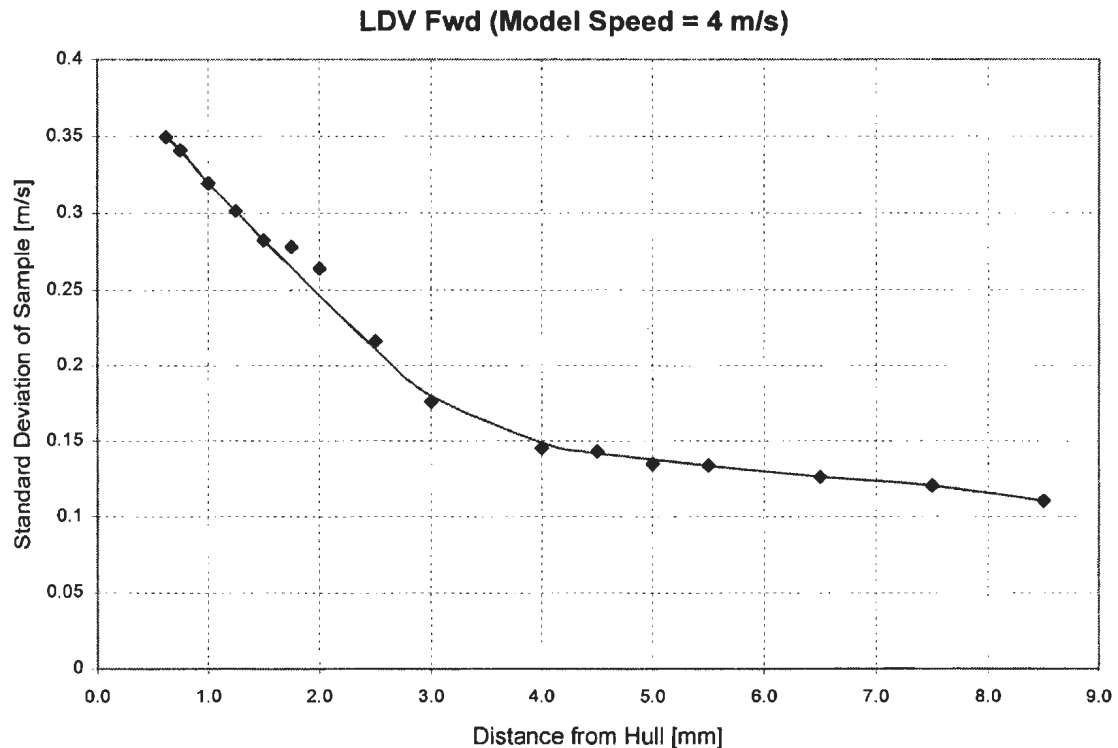


Figure 2.27 – Standard Deviations from LDV Data

2.4 Experimental Uncertainty

During the second phase of experiments (used to determine the boundary layer velocity profiles with the LDV), data was also collected for: model speed, tow force, trim, sinkage and hull pressure. For a given LDV configuration (aft or forward location), the model was run at essentially the same ballast condition for an average of about 25 runs for each model speed. The only changes from run to run were small vertical movements (a few millimeters) of the LDV probe as it measured the velocity at different positions in the

boundary layer. These runs were used to estimate the random errors for certain measurements. An example of the procedure used is given below for tow force.

There were 30 tests performed at 4.0 m/s for the model with the LDV in the aft position measuring boundary layer velocities. Assuming that the small changes in the model's center of gravity caused by the movement of the LDV probe from run to run were negligible, these tests can be considered to be identical. Although identical, the 30 tow force values showed some variation resulting from precision error associated with this measurement. Table 2.3 divides the tow force values into "Bins" and gives the number of values that fell into each bin. The "Normalized" values are the bin values divided by the mean of the tow force values. Figure 2.28 shows the histogram given by the data in Table 2.3. The curve produced is similar to the characteristic bell-shape associated with random error. The total range of the variation for this case was found to be ± 0.3 N, however, when other cases were examined the total variation for the tow force measurement was determined to be approximately ± 0.5 N.

Misc. Info.	Bin [N]	Normalized	Frequency
Max. Value [N] = 48.4801	Less	0.992	0
Min. Value [N] = 47.9026	47.9026	0.995	1
Mean Value [N] = 48.1508	48.0470	0.998	7
(Max. - Min.) [N] = 0.5775	48.1913	1.001	10
Number of Values = 30	48.3357	1.004	8
	48.4801	1.007	4
	More	1.010	0

Table 2.3 – Typical Instrument Variation

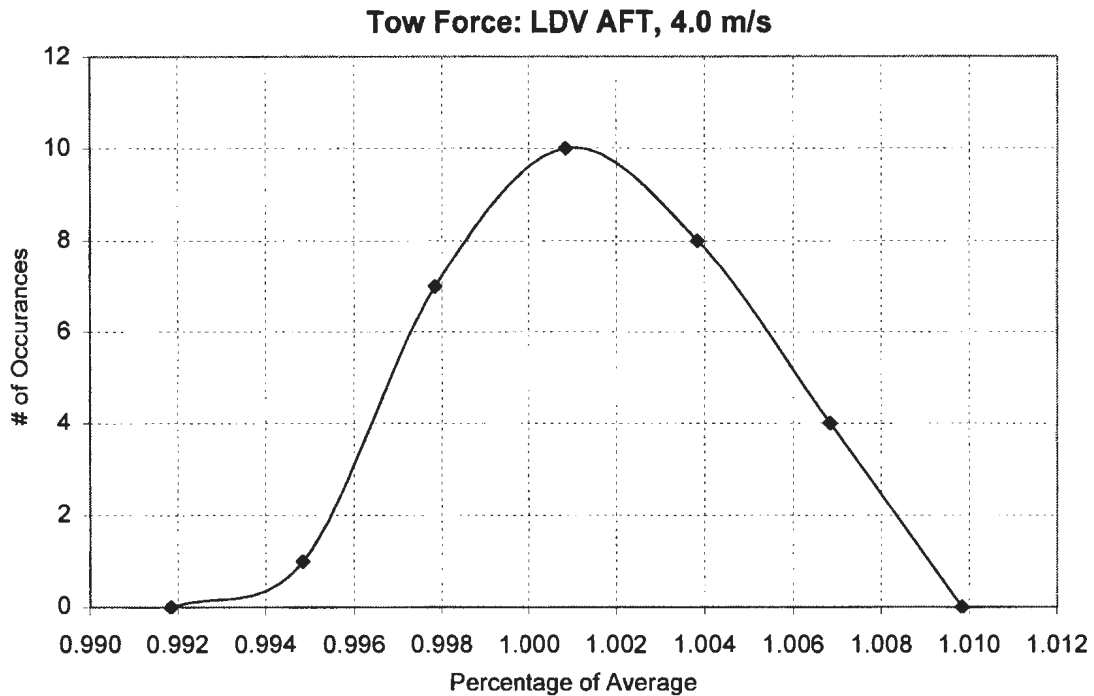


Figure 2.28 – Typical Instrument Histogram

A similar procedure was applied to the other parameters measured. The results of the analysis are given in Table 2.4. The precision values “from tests” represent the average range of values of each parameter over sets of identical tests. For example, the range of tow force values at one model speed may be ± 0.3 N, but the average over all model speeds was found to be ± 0.5 N. The precision for each instrument, provided by the manufacturer, is also given. The most notable of the results were for the LVDT and pressure transducers. The large value of uncertainty for sinkage was a result of the sensitivity of this measurement to factors such as model trim, small surface disturbances, and long period “sloshing” waves in the tank. The large uncertainties for the pressure transducers were a result of both noise in the signal, and from the fact that the pressures measured covered only a small portion of the total range of these instruments (more

sensitive transducers were not available for these tests). A complete set of the phase II data for these instruments is tabulated in Appendix C.

Instrument	Notes:
Tow Force	<i>Instrument: 50 lb. S-Shaped Load Cell</i> <i>Precision (from manufacturer) = ± 0.2 N (0.01 lbs.)</i> <i>Precision from tests = ± 0.5 N</i>
Trim	<i>Instrument: 14.9° inclinometer</i> <i>Precision (from manufacturer) = $\pm 0.005^\circ$</i> <i>Precision from tests = ± 0.05 degrees</i>
Sinkage	<i>Instrument: LVDT (150mm range)</i> <i>Precision (from manufacturer) = ± 0.3mm</i> <i>Precision from tests = ± 5 mm</i>
Pressure Transducers B-Type	<i>Instrument: Endevco Model 8510B: 100kPa (15 psi)</i> <i>Precision (from manufacturer) = $\pm 0.8\%$ of full pressure</i> <i>Precision from tests = $\pm 15\%$</i>
Pressure Transducers C-Type	<i>Instrument: Endevco Model 8510C: 100kPa (15 psi)</i> <i>Precision (from manufacturer) = $\pm 0.17\%$ of full pressure</i> <i>Precision from tests = $\pm 15\%$</i>
Model Speed	<i>Instrument: Carriage speed sensing system</i> <i>Precision (from manufacturer) = ± 1 mm/s</i> <i>Precision from tests = ± 2 mm/s</i>

Table 2.4 – Instrument Precisions

The test data was also influenced by other uncertainties shown below in Table 2.5. These parameters could not be analyzed in the same manner as those described above. They were instead estimated by the author to provide a rough indication of their precision. In the table, “Model Alignment” refers to the alignment of the model in the tank relative to

the carriage direction. “LDV Alignment” refers to the alignment of the lasers relative to the longitudinal axis of the model.

Parameter	Notes:
Model Weight	<i>Estimated uncertainty: ± 0.05 kg</i>
Model C.G.	<i>Estimated uncertainty: ± 0.01 m (on each axis)</i>
Static Trim Angle	<i>Estimated uncertainty: $\pm 0.05^\circ$</i>
Resting Draft	<i>Estimated uncertainty: ± 3 mm</i>
Model Alignment	<i>Estimated uncertainty: ± 1.0 degrees</i>
LDV Velocity	<i>Estimated uncertainty: ± 0.05 m/s</i>
LDV Alignment	<i>Estimated uncertainty: ± 1.0 degrees</i>
LDV Position (in B.L.)	<i>Precision of micrometer tables: ± 0.01 mm</i>
Model Geometry	<i>Estimated uncertainty: ± 0.5 mm</i>
Tow Point Location	<i>Estimated uncertainty: ± 2 mm (on each axis)</i>

Table 2.5 – Other Model Uncertainties

2.5 Summary

Tests were performed on a 1/8 scale model of a planing vessel to generate a set of performance data to be used for validation of numerical simulations. Sample results were presented for the measurements of resistance, running trim, sinkage, hull pressures, wave profiles, and boundary layer velocity profiles. Resistance and running trim results showed characteristics common to planing craft. Hull pressure measurements were not reliable quantitatively, but did show general trends. Boundary layer thicknesses were found to increase in the direction of flow and to decrease with increasing model speeds. The results from these tests were used to evaluate the numerical simulations discussed in Chapters 3 and 4.

CHAPTER 3

NUMERICAL SIMULATIONS

3 NUMERICAL SIMULATIONS

Before dynamic equilibrium was addressed, simulations of the flow field around the model hull were first performed with Fluent (version 5.3.18) in order to establish the optimum configuration for this type of problem. CFD simulations can be lengthy operations requiring considerable computer resources. It is therefore advantageous to determine the most efficient combination of mesh and solution parameters in the simulation, which lead to the best results in the shortest time. Following a brief review of related literature, this chapter discusses the methods used for setting up the planing hull problem, such as mesh creation and solver configuration. The analysis method is then described, followed by a discussion of typical simulation results.

The field of computational fluid dynamics is an extremely active area of research. As a result, there is considerable published work available and new developments occur

frequently. The following survey is not intended to completely encompass the body of existing literature. It is instead limited to work directly related to methods specifically relevant to the proposed research. A brief review is first given on work relating to ship resistance in general. This consists of two review-type reports on the subject followed by a few examples of specific work in numerical ship resistance.

The final report and recommendations to the resistance committee of the most recent International Towing Tank Conference (Stern *et al.*, 1999) contains a thorough review of the state-of-the-art of numerical methods for ship flow and ship resistance calculations. It noted that most examples of solvers for the viscous flow around a ship hull had not yet met up with the promise of this technique. Difficulties in simulating and validating full scale flows have resulted in most practical prediction work being conducted at model scale. Currently, the accuracy of many solvers is more beneficial for providing qualitative evaluations of flows rather than concrete quantitative results. The report discussed the various grid generation strategies with respect to ship flow problems; it noted that this is often the most time consuming part of a CFD calculation. Structured grids and multi-block structured grids are currently the most commonly used in ship flow problems. The application of unstructured grids in ship hydrodynamics is still relatively limited. Various solution methods were also discussed, including those for capturing the free surface such as marker-and-cell (MAC), volume-of-fluid (VOF), and level set techniques. Most methods for steady flow calculations opt for fully time-dependent solutions. During a simulation, the hull was usually accelerated from rest to the desired speed where time integration would continue until a steady-state had been obtained. This method was found to provide some numerical advantages over non time-dependent solutions. An area noted

for improvement was the proper simulation of the wake field for most vessel types. Far field waves were consistently under-predicted by RANS/FS codes (RANS solvers with free surfaces) and lacked detail. This has been attributed to poor spatial resolution. As with RANS solvers for any application, the presence of a turbulence model limits the accuracy of the solution. Better turbulence models tuned for ship flow problems were seen to be desired.

A work by Hochbaum and Schumann (1999) discussed the development of a RANS (Reynolds averaged Navier Stokes) solver for computing the free surface viscous flow around a ship model at steady forward speed through calm water. It employed the volume of fluid method with a $k-\epsilon$ turbulence model (Wilcox, 1993) and captured the free surface using a level set technique. Surface tension was not taken into account and wall functions were used for calculations near solid boundaries. The conservation equations were discretized using a non-orthogonal body fitted structured grid. Coarse and fine grid meshes were tested for a Series 60 ship model (only half the ship was modeled with a plane of symmetry at the longitudinal axis). The model was accelerated from rest to steady speed. It was found that the coarse grid solution underestimated the frictional resistance and overestimated the pressure resistance leading to small differences when comparing overall resistance between coarse and fine grids. The fine grid of approximately 400,000 cells took about 150 hours to compute a steady state solution on an HP workstation. The level set technique used here was found to be comparable to other more complicated moving grid methods in the near field, but became numerically damped in the far field.

The work presented in Alessandrini and Delhommeau (1996) was the predecessor to that of Gentaz et al. (1999). It described an original method for the solution of the Navier-Stokes equations with a free surface for the calculation of free surface flow of viscous incompressible fluid around a boat hull moving with steady rectilinear motion through calm water. A $k-\epsilon$ turbulence model was used. The 3D RANS equations were solved using a fully coupled method that accounted for the exact free surface conditions and the kinematic conditions near the hull on a domain meshed with multigrid techniques. A Series 60 hull shape (block coefficient = 0.6) was tested with coarse (190,005 nodes) and fine (314,265 nodes) grids. Accelerating from rest, 300 time steps were required to achieve steady state taking about 30 hours of CPU time on an HP-J200 workstation (for the coarse mesh). The results were found to be comparable to experimental results but further grid refinement was seen to be needed (500,000 to 600,000 nodes) for better resolution of physical quantities.

Takai and Zhu (1994) presented results from numerical simulations of free surface viscous flows about a ship hull using an arbitrary-Lagrange-Euler finite volume method based on the solution of the 3D time dependent RANS equations in a curvilinear boundary-fitted coordinate system. The method was developed to better simulate wave-ship interactions by accounting for moving or deforming boundaries. An algebraic sub-grid eddy viscosity model was used (Smagorinsky formulation with Van Driest damping function). The model began at rest and was accelerated to a steady speed. Time marching continued until the solution converged to a tolerance. Two simulations of a Series 60 (block coefficient = 0.6) were presented. The first at a Froude number of 0.160 consisted of 72,075 nodes and took 200 minutes of CPU time on a NEC SX-3 computer. A second

simulation at $Fn=0.315$ with 228,811 nodes took 630 minutes. The resulting wave profiles showed good agreement with experimental results.

Löhner, Yang, and Oñate (1998) developed an unstructured grid-based parallel method for solving viscous free-surface hydrodynamics problems. The overall scheme combined a finite-element, equal order, projection type three-dimensional incompressible flow solver with a finite element, two dimensional advection equation solver for the free surface equation. Unstructured tetrahedral grids were formed using an advancing front technique. Meshing near solid boundaries was done at a higher resolution to capture the boundary layer. Two turbulence models were used: the Baldwin-Lomax model and the $k-\epsilon$ model. For steady-state applications, the surface mesh was not updated at every time step in order to reduce computational costs. Results from a submerged NACA profile and simulations with the Wigley hull showed good quantitative agreement with experimental results. Computations were performed on a 16 processor R10000 SGI Origin 2000 in shared memory mode. The processing time for a run containing about 1 million tetrahedra with the $k-\epsilon$ turbulence model, including output for 100 time steps, was approximately 1 to 2 hours.

3.1 Problem Set-up and Description

Each model speed and hull orientation for these tests (discussed here and in Chapter 4) was run as an independent simulation. For these initial tests, the orientation of the model at a given speed was matched to that given by the experimental results (see Chapter 2). The numerical model consisted of a meshed fluid volume of air and water with boundaries defining the hull and outer limits of the domain. Flow, both air and water,

would enter one side of the domain, pass by the stationary model hull and leave through the opposite side of the domain. The system would then be solved for a series of time steps until steady-state conditions of flow developed. The free surface was determined with the volume-of-fluid, or VOF method which is a “surface-capturing” technique (see Section 1.3.4), so the geometry of the domain and mesh was unchanged by the solution process.

The method used to generate the mesh defining the flow domain used in these simulations, as well as those discussed in Chapter 4, is given in the following section.

3.1.1 Flow Domain & Mesh

The first step in setting up a numerical model is to define the extent of the domain. For interior flows such as a building’s ventilation system, the domain is fixed by the geometry. Exterior ship flows, however, have no such rigid outer limits. For such cases, the domain must be small enough for efficiency, but large enough that the flow field around the hull is unaffected by flow features that may be reflected and/or produced at the outer boundaries. The planing model domain was defined by a box (referred to as a ‘tank’) 5.5 m long, 1.6 m wide and 2.1 m tall. The still waterplane was defined at approximately 60% of the domain height. The model and flow field were symmetrical about the x-z plane at the model’s centerline, so only half the width of the above domain needed to be meshed. A symmetric boundary condition was then applied at this location. The planing hull model domain is shown in Figure 3.1.

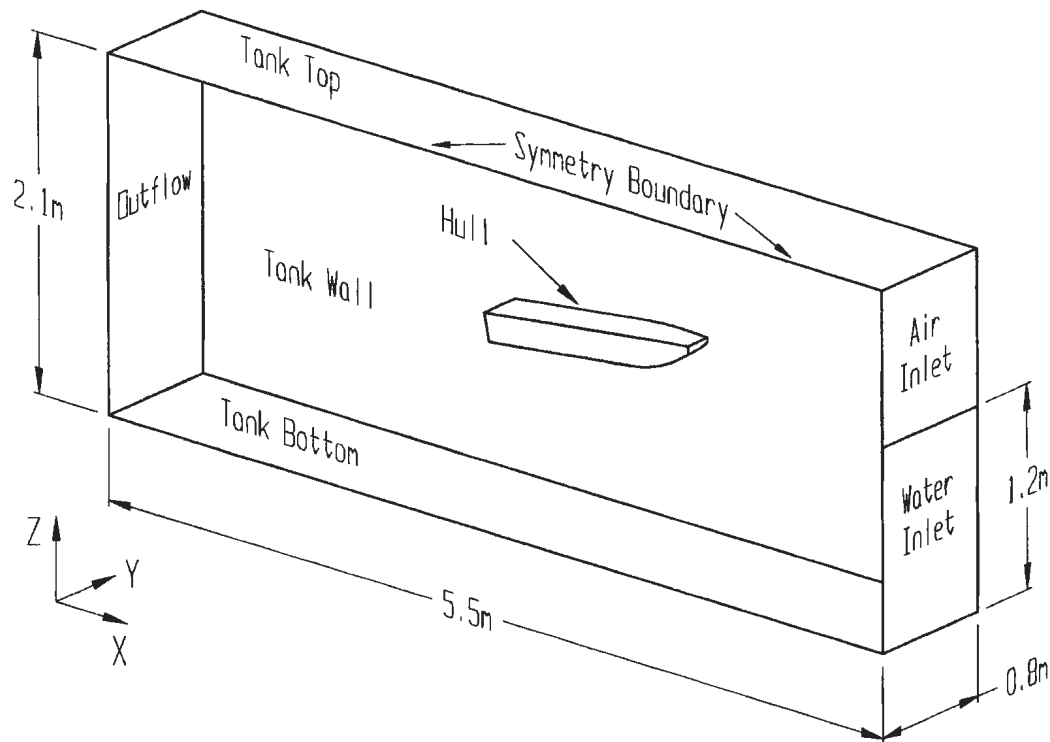


Figure 3.1 – Planing Hull Model Domain

The hull itself consisted of several surfaces used to facilitate post-processing functions. These surfaces, shown on a half model of the hull in Figure 3.2, consist of the hull bow surface, hull chine surface, hull bottom surface, hull flat surface, hull side surface, hull top surface, and hull transom surface. The centerline, chine line and outer chine line are also identified in the figure.

Once the domain was defined, it was discretized into a mesh of elements. For efficiency and stability in the solution, the mesh should be defined such that it is dense in areas where the flow is most dynamic and coarse in areas where there is little activity. In the case of ship flow, this usually means high grid density near the hull and about the waterplane (to capture wave profiles). Areas far from the hull can be fitted with coarser

meshes. For the current study, which focused on fluid forces on the hull, resolving the wave profiles was not a priority so dense meshes were concentrated solely around the hull surfaces.

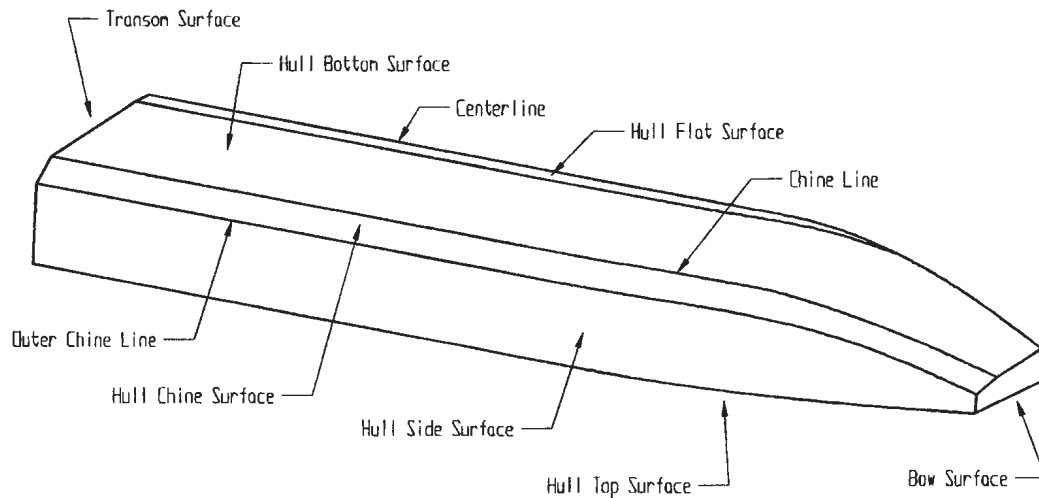


Figure 3.2 – Model Surfaces and Lines

Developing an efficient 3D mesh in terms of grid density that is also free from excessively distorted elements can be a challenging task, even for simple geometries. Problems usually arise in transition areas between fine and coarsely meshed regions, which if not gradual enough can contain unusable elements. This problem was avoided by taking advantage of the flexibility of unstructured hybrid adaptive meshes. The fluid domain was divided into two zones for meshing. The first zone consisted of the region closely surrounding the model (size: length = 3.0m, $\frac{1}{2}$ width = 0.8m, height = 1.2m). This zone was meshed with unstructured tetrahedral elements of medium density (average element size ranging from 4-10 cm). Elements in this zone were later refined for increased resolution next to the hull. The second zone, which consisted of the rest of the

domain, was coarsely meshed with structured hexahedral elements (average element size of 10 cm). This meshed domain, shown in Figure 3.3, was used as the base from which more refined meshes were developed.

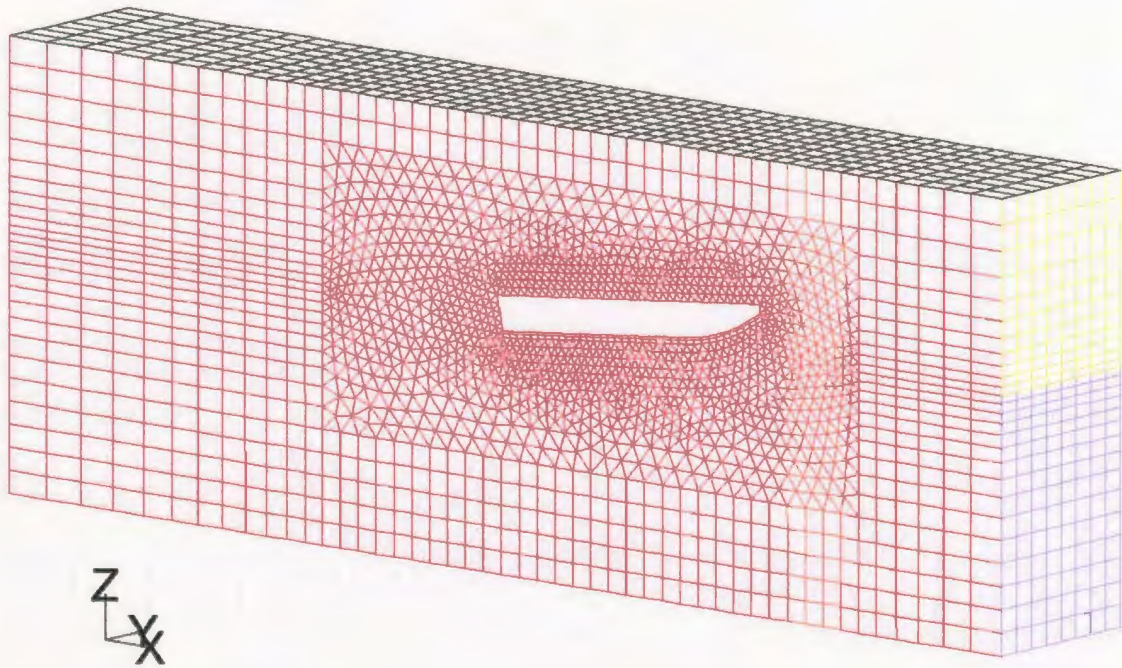


Figure 3.3 – Base Domain Mesh

The base mesh described above was created with the meshing software Gambit (version 1.2.4). Computer aided design (CAD) software was used to generate the domain and hull geometry that was then imported into Gambit from files in standard CAD formats (both ACIS and IGES). Once in Gambit, the hull geometry was oriented to the desired trim and sinkage values relative to the waterplane. The zone volumes were defined and meshed as shown in Figure 3.3. Boundary conditions were also defined in Gambit by grouping and

naming element faces located on the symmetry plane, inlet and outlet areas, tank walls, and hull. A Fluent-ready mesh file was then generated for the given case.

Once the base mesh was generated, Fluent was used to set the case parameters and refine the mesh to the desired level of resolution. As discussed in Chapter 1, mesh adaptation can be used to refine or coarsen elements based on a variety of criteria such as velocity or pressure gradient. These are usually applied after the solution has progressed and/or stabilized to a certain level. Another adaptation criterion, based on geometry, can be applied at any time and was used to create a refined mesh around the hull before the solution operations were started. Elements were selected for refinement based on whether they fell within a set distance from the hull surfaces. These elements were then subjected to refinement by subdivision (non-conformal). Section 1.3 describes both conformal and non-conformal approaches to refinement. The approach of sub-division with hanging nodes was chosen because it was found to be more robust than its counterpart for this type of problem.

The meshes generated for the planing hull simulations were hybrid meshes (i.e. they contained more than one type of element). Figure 3.4 shows the refinement process for each of the elements used in a typical mesh. Hexahedra or box elements appear in the outer areas of the domain. Pyramid elements were used at the transition from hexahedra to tetrahedra (from the outer zone to the inner zone of the domain). Tetrahedra were found in the inner areas near the hull. Wedge elements were used in contact with, and for a few layers out from, the hull surfaces. Their prismatic shape tends to be less

problematic with the higher aspect ratios needed in this area (wide thin elements stacked to give greater resolution normal to the hull surface).

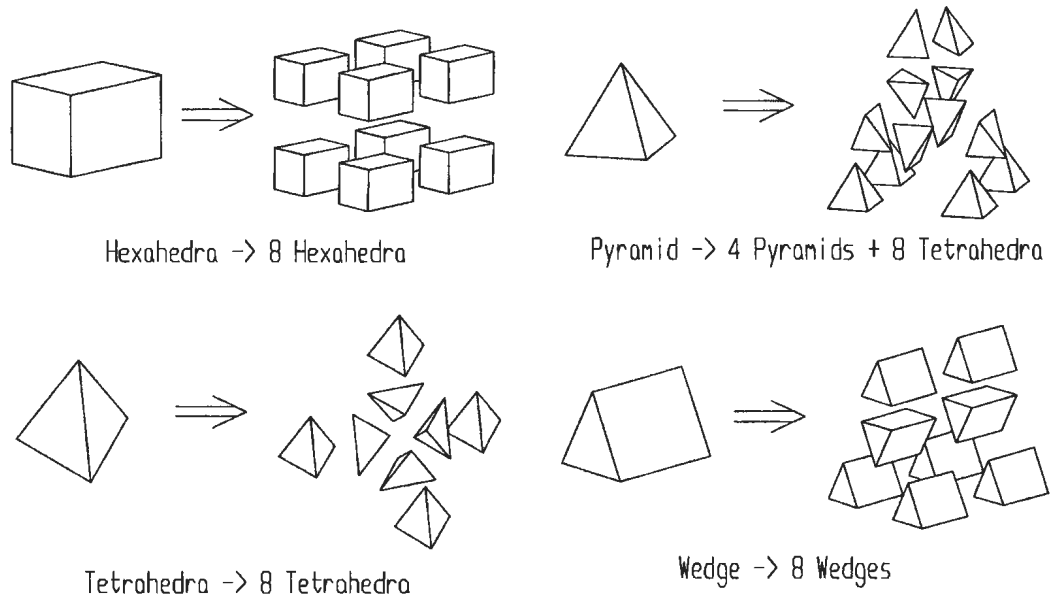


Figure 3.4 – Element Refinement

The meshes for all of the planing hull simulations were constructed in the same manner. The model orientation was first set to the correct sinkage and trim and the inner and outer zones were meshed as shown in Figure 3.3. Elements near the hull surface were then refined to provide greater resolution in this area. Mesh sizes produced from this process ranged in size from approximately 125,000 to 140,000 elements. The refined hull surface mesh is shown in Figure 3.5 and the refined domain in Figure 3.6.

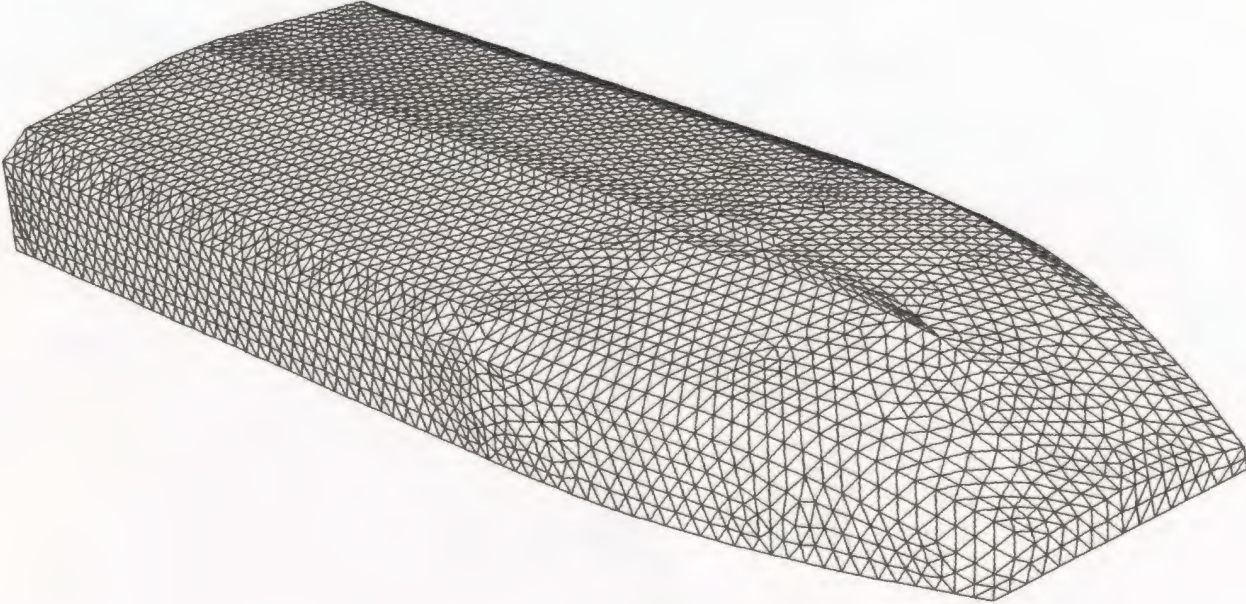


Figure 3.5 – Hull Surface of Refined Mesh

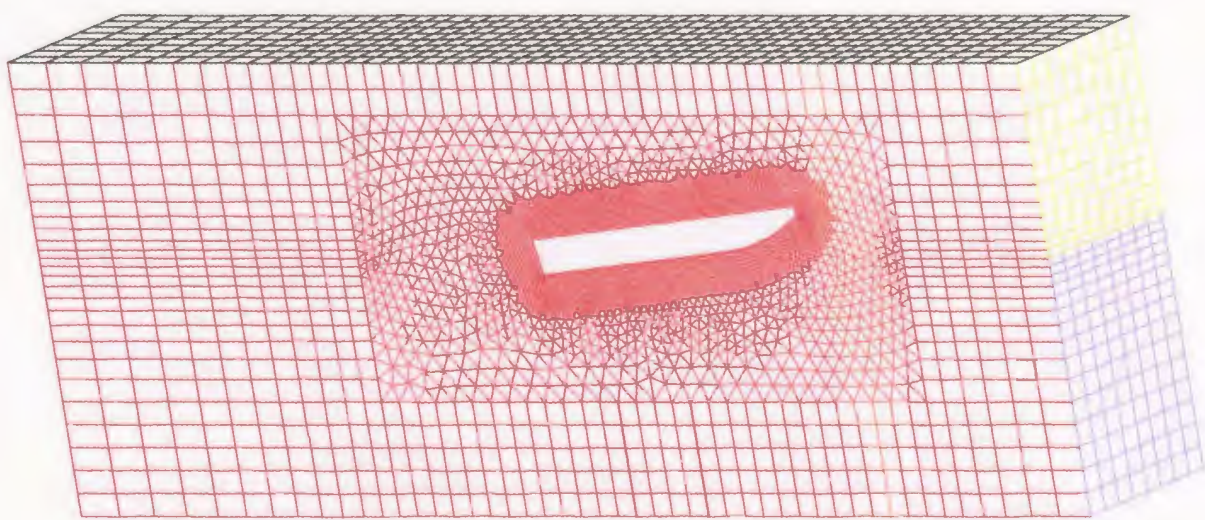


Figure 3.6 – Refined Domain Mesh

3.1.2 Solver Parameters

The next step in developing a CFD simulation is to choose the appropriate solver settings including which governing equations are to be solved, and how they should be discretized. As discussed in Chapter 1, the Fluent solver has several options for adjusting the numerical technique used, in order to reduce error and improve performance. The selection of solver parameters for the planing hull simulations was made partly through necessity (not all options were available when using the volume-of-fluid method), partly from recommendations in the Fluent literature, and partly from trial and error evaluations of various solver setting combinations. The final settings are listed at the end of this section in Table 3.1.

A key parameter for solution stability for these tests was found to be the time-step size. If chosen too large, the solution would become divergent. The optimum time-step size needed is related to the Courant number. This non-dimensional number, which should be less than 1 for stability, is a ratio of the time-step size to the time it takes for a particle to pass through a given element in the flow field. Smaller grid sizes or higher velocity flows therefore require smaller timesteps in order to avoid divergence. To be assured of convergence for all of the planing hull simulations, the time-step size was determined to be 0.001 seconds. At slower model speeds this value could be increased without penalty, but as there was little improvement in processing time, a single value was used for simulations at all speeds.

Another consideration is how many time-steps were needed before the flow field stabilized. The planing hull simulations were for the steady state condition: a model

traveling at constant speed through calm water. However, an unsteady solution scheme was required when using the volume-of-fluid method. The simulation started from a guessed initial solution (see Section 3.1.3), and then proceeded through a transition period before achieving steady flow characteristics (changes in the solution in successive time-steps were negligible). The required simulation time was determined by monitoring the forces on the hull surfaces (see Section 3.1.4) until they stabilized. Figure 3.7 shows the trimming moment history of a typical simulation (a rolling average of 0.06 seconds was used in order to smooth small amplitude oscillations found in these traces). The transition to steady state for hull forces required approximately 2.5 seconds of real time, or 2500 timesteps. This time was found to be consistent regardless of the model speed and was therefore used for all planing hull simulations.

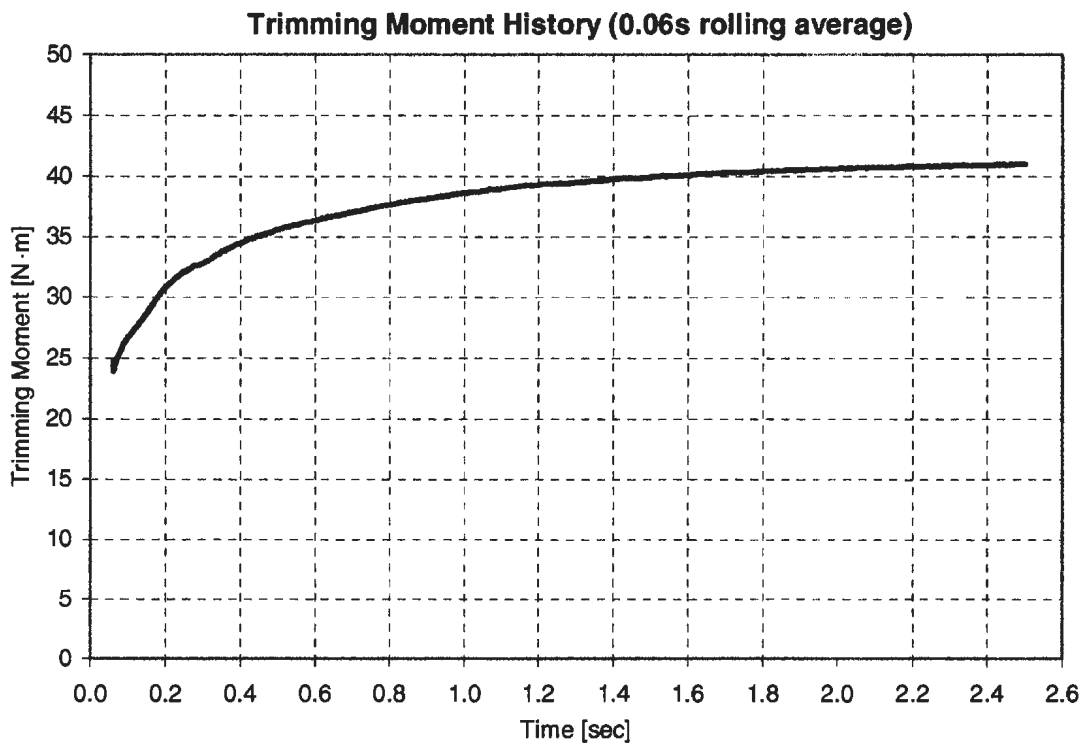


Figure 3.7 – Trimming Moment History

Parameter	Setting
Time Step Size	0.001 seconds
Number of Time Steps	2500
VOF Scheme	Geo-Reconstruct
VOF Body Force Weighted	Yes
Solve VOF Every Iteration	No
Solver	Segregated, Unsteady
Viscous Model	Laminar
Unsteady Formulation	1 st Order Implicit
Operating Pressure	101,325 Pa
Operating Density	0.0 kg/m ³
Gravity	9.81 m/s ²
Water Density	998.2 kg/m ³
Water Viscosity	0.001003 kg/m·s
Air Density	1.225 kg/m ³
Air Viscosity	1.7894 x 10 ⁻⁵ kg/m·s
Pressure Discretization	Body Force Weighted
Momentum Discretization	First Order Upwind
Pressure-Velocity Coupling	PISO
Hull Surface Boundary Condition	Wall (no slip)
Tank Surface Boundary Condition	Wall (allows slip)
Symmetry Boundary Condition	Symmetry
Water Inlet Boundary Condition	Velocity Inlet: Water at Model Speed
Air Inlet Boundary Condition	Velocity Inlet: Air at Model Speed
Outflow Boundary Condition	Outflow

Table 3.1 – Solver Parameters

3.1.2.1 Turbulence

During the initial phases of testing, several different solver configurations were investigated, such as turbulence modeling. Turbulence modeling (see Section 1.3.3) is an attempt to mimic the effects of turbulence on global flow variables without actually simulating the turbulent activity (which would require extremely large numbers of elements). Apart from the increased processing time required by turbulence models, there were also difficulties with solution divergence. ‘Hot spots’ of turbulence generation would appear in the spray root region or at the air/water interface causing the solution to break down. These were attributed to the fact that the turbulence models supplied by Fluent were not designed for this type of flow. There was the potential of solving, or at least minimizing, these difficulties by creating or modifying a turbulence model through Fluent’s user-defined function capability. However, this would have been a significant undertaking that was beyond the scope of this research. It was therefore decided to focus on developing solutions without turbulence modeling.

3.1.3 Initialization

After the grid and boundary conditions have been established for a given case, the entire system needs to be assigned initial ‘guess’ values for all of the flow variables before the solution can be computed. This is called initialization. An unstructured CFD solver creates a large set of coupled equations based on the discretization scheme and the fundamental flow equations to be satisfied for a simulation. This system of equations is most efficiently solved using an iterative approach wherein a trial solution is continuously improved until successive changes are within a predefined tolerance. In

many cases, this approach will not be successful if a poor initial trial solution was used to begin the process. The system may diverge (successive iterations cause the trial solutions to get worse), or the system may converge to a solution that is clearly incorrect in terms of the physical phenomena being investigated. Proper initialization of the flow variables is therefore an important step for a successful CFD analysis.

The flow variables for the planing hull simulations were initialized as follows. All x-component velocities were set at the model speed. All y-component and z-component velocities were set to zero. All pressures were also set to zero. The volume of fluid variables, however, needed to be initialized to create a level water plane at the correct height. All cells below the waterplane required a water volume fraction equal to 1, while all cells above the waterplane required a water volume fraction of 0. This was not a straightforward task due to the scattered nature of the unstructured grid.

Initialization in Fluent can be performed on groups of cells provided that they can be selected within a rectangular box, or they exist within a predefined volume created when the original geometry was meshed. If the free surface was defined in the geometry, then all cells within the domain will exist entirely above or below this surface. Initialization of the volume fraction variables in this case would be done in two steps. First, the entire domain would be assigned a volume fraction of 0. The cells below the water plane would then be selected and assigned a volume fraction of 1. A 2D example of an initialized volume fraction system with a predefined free surface is shown in Figure 3.8.

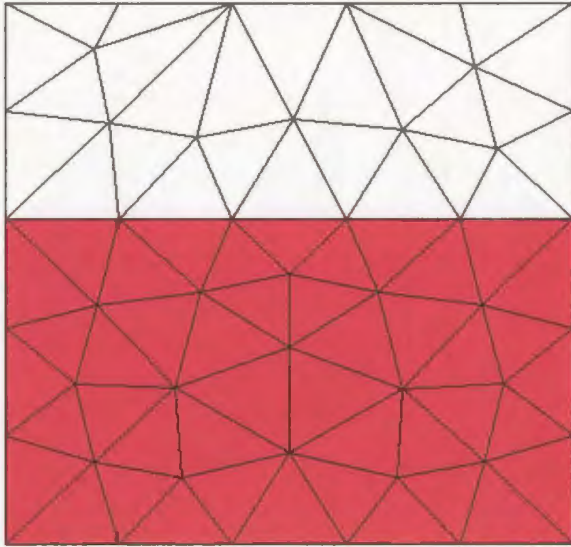


Figure 3.8 – Initialization with Predefined Free Surface

Although this approach is simple at the solver stage, it requires an extra constraint on the geometry at the meshing stage that can cause numerous complications, particularly in 3D systems. The alternative is to eliminate this constraint and allow elements to be generated anywhere on or through the waterplane. Unfortunately, initialization by the above approach will no longer produce a smooth free surface. In this case, elements overlapping the waterplane will be assigned a volume fraction based on the location on the element's center. This can produce a hard jagged edge (a crinkly surface in 3D) as shown on the left in Figure 3.9.

The poor quality of this volume fraction initialization leads to almost immediate divergence when the solver was started and was therefore unusable. This drawback was overcome by taking advantage of User-Defined Functions (UDFs). A UDF is a set of instructions written in the c programming language that can access and manipulate Fluent variables. An initialization UDF was written by the author to properly set the volume

fraction variables for elements that overlap the waterplane so that a smooth free surface was created. The function would visit each element in turn and check its location relative to the waterplane, assigning either 0 or 1 as needed. If the element overlapped the free surface, the volume of the element below the waterplane was calculated and divided by the total element volume to define its volume fraction. This function, first written for 2D triangular meshes was then expanded for all 2D and all 3D element shapes including hybrid meshes, for any orientation of the waterplane. Figure 3.9 shows an unstructured mesh with and without initialization with this UDF. The resulting smooth free surface allows the solver to achieve converged solutions.

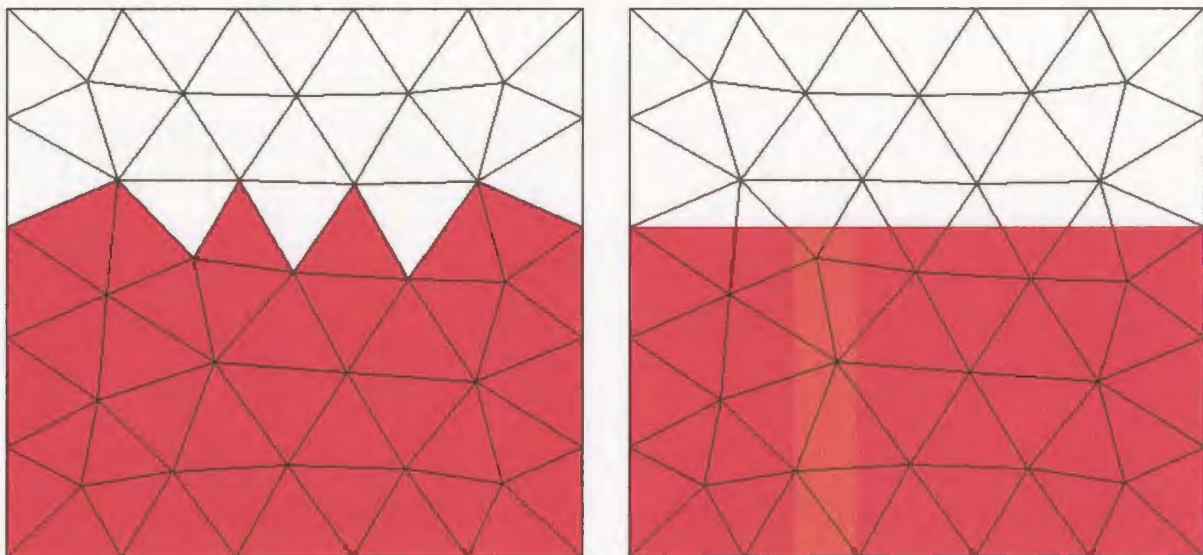


Figure 3.9 – Initialization with and without UDF

3.1.4 Determination of Measured Quantities

Several key quantities were measured during the CFD computations in order to evaluate the system for comparison with experimental results. They consisted of the net x-force on

the model (drag), net z-force on the model (lift), net moment about the y-axis at the tow point (trimming moment), wetted surface area, wetted centerline length, and wetted chine length. These quantities were measured and recorded at every time step for each simulation. Other measurements such as pressure distribution along the hull or wave shape near the transom were only evaluated for specific test cases.

Forces and moments are evaluated in CFD by integrating the pressure field over a surface, adding the frictional forces and then taking the desired vector component. Fluent has these calculations as built-in functions. All that is needed is to specify the desired surfaces and the vector component for forces, or the moment center for moments. The resulting output lists the frictional, pressure and total force or moment for each surface in a tabular form. During a simulation, this information was stored in a text output file that was read and evaluated during post-processing operations.

The wetted surface area of the hull was calculated in a similar manner as the forces. The volume-fraction of water variable, which takes on values between 0 (completely dry) and 1 (completely wet), was integrated over the hull surfaces. Integration of this quantity yields the wetted surface area directly, and can be accessed by another built-in function. The output was a single number that was also stored in the output text file for each timestep during a simulation.

Determination of the wetted centerline and chine lengths could not be done directly through built-in Fluent functions. It required the use of an external function written by the author for this purpose. Similar to the wetted area calculation, the evaluation of the wetted lengths depended on the values of the volume-fraction of water along the desired

line on the hull. At each timestep, Fluent was instructed to export the values of water volume fraction for a given surface (which contains either the centerline or the chine) to a temporary text file. An external function was then called that would read this file, determine which nodes lie on the appropriate line, and then calculate the wetted length.

The wetted length in a volume-of-fluid calculation is not a clear point due to the nature of the interface capturing method. It was calculated from two values; the x-coordinate of the node furthest forward that was completely wet, and the x-coordinate of the node furthest aft that was completely dry. The average of these two points yielded the x-coordinate of the air/water interface. Knowledge of the orientation of the model relative to this world coordinate was then used to determine the wetted length along the hull. Figure 3.10 shows the water volume fraction along the chine of a typical simulation. The points of interest for the wetted length calculation are identified.

Figure 3.11 shows a sample of the commands issued to Fluent for a typical simulation. This group of commands was executed n-times where 'n' is the number of timesteps. First, the timestep size was set, and then the solver was run for a single timestep. Force, moment and wetted area data were calculated and exported to the output text file. Old versions of the text files containing the chine and centerline volume-of-fluid data were removed and replaced with current versions. The external function 'get_lengths' was then executed, given the current trim and sinkage values (model orientation), and the resulting wetted length values were exported to the output file. The loop then repeated.

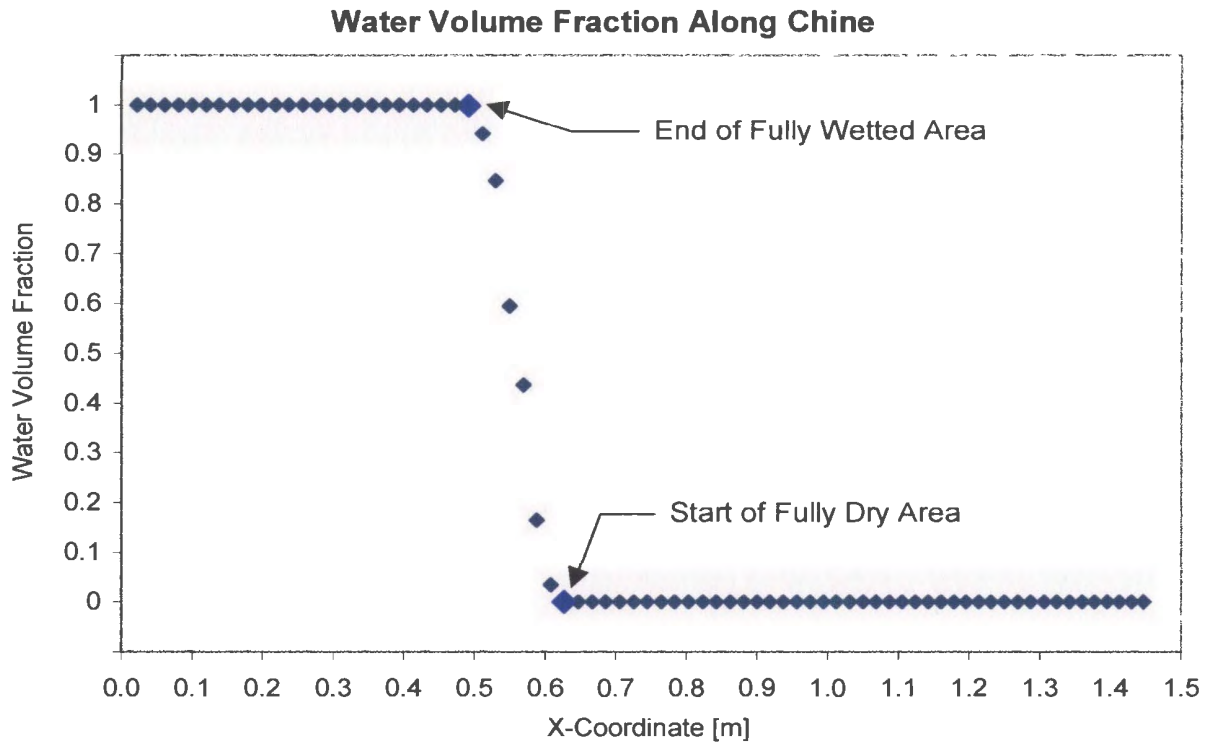


Figure 3.10 – Water Volume Fraction Along Chine

```

This set of commands is performed n-times
{
  solve set time 0.001000  Set time-step size
  solve dual 1 50          Solve 1 time-step max 50 iterations
  report wall-forc 1 0 0   Export drag forces
  report wall-forc 0 0 1   Export lift forces
  report wall-mom 0.220012 0.000000 0.059410  Export trimming moment about tow point
  report surface-int (hull_surfs) vof-water  Export wetted area
  !rm center.txt          Remove old 'chine.txt' file
  export center.txt (hull_flat) vof-water    Export chine vof data to file
  !rm chine.txt           Remove old 'center.txt' file
  export chine.txt (hull_chine) vof-water    Export center vof data to file
  !get_lengths 5.041260 5.760768           Calculate wetted lengths given trim & sinkage
}

```

Figure 3.11 – Sample of Commands Used Each Time-Step

3.1.5 Grid Dependence Study

A primary factor in the accuracy of a CFD simulation is the grid or mesh used to discretize the problem geometry. In many cases, different meshes can produce different solutions for the same simulation. This is called grid dependence and should be avoided, as there should only be one solution for a given problem. Grid dependent solutions are usually caused by poorly constructed meshes or by meshes with insufficient resolution. Care has to be taken to ensure that there is adequate resolution of the geometry in regions where flow variables have large gradients. However, too much resolution can result in unnecessarily large meshes that increase both processing time and memory requirements (both in RAM and disk space needed to store large data files). Finding the optimum mesh is therefore an important step when performing CFD simulations. This section describes the procedure that was used to determine the optimum mesh for the planing hull model and flow domain.

As described in Section 3.1.1, the domain mesh was created from a base grid that was refined near the hull surfaces. Two factors were investigated for grid dependence in the solution: the refinement envelope (the distance from the hull that elements were refined), and hull surface mesh resolution. The goal was to determine the minimum number of elements needed for a grid independent solution. Typically, this problem obeys the law of diminishing returns. The solution does not improve as quickly as the increase in computational costs from the larger meshes. Eventually a point is reached where only marginal gains are achieved from further refinement. This was considered to be the optimum mesh.

A test case for the study was chosen as the design ballast condition at 5.0 m/s (running trim = 5.26°, sinkage = 32.7 mm). The first set of simulations focused on changing the size of the refinement envelope used to increase resolution near the hull. Three distances were tested: 0.10m, 0.15m and 0.20m. A plot of the time history of the trimming moment for these simulations is shown in Figure 3.12. The results show a high degree of grid dependence between the refinement envelopes of 0.10m and 0.15m but little change is found when extending the envelope to 0.20m. Similar results were found with both drag and lifting forces. Further expansion was not found to be worth the increased computational times.

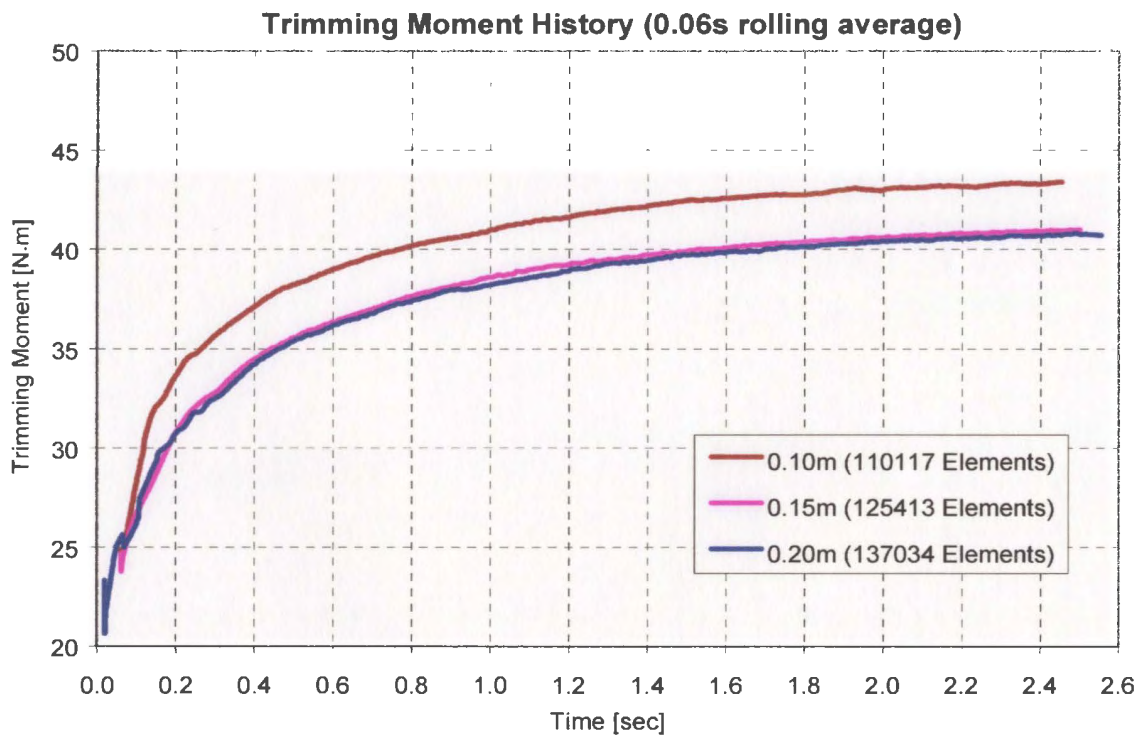


Figure 3.12 – Trimming Moment (Refinement Envelope)

The second set of simulations focused on the resolution of the surface mesh on the hull. Again, three resolutions were examined for the test case, each with a refinement envelope of 0.20m. In terms of the maximum size of the sides of the surface elements, the three resolutions were 1.375cm, 1.125cm, and 1.000cm. Figure 3.13 shows the lift force history for these simulations. The solution was found to be relatively insensitive to this parameter. Only a small change was found between the 1.375cm grid and the 1.125cm grid. Further refinement to a 1.000cm grid provided even less improvement. Results for the drag force history were similar. The trimming moment histories for these three cases were found to be virtually identical.

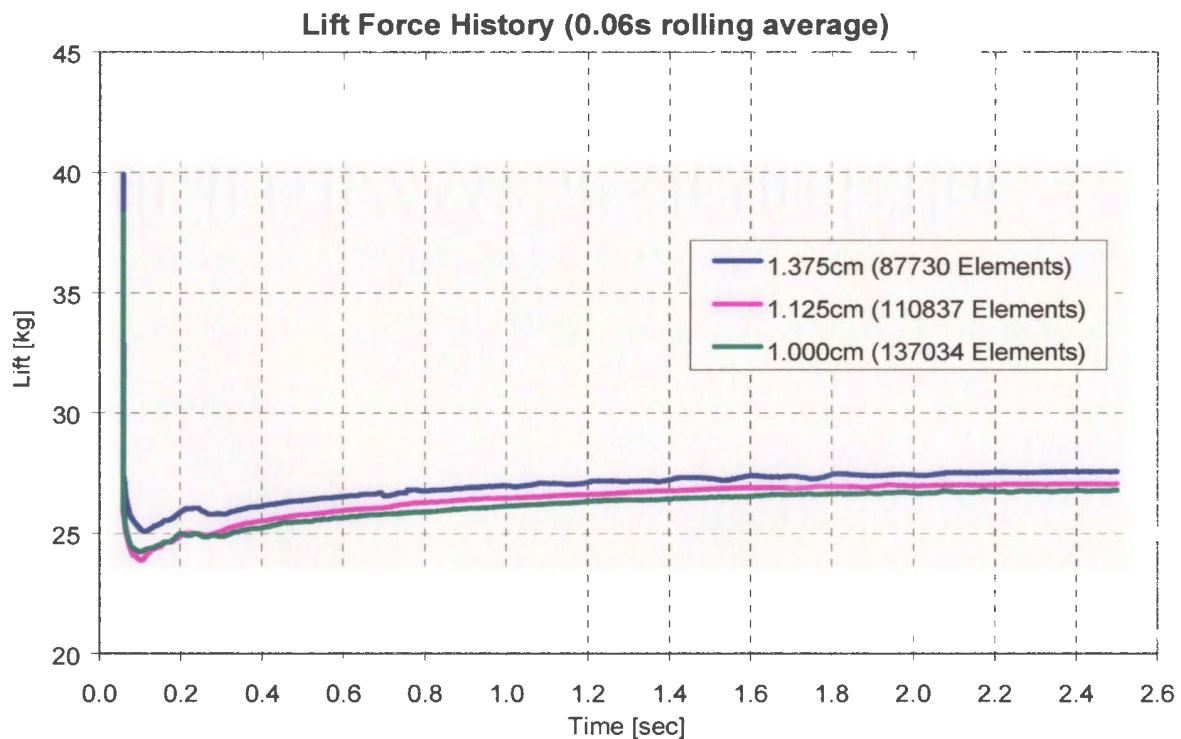


Figure 3.13 – Lift Force History (Hull Surface Refinement)

The results from the grid dependence study indicated that a close to optimum mesh for this type of simulation required a refinement envelope of 0.20 m with a surface mesh of

1.0 cm (maximum size of element sides). Although both sets of tests show that further refinement will likely produce some improvement in the solutions, the magnitude of these improvements were comparable to the level of uncertainty provided by the physical experiments and therefore did not justify the resulting increases in computational costs for these simulations.

3.2 Method of Analysis

This section describes the methodology used to analyze the results from a given CFD simulation of the planing vessel. Due to previously discussed restrictions on grid size (see Section 3.1.2), the boundary layer on the hull was not properly resolved and hence the frictional forces could not be predicted accurately. This limitation was addressed by using similar techniques used in physical model testing when converting test results to full scale: the separation of hull forces into frictional and pressure components. The numerical simulations provided the pressure forces while the frictional forces were determined by calculation of the skin friction using empirical data for the turbulent flat plate friction line (Lewis, 1988).

The wetted lengths of the numerical model were used to calculate the Reynolds number using the mean wetted lengths (Savitsky, 1964) as given by equations [3.1] and [3.2].

$$L_m = \frac{L_k + L_c}{2} \quad [3.1]$$

$$Re = \frac{V \cdot L_m}{\nu} \quad [3.2]$$

where,

- L_m is the mean wetted length
- L_k is the wetted length along the centerline
- L_c is the wetted length along the chine
- Re is the Reynolds number
- V is the model speed
- ν is the kinematic viscosity of water

The Reynolds number was used with the Schoenherr friction line (1947 ATTC Line), given by equation [3.3], to determine the coefficient of friction. This friction line is shown in Figure 3.15 (along with the ITTC 1957 model-ship correlation line). The ranges of Reynolds numbers for both the model and full scale vessel are also given in the figure.

$$\frac{0.242}{C_F} = \log_{10}(Re \cdot C_F) \quad [3.3]$$

$$F_F = \frac{1}{2} \cdot \rho \cdot A_w \cdot V^2 \cdot C_F \quad [3.4]$$

where,

- C_F is the coefficient of friction
- F_F is the frictional force on the hull
- A_w is the wetted surface area of the hull
- ρ is the density of water

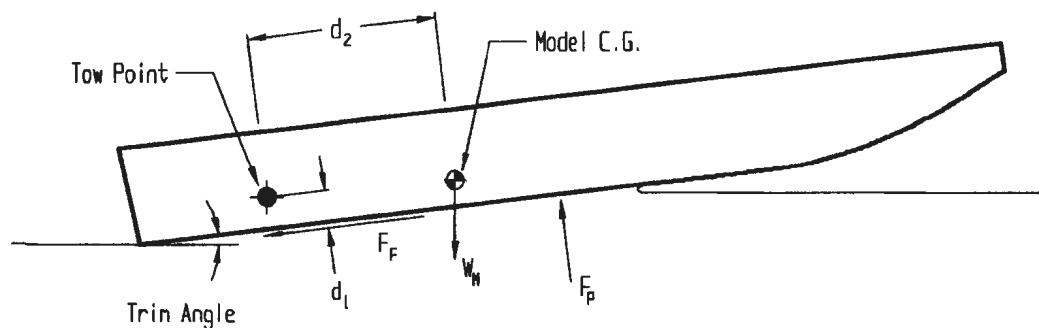


Figure 3.14 – Forces on Model

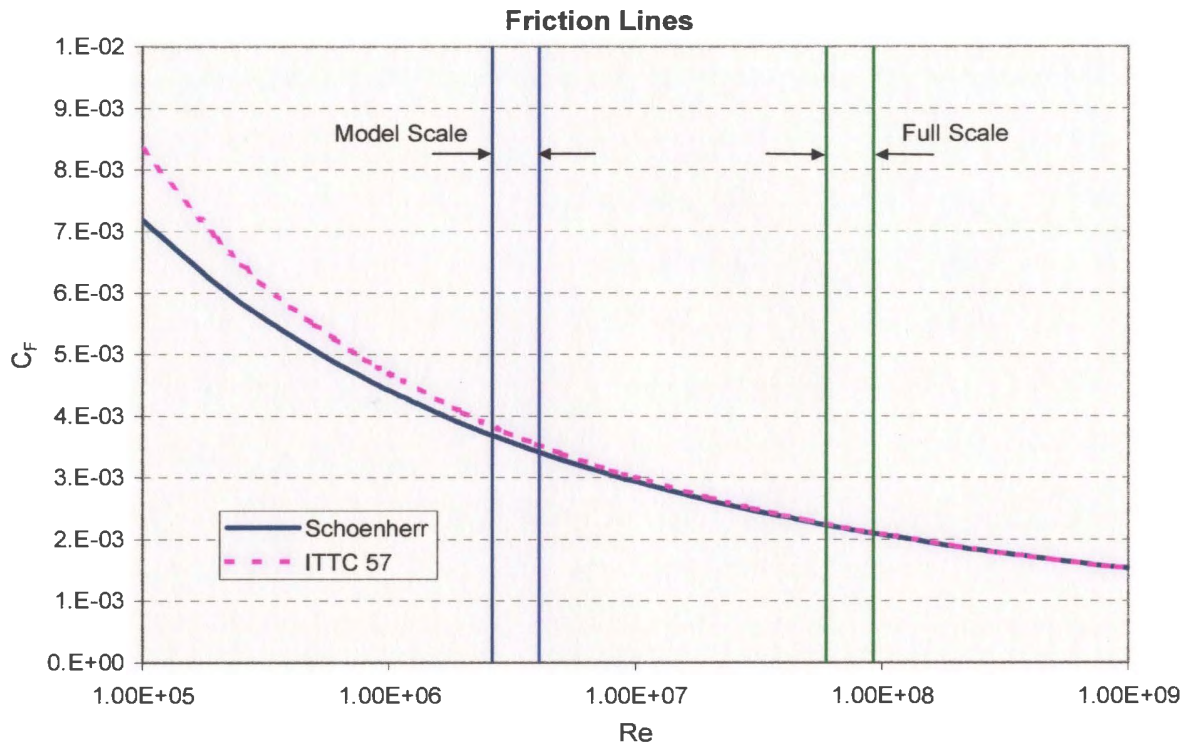


Figure 3.15 – Friction Lines

In Figure 3.14, a primitive diagram of the external forces on the hull is shown. The model's tow point and center of gravity are identified as well as the trim angle, frictional force component and pressure force component. The perpendicular distance between the hull bottom and the tow point, d_1 , used to determine the net moment, is also given.

The total resistance on the hull is the sum of the pressure and frictional forces as shown in equation [3.5]. The pressure forces in the x-direction were determined by summing the pressure on each individual hull surface element as given by equation [3.6]. This was done automatically by Fluent. The frictional resistance component was taken as the component of the frictional force in the x-direction, which was dependent on the trim angle as shown in equation [3.7].

$$R_T = R_P + R_F \quad [3.5]$$

$$R_P = \sum_{\substack{\text{Hull} \\ \text{Surface}}} F_{Pxi} \quad [3.6]$$

$$R_F = F_F \cdot \cos \tau \quad [3.7]$$

where,

R_T is the total resistance on the hull

R_P is the resistance due to flow pressure on the hull

R_F is the frictional resistance on the hull

F_{Pxi} are the pressure forces on each surface element on the hull in the x-direction

τ is the trim angle

The net lift on the hull was found in a similar manner, by summing the components of the pressure and friction forces in the z-direction as shown in equations [3.8] - [3.10]. Note that the frictional contribution of total lift is negative for positive trim angles.

$$L_T = L_P + L_F \quad [3.8]$$

$$L_P = \sum_{\substack{\text{Hull} \\ \text{Surface}}} F_{Pzi} \quad [3.9]$$

$$L_F = F_F \cdot \sin \tau \quad [3.10]$$

where,

L_T is the total lift force on the hull

L_P is the lift due to flow pressures on the hull

L_F is the lift due to frictional forces on the hull

F_{Pzi} are the pressure forces on each surface element on the hull in the z-direction

The net moment of the hull about the pitch axis at the tow point was needed for the equilibrium simulations discussed in Chapter 4. In line with the total resistance and lift

calculations, the pressure component of the net moment was determined through integration of pressure forces by Fluent and the frictional component was calculated by equation [3.13]. Also shown, by equation [3.14], is what will be referred to as the required moment. It is the moment caused by the weight and center of gravity of the vessel about the tow point. For equilibrium, the total moment created by the flow must equal the required moment.

$$M_T = M_p + M_f \quad [3.11]$$

$$M_p = \sum_{\text{Hull Surface}} F_{pi} \cdot d_i \quad [3.12]$$

$$M_f = F_f \cdot d_1 \quad [3.13]$$

$$M_R = W_M \cdot d_2 \cdot \cos(\tau) \quad [3.14]$$

where,

M_T is the total moment on the model exerted by the flow about the tow point

M_p is the moment on the model exerted by flow pressure about the tow point

M_f is the moment on the model exerted by friction about the tow point

M_R is the moment on the model exerted by its weight about the tow point

W_M is the weight of the model

F_{pi} are the pressure forces on each surface element on the hull

d_i are the moment arms for each surface element to the tow point

d_1 is the perpendicular distance from the hull bottom to the tow point

d_2 is the distance from the tow point to the model's center of gravity (parallel to the hull bottom)

This method was used to determine the net forces and moments on the hull for all of the simulations performed in Chapter 4.

3.3 Results from Initial Simulations

Many aspects of the planing hull simulations were similar between cases of varied model speed and hull orientation. The magnitudes of parameters differed, but trends were qualitatively similar. This section provides a general evaluation of some of these characteristic features.

3.3.1 Hull Pressures

Accurate simulation of the pressure field around the hull was the key objective of these simulations. It was used to determine the global parameters of drag, trim angle and sinkage for the dynamic equilibrium simulations. The hull pressure field for a planing vessel is dominated by the spray root region near the leading edge of the wetted surface area. The pressure peaks in this area provide the primary contributions to lift and pressure drag. The forward location of this pressure peak also means that it is largely responsible for the trimming moment of the vessel. This section examines the pressure profile of a typical CFD simulation of the planing vessel model.

The pressure profile for a CFD simulation of the model at 5.0 m/s forward speed is shown in Figure 3.16. It is given as a pressure elevation plot, showing the pressure at each location on the hull as a 3D surface colored by value. The pressures are expressed in terms of a pressure coefficient defined by equation [3.15].

$$C_P = \frac{P}{\frac{1}{2} \cdot \rho \cdot V^2} \quad [3.15]$$

where,

C_P is the pressure coefficient

- P is the pressure at a given location
 V is the model speed

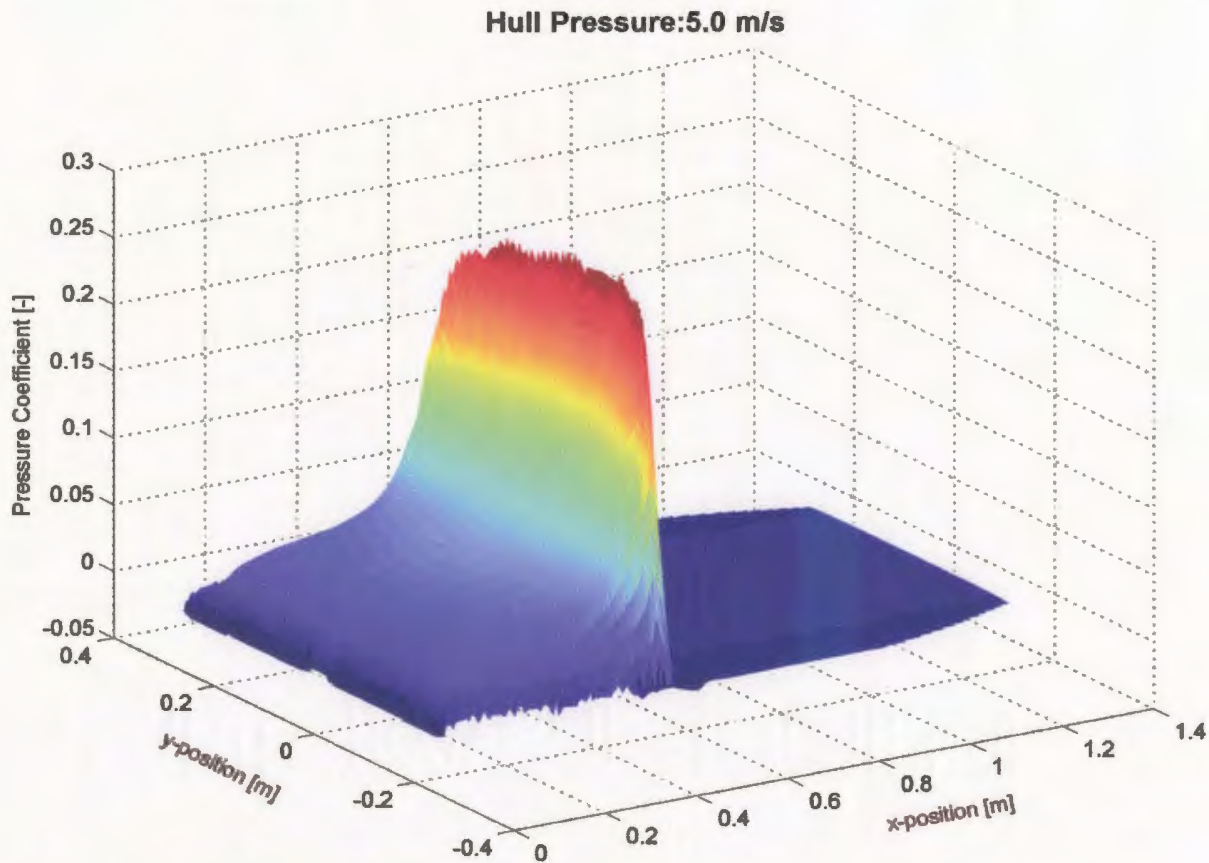


Figure 3.16 – Hull Pressures (Elevation Plot)

Pressure profiles were generally as expected for this type of vessel. The dry part of the hull was exposed to atmospheric pressure. The pressure increased sharply at the leading edge of the air/water interface. The pressure peaked and then decreased quickly and then more gradually in the direction of the transom. This typical pressure profile shape tended to shorten in length and decrease in height when moving transversely away from the centerline as shown in Figure 3.17. This was primarily a function of the deadrise of the hull. These results were consistent with experimental data on prismatic hulls presented in Hirano *et al.* (1990). Peak pressure coefficients were found to range between 0.1 and

0.45, consistently much lower than the theoretical value of 1 for a 2D plate. Pressure profiles were of significant importance to the equilibrium analysis, which is discussed further in the next Chapter.

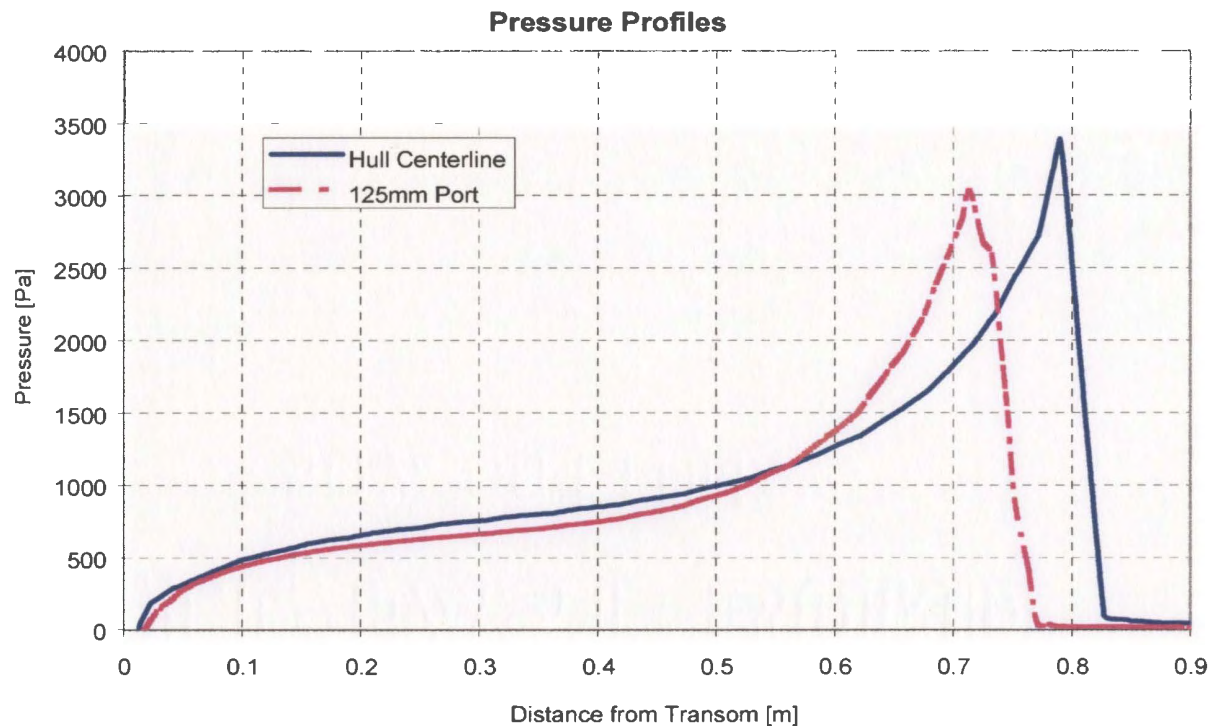


Figure 3.17 – Pressure Profiles on Two Transverse Cuts

3.3.2 Flow Velocities

The velocity field of the flow around the hull is also an important indicator of the vessel performance. Some of their basic characteristics are presented below.

Figure 3.18 shows the pathlines of particles released just forward of amidships on a horizontal line at a depth of 5.0 mm below the still waterline. They are representative of the flow pattern outside of the boundary layer but inside the affected region of the hull flow. The pathlines ran in a straight line until they approached the hull, at which time

they diverged slightly towards the chines. The closer to the sides a pathline originated, the greater was the deflection of its path. In Figure 3.19, the particles were released 10 mm above the still waterline and represent the path of the air, and perhaps some spray near the water surface. These lines ran straight until they came near the hull/waterplane intersection at which time they also changed direction towards the chines. The pathlines near the centerline made turns exceeding 90 degrees as they approached what was essentially a solid wall formed by the meeting of the water and the hull. Both of these flow patterns closely match those of experimental results presented in Savitsky (1964) and Payne (1988).

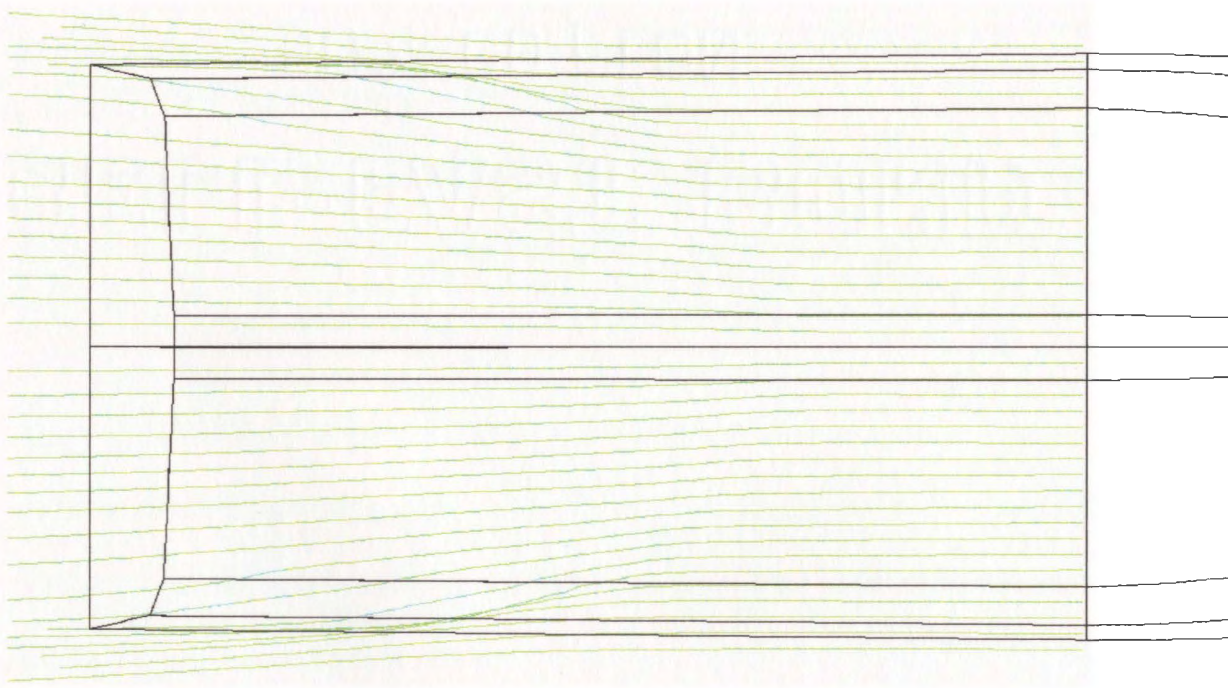


Figure 3.18 – Pathlines of Particles Released Below The Waterline

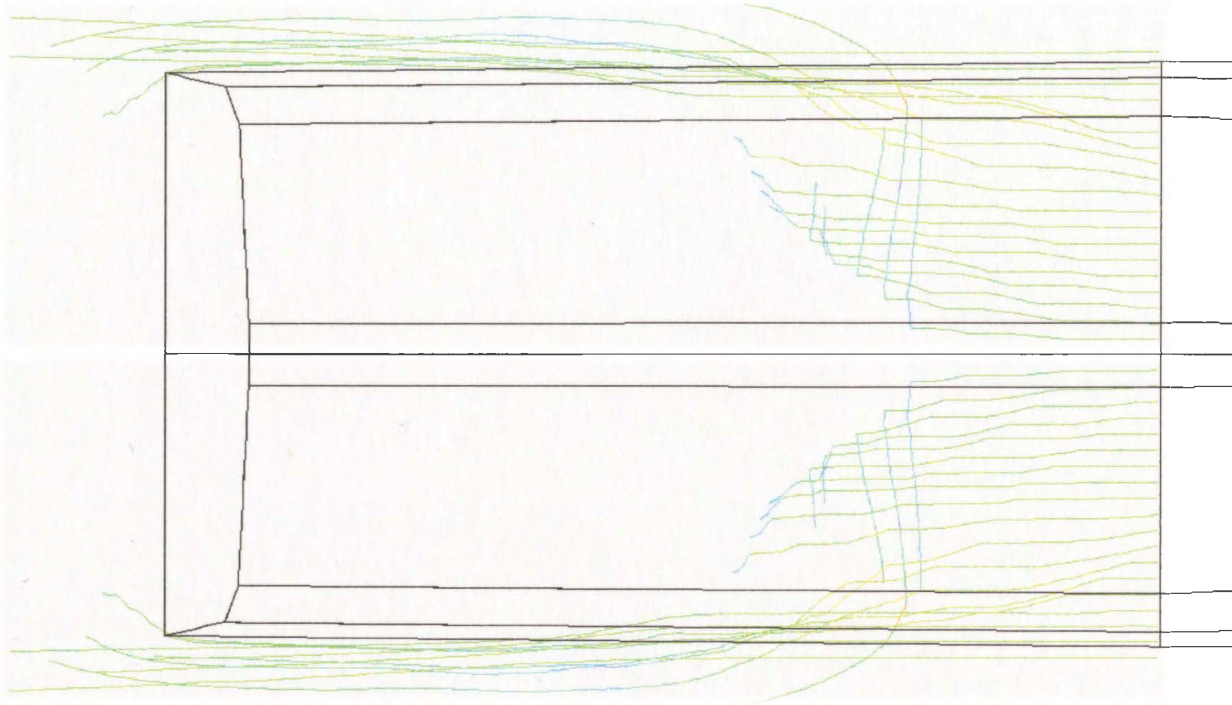


Figure 3.19 – Pathlines of Particles Released Above The Waterline

Another noteworthy flow pattern in the CFD simulations was seen near the transom. The air flow over the top of the hull was drawn into a vortex behind the flat transom. A plot of the velocity vectors showing this flow is given in Figure 3.20.

The velocity in the pressure peak region also exhibited the expected pattern, although resolution was limited by the mesh size. Figure 3.21 shows the pressure contours on a vertical plane slicing through the model's centerline. The high pressure region on the hull (shown as red) is enlarged in Figure 3.22 with a plot of the velocity vectors (vectors were colored by velocity magnitude ranging from blue to red). Flow in this region was directed out of plane just before the region of highest pressure.

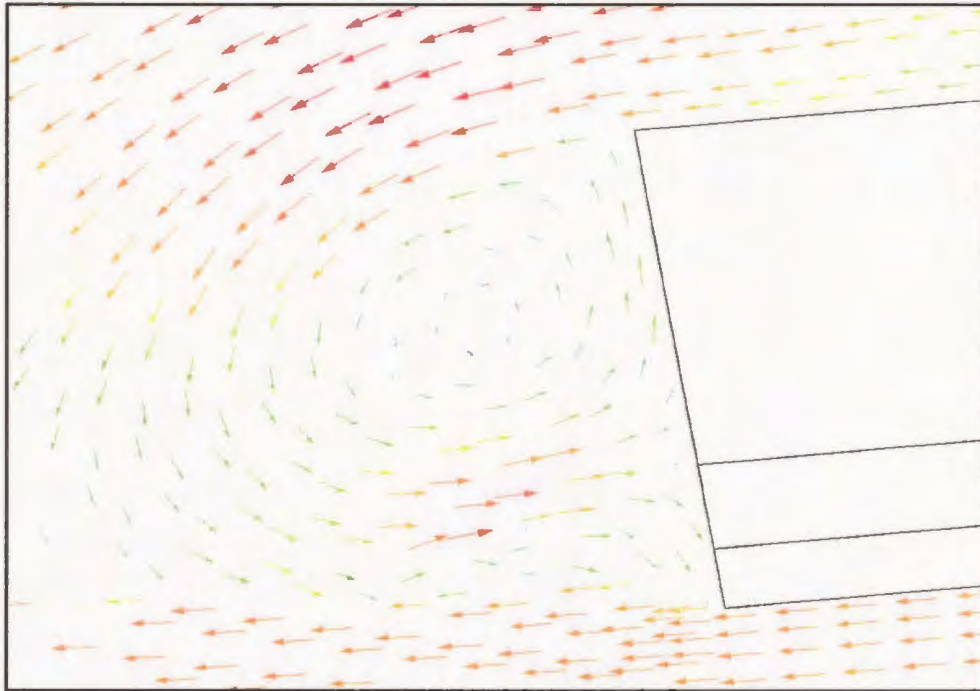


Figure 3.20 – Velocity Vectors Near Transom

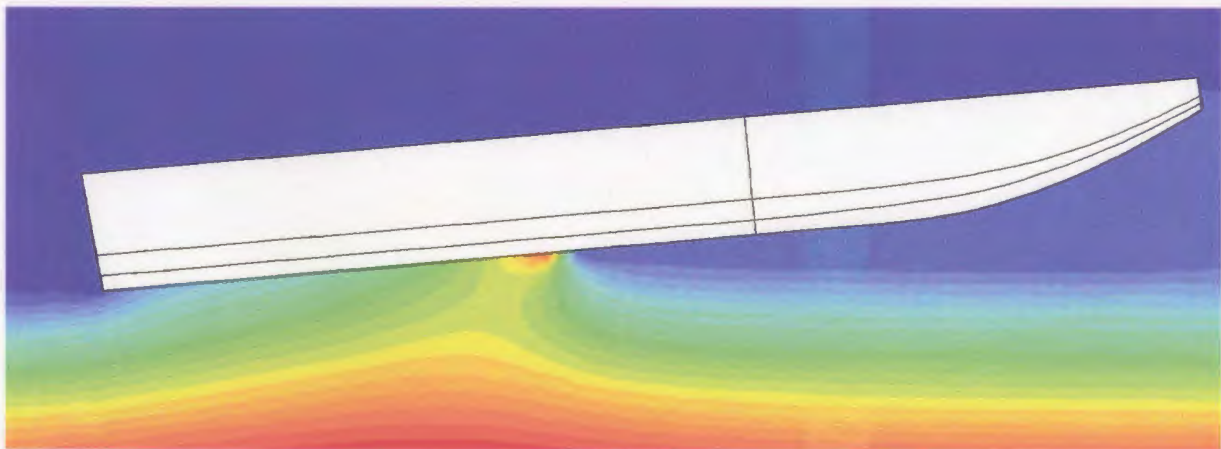


Figure 3.21 – Pressure Contours at Centerline Plane

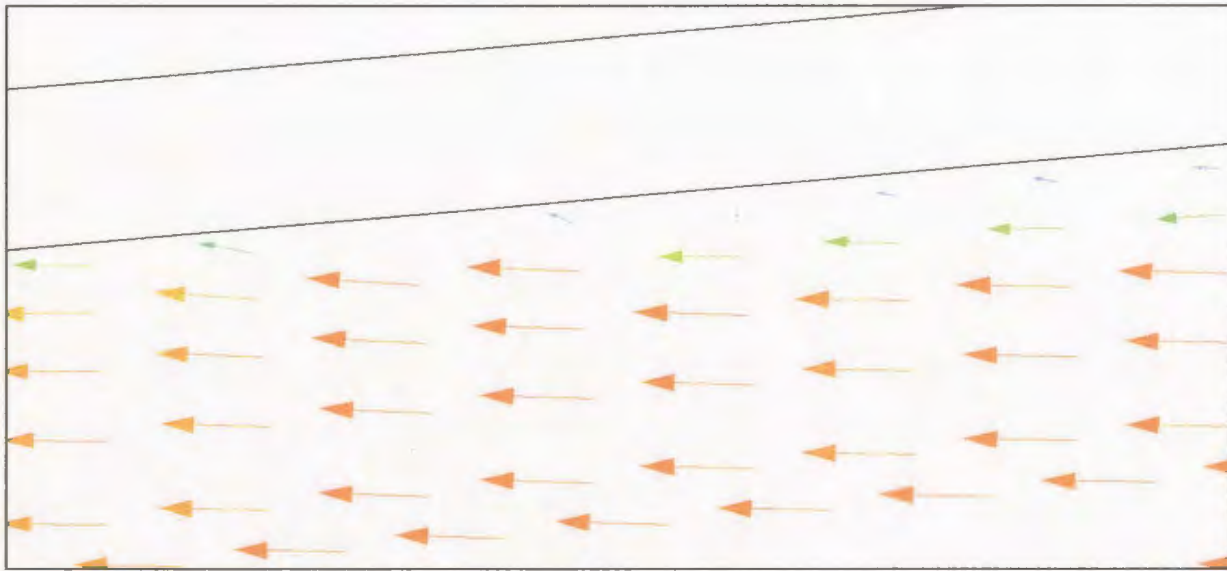


Figure 3.22 – Velocity Vectors Near Pressure Peak Location

3.3.3 Free Surface

The free surface in a volume-of-fluid (VOF) simulation is determined implicitly from the volume fraction of water in each cell. This method requires a certain level of grid resolution at the air-water interface for the free surface to be ‘captured’ accurately. The grid used for the planing hull simulations had relatively large grid cells in the far field where waves were being produced and as a consequence, the free surface was smeared across too large an area for these waves to be sufficiently resolved for analysis. The development of a grid in the far field that could be used to evaluate the wave properties of the simulations would have greatly increased the element count of the model to a point where calculation times would have become unreasonably large. So although experimental wave data was collected (see Section 2.3.5) for detailed validation of wave profiles from the CFD simulations, the lengthy computation times of the model made this impractical for the current study.

Examples of the free surface results that were produced are given below. Figure 3.23 shows the free surface on the centerline plane (symmetry plane) of the model. The transom was dry as a gently sloping wave was produced behind the model. Free surface contours at elevations of $\pm 15\text{mm}$ at 5mm increments are shown in Figure 3.24. The stern wave is shown as well as the beginnings of the system of divergent waves. These results are qualitatively in agreement with the waves observed during the physical experiments, which are shown in Figure 3.25 (coloured by elevation of the surface, blue represents the lowest levels, red represents the highest).

The air/water interface on the hull, which designates the wetted surface area, wetted centerline length and wetted chine length, is shown in Figure 3.26. The shape and contact area closely matched those from the physical experiments. An image from the underwater video of the physical model experiments is given in Figure 3.27 showing a similar interface shape as the CFD results.

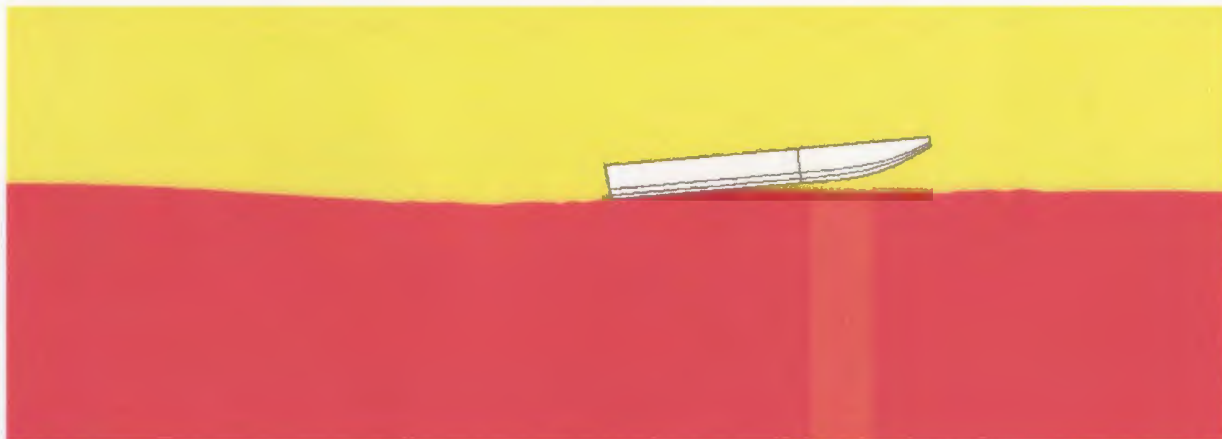


Figure 3.23 – Free Surface at Centerline Plane

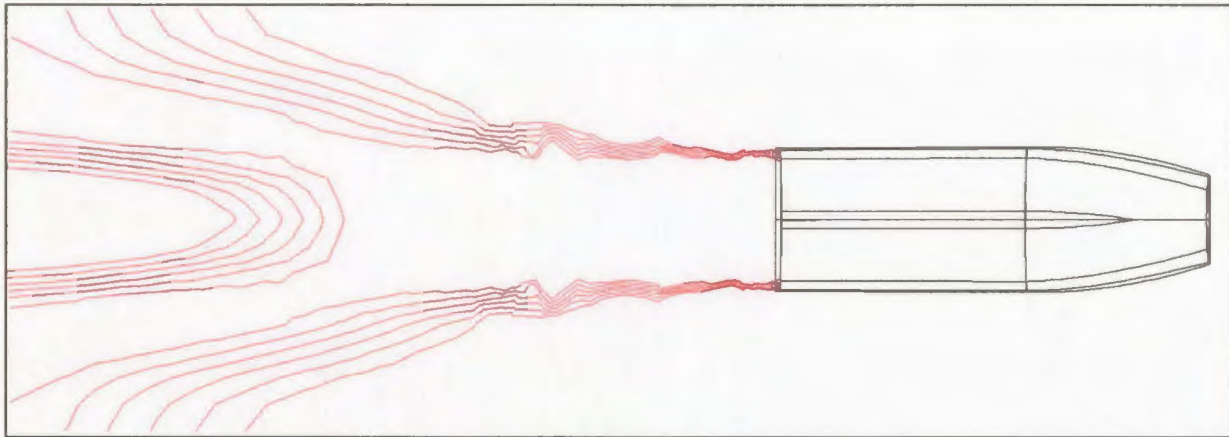


Figure 3.24 – Free Surface Contours

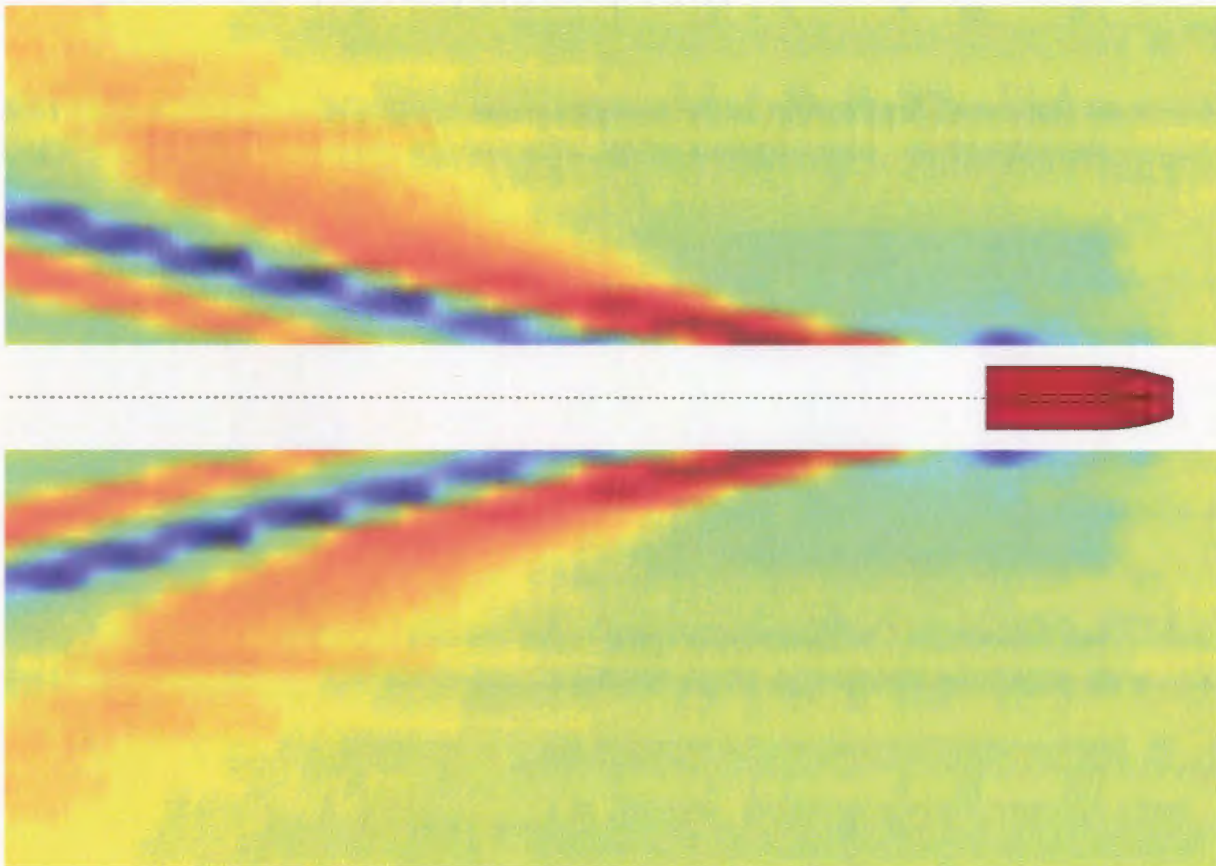


Figure 3.25 – Wave Profiles from Physical Experiments

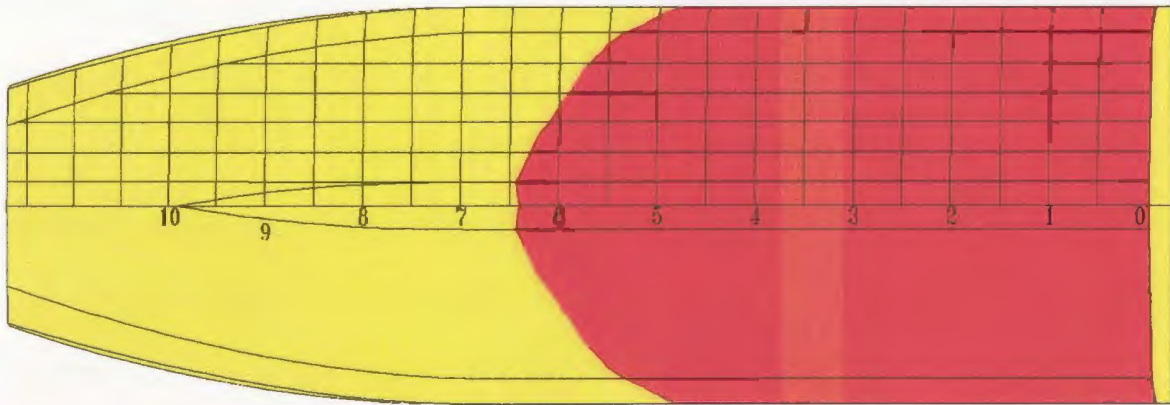


Figure 3.26 – Wetted Surface Area from CFD



Figure 3.27 – Wetted Surface Area from Experiments

3.4 Discussion

This chapter described the procedure used to create and run the CFD simulations of the Niagara Jet Boat planing hull, along with typical results. The presented material was the culmination of a lengthy trial and error process needed to achieve a workable combination of meshing strategy and solution technique. The final process was found to be robust over the entire range of model speeds and hull orientations tested. However, computing time restrictions prohibited the use of a mesh density capable of adequately resolving the free surface waves and boundary layer.

Hull pressures were found to take on expected distributions; more discussion on these is given in the next chapter. Flow velocities were also found to align in patterns consistent with experimental observations. The free surface, though weakly resolved, still exhibited qualities closely matching those of the physical test results. Having established a stable and well behaved process for performing planing hull CFD simulations, sets of tests were then performed to evaluate the method in terms of parameters such as drag and trim angle. A description of these tests and their results are given in the following chapter.

CHAPTER 4

EQUILIBRIUM SIMULATIONS

4 EQUILIBRIUM SIMULATIONS

The evaluation of CFD for predicting planing hull performance was undertaken in three stages. The first was used to compare the numerical simulations directly with the physical experimental results by matching the hull orientations for each model speed. The next stage allowed the model to move vertically in the CFD simulation at a fixed trim angle until the net lift balanced the model weight. The third and final stage permitted movement in both vertical position and trim angle until the model achieved equilibrium in both lift and trimming moment at speed. The ability of a CFD simulation to predict the at-speed orientation of a planing hull is critical for accurately evaluating its performance, as resistance is intimately linked to sinkage and trim angle. This chapter presents the procedure used to allow Fluent to solve this problem, along with the results and analysis of the simulations.

4.1 Literature Review

Solving for dynamic equilibrium is an essential part of evaluating planing hull performance. Even empirical methods, such as Savitsky (1964), attempt to adjust the external flow induced forces and moments to match the distributed weight of the vessel. However, these techniques rely on algebraic relations based on regression analysis of experimental data for specific hull types, thereby limiting their applicability. In theory, CFD methods can be used to simulate the flow around any hull shape, though only for a fixed orientation. By extending the capability of a CFD code to include the solution of dynamic equilibrium, a tool is created that can predict planing hull performance, regardless of hull shape. The same techniques could also be used to solve a wide variety of similar problems where equilibrium is required. This section reviews some published literature related to the solution of dynamic equilibrium of a vessel for performance prediction.

Savitsky (1964) discussed the basic hydrodynamic characteristics of prismatic planing hulls. Based on previously published work, empirical equations for lift, drag, wetted area, center of pressure, and porpoising limits as functions of speed, trim angle, deadrise angle and loading were given. A procedure was presented for using these equations to predict the performance of a prismatic planing hull. This paper, and the work it was derived from, presents one of the earliest methods for predicting planing hull performance and is still widely used today. This iterative method was based on choosing trim angles, which were then fed into empirical equations that produced values for lift and moment. Iterations continued until these values balanced those produced by the hull's weight and center of gravity.

Ikeda *et al.* (1993) addressed the need to include the effects of trim and sinkage in high speed craft predictions by performing a set of captive model tests with systematic variations of the model's position and attitude. Nine model shapes were tested. The model was fixed to the tow carriage by a three-component dynamometer that measured lift, drag and trimming moment. Sinkage and trim were incrementally varied to create a database of the hydrodynamic forces for each model over a range of Froude numbers. A computer program was also developed to use this database to estimate the sinkage, trim angle, and resistance of a given model at speed for a given ballast condition (displacement and LCG). Hydrodynamic forces could be determined by interpolation from the database for a given vessel attitude in an iterative scheme until they were in equilibrium with the model's weight and LCG. Simulations of this type were found to be in good agreement with results obtained from free-attitude model tests.

Brizzolara *et al.* (1998) presented comparisons of wave patterns and wave resistance from both numerical and experimental results. A high speed monohull and two catamaran type hulls were used in model tests at Froude numbers up to 0.9. Their boundary element code, previously used for slower speed vessels, was extended for use on high speed vessels by including calculations of dynamic equilibrium. Forces and moments were evaluated after each iteration and the model's position was updated and re-meshed. The cycle continued until convergence was achieved (usually under 10 iterations). Results for the Wigley hull in the speed range from 0.2 to 0.8 were shown to be under-predicted for sinkage, trim, and wave resistance, though trends in the data were roughly followed.

Subramani *et al.* (2000) extended a CFD code (CFDSHIP-IOWA) for surface-ship boundary layers, wakes and wave fields to include the capability of predicting sinkage and trim. Simulations were performed on hulls of the naval combatant FF1052 and the Series 60. The CFD code uses the finite volume method for block-structured grids. It employed the Baldwin-Lomax turbulence model and accounted for the free surface boundary conditions with the aid of a body-free-surface conforming grid. Dynamic trim and sinkage were calculated iteratively. Forces and moments on the hull were summed at the end of each iteration. The hull was then re-positioned and the domain grid regenerated for the next iteration, or until equilibrium was achieved. Simulations on the two hulls used mesh sizes from 216,000 to 906,000 nodes. When compared with model experimental data, it was found that although the trends in sinkage and trim were predicted correctly, the percentage difference in absolute values varied with Froude number.

Yang *et al.* (2000) extended their unstructured, free surface, inviscid, finite element based flow solver (see Löhner *et al.*, 1998) to account for sinkage and trim effects in steady ship flows. Simulations began with the model in its “at-rest” position. The flow solution was then calculated and used to determine sinkage and heave corrections for the next iteration. The near field mesh moved with the hull, far field meshes remained fixed, while intermediate mesh elements were smoothed for even transition from the near to far field grids. Iterations continued until dynamic equilibrium was achieved. Sinkage and trim corrections at each iteration were based on current flow results in conjunction with the vessel’s waterplane area and moment of inertia. Tests were performed for the Wigley and Series 60 hulls over a range of Froude numbers. Results indicated significant differences

in wave drag between fixed and free to trim and sink configurations, in agreement with experimental observations.

The importance of dynamic equilibrium calculations in vessel performance prediction has been addressed by all of the above authors. The procedure was similar in all cases.

Different hull orientations were tested in an iterative scheme until forces and moments matched the required values. Planing vessel performance is the most sensitive to hull orientation making the additional equilibrium calculations essential. This problem was addressed in the current work by using a similar iterative technique. A low dead-rise planing hull was chosen (more conventional hull shapes were used by Yang et al. 2000, and Subramani et al. 2000). Simulations were performed using a RANS CFD code with a free surface capturing method.

4.2 Procedure

The CFD code Fluent v5.3 was not designed to solve problems where parameters in the simulation are a function of the results of the simulation. For instance, the terminal velocity of a falling object is dependent on the net drag, which must equal the object's weight. Another example is the flow dependent geometry problem of a planing hull. At a given speed, the orientation of the hull is a function of the pressure forces exerted on its surfaces such that they balance the distributed weight of the vessel. The solution of these types of problems can be achieved by using the CFD solver in an iterative loop controlled by an external equilibrium program.

The equilibrium program, written by the author for this study, relied on the fact that both Gambit v1.2 (mesh generator) and Fluent v5.3 (CFD solver) could be run in batch mode; they can be executed from a command prompt. The instructions or commands for the program were read line by line from a pre-existing text file. The equilibrium program created appropriate command files for each code (Gambit command files are referred to as “Journal Files” and Fluent command files are referred to as “Scheme Files”). The mesh generator and solver were then executed in batch mode. The CFD solver created a text output file of the results of the simulation (see Section 3.1.4) that could be read and evaluated by the equilibrium program. The program ends if equilibrium was achieved, otherwise a new orientation of the model was determined and the cycle began again. A simplified flowchart of this process is shown in Figure 4.1.

The first step in the equilibrium program used for the planing hull simulations was to set an initial hull orientation. This can be an arbitrary assignment, though a good initial guess can lead to fewer iterations. Step (2) created a text file of Gambit commands that were used to generate the mesh and define the boundary conditions for a given simulation. The hull and domain were first imported as ACIS solids (‘.sat’ format) and the hull was oriented as required. Boundary surfaces were then defined, such as the hull, inlets, outlets, and outer walls. The domain surfaces and volumes were meshed to preset specifications and the final mesh was then exported to a file in a Fluent ready format.

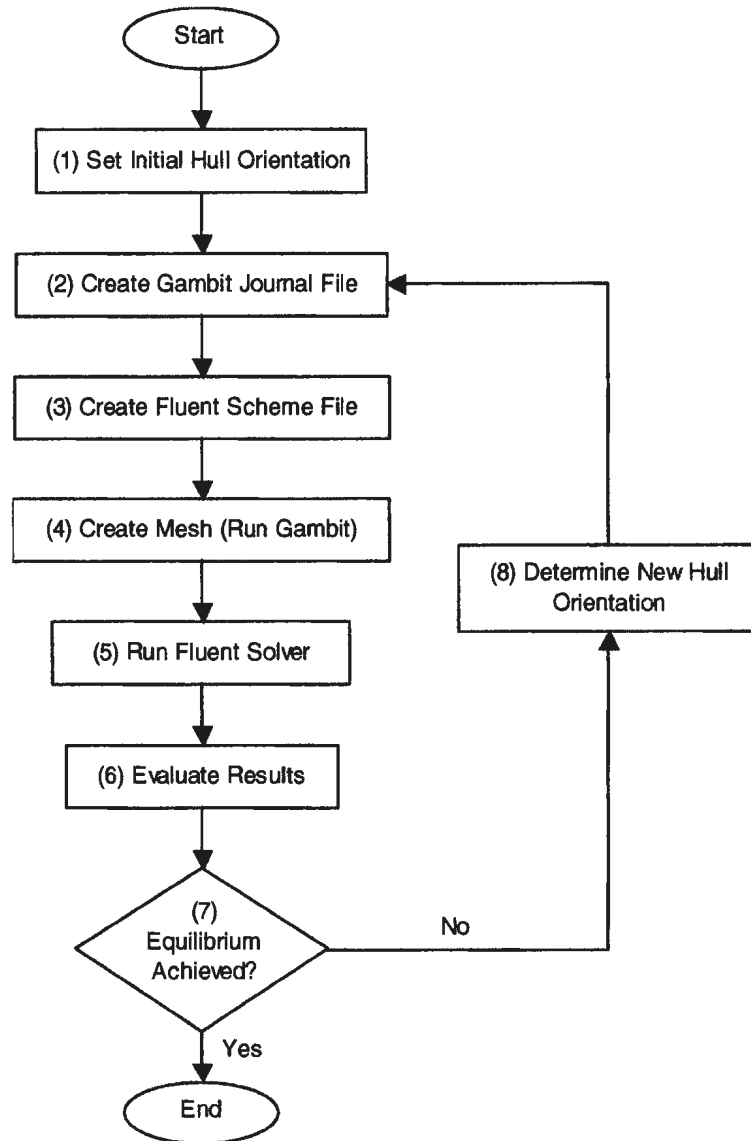


Figure 4.1 – Flowchart for Equilibrium Program

The next step was also used to create a text file, but for the CFD solver. These commands instructed Fluent to load in the mesh and set various parameters, such as activating the volume-of-fluid model and defining gravity, inlet flow speed and fluid properties. The simulation was then initialized (see Section 3.1.3) and the solution process initiated.

Steps (4) and (5) set in motion the solution of the current iteration by first running Gambit with the newly created journal file followed by Fluent with its scheme file. While the solver was running, information on each timestep, including solution residuals, hull forces, hull moments, wetted lengths, and wetted areas were continually exported to a text file. Once completed, this text file was read by the equilibrium program in step (6). The forces, moments, wetted lengths and areas were used to evaluate the current state of equilibrium (as discussed in Section 3.2). If an equilibrium condition was not achieved, step (8) would be called to improve the hull position for the next iteration.

Three types of simulations were run for the planing hull model. The first type was a truncated version of the flowchart in which the initial hull orientation was set to match that measured during the physical experiments with (7) and (8) omitted. This is referred to as a 0-degree of freedom model. The next type was a 1-degree of freedom model where equilibrium was only evaluated for lift, using the hull's vertical position relative to the still water line as the parameter altered in each iteration. Full equilibrium was then calculated in a 2-degree of freedom model that balanced both vertical forces and trimming moments by altering the hull's vertical position and trim angle. The results from these simulations are presented in Sections 4.3 - 4.5 respectively.

4.3 0 - Degrees of Freedom

This section presents the results of CFD simulations where the orientation of the hull was set to match those determined from the physical experiments for each speed. These tests were used to directly compare the experimental and computational results for the planing hull model.

The CFD results for the 0-degree of freedom case were higher than those seen in the experimental results. Shown in Figure 4.2 are the total resistance curves for the experimental results, the CFD results, and those obtained by applying Savitsky's method (Savitsky, 1964). The results from Savitsky's method under predicted those of the experimental results, though at higher speeds the results tended to improve. The CFD results were well above those from the experimental results, particularly in the 3.0 m/s to 4.0 m/s range. Similar trends are seen in Figure 4.3, which shows only the component of resistance from pressure forces. Savitsky's method uniformly under predicted the experimental data, while the CFD results peaked at 3.0 m/s.

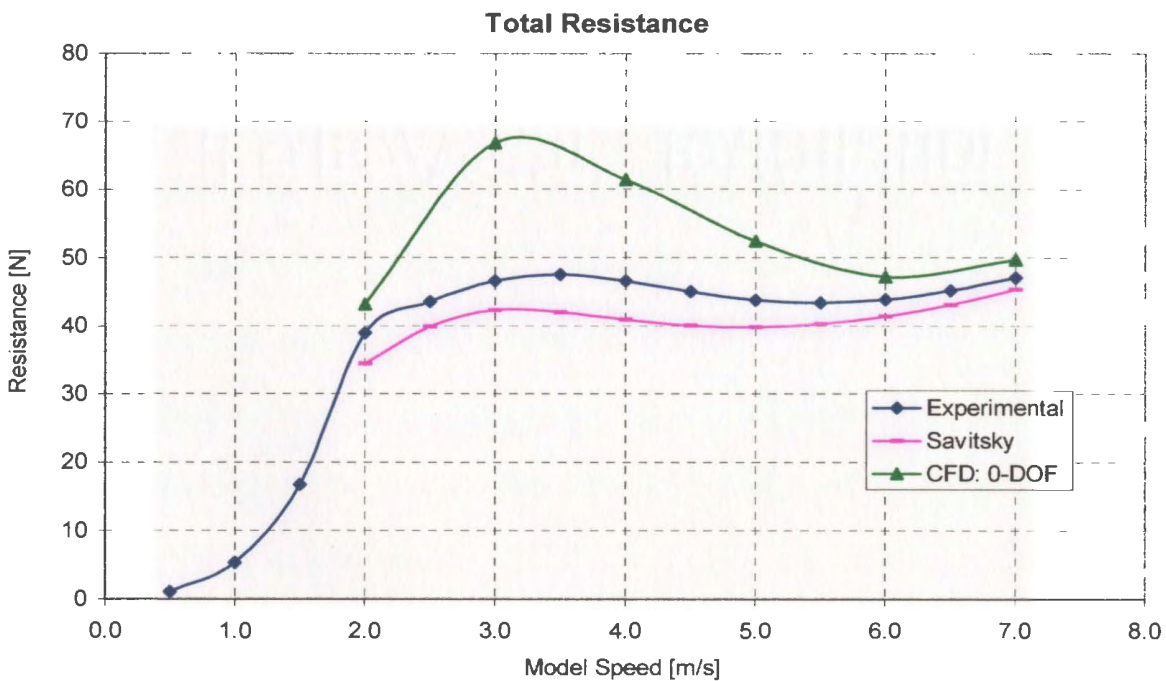


Figure 4.2 – Total Resistance: 0-DOF

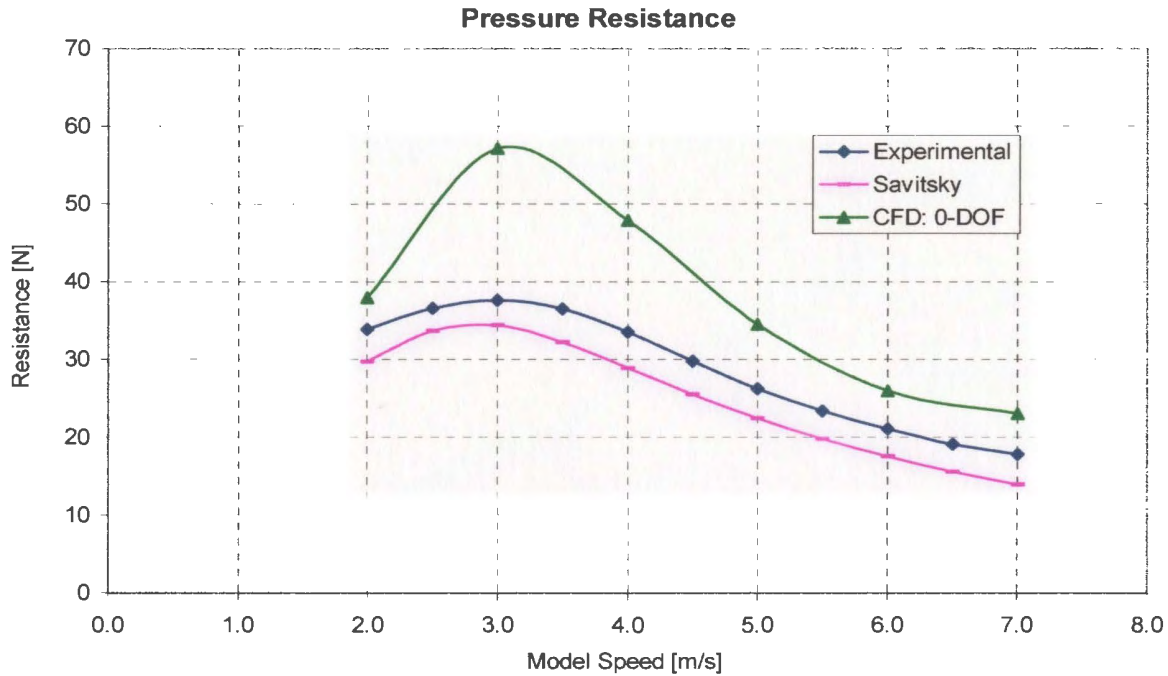


Figure 4.3 – Pressure Resistance: 0-DOF

The frictional resistance results, shown in Figure 4.4, were well behaved between the three sets of data. This was primarily a consequence of the similarly compliant wetted surface area results shown in Figure 4.5¹. Small deviations in the CFD results were likely due to experimental error in the determination of sinkage used to set the vertical position of the numerical model for these simulations. As these variations were small, they cannot account for the high values of total resistance. These were instead attributed to an over-prediction of hull pressure forces.

¹ A 1% error in wetted area leads to a 1% error in frictional resistance. A 1% change in Reynold's Number leads to less than a 0.2% change in frictional resistance.

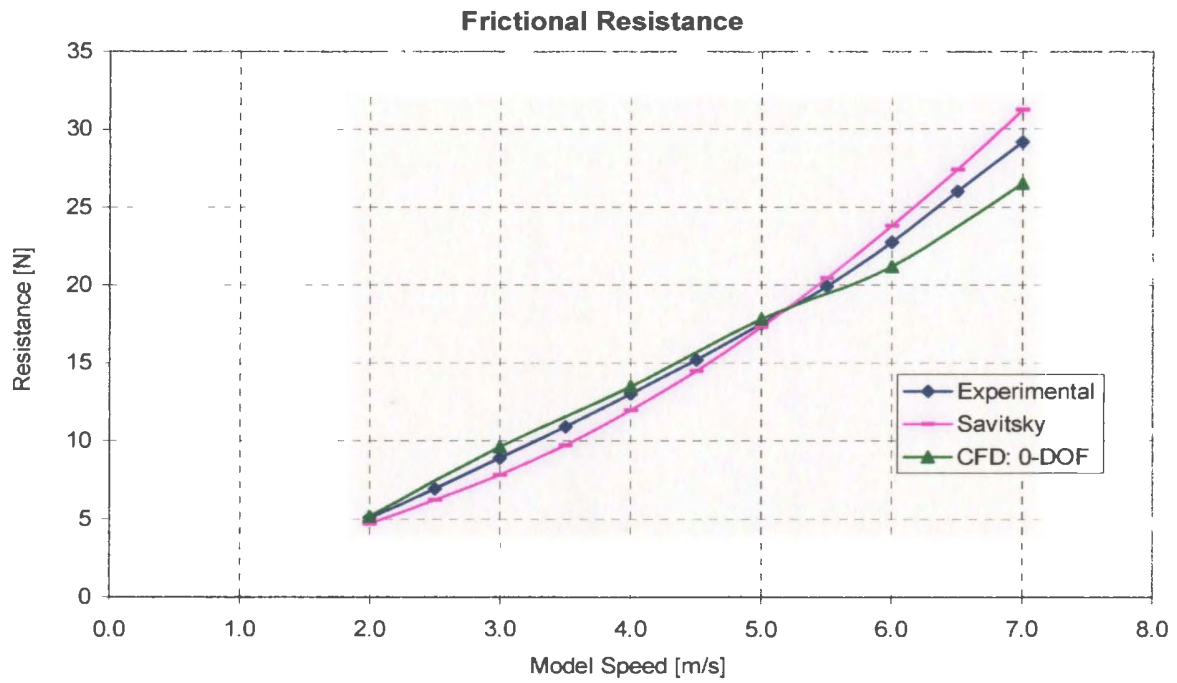


Figure 4.4 – Frictional Resistance: 0-DOF

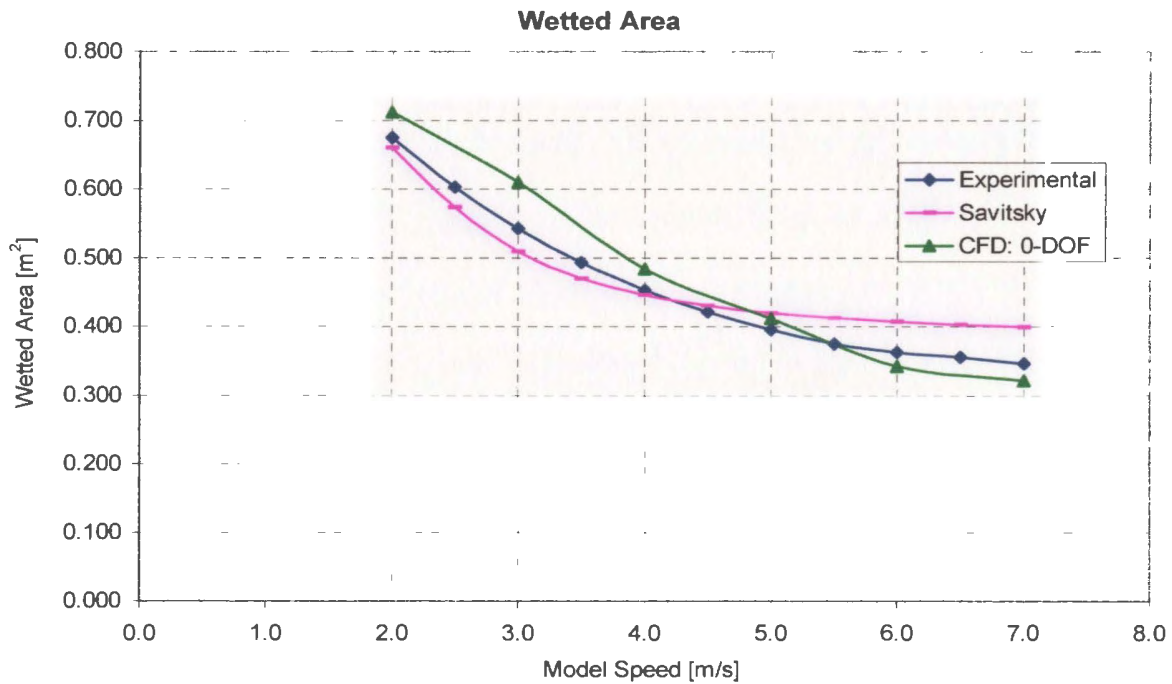


Figure 4.5 – Wetted Area: 0-DOF

The high resistance results for the CFD simulations were a consequence of high pressures being computed on the hull. The experimental pressure tap results gave some indication as to where on the hull the pressure was being over-predicted in the CFD simulations. Figure 4.6 shows the hull pressures measured during the physical experiments alongside those from CFD at the same locations. The four positions are labeled in terms of their distance from the transom measured parallel to the hull bottom. The 90mm and 530mm positions were on the centerline while the 620mm and 275mm positions were 50mm to the port side. As discussed in Section 2.3.4, experimental hull pressures near the stagnation region increased with increasing speed, whereas the pressures near the transom showed decreasing trends with increasing model speed (i.e. once planing speeds were reached). The CFD results also followed these trends, although there were differences in the magnitudes when compared with the experimental values. The forward pressures seem to be under predicted while the aft pressures were over-predicted. In other words, the pressure profiles indicated by the experimental results show considerably larger variation along the hull than produced by the CFD simulations. Generally, the region of over-predicted pressure (near the aft of the hull) was larger than the under-predicted region, which was isolated near the leading edge of the air/water interface². The net result of these higher than expected pressures led to both excessive drag and lift on the numerical model, despite a close correlation for wetted area and frictional resistance.

² The forward pressures were sensitive to the location of the leading edge due to a large pressure gradient near this region. Aft pressures were less sensitive due to a relatively smaller gradient.

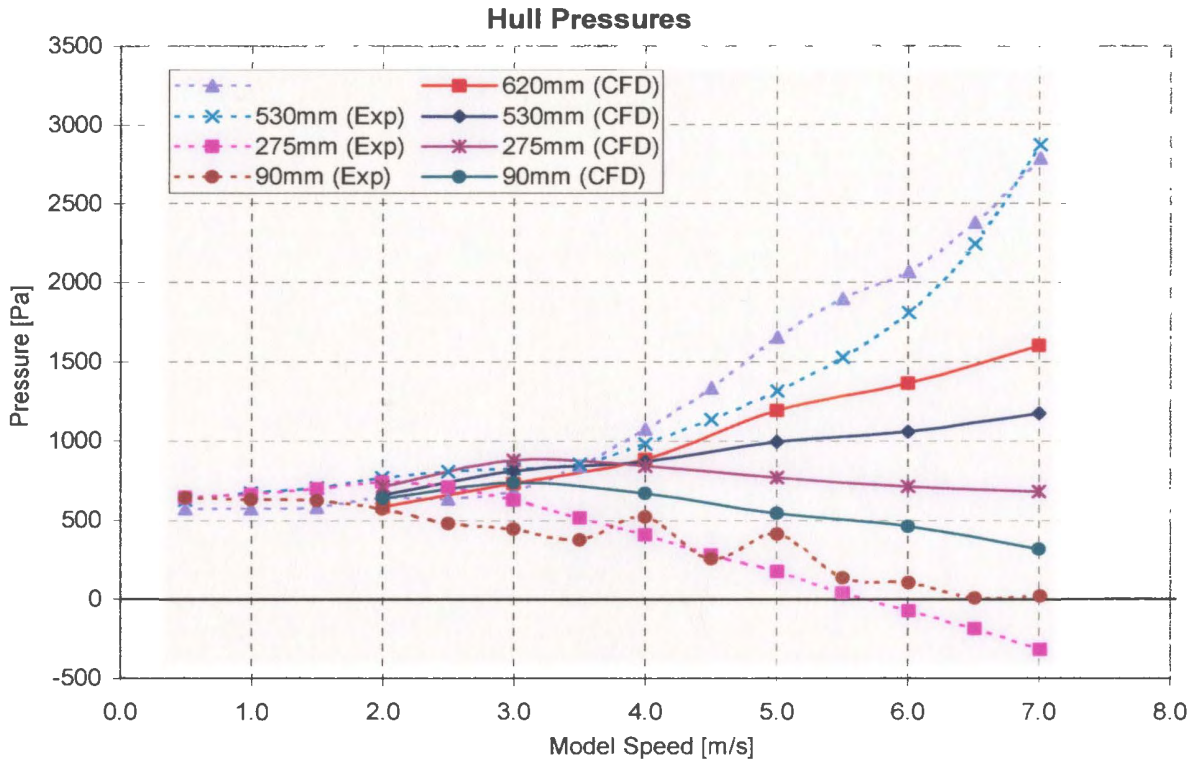


Figure 4.6 – Hull Pressures

The above pressures are also shown below in distributions along the centerline of the hull for the CFD simulations. Given in terms of pressure coefficient, several characteristics became apparent between model speeds. The wetted length was seen to decrease, as given by the locations of the peak pressures. The peak pressures, in terms of pressure coefficient, also decreased with increasing speed; although this was actually found to be a consequence of trim angle (see Section 4.5). The figure also shows the relative contributions to net lift from hydrostatic and dynamic forces. At the slower speeds, there was a pronounced hump in the aft region caused by hydrostatic pressure. As speed increased this hump gradually dissipated.

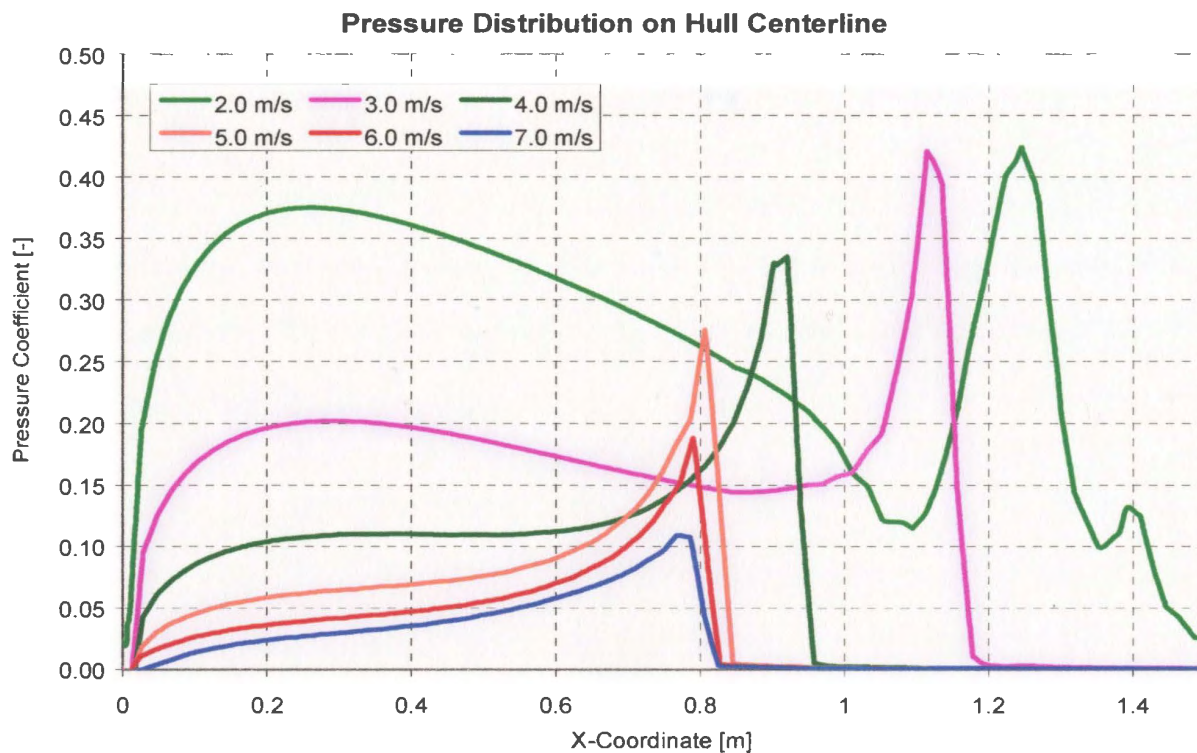


Figure 4.7 – Pressure Distributions on Hull Centerline

As discussed in Section 3.2, the boundary layer was not adequately resolved in the CFD simulations for accurate frictional resistance predictions. This is illustrated by Figure 4.8, which shows the results of the experimental LDV measurements (see Section 2.3.6) and the velocity results from the CFD simulations at the same locations. The profile shapes from the CFD simulations were flat, a consequence of the limited number of cells near the hull surface. The resulting shear stresses were therefore greatly under predicted.

There was also a difference in the free stream velocities between the experimental and numerical results. At a distance of about 12mm from the hull (measured perpendicular to the hull surface), the profiles stabilized to constant velocity values. In the experimental results, the forward position shows a velocity equal to the model speed, while the aft position shows a slight acceleration with a velocity about 5% higher than the model

speed. A similar acceleration was seen in the CFD values, but both profiles were shifted towards slower velocities.

In fact, if the change in velocity is plotted against trim angle, as was done with the LDV results in Section 2.3.6, the CFD results also exhibited a linear relationship. As shown in Figure 4.1, the slope of the CFD and experimental curves were a close match, only with the CFD curve shifted downwards.

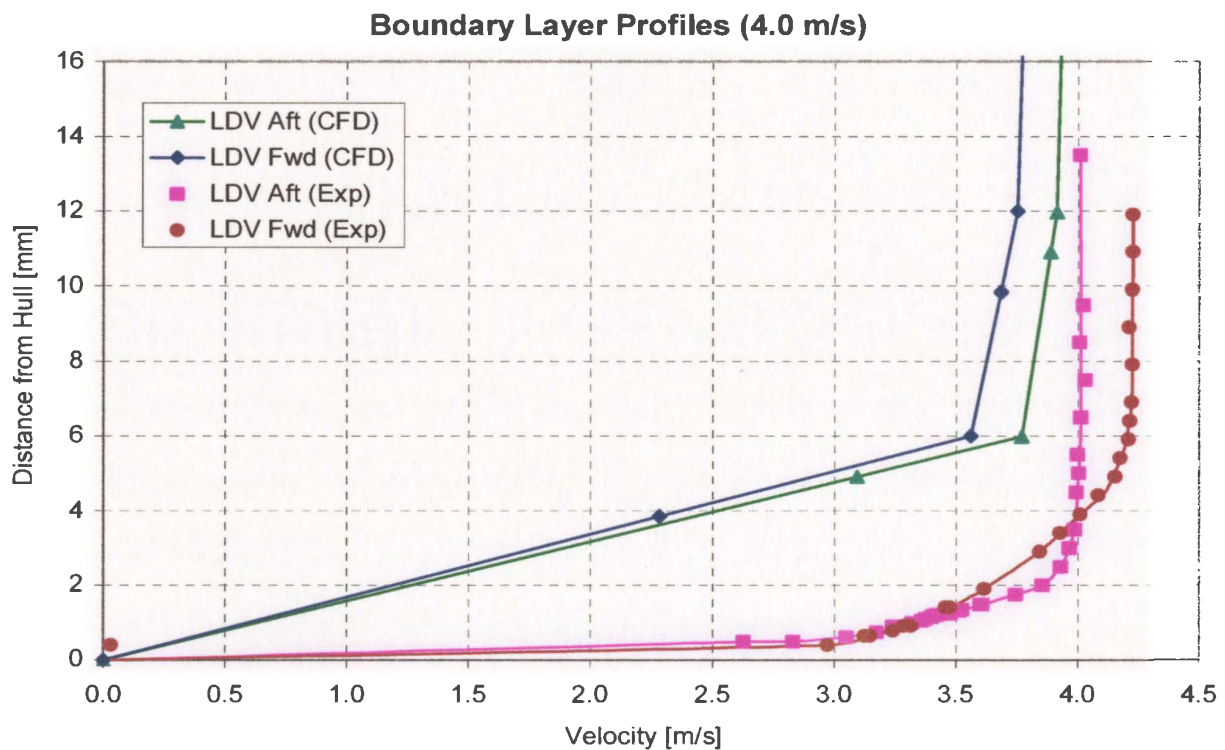


Figure 4.8 – Boundary Layer Velocity Profiles

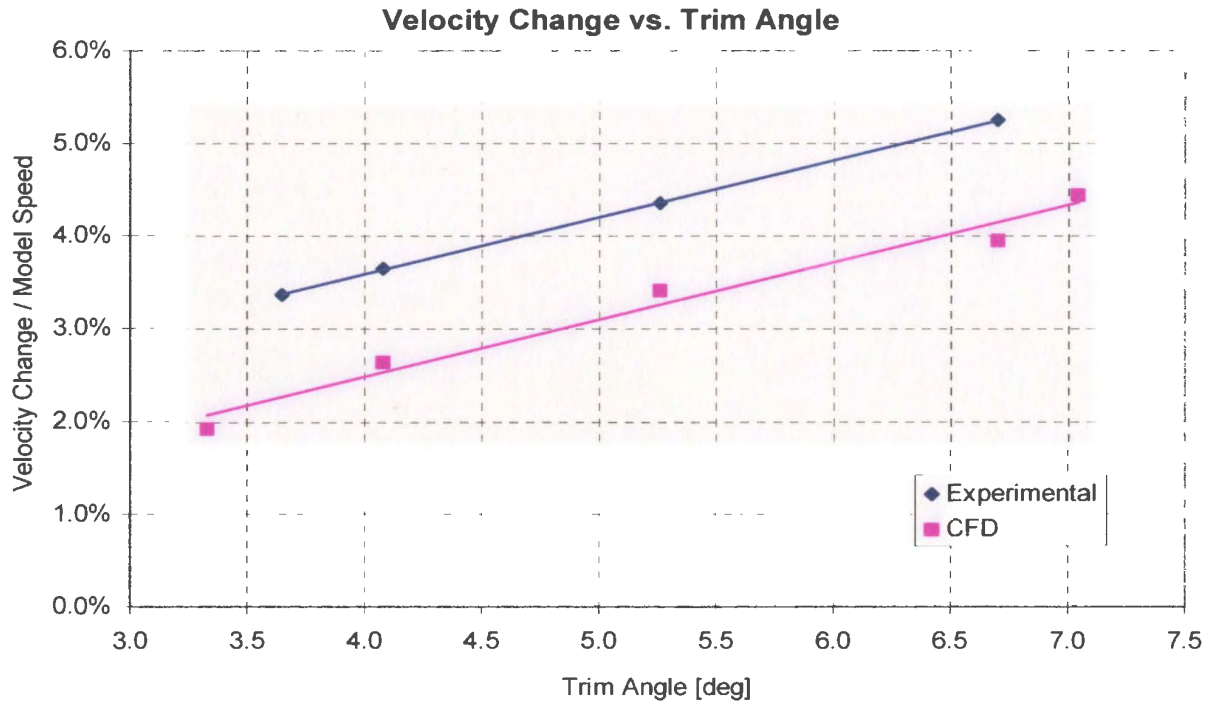


Figure 4.9 – Velocity Change vs. Trim Angle

In order to clarify the differences between the numerical and experimental free stream velocities and pressures, their profiles along the centerline of the hull were examined.

Figure 4.10 shows the total pressure from a typical CFD simulation along with experimental values. Also shown is the CFD velocity profile with experimental values (measured at two positions on the hull using a laser Doppler velocimeter). Velocities were taken at a position 15 mm from the hull surface to ensure they were outside of the boundary layer.

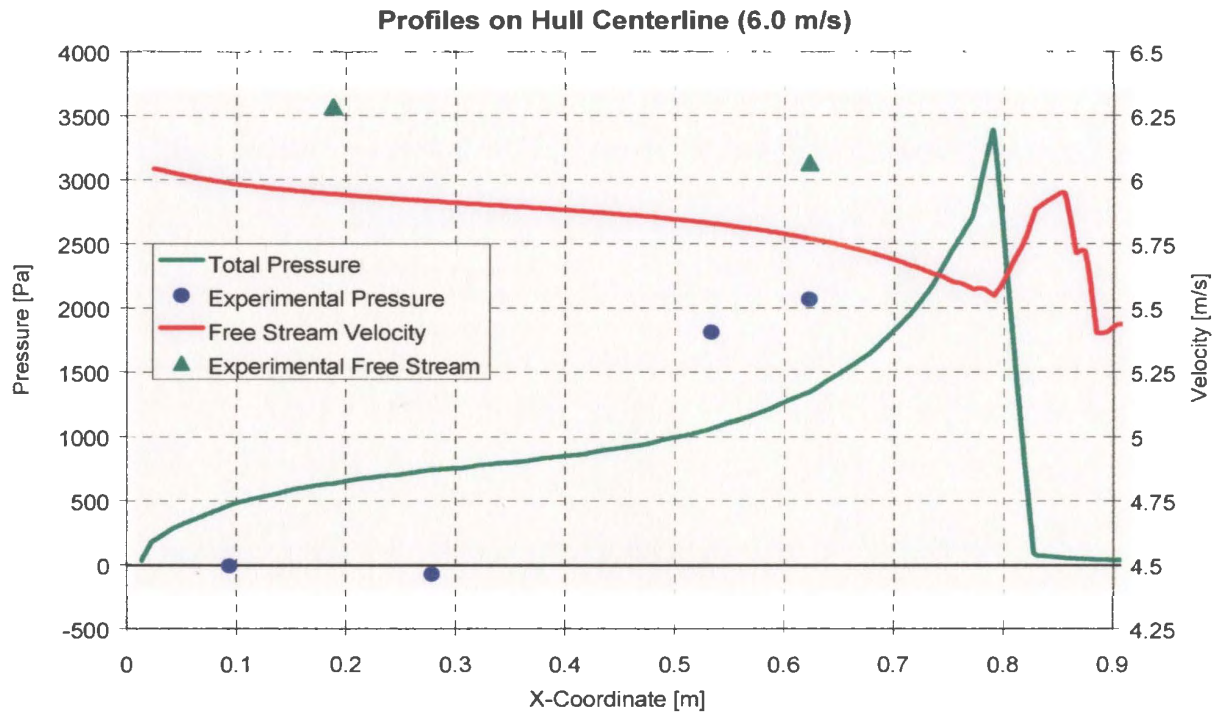


Figure 4.10 – Pressure and Velocity Profiles on Hull Centerline

These results were typical for this set of tests. Pressure was under predicted at the front of the hull and over predicted at the aft part of the hull. The apparent shift between the CFD results and LDV results from the physical experiments could be explained by a possible bias error in the physical measurement. However, the simulations significantly over predicted the net pressure force, suggesting that velocities were indeed being under predicted in the aft region.

The results from the 0-degree of freedom simulations were found to follow the trends expected for a planing hull, although net pressure was over predicted. As net lift was higher than required for equilibrium, the next step was to balance net lift to the model's weight (in isolation of trim angle and trimming moment). This process is presented in the next section.

4.4 1 – Degree of Freedom

In this set of tests, the model's vertical position relative to the waterline was altered by the equilibrium program so that net lift balanced the model's weight. The trim angle used for each speed was that measured during the physical experiments. The goal of these tests was to determine the sensitivity of the model to sinkage, and to establish whether deviations in the 0-degree of freedom model could be attributed to experimental error in this parameter.

Figure 4.11 shows expanded versions of steps (6) through (8) of the flowchart in Figure 4.1 used for this set of tests. The calculations for steps (6a) – (6c) are outlined in Section 3.2. From these, a check was performed to determine if the net vertical force on the CFD model was equal to the weight of the vessel. A tolerance was used here to accommodate the fact that CFD calculations are not exact. Agreement of these values ended the program successfully. If equilibrium was not achieved, then another check was performed to confirm that the iteration count was not exceeded, and the values calculated in step (6) were reasonable. This check was to ensure that the current solution was not divergent; such cases produce extreme values for calculated forces. Passing this test, the next step was to determine a new value for sinkage to be used in the subsequent iteration. The secant method was chosen as an efficient means to advance toward the correct solution. This commonly used iterative, non-linear root finding scheme is shown below in equation [4.1]. One last check was performed to ensure that the new value for sinkage was reasonable (i.e. the vessel was not completely submerged or airborne) and the loop was restarted at step (2).

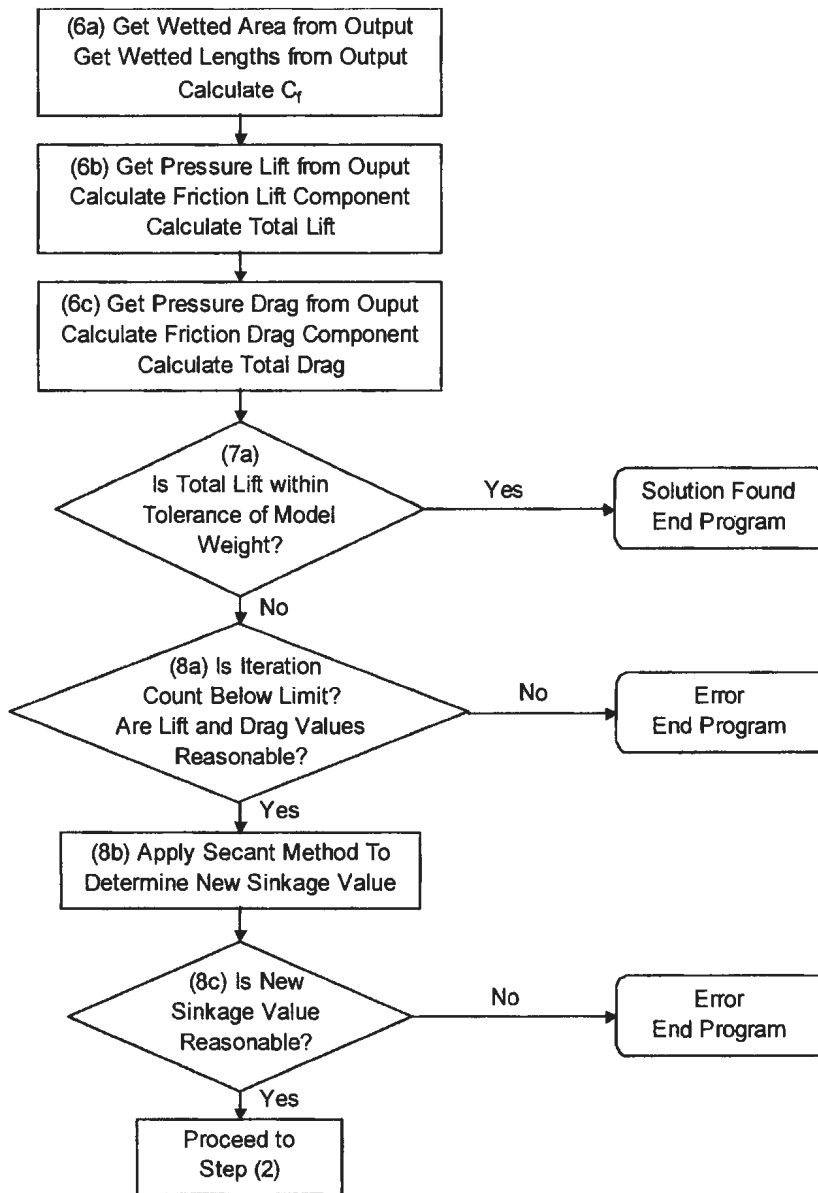


Figure 4.11 – Expanded Flow Chart for 1-Degree of Freedom

$$x_{i+1} = x_i - y_i \cdot \frac{(x_i - x_{i-1})}{(y_i - y_{i-1})} \quad [4.1]$$

where,

x_{i-1} = Previous Sinkage Value

y_{i-1} = Previous Net Lift - Model Mass

x_i = Current Sinkage Value

y_i = Current Net Lift - Model Mass

x_{i+1} = New Sinkage Value

The results from this set of numerical simulations showed improvement over the 0-degree of freedom tests. The resistance curves for the CFD runs, the experimental tests, and Savitsky's method are presented in Figure 4.12 and Figure 4.13. The total resistance results were fairly close to the experimental results. The hump speed, hollow and resistance increase were all clearly followed by the CFD curve, showing improvement over the empirical Savitsky results. In order to better interpret the numerical results for total resistance, they have been decomposed into contributions from pressure and frictional forces.

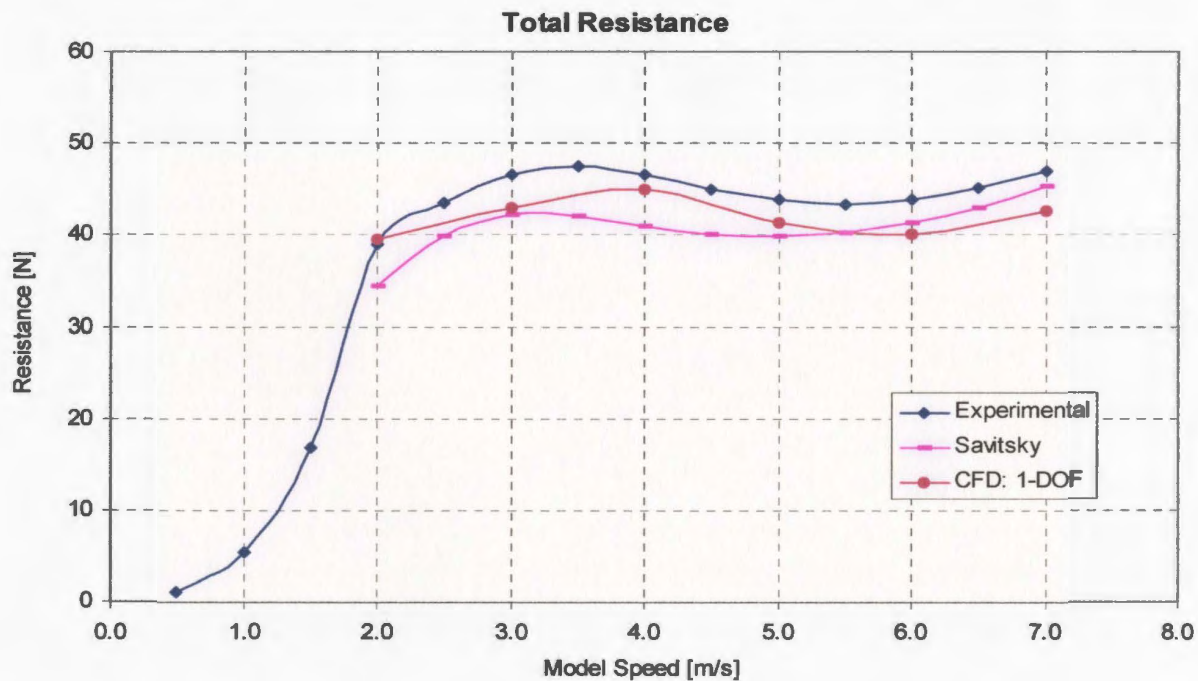


Figure 4.12 – Total Resistance: 1-DOF

The frictional resistance (calculated from the model's mean wetted length and wetted area according to the method described in Section 3.1.4) was seen to be slightly lower than the experimental values. This was primarily a function of the wetted area, which followed a similar trend. The low wetted area results, shown in Figure 4.14, were themselves attributed to the fact that the final sinkage values for the simulations that satisfied the 1-degree of freedom equilibrium condition were higher than those measured during the physical experiments. Shown in Figure 4.15, the sinkage values for both the CFD and experimental results are given. Although the experimental values had a relatively high degree of uncertainty (as discussed in Section 2.4), the CFD results were still uniformly larger. One consequence of this was that at a given speed, the numerical model was farther out of the water than the physical model, thereby having less hull submerged and therefore less wetted area. This confirmed that the pressure forces calculated by the numerical method were greater than those produced by the actual flow.

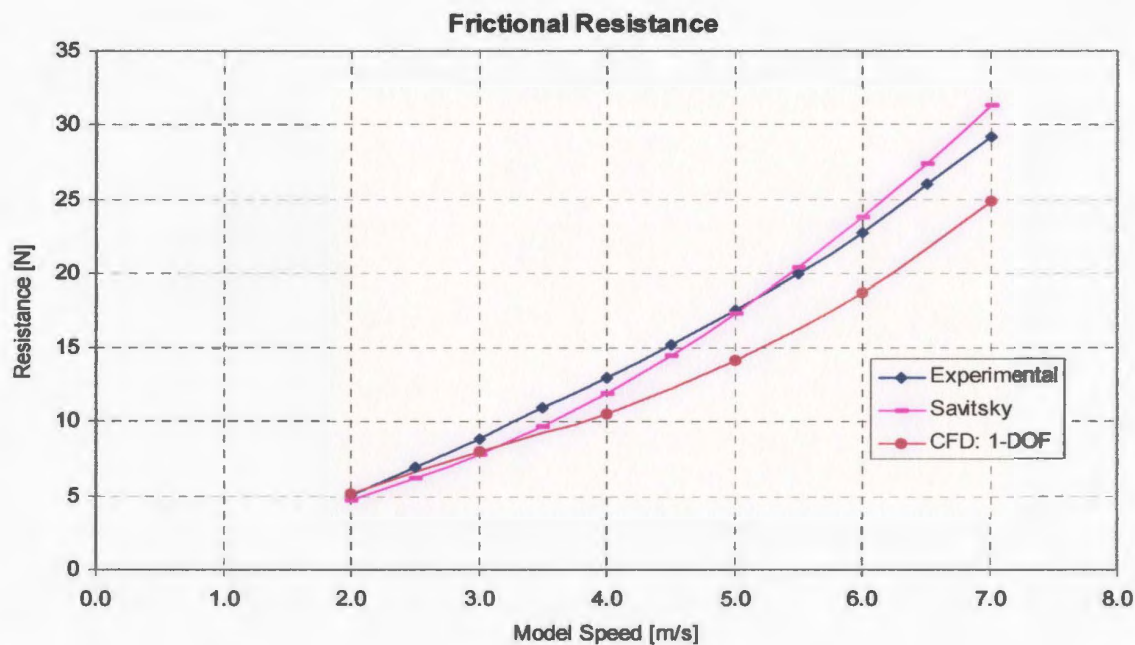


Figure 4.13 – Frictional Resistance: 1-DOF

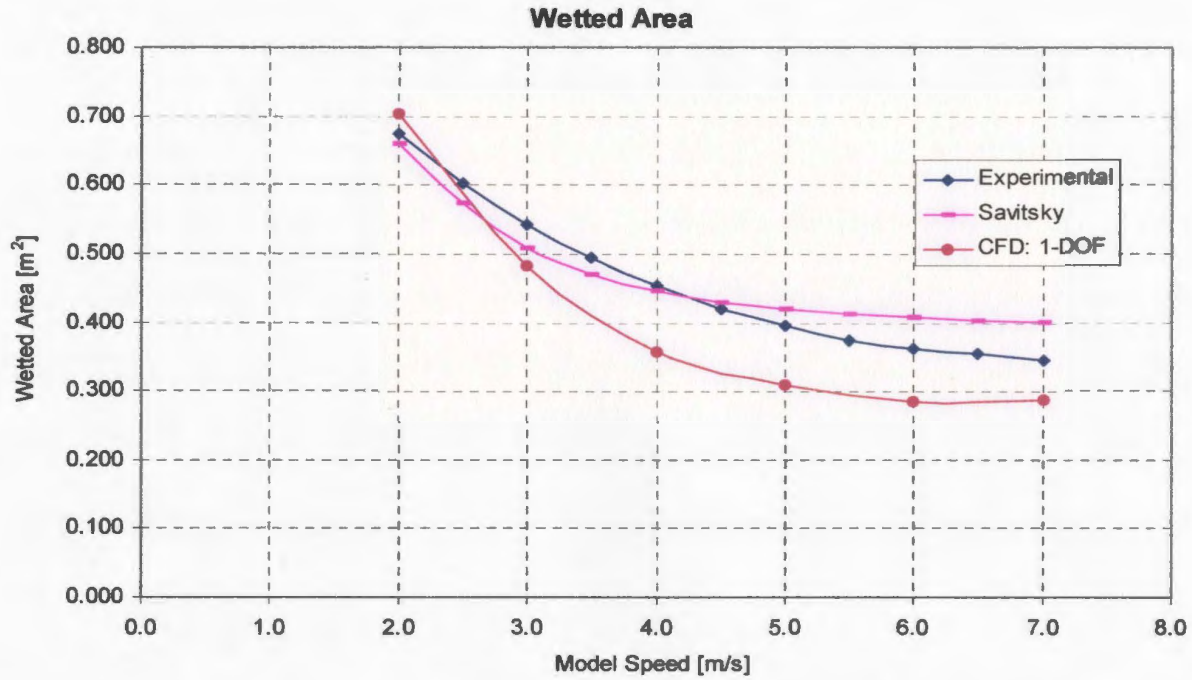
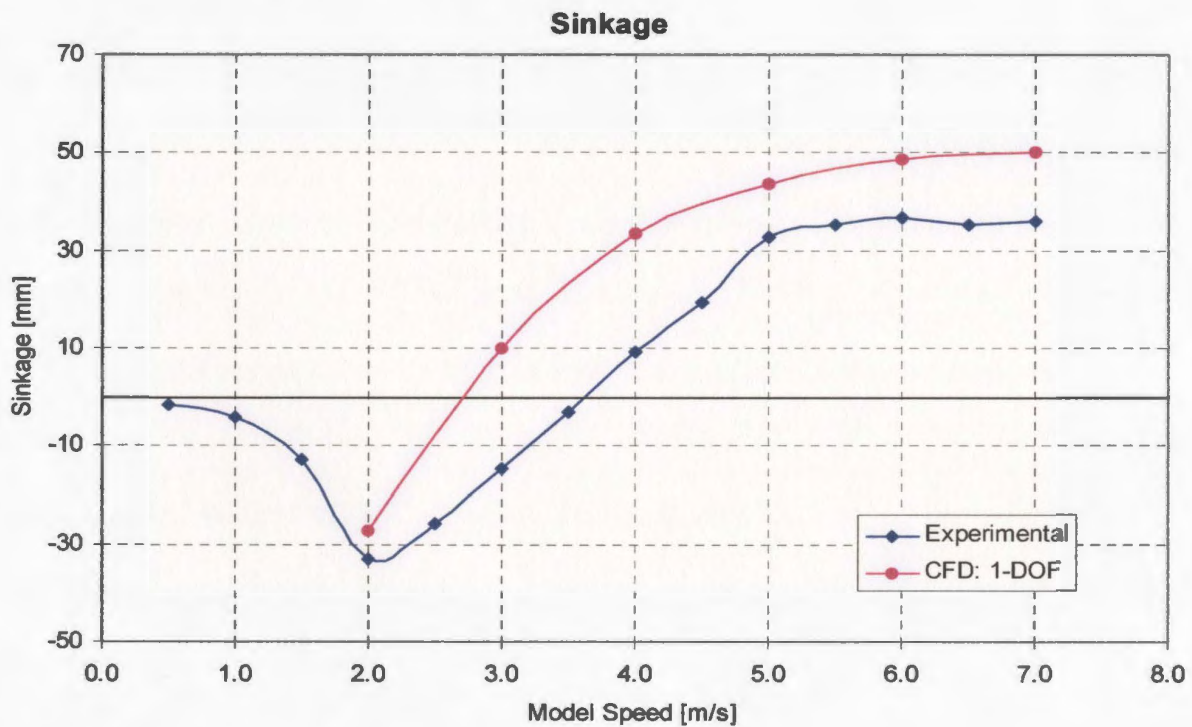


Figure 4.14 – Wetted Area: 1-DOF

Figure 4.15 – Sinkage: 1-DOF³

³ The sinkage values in this Figure represent the vertical distance the tow point moved from its resting position at zero speed. Positive values indicate an upward movement.

The pressure resistance was computed for the experimental results by first calculating the frictional component, and then subtracting that value from the total resistance. The numerical pressure resistance was computed by directly integrating the pressure forces over the hull area, while the pressure forces for Savitsky's prediction were determined from empirical formulae. Shown in Figure 4.16, the results of the 1-degree of freedom CFD simulations closely match those from the experimental results, despite the differences in sinkage, wetted area and frictional resistance. This match was attributed to a combination of the nature of the 1-degree of freedom constraint, and the shape of the hull.

The 1-degree of freedom simulations require that the net lift (vertical force) exerted on the model was equal to the model's weight. When planing at high speeds, the portion of the hull in contact with the water was essentially planar in the longitudinal direction. This and the fact that the transom was dry means that the system can be crudely represented as a flat plate with a pressure force acting perpendicular to it. This force can be expressed as a vertical component (lift) and a horizontal component (drag), whose magnitudes depend on the size of the pressure force and the trim angle of the plate (see part A in Figure 4.17). In a 1-degree of freedom simulation, the trim angle was held constant while the vertical position of the hull was altered, thus changing the location and magnitude of the resultant pressure force on the hull. As the location of this force is not relevant to the decomposition of the vector into lift and drag on a flat plate, altering the vertical position of the model was therefore equivalent to simply changing the magnitude of the resultant pressure force. The end result was that by requiring the lift component of this pressure

force to be equal to the model weight⁴, the drag force was inadvertently fixed to a value dependent only on the trim angle (given by equation [4.2]).

$$D_p = W_{\text{Model}} \cdot \tan(\tau) \quad [4.2]$$

where,

D_p is the pressure drag

W_{Model} is the model weight

τ is the trim angle

The drag force given by equation [4.2] is also shown in Figure 4.16 (labeled ‘Pressure Vector’). There was a close match between both the experimental and numerical results to the theoretical values, particularly between 4.0 and 6.0 m/s. There were, however, discrepancies such as at 3.0 m/s. The numerical value was near the theoretical curve, but the experimental value was somewhat larger. The reason for this difference lies in the hull shape, and the difference in sinkage values for the numerical and experimental results.

As discussed, the CFD sinkage values were all somewhat larger than the experimental values, so the CFD hull was relatively higher in the water. The numerical simulation at 3.0 m/s had a water contact area that still satisfied the ‘flat plate’ model and therefore had a pressure drag matching the theoretical value. In the physical experiments at this speed, the model was slightly lower in the water and the contact area included a region of the hull that began sloping upward towards the bow. This changed how the resultant pressure force was decomposed into lift and drag components. An illustration of this effect is

⁴ The constraint was actually that the net lift on the hull was equal to model weight; however, the contribution to net lift from frictional forces was in all cases less than 1%.

shown in Figure 4.17. Part A) in the figure shows the flat plate case, while part B) simplifies the curved hull case with two flat plates at different angles. Although the net lift for the two cases is identical, case B) has a slightly larger drag value.

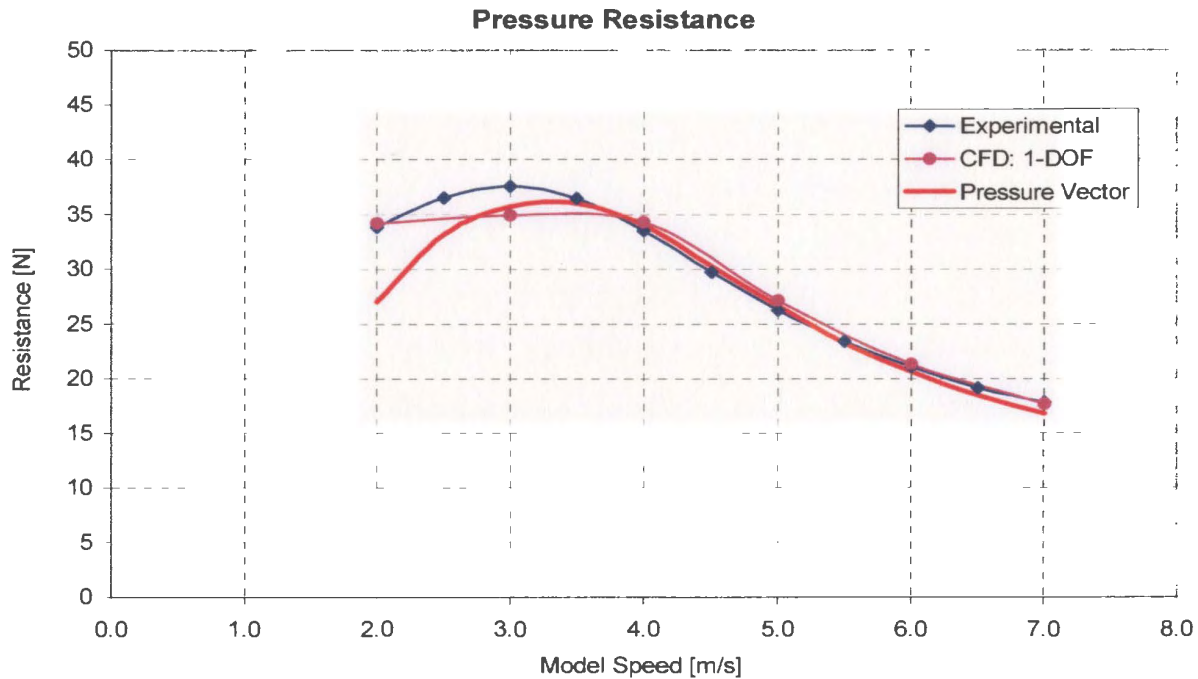


Figure 4.16 – Pressure Resistance: 1-DOF

The differences in contact area between the experimental and numerical simulations are best described in terms of the length of the wetted centerline. These lengths denote the maximum distance that the wetted surface area extended forward on the hull bottom. Shown in Figure 4.18, the wetted lengths for both the CFD and experimental tests are presented. Also shown in the figure is a line designating the point at which the hull begins to curve upward towards the bow. Points below this line followed the flat plate model and had pressure drag measurements matching the theoretical values. Points above this line tended to have higher pressure-drag values than given by equation [4.2].

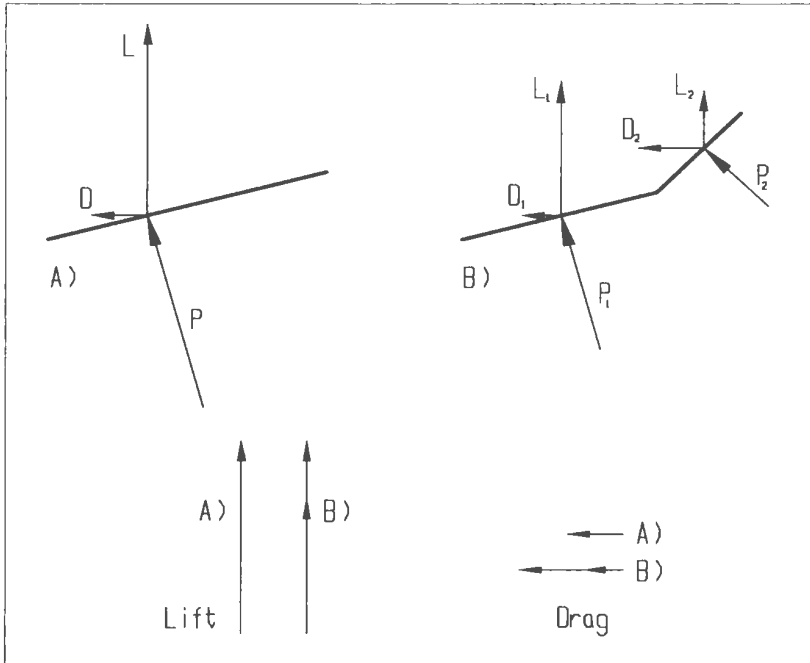


Figure 4.17 – Lift and Drag Vectors

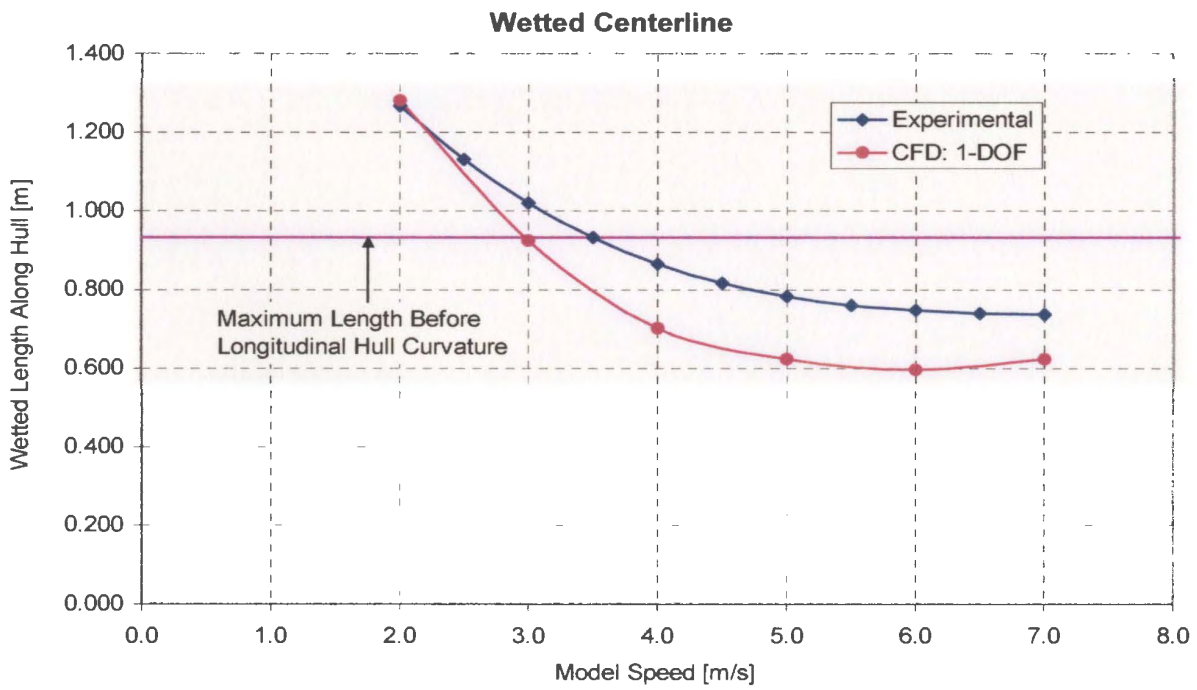


Figure 4.18 – Wetted Centerline Length: 1-DOF

The results from this set of simulations led to the following conclusions. They show that by removing the frictional drag (calculated by the method discussed) from the total measured drag, the resulting pressure drag falls on the curve predicted by simple theory, thereby validating the pressure/friction separation procedure⁵. This also supports the use of the method for the CFD case, which can result in large savings in mesh size and computation time. The 1-degree of freedom CFD results match the curve from simple theory, showing that the equilibrium solving procedure was working properly. The high values of sinkage and low values of wetted area for the CFD results compared with the physical experiments show that net pressure was being over predicted. Examination of the flow field in the CFD simulations suggested that the pressures on the hull were higher in the aft region and lower near the air/water interface than the experimental measurements. Free stream velocities followed the experimental trends, but were offset to lower values. In general, the computed flow was qualitatively consistent with experimental observations of planing hull flow, but actual values tended to deviate from the physical data.

4.5 2 – Degrees of Freedom

The last set of simulations involved solving for full dynamic equilibrium of the steady state motion of a planing hull through calm water. Both sinkage and trim values were used to determine the model orientation in which the net vertical force and net trimming moment on the hull were zero. The equilibrium program was an expanded version of the 1-degree of freedom model. The additional steps in the process are shown in Figure 4.19.

⁵ In fact, provided the water contact area is within the portion of the hull without longitudinal curvature and the transom is dry, the frictional component of drag could be determined simply by subtracting the

Step (6) was appended to include (6d) used to calculate both the trimming moment for the current iteration as well as the required trimming moment, which was a function of trim angle (see Section 3.2). Step (7) would then proceed, as in the 1-degree of freedom case, until (7a) was satisfied at which time the trimming moment check would begin. This process was essentially another 1-degree of freedom loop that would either exit the program with a completed solution (or with an error) or start the next iteration with a new trim angle.

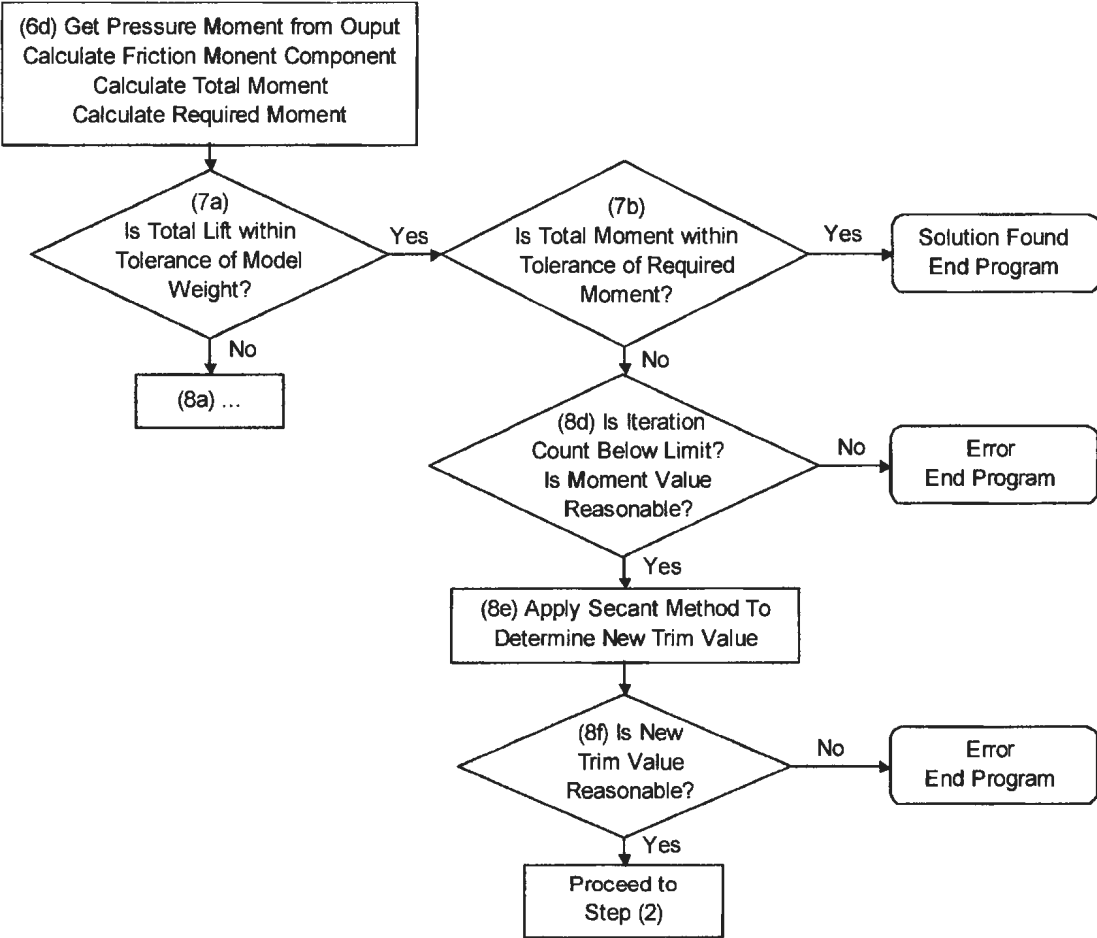


Figure 4.19 – Expanded Flow Chart for 2-Degree of Freedom

theoretical pressure drag from the measured total drag.

This procedure is best illustrated with a graphical representation of the numerical results as shown in Figure 4.20 and Figure 4.21 (for a single model speed). The first figure is a plot of calculated lift as a function of both trim angle and sinkage. The resulting surface was defined by a series of curves of constant trim angle. The 1-degree of freedom equilibrium was achieved for each of these curves when the net lift was equal to the model mass (29.55 kg). These points are identified on the lift versus sinkage curves for each of the five trim angles. Connecting these points produces a 1-degree of freedom solution curve on the net lift surface.

The next step in the process was to plot the net calculated moment against trim angle and sinkage as shown in Figure 4.21. Using the coordinates of sinkage and trim angle for the 1-degree of freedom solution curve determined above, this curve was re-created on the net moment surface. Also shown in this plot is the moment required by the model to balance the moment created by its weight and center of gravity. The solution to the 2-degree of freedom equilibrium problem was the point at which the 1-degree of freedom solution curve intersected the surface of required moment. This point is also identified in the figure at approximately 5.4 degrees trim angle and 9.9 mm sinkage.

Another aspect of the problem illustrated by this graphical example was the essentially linear nature of the numerical results with respect to sinkage and trim angle (over a small range of values). This behaviour was exploited as a time saving measure by reducing the number of iterations required for an equilibrium solution to a minimum of 4. Two sinkage values for each of two trim angles were run for each model speed (extra runs were occasionally included to ensure the validity of the linear approximation). Interpolation of regression lines was then used to determine the required equilibrium values.

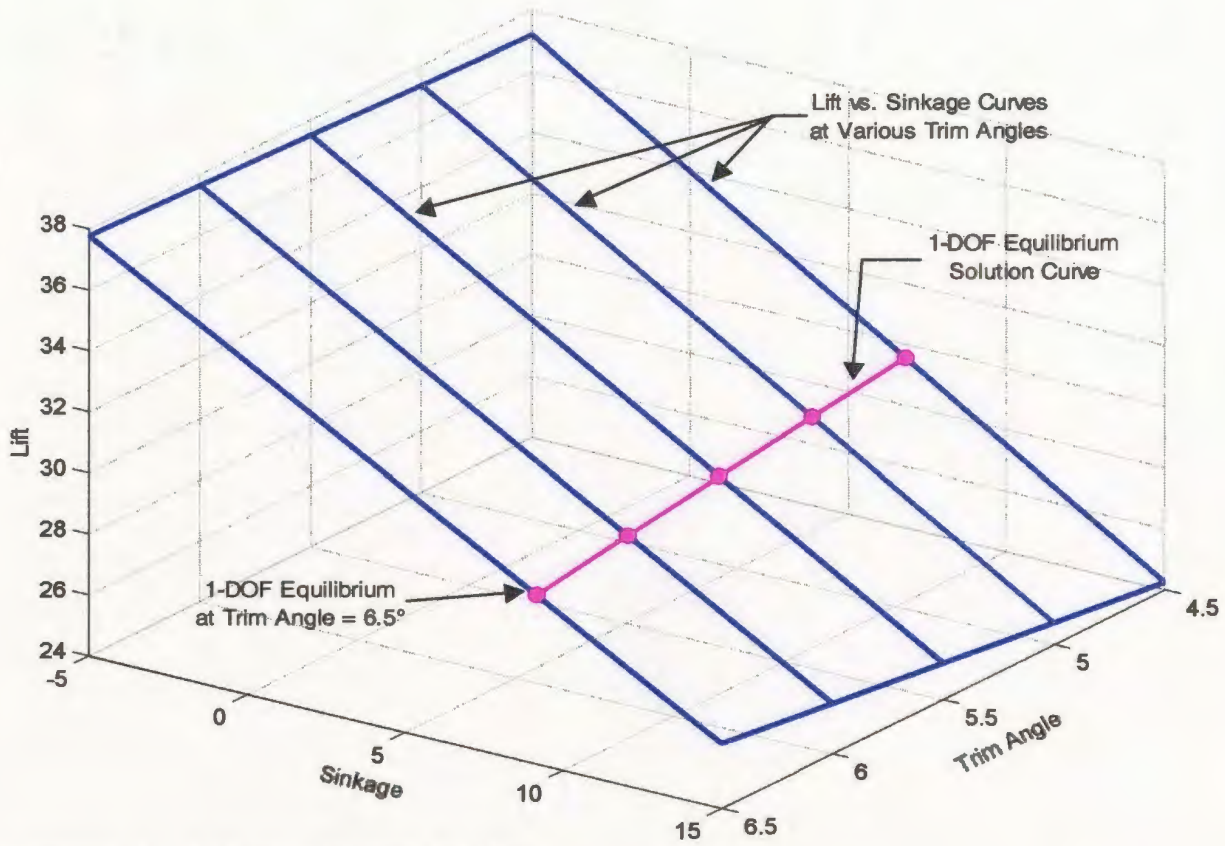


Figure 4.1 – Lift vs. Sinkage & Trim

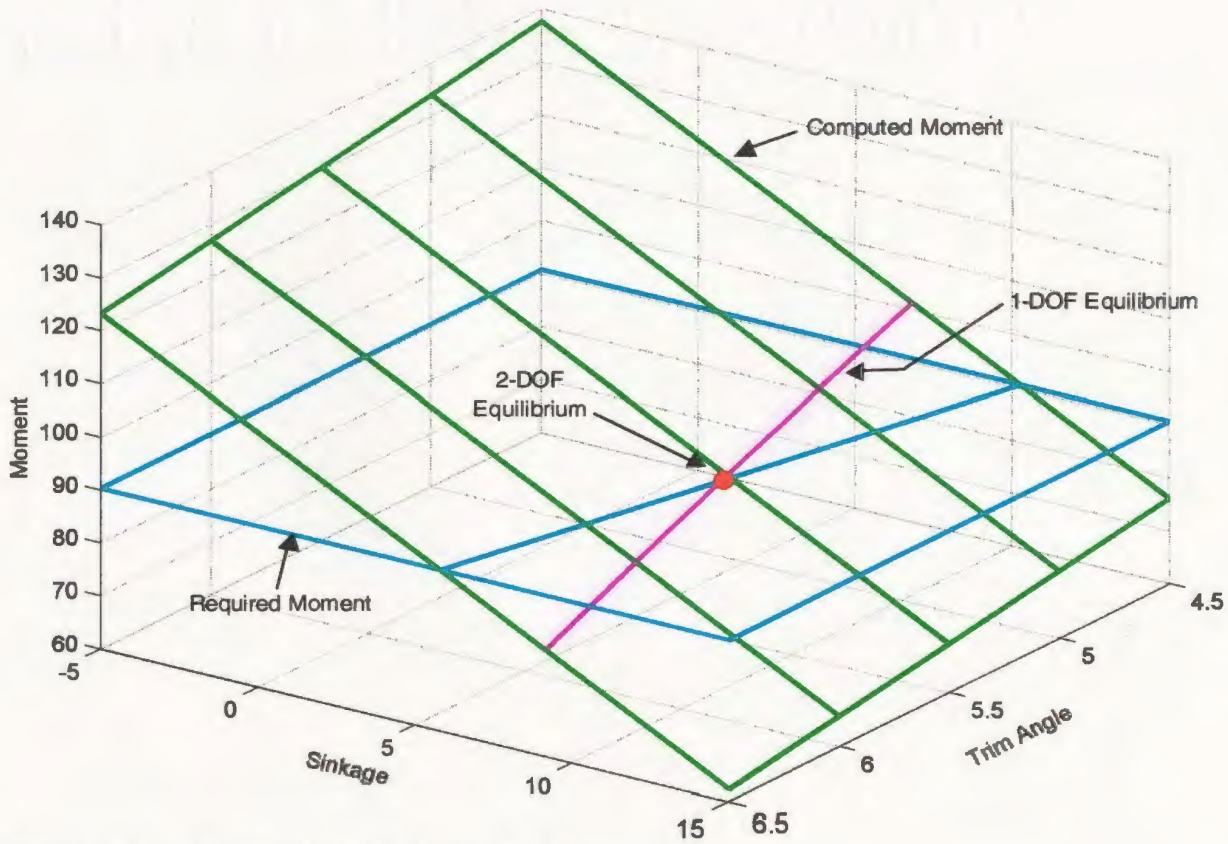


Figure 4.2 – Moment vs. Sinkage & Trim

The results from this set of simulations generally under predicted those of the physical experiments, except for sinkage, which was over predicted. These trends were consistent with excessive pressure forces being computed for the planing conditions. As discussed for the 1-degree of freedom case, the CFD hull was being lifted higher than expected to balance the model's weight at the experimental trim angle. The resulting decrease in wetted area not only produced low values of frictional drag, but also shifted the location of the net pressure force farther aft. Due to a smaller 'moment arm'⁶ the net trimming influence on the model was also substantially reduced.

As the magnitude of net pressure force was effectively fixed by the lift equilibrium requirement, the only alternative left to increase the trimming moment was to shift its location forward. This was achieved by lowering the running trim angle. Other consequences of this move were an increase in wetted area, and hence frictional drag, a decrease in sinkage, and a decrease in pressure drag.

The results for running trim and sinkage are shown in Figure 4.22 and Figure 4.23 respectively. The trends were roughly followed, though there were shifts in the relative locations of the curves on the plots. The trim angles were all uniformly lower and the peak shifted from approximately 3.2 m/s to between 2.0 m/s and 3.0 m/s. Sinkage values were improved slightly from the 1-degree of freedom model, but were still higher than the experimental values.

⁶ Trimming moment was calculated about the model's tow point, located near the transom.

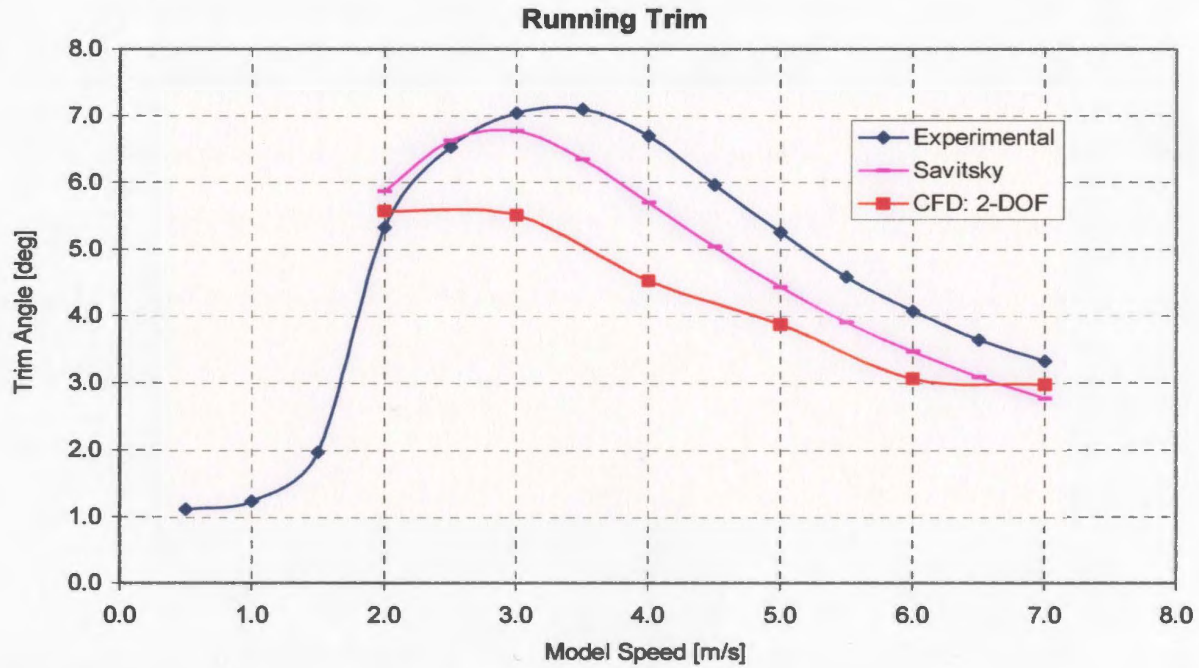


Figure 4.22 – Running Trim: 2-DOF

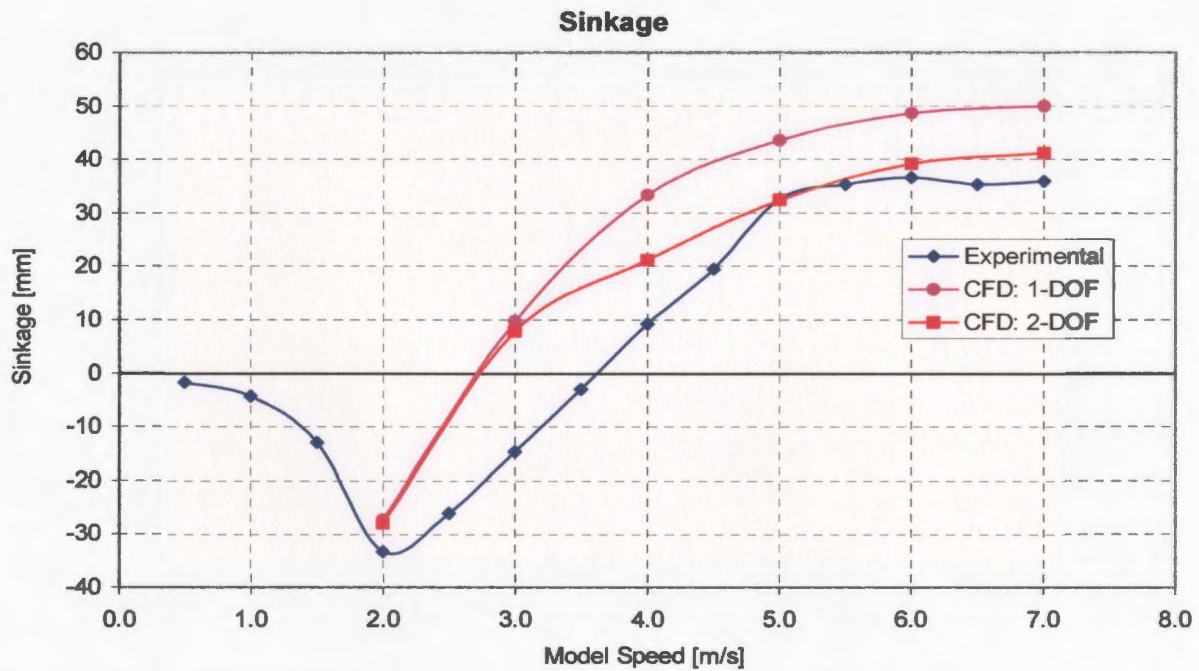


Figure 4.23 – Sinkage: 2-DOF

Figure 4.24 gives an illustration of typical model orientations for the three sets of simulations that were performed. The top hull has a trim and sinkage corresponding to the experimental measurements, or the 0-degree of freedom model. The second hull has the same trim angle but has been lifted higher out of the water and represents the 1-degree of freedom model. The last hull shows the 2-degree of freedom orientation, lower in the water than the second hull and with a smaller trim angle.

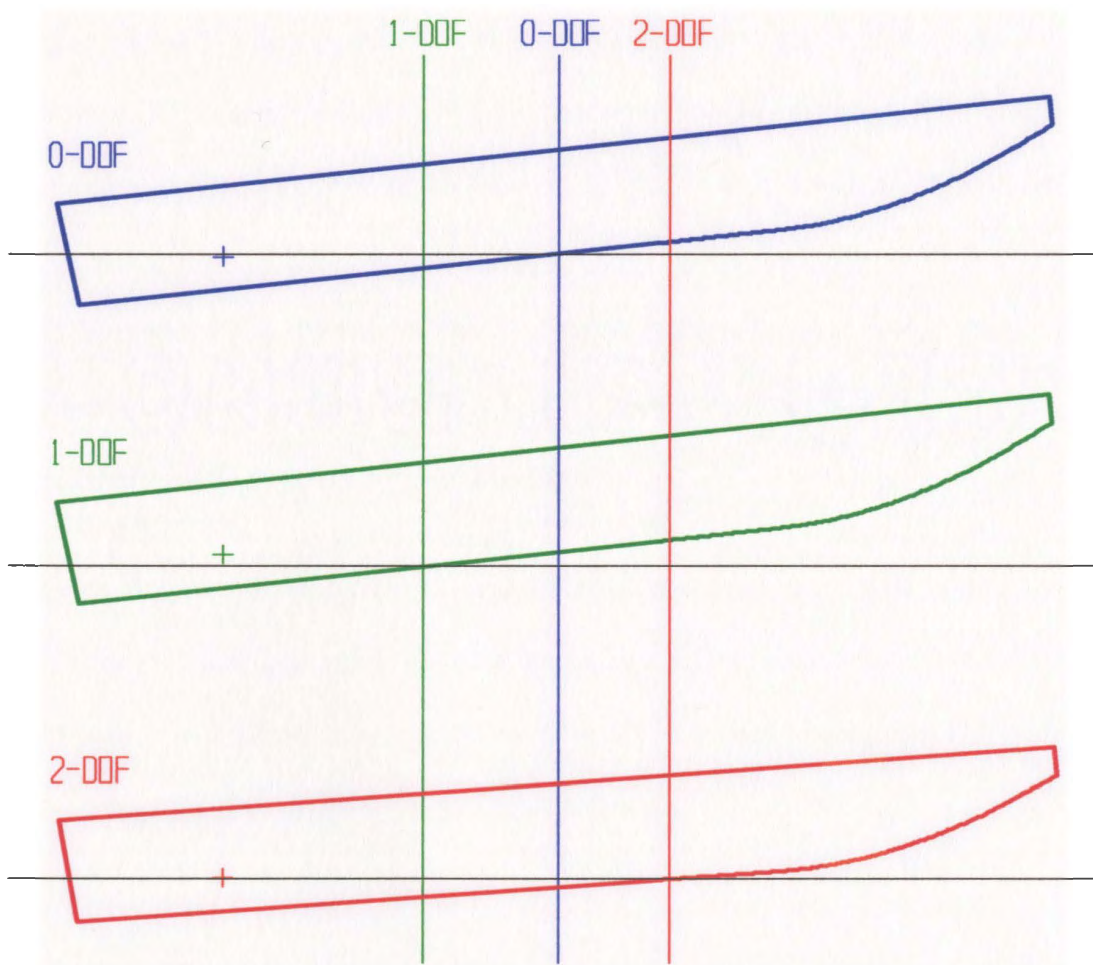


Figure 4.24 – Hull Orientations

At high speeds, the wetted lengths followed the pattern shown in the above figure. The 2-degree of freedom orientations tended to have larger wetted lengths than the experimental values even though they had equivalent trimming moments. This increase in length was attributed to the fact that the net pressure force did not shift proportionately with the wetted length. The pressure distributions smeared and had lower peak values for lower trim angles. The peak pressure coefficients tended to decrease with increasing speed. This was not, however, a result of the increase in speed, but was instead due to changing trim angle. Shown in Figure 4.25 is a plot of peak pressure coefficients against trim angle for various 2-DOF simulations. A clear linear relationship was seen that was not speed dependent (e.g. runs were performed at 4.0 m/s and 5.0 m/s at approximately 5.2 degrees trim, both simulations had essentially the same peak pressure coefficients). Experimental values presented in Hirano (1998) were also in agreement with this result. They tested prismatic hulls at various speeds, all at a trim angle of 6.0 degrees and measured peak pressures coefficients between 0.3 and 0.4.

The increased wetted lengths illustrated in Figure 4.24 also led to larger wetted areas. Whereas the 1-degree of freedom simulations under predicted wetted area, the 2-degree of freedom results showed a slight over prediction as shown in Figure 4.26. A similar result was seen in the frictional drag results shown in Figure 4.27.

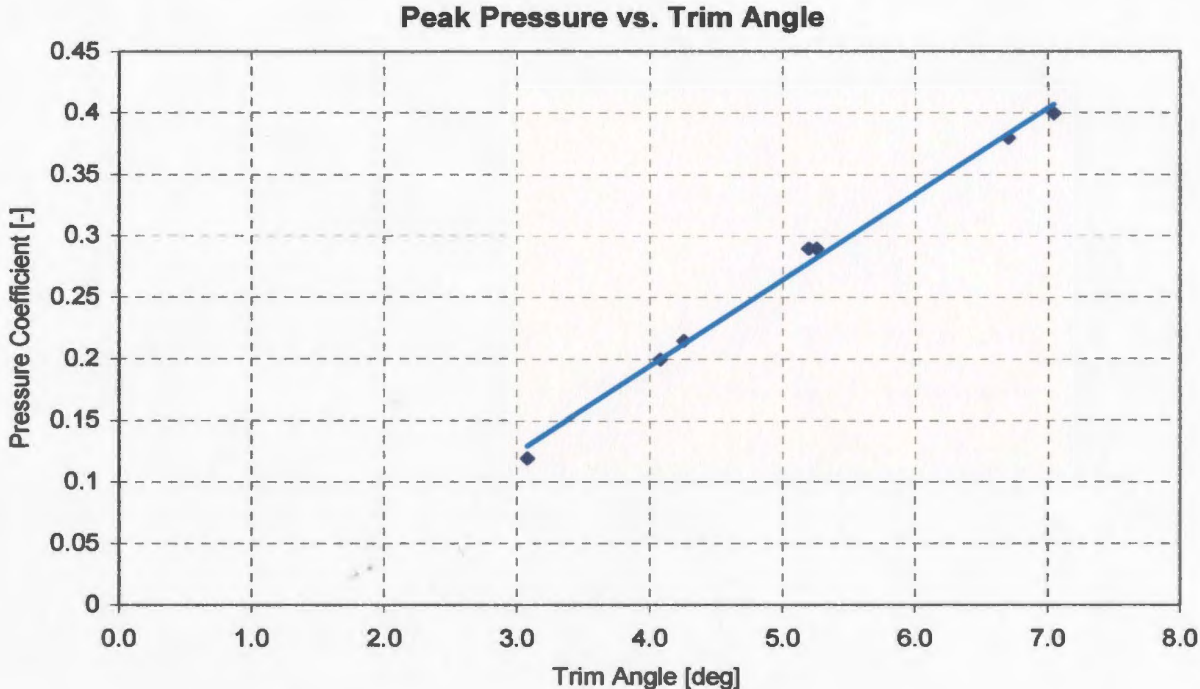


Figure 4.25 – Peak Pressure vs. Trim Angle

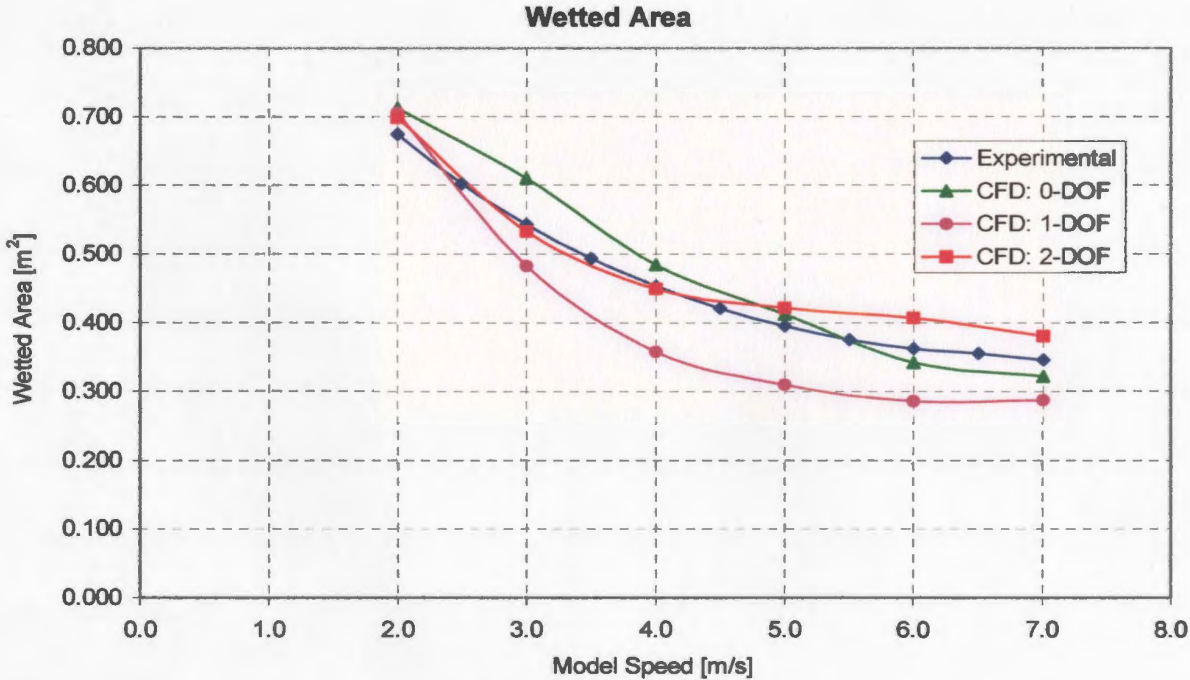


Figure 4.26 – Wetted Area: 2-DOF

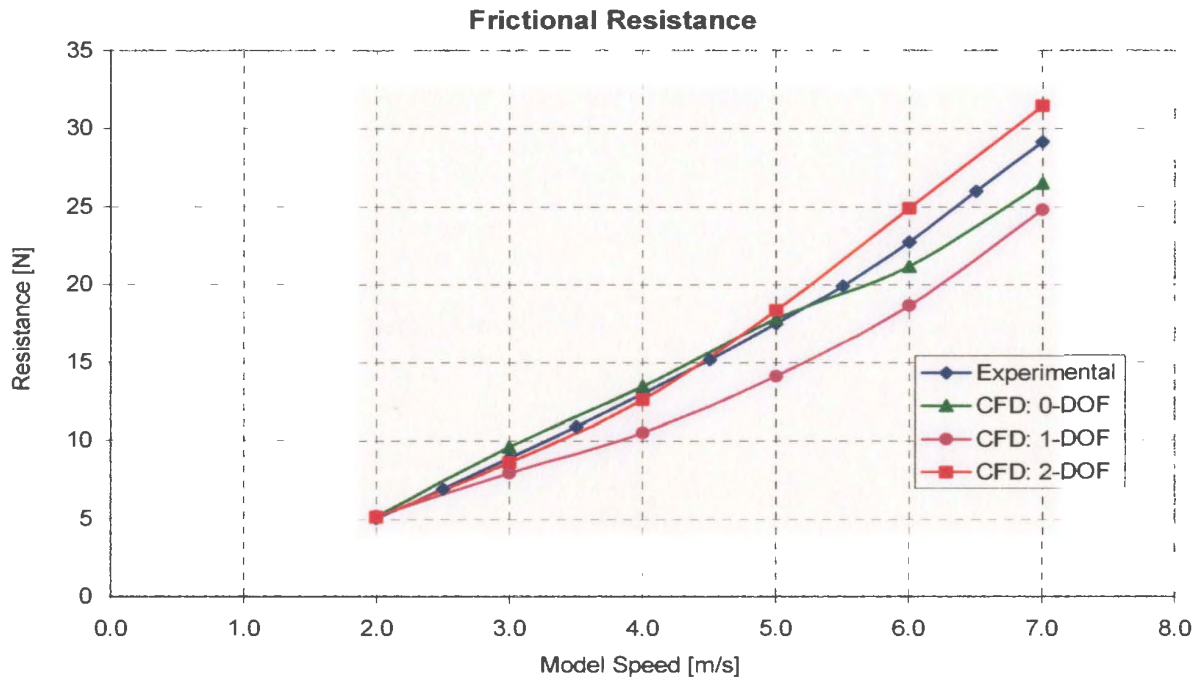


Figure 4.27 – Frictional Resistance: 2-DOF

Pressure resistance values were lower in the 2-degree of freedom simulations, a direct consequence of smaller trim angles. They were, however, still in agreement with theoretical values calculated using equation [4.2], provided the wetted lengths supported the flat plate assumption. This reduction in values, shown in Figure 4.28, demonstrates the importance of trim angle when evaluating planing vessel performance. The results for total resistance are shown in Figure 4.29. In general, the improvement in frictional resistance was not enough to counter the reduced pressure drag. The resulting total resistance curve for the 2-degree of freedom system was therefore shifted downwards from the experimental. The hump and hollow portions of the curve also shifted towards slower speeds.

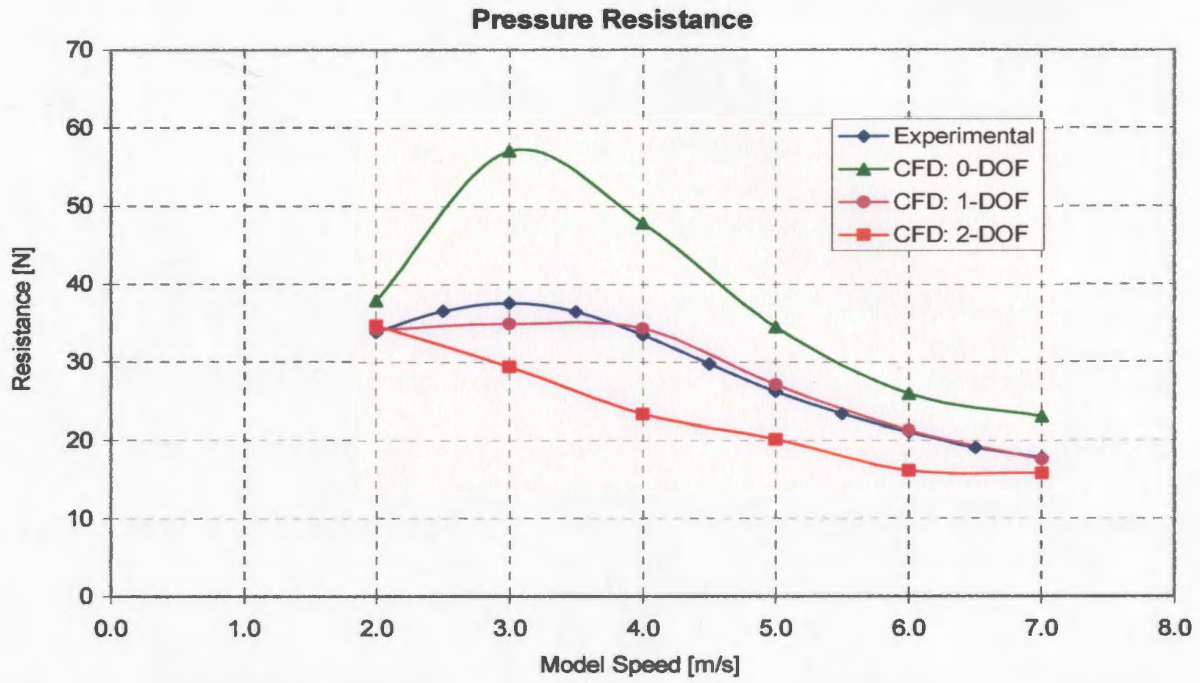


Figure 4.28 – Pressure Resistance: 2-DOF

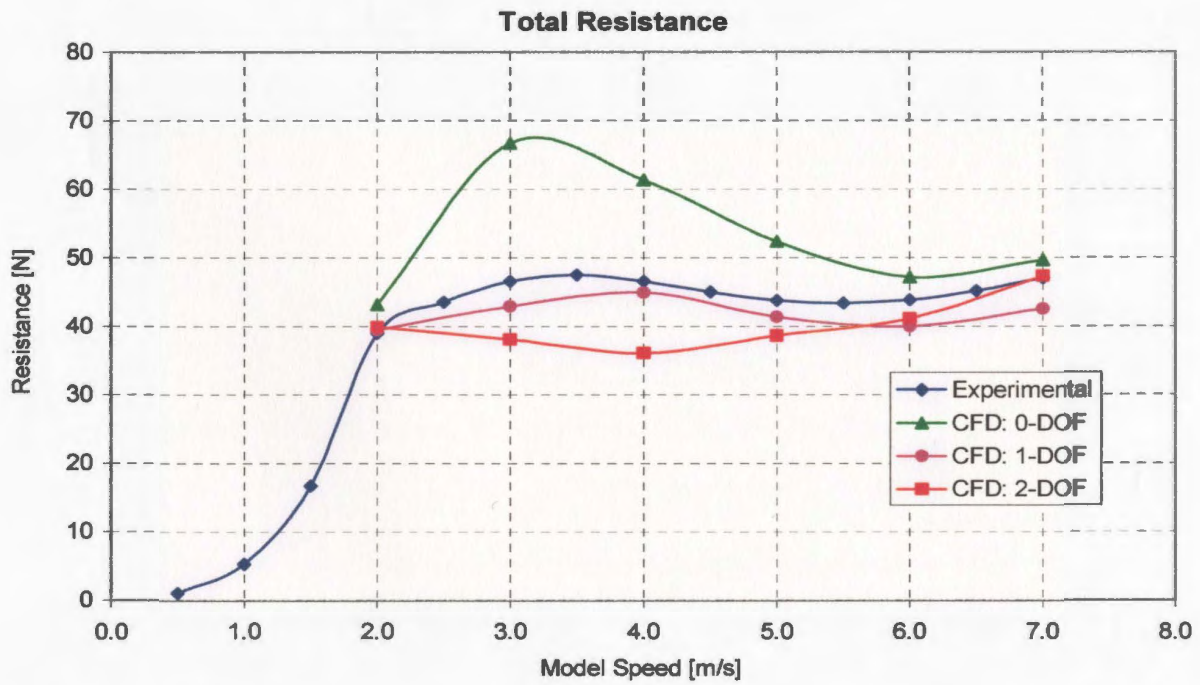


Figure 4.29 – Total Resistance: 2-DOF

It was observed for the highest speed (7.0 m/s) for this set of simulations that the trim angle, and hence pressure resistance, seemed slightly higher than would be suggested by the trend set by the previous speeds. There were difficulties at this speed achieving convergent solutions for hull orientations less than 3.3° trim. The equilibrium position (which was less than 3.3° trim) was instead determined by extrapolation of results from higher trim angles. This difficulty with divergent solutions at low trim angles was not encountered for any of the other speeds; the 7.0 m/s point seemed to be unusually sensitive to trim angle. This fact is shown graphically in Figure 4.30. The moment slope was defined as the change in the trimming moment on the hull given a 0.1° change in trim angle. A quadratic regression line is also shown in the figure that closely matched the trend of the moment slope values when plotted against model speed. The 7.0 m/s point shows a moment slope value 40% higher than predicted by the trend.

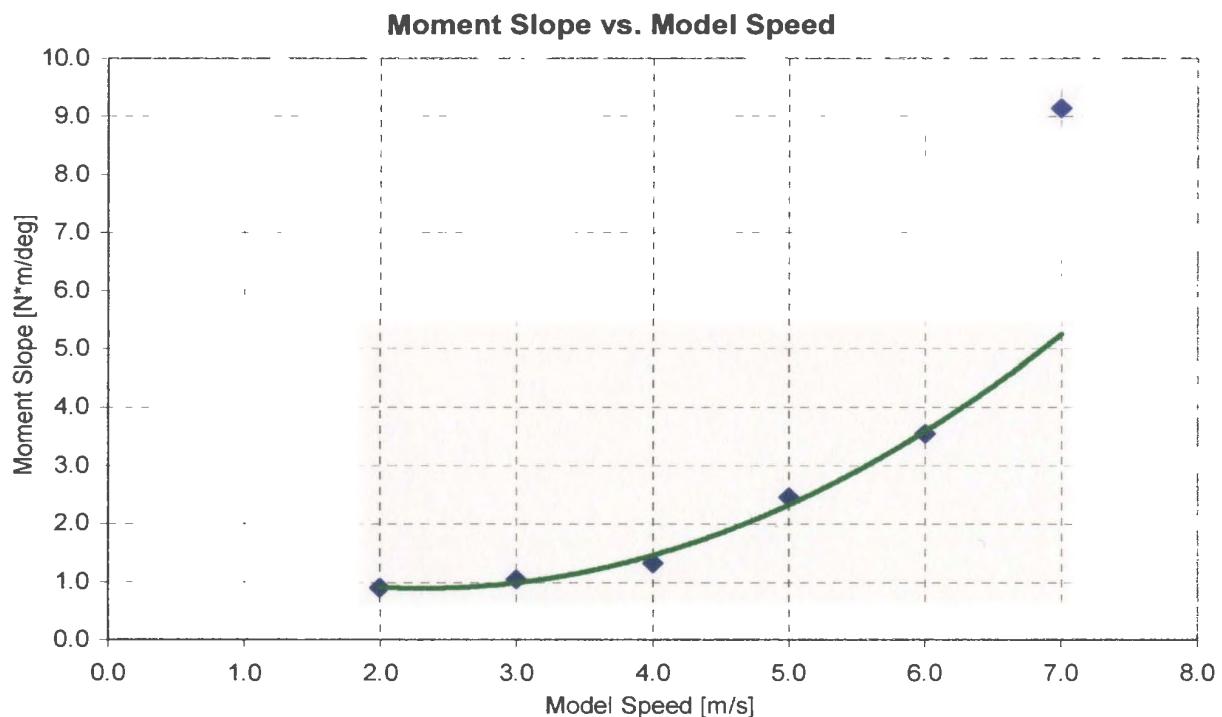


Figure 4.30 – Moment Slope vs. Model Speed

This result has a parallel in the physical experiments. It was found when testing the physical model at speeds of 7.0 m/s and greater, the hull would begin to exhibit the dynamic instability called porpoising (see Thornhill *et al.*, 2000). The threshold when porpoising would begin was identified (as discussed in Chapter 2) when the change in trim angle from the resting to the at-speed condition dropped below approximately 2.1° . This translates to any trim angle below 3.2° for the design ballast condition (the 7.0 m/s case was on the threshold when the dynamically unstable behaviour first became evident).

It was proposed by Celano (1998) that porpoising occurs when the pitching moment becomes increasingly sensitive to trim angle. At some critical value, the trimming moment caused by some small disturbance causes the vessel to change trim in response, which then creates an even larger opposing trimming moment. The unstable system then oscillates at a constant or increasing amplitude. In this case, the numerical model seems to have identified the critical trim angle when trimming moment becomes particularly sensitive to trim angle. This was the same value of trim angle observed in the physical experiments.

4.6 Discussion

Predicting the performance of a planing hull requires the solution of dynamic equilibrium, regardless of the method used. It is through balancing lift and trimming moment with the model's weight and center of gravity that the proper trim angle and sinkage are determined. These parameters are essential for an accurate prediction of resistance. The goal of this research was to extend the ability of a commercial CFD

package to handle this type of calculation, thereby making it a powerful tool for estimating planing hull performance.

The first step was to evaluate the CFD method in a direct comparison with physical experimental data. The results of this test showed that trends and flow patterns were qualitatively in agreement. However, there was a slight over prediction of net pressure leading to high lift and drag values (by as much as 20 N). The numerical model was then tested in 1-degree of freedom (movement in vertical position only) to balance the lift forces with the model's weight. The pressure drag improved to within 5% of the experimental values, although this did lead to a smaller wetted area and hence an under predicted frictional resistance by up to 10%. In simulations involving full dynamic equilibrium, trim angle was found to decrease as much as 2° in order to balance the trimming moment while simultaneously satisfying the lift requirement. This increased the wetted area, but decreased the pressure drag, leading to low total resistance results.

All of the CFD results followed trends characteristic of a planing hull. However, for each set of tests, the curves were shifted or stretched in reaction to the requirements of each case, in response to high net computed values of pressure. For both cases of dynamic equilibrium (1-degree of freedom and 2-degrees of freedom), these high hull pressures led to low total resistance values. This result may be counter-intuitive, but was a consequence of the model's ability to change its orientation in response to the flow field.

The cause of the relatively high pressures in the CFD simulations was not determined. They could be caused by insufficient grid resolution, a common problem in numerical approaches. A grid dependence study was conducted, but the effect of large increases in

the number of elements (on the order of 10 times or more than those used here) was not investigated due to the lack of availability of appropriate computer resources. Another possible contributing factor was the lack of turbulence modeling in these tests. Proper turbulence simulation could alter the character of the pressure profiles and lower the net pressure. The treatment of spray was also a possible contributing factor. Although the VOF free surface capturing method does allow for fluid to be ejected from the near hull above the free surface, it was not necessarily equivalent to the spray produced in the physical experiments. This phenomena may need to be modeled in future simulations. Despite the high pressure values encountered, the results of these predictions were valuable and the procedure for solving dynamic equilibrium was proven to be successful.

CHAPTER 5

CONCLUSIONS

5 CONCLUSIONS

Evaluating the performance of a vessel is a necessary step in any design. The use of numerical methods such as computational fluid dynamics has several advantages over more traditional methods in that they provide detailed results while being cost efficient. The present work has focused on evaluating and expanding a commercial CFD code for predicting the performance of planing hulls. The research involved augmenting an openly available commercial code to solve for the flow around a planing vessel, including the calculations needed to balance forces and moments for dynamic equilibrium, an essential requirement for high speed vessels.

5.1 Physical Experiments

The results from physical tests showed the characteristic traits of a planing vessel. Resistance was found to grow with increasing model speed, peaking at a hump, then

decreasing for a period, bottoming out, then increasing once again. Trim angle was found to increase with model speed, peaking at the same speed as resistance, then decreasing with increasing model speed. The model was found to sink deeper in the water at low speeds (relative to its at-rest position), and then lift higher with increasing model velocity, leveling off at the highest speeds tested.

A wave probe array was found to be an effective technique for measuring and evaluating the wave profiles produced by the model. Transverse waves were found to increase in wavelength and decrease in height with increasing model speed, virtually disappearing altogether at planing speeds. Divergent waves increased in wave height with increasing model speed, peaking at the same “hump” speed identified by the resistance and running trim results, then decreased with increasing model speed. The average angle of the divergent waves made with the model’s path was found to decrease with increasing model speed to a minimum of 12° at the highest speed tested. Wave making resistance was estimated through calculation of wave energies, and was found to follow similar trends as pressure drag on the hull, although the magnitudes were roughly half of the pressure drag values. This suggested that a significant portion of the pressure drag on the hull was produced from spray and/or turbulence generation.

The hull pressure measurements produced clear trends when plotted against model speed. Forward pressures were found to steadily increase with model speed, while aft pressures were found to steadily decrease even to negative gauge pressures at the highest speeds. This result contradicts much of the literature describing planing hull pressure profiles (Savitsky, 1964 & Payne 1988). However, the level of noise in the signals and the limited

number of pressure transducers meant that further experimental work is required to draw unambiguous conclusions.

Mapping of the velocity profile in the hull's boundary layer with a laser Doppler velocimeter was performed successfully. Variations in velocity were measured over as little as a 2.5×10^{-5} m change in measurement position (relative to the hull's surface). Boundary layer thickness was found to increase from the forward to the aft part of the hull as expected. The boundary layer also decreased in thickness with increasing model speed. The free stream velocity measured by the LDV (the velocity just outside of the boundary layer) was found to increase from a value near the model speed at a forward position (620 mm from transom) to a value exceeding the model speed at an aft location (185 mm from transom) for all model speeds tested. The percentage increase in velocity was found to be linearly related to running trim angle; lower trim angles led to smaller increases in velocity.

When the free stream velocities determined by the LDV were used to calculate the pressure change from the forward to the aft locations using Bernoulli's equation (including the effect of hydrostatic head which is not used in simple 2D planing theory), the resulting curve did not match the changes measured with the pressure transducers on the hull. The direct measurements had larger negative magnitudes and a steeper slope compared with the calculated values (differences between results ranged from 400 to 1400 Pa). This suggested that significant levels of vorticity may have been present in the flow that increased with increasing model speed. CFD using the full RANS equations may therefore be better suited to this problem than potential flow analysis.

The experimental model tests conducted for this research generated a comprehensive set of performance data for this vessel over a range of speeds and ballast conditions. This information was necessary for the current project, but could be used for future CFD validation work as well. The innovative techniques for vessel wake evaluation and boundary layer velocity profile measurement documented here may also be useful for gathering hydrodynamic data on a wide variety of marine vehicles.

5.2 Numerical Simulations

The CFD simulations of the planing hull for this research were performed using Fluent (v5.3) and Gambit (v1.2). The decision to use this commercial software was made after an extensive review of the state of the art in CFD techniques. Options such as developing code, and using/augmenting research or public domain codes were investigated, but the benefits of a commercial code that had the required characteristics, of an unstructured solver with free surface capturing, clearly made it the best choice.

After a period of trials with the software, several conclusions were established for the planing hull problem. Although the simulations were of a steady flow, a transient (time-dependent) solution scheme had to be used. The time step size needed to be very small, on the order of a thousandth of a second, to ensure a convergent solution. Subsequently, the number of time steps had to be large (a minimum of 2500 were used) for the flow induced forces and moments on the hull to stabilize.

A consequence of the large number of small time steps was increased computation times for the planing hull simulations. It was therefore necessary to limit the size of the mesh in

order to make the computation times reasonable. This was done by sacrificing resolution in the boundary layer region of the hull; as a result, the computed frictional forces were greatly under-predicted. These forces were instead calculated using the ATTC friction line, as was done with the physical experimental results. This approach allowed mesh sizes to be in the range of 120,000-150,000 elements. A single planing hull flow simulation with this mesh size took approximately 2-4 days of computation time on a 500au DIGITAL Personal Workstation.

The standard turbulence models, such as the $k-\epsilon$ and Spalart-Allmaras models, could not be directly used in the planing hull simulations. They created excessive turbulence generation at the air/water interface at the leading edge of the flow on the hull that quickly led to divergence of the solution. This was attributed to the fact that the turbulence models supplied by Fluent were not designed for this type of flow. It may be possible to create or modify a turbulence model for this problem; however, this is a significant undertaking that was beyond the scope of the project. It was therefore decided to focus on developing solutions without turbulence modeling.

Another problem encountered with the simulations was related to the fully unstructured mesh used to discretize the domain. The mesh had to be assigned initial values to begin the iterative solution process. Elements crossing the waterplane were not being assigned the correct water volume fraction by Fluent, leading to divergent solutions. A function was written by the author that manually visited each cell in the domain, determined, and then assigned the correct initial values; convergent solutions were then achieved.

The results from these trial simulations showed that the numerical model was qualitatively consistent with experimental observations. A stern wave formed that created a dry transom at planing speeds, and surface waves were comparable to the experimental profiles (in the limited range of the domain). The wetted surface contact area on the hull was in good agreement with underwater video of the physical model. Pressure profiles exhibited the expected trends, peaking at the leading edge of the wetted area, and decreasing towards the transom. Streamlines near the hull bent towards the chine in proportion with their distance from the centerline, in agreement with experimental observations presented in Savitsky (1964). The positive results in this phase of the research then prompted the next phase, where sets of simulations were performed to provide a more comprehensive comparison with the experimental results.

5.3 Equilibrium Simulations

The equilibrium simulations were performed in three stages. The first was used to compare the numerical simulations directly with the physical experimental results by matching the hull orientations for each model speed. The next stage allowed the model to move vertically in the CFD simulation at a fixed trim angle until the net lift balanced the model weight. The third and final stage permitted movement in both vertical position and trim angle until the model achieved equilibrium in both lift and trimming moment at speed.

The first step was to evaluate the CFD method in direct comparison with physical experimental data. The total resistance results were over predicted, but followed the trends of the physical experiments. On further examination, it was found that wetted area

and frictional resistance based on the ATTC friction line were in good agreement.

Pressure resistance on the hull, however, was high, leading to over predicted lift and drag values. The level of over prediction was found to be related to model speed; the largest difference between the numerical and experimental results (approximately 20 N) was at the hump speed of 3.0 m/s. Results tended to improve at higher model speeds (to a difference within 4 N).

Although the experimental trends were followed by the numerical pressure results, a detailed comparison showed that the computed hull pressures were under predicted at the forward part of the hull and over predicted in the aft region. Free stream velocities near the hull also followed the experimentally determined trends, but with lower values (differences were approximately 0.1 – 0.2 m/s). The lower computed velocities were consistent with the high pressures leading to the over prediction of resistance.

The next stage of tests involved solving for the equilibrium position in 1-degree of freedom. The model was moved vertically with fixed trim until the net lift balanced the model's weight. This involved the use of an external program, written by the author, which controlled the execution of the solver and mesher, and evaluated the simulation results. It relied on an iterative scheme where successive model orientations were evaluated in search of the equilibrium solution. This equilibrium program, a key component of the research, was implemented successfully.

It was found from this set of simulations that the high pressure forces, identified in the 0-degree of freedom simulations, lifted the hull higher in the water at speed (in the range of 10-20 mm), although the experimental trend was still followed. This led to smaller

predicted wetted areas and as a result, frictional resistance was under predicted by as much as 10%. Pressure drag values, however, showed improvement over the previous simulation set, particularly at higher speeds where values were within 1-2 N of the experimental results.

The last set of simulations involved solving for dynamic equilibrium in 2-degrees of freedom. Vertical position and trim angle were both altered until both the computed lift and trimming moment balanced the model's weight and center of gravity. An extended version of the equilibrium program for the 1-degree of freedom simulations was successfully developed for this case.

It was found for this set of simulations that trim angles were under predicted (by as much as 2°) in order to balance the trimming moment while simultaneously satisfying the lift requirement. This improved the wetted area over the previous simulation set, but decreased the pressure drag, leading to low total resistance results. Sinkage values were also found to improve compared with the 1-degree of freedom results, but were still high compared with the physical experiments.

In general, all of the CFD results followed trends characteristic of a planing hull determined by the physical experiments. However, for each set of tests, the curves were shifted in reaction to the equilibrium requirements of each case in response to high net computed pressures. For both cases of dynamic equilibrium (1-degree of freedom and 2-degrees of freedom), these high hull pressures led to low total resistance values. This result may be counter-intuitive, but was a consequence of the model's ability to change

its orientation in response to the flow field. It also demonstrates the importance of dynamic equilibrium and vessel orientation when evaluating performance.

In conclusion, this approach of predicting planing hull performance shows great potential. It is unrestricted in hull form, and relies on a readily available commercial code that receives frequent upgrades and improvements. CFD techniques have the advantage of providing detailed descriptions of the flow field, pressure, velocities, and free surface distortions that other methods, including physical experiments, cannot. The equilibrium solving method was shown to be effective and could be applied to wide variety of problems where the flow and geometry are inter-related. Experimental trends for resistance, trim, and sinkage were followed, and the behavior of the numerical model was consistent with experimental observations. When evaluating a novel design or if a high degree of detail is desired, CFD methods with dynamic equilibrium become a practical and logical alternative to other methods, particularly as the power of modern computers continues to increase while decreasing in cost.

5.4 Recommendations for Future Work

Despite good qualitative agreement between the numerical and experimental results, values of parameters such as resistance were found to be affected by an over prediction of hull pressure forces. The cause of this was not determined, although several possibilities were considered.

The first could be insufficient grid resolution, a common problem in numerical approaches. A grid dependence study was conducted, but the effects of large element

count increases (on the order of 10 times or more than those used here) could not be investigated due to insufficient computing resources. Further work may focus on expanding the grid dependence study to include meshes with much higher resolution.

Another possible contributing factor was the lack of turbulence modeling in these tests. Proper turbulence simulation could alter the character of the pressure profiles and lower the net pressure. As mentioned, the standard turbulence models such as the Spalart-Allamaras and $k-\epsilon$ models produced excessive turbulence production in the spray root region near the hull that led to divergence. Future work involving the creation of new turbulence models or modifying current ones to handle this type of flow could lead to improved predictions.

The treatment of spray was also a possible contributing factor to the high pressure forces on the hull. Although the VOF free surface capturing method did allow fluid to be ejected above the free surface from the near hull region, it was not necessarily equivalent to the spray produced in the physical experiments. Predictions could improve if this phenomenon were successfully modeled in future simulations.

The physical model experiments created a few questions in terms of velocity and pressure relationships on the hull when planing. Additional physical experiments involving a greater number of more sensitive hull pressure taps, in conjunction with LDV measurements of velocity at more locations on the hull, could help clarify the flow dynamics. This would also be useful in further identifying the differences between the numerical and physical flows, thereby aiding in the advancement of this CFD analysis of planing hulls.

References

- AIAA, 1998, "Guide for the Verification and Validation of Computational Fluid Dynamics Simulations", G-077-1998.
- Alessandrini B., Delhommeau G., "A Multigrid Velocity-Pressure-Free Surface Elevation Fully Coupled Solver for Calculation of Turbulent Incompressible Flow Around a Hull", 21st Symp. Naval Hydrodynamics June 24-28 1996, Trondheim, Norway, vol. 2, pp. 40-55, 1996.
- Ashford G.A., "An Unstructured Grid Generation and Adaptive Solution Technique for High-Reynolds-Number Compressible Flows", Ph.D. Thesis, Aerospace Engineering and Scientific Computing, University of Michigan, 1996.
- Baker A.J., "Finite Element Method". Chapter 28 of The Handbook of Fluid Dynamics. (ed. R.W. Johnson), CRC Press, New York, 1998.
- Baker A.J., Finite Element Computational Fluid Dynamics. Taylor and Francis, Washington DC, 1983.
- Baldwin B.S., Lomax H., "Thin Layer Approximation and Algebraic Model for Separated Turbulent Flows", AIAA Paper 78-257, AIAA 16th Aerospace Sciences Meeting, Reno, Nevada, January 1978.
- Brizzolara S., Bruzzone D., Cassella P., Scamardella A., Zotti I., "Wave Resistance and Wave Patterns for High-Speed Crafts; Validation of Numerical Results by Model Test", 22nd Symp. on Naval Hydrodynamics, Washington D.C., August 9-14, 1998.
- Caponnetto M., Castelli A. et al. "America's Cup Yacht Design Using Advanced Numerical Flow Simulations". EPFL Supercomputing Review, pp24 – 28, November 1998.
- Celano T., "The Prediction of Porpoising Inception for Modern Planing Craft", SNAME Preprints: Annual Meeting Technical Sessions 1998, pp. 10-1 – 10-22, San Diego, USA, November 1998.
- Chappell J.A., Bull P.W., "Multi-zonal Multi-block Grids for Hydrodynamic Simulations", Proc. Numerical Grid Generation in Computational Field Simulations, Greenwich England, pp.141-150, 1998.
- Cowles G., Martinelli L., "A Viscous Multiblock Flow Solver for Free-Surface Calculations on Complex Geometries", 22nd Symp. Naval Hydrodynamics Aug. 9-14 1998, Washington D.C., pp. 100-115, v. 4, 1998.

- Currie I.G., Fundamental Mechanics of Fluids. McGraw-Hill Inc., 1974.
- Dean R.G., Dalrymple R.A., Water Wave Mechanics for Engineers and Scientists. World Scientific. Singapore, 1984.
- Deng G., Visonneau M., “Evaluation of Eddy Viscosity and Second-Moment Turbulence Closures for Steady Flows Around Ship Hulls”, 21st Symp. Naval Hydrodynamics June 24-28 1996, Trondheim, Norway, vol. 2, pp. 162-176, 1996.
- Du Cane P., High Speed Small Craft 3rd Ed. Temple Press Books, London. 1964.
Payne P.R., Design of High Speed Boats Volume 1: Planing. Fishergate Inc. Annapolis. 1988.
- Du Cane, Peter, 1974, High speed small craft, David and Charles, 4th Ed.
- Feistauer M., Mathematical Methods in Fluid Dynamics. John Wiley & Sons, New York, 1993.
- Fluent User’s Manual. Release 5.3.18. Copyright Fluent Incorporated, 1998.
- Gentaz L., Guillerm B., Alessandrini B., Delhommeau G., “Three-Dimensional Free Surface Viscous Flow Around a Ship in Forced Motion”, 7th Int. Conf. Numerical Ship Hydrodynamics. Nantes, France, pp. 4.2-1 to 4.2-12, July 19-20, 1999.
- Hino T., “Navier-Stokes Computations of Ship Flows on Unstructured Grids”, 22nd Symp. Naval Hydrodynamics Aug. 9-14 1998, Washington D.C., pp. 116-142, v. 4, 1998.
- Hirano S., Uchido S., Himeno Y., “Pressure Measurement on the Bottom of Prismatic Hulls”, Kansai Soc. Nav. Arch. J., No.213, March 1990.
- Hirsch C., Numerical Computation of Internal and External Flows: Volume 1, Fundamentals of Numerical Discretization. John Wiley & Sons, New York, 1988.
- Hirt C.W., “Free Surface Modeling Methods”, <http://www.flow3d.com/freesmod.shtml>, Flow Science Inc., Copyright 1999.
- Hochbaum A.C., Schumann C., “Free Surface Viscous Flow Around Ship Models”, 7th Int. Conf. Numerical Ship Hydrodynamics. Nantes, France, pp. 2.3-1 to 2.3-12, July 19-20, 1999.
- Ikeda Y., Yokomizo K. et al., “Simulation of Running Attitude and Resistance of a High Speed Craft Using a Database of Hydrodynamic Forces Obtained by Fully Captive Model Experiments”, FAST '93, 2nd International Conference on Fast Sea Transportation. 1993.
- Lewis E.V (ed.), “Principles of Naval Architecture Second Revision”. Society of Naval Architects and Marine Engineers (SNAME), Jersey City, 1988.

- Lighthill J., Waves in Fluids. Cambridge University Press. New York, 1978.
- Löhner R., Yang C., Oñate E., “Viscous Free Surface Hydrodynamics Using Unstructured Grids”, 22nd Symp. on Naval Hydrodynamics. Washington DC, pp. 128-142, August 9-14, 1998.
- Mish K.D., “Computer Science”. Chapter 30 of The Handbook of Fluid Dynamics. (ed. R.W. Johnson), CRC Press, New York, 1998a.
- Mish K.D., “Finite Difference Method”. Chapter 26 of The Handbook of Fluid Dynamics. (ed. R.W. Johnson), CRC Press, New York, 1998b.
- Miyata H., “Time-Marching CFD Simulation for Moving Boundary Problems”, 21st Symp. Naval Hydrodynamics June 24-28 1996, Trondheim, Norway, vol. 2, pp. 1-21, 1996.
- Morton K.W., Numerical Solution of Convection-Diffusion Problems (Applied Mathematics and Mathematical Computation 12). Chapman & Hall, London, 1996.
- Owen S. “Mesh Generation: A Quick Introduction”, 1999, (notes from the web page) <http://www.andrew.cmu.edu/user/sowen/mesh.html>
- Patankar S.V., Karki K.C., Kelkar K.M., “Finite Volume Method”. Chapter 26 of The Handbook of Fluid Dynamics. (ed. R.W. Johnson), CRC Press, New York, 1998.
- Patankar S.V., Numerical Heat Transfer and Fluid Flow. Hemisphere, New York, 1980.
- Payne P.R., “Design of High-Speed Boats Volume 1: Planing”, Fishergate Inc., Annapolis, 1988.
- Peyret R., Taylor T., Computational Methods for Fluid Flow. Springer-Verlag, New York, 1983.
- Peyret, R. (ed.), Handbook of Computational Fluid Mechanics. Academic Press, New York, 1996.
- Preparata F.P., Shamos M.I., Computational Geometry: An Introduction. SpringerVerlag, New York, 1985.
- Reynolds O., “On the dynamical theory of Incompressible Viscous Fluids and the Determination of the Criterion”, Philos. Trans. R. Soc. London, Ser. A, 186, pp.123-64, 1895.
- Sato Y, Miyata H., Sato T., “CFD Simulation of 3-Dimensional Motion of a Ship in Waves: Application to an Advancing Ship in Regular Heading Waves”. J. Marine Science and Technology, vol. 4, no. 3, pp.108-116, 1999.

- Savitsky D., "Hydrodynamic Design of Planing Hulls", Marine Technology, vol. 1, no. 1, pp. 71 – 95, October 1964.
- Shima N., Prediction of Turbulent Boundary Layers with a Second Moment Closure. J. of Fluids Engineering, vol. 115, pp.1-27, 1993.
- Speziale C.G., "Analytical Methods for the Development of Reynolds-Stress Closures in Turbulence", Ann. Rev. Fluid Mech., vol. 23, pp.107-157, 1991.
- Speziale C.G., "Analytical Methods for the Development of Reynolds-Stress Closures in Turbulence", Ann. Rev. Fluid Mech., vol. 23, pp.107-157, 1991.
- Stern F. (Chair), Raven H.C., Bulgarelli U., Gustafsson L.T., Maksoud M.A., Perez-Rojas L., Suzuki T., Zhou L., "The Resistance Committee Final Report and Recommendations to the 22nd ITTC", Seoul, Korea, September 5-8, 1999.
- Stroustrup B., The C++ Programming Language 3rd Edition. Addison-Wesley, Berkeley, California, 1997.
- Subramani A.K., Paterson E.G., Stern F., "CFD Calculation of Sinkage and Trim", J. Ship Research, vol. 44, no. 1, pp.59-82, March 2000.
- Takai M., Zhu M., "Finite-Volume Simulation of Viscous Flow about Ship with Free-Surface by Arbitrary-Lagrange-Euler Method", ICHD-96, CFD Workshop Tokyo 1994: An International workshop for Improvement of Hull Form Designs, Tokyo Japan, vol. 1, pp.85-94, March 22-24 1994.
- Thornhill E., "Development of Waterjet Testing Techniques", Thesis submitted to the Memorial University of Newfoundland, Faculty of Engineering and Applied Science, St. John's Newfoundland, Canada, 1999.
- Thornhill E., Veitch B., Bose N., "Dynamic Instability of a High Speed Planing Boat Model". Marine Technology, July 2000.
- Versteeg H.K., Mallalasekera W., An Introduction to Computational Fluid Dynamics – The Finite Volume Method. Longman Group Ltd., Harlow. 1995.
- Weighardt K., Krux J., Nomineller Nachstrom auf Grund von Windkanal Versuchen. Jahrb. Der Schiffbau Technischen Gesellschaft (STG), 1980.
- Wilcox D.C., Turbulence Modeling for CFD. DWC Industries Inc., California, 1993.
- Yang C., Löhner R., Noblesse F., Huang T.T., "Calculation of Ship Sinkage and Trim Using Unstructured Grids". ECCOMAS 2000, 11-14 September 2000, Barcelona.

Yourdon E., Decline and Fall of the American Programmer. Yourdon Press, New York, 1993.

APPENDIX A

Results from Physical Model Tests

Phase I

A.1 Results from Physical Model Tests: Phase I

The physical tests of the planing hull model were performed in two phases. The first phase tested a range of ballast conditions and focused on measurements of tow force, running trim, sinkage, hull pressures and wave profiles. A discussion of these results is given in Chapter 2. This appendix contains a summary of the data set collected during the first phase of testing (except for wave profile data).

Table A.1 lists the ballast all the ballast conditions tested along their respective LCGs, VCGs, resting trim angles, drafts (at heave post location or tow point), and pitch inertias. The VCGs and pitch inertias were measured with the model in a swing frame and do not include the effects of the yaw restraint or heave post.

The test results are given in Tables A.3 – A.7. Descriptions of the various columns in these tables are given in Table A.2. Note that pressure values are given relative to the resting position of the model for each ballast condition.

Mass [kg]	LCG [m]	VCG [mm]	Resting Trim [deg]	Draft at Tow Point [mm]	Pitch Inertia [kg·m ²]
29.6	0.49	0.023	2.0°	73.5	14.10
29.6	0.53	0.026	1.1°	71.7	15.71
29.6	0.57	0.041	0.4°	61.8	14.79
25.2	0.53	0.021	1.0°	60.0	15.47
33.9	0.53	0.036	1.3°	75.5	17.10
29.6*	0.53	0.050	1.1°	71.7	16.15
29.6**	0.53	0.039	1.1°	71.7	15.17

* LDV in Aft Position

** LDV in Forward Position

Table A.1 – Static trim angles and drafts (at tow point) for ballast conditions

#	Column	Description
1	Model Speed [m/s]	Tared result. Model speed was determined from the measured carriage speed. Value given is equal to the difference between the measured carriage speed at the set speed with that measured at rest.
2-9	PT1 – PT9 (gauge) [Pa]	Tared results. The remaining columns give the results from the pressure transducers mounted in the hull. PT locations are given in Figure 2.6. Results from PT5 were not listed because it malfunctioned during tests. Values given are equal to the difference in the gauge pressures measured at speed with those measured at rest.
10	Tow Force [N]	Tared result. Value given is equal to the difference between the measured tow force at speed with that measured at rest.
11	Trim Reference [deg]	Value is that measured at rest before each run. Zero trim is defined when the bottom of the hull is parallel to the water surface. Positive values indicate trimming by the bow.
12	Trim Untared [deg]	Value is that measured at speed. Reference of zero trim is if the bottom of the hull were parallel to the water surface. Positive values indicate trimming by the bow.
13	Sinkage Tared [mm]	Tared result. Value given is equal to the difference between the measured heave post position at speed with that measured at rest. Positive values mean the heave post moved vertically upward.

Table A.2 – Column Descriptions for Result Tables

Model Speed [m/s]	PT1 (gauge) [Pa]	PT2 (gauge) [Pa]	PT3 (gauge) [Pa]	PT4 (gauge) [Pa]	PT6 (gauge) [Pa]	PT7 (gauge) [Pa]	PT8 (gauge) [Pa]	PT9 (gauge) [Pa]	Tow Force [N]	Trim Refer. [deg]	Trim Untared [deg]	Sinkage Tared [mm]
4.00	580.1	403.7	239.4	440.2	-208.7	144.1	385.2	-195.5	37.88	0.98	5.92	8.8
4.00	571.1	363.1	433.7	406.2	-236.1	202.4	383.8	-334.6	37.97	1.02	5.92	9.1
4.50	810.2	541.8	297.8	535.7	-320.7	150.1	395.6	-354.0	37.38	1.00	5.31	17.2
4.50	833.5	518.3	555.0	516.4	-332.7	230.1	418.5	-419.8	37.39	0.96	5.29	19.4
5.00	1110.4	660.7	643.2	641.1	-455.5	263.7	459.4	-424.9	36.97	1.01	4.66	25.6
5.00	1072.7	664.1	622.2	610.2	-465.2	267.4	425.9	-446.6	36.99	1.04	4.66	22.4
5.50	1367.5	886.2	732.2	781.1	-566.2	318.8	503.3	-494.0	37.25	0.99	4.10	31.9
5.50	1337.2	891.9	729.5	753.1	-571.3	332.7	497.6	-489.4	37.35	0.99	4.10	24.5
6.01	1628.5	1194.1	543.1	1033.8	-663.6	330.0	526.6	-653.1	38.36	0.98	3.63	31.2
6.01	1621.7	1186.5	834.0	1007.2	-686.8	430.6	532.9	-518.7	38.48	0.95	3.63	29.7
6.51	1757.1	1224.7	351.1	936.2	-1032.0	392.5	-16.4	-730.1	40.06	1.00	3.27	32.1
6.51	1964.0	1574.8	933.6	1340.9	-799.8	525.3	631.2	-550.6	40.10	0.96	3.25	28.5

Table A.3 – Phase I Experimental Results: Model Weight 25.2 kg, Model LCG = 0.528 m

Model Speed [m/s]	PT1 (gauge) [Pa]	PT2 (gauge) [Pa]	PT3 (gauge) [Pa]	PT4 (gauge) [Pa]	PT6 (gauge) [Pa]	PT7 (gauge) [Pa]	PT8 (gauge) [Pa]	PT9 (gauge) [Pa]	Tow Force [N]	Trim Refer. [deg]	Trim Untared [deg]	Sinkage Tared [mm]
4.00	969.4	578.6	642.3	609.4	-230.1	200.5	416.2	-356.1	49.23	1.95	7.46	23.1
4.00	933.9	569.2	641.2	579.1	-224.7	201.6	400.4	-390.5	49.36	1.99	7.48	17.4
4.50	1355.3	803.3	778.0	798.7	-360.2	219.4	433.7	-428.5	46.31	1.98	6.50	32.0
4.50	1298.2	850.7	781.1	724.1	-361.8	234.6	393.7	-508.3	46.33	2.02	6.51	32.0
5.00	1739.9	1096.5	914.6	996.6	-473.7	273.6	461.0	-513.5	44.33	1.98	5.62	40.4
5.00	1677.1	1194.8	904.9	902.3	-475.8	268.2	425.8	-569.0	44.30	1.98	5.63	40.7
5.51	2050.4	1475.2	1014.1	1262.6	-571.5	361.9	495.3	-582.8	43.38	2.02	4.89	43.2
5.50	1943.9	1662.3	1025.2	1155.9	-596.7	350.1	451.4	-598.4	43.42	2.02	4.90	44.5
6.01	2510.9	2031.6	1120.7	1671.2	-686.2	422.2	564.0	-607.0	43.48	2.01	4.30	46.1
6.00	2396.5	2355.1	1144.6	1424.6	-681.5	416.0	544.9	-609.7	43.53	1.96	4.30	42.5

Table A.4 – Phase I Experimental Results: Model Weight 29.55 kg, Model LCG = 0.493 m

Model Speed [m/s]	PT1 (gauge) [Pa]	PT2 (gauge) [Pa]	PT3 (gauge) [Pa]	PT4 (gauge) [Pa]	PT6 (gauge) [Pa]	PT7 (gauge) [Pa]	PT8 (gauge) [Pa]	PT9 (gauge) [Pa]	Tow Force [N]	Trim Refer. [deg]	Trim Untared [deg]	Sinkage Tared [mm]
0.50	9.3	27.6	52.4	28.7	17.0	-15.0	64.6	-38.2	1.12	1.09	1.12	-1.6
1.00	13.4	73.8	117.6	72.5	36.4	11.2	135.5	-50.6	5.36	1.12	1.24	-4.2
1.50	18.8	105.9	162.5	106.8	70.7	72.9	229.6	-55.8	16.79	1.08	1.98	-12.8
2.00	79.6	169.4	231.4	173.3	113.4	170.5	333.5	-109.9	38.97	1.07	5.33	-33.1
2.50	72.9	208.2	286.6	211.4	79.8	185.3	393.6	-202.8	43.55	1.10	6.53	-26.0
3.00	122.3	226.2	296.8	207.2	-0.7	156.5	413.3	-236.2	46.57	1.14	7.04	-14.6
3.50	280.5	255.5	380.8	301.6	-114.1	209.9	417.8	-303.0	47.47	1.15	7.10	-2.9
4.00	512.8	384.4	475.1	394.8	-220.7	204.7	425.9	-159.0	46.58	1.11	6.70	9.3
4.50	770.3	536.0	575.2	503.8	-346.7	214.0	449.8	-423.3	44.98	1.09	5.97	19.6
5.00	1092.8	717.0	689.8	658.3	-453.5	256.5	475.2	-269.5	43.80	1.10	5.26	32.7
5.50	1335.3	929.1	781.0	756.2	-586.9	373.6	507.0	-545.4	43.35	1.10	4.59	35.3
6.01	1502.8	1211.5	878.8	821.0	-698.7	378.6	564.9	-576.5	43.86	1.11	4.08	36.6
6.51	1815.9	1644.1	962.0	992.1	-810.1	432.7	618.5	-669.4	45.18	1.09	3.65	35.4
7.01	2221.1	2270.1	1014.1	1222.9	-940.9	666.2	662.0	-660.9	47.04	1.14	3.33	35.9

Table A.5 – Phase I Experimental Results: Model Weight 29.55 kg, Model LCG = 0.534 m

Model Speed [m/s]	PT1 (gauge) [Pa]	PT2 (gauge) [Pa]	PT3 (gauge) [Pa]	PT4 (gauge) [Pa]	PT6 (gauge) [Pa]	PT7 (gauge) [Pa]	PT8 (gauge) [Pa]	PT9 (gauge) [Pa]	Tow Force [N]	Trim Refer. [deg]	Trim Untared [deg]	Sinkage Tared [mm]
4.00	288.2	304.9	183.5	368.4	-155.6	198.5	431.4	-287.8	44.56	0.37	5.97	3.0
4.00	308.8	301.7	370.2	354.3	-172.1	247.3	429.0	-324.8	44.62	0.39	5.99	1.0
4.50	475.8	412.2	260.1	457.5	-282.2	234.7	443.2	-151.6	44.06	0.32	5.49	13.4
4.50	503.7	408.1	455.5	443.7	-284.5	261.3	439.5	-401.3	44.06	0.32	5.50	11.3
5.00	703.3	533.6	525.3	541.4	-430.1	317.2	458.9	-389.2	43.57	0.32	4.89	16.7
5.00	712.9	527.5	527.9	515.1	-414.7	321.8	466.3	-441.3	43.63	0.39	4.90	14.8
5.50	902.6	675.7	618.1	614.3	-545.0	354.1	483.8	-471.5	43.68	0.39	4.33	26.9
5.50	926.2	674.6	603.8	560.6	-533.8	378.9	498.6	-273.2	43.67	0.35	4.32	28.3
6.01	1117.3	850.8	425.9	719.8	-648.5	429.9	542.6	-499.9	44.47	0.35	3.85	27.5
6.00	1126.7	841.5	709.4	708.0	-654.1	457.9	537.6	-551.2	44.38	0.39	3.85	28.5
6.51	1301.6	1046.0	372.7	662.5	-887.2	332.9	254.9	-679.3	45.95	0.34	3.47	33.6
6.51	1340.4	1048.4	812.5	800.2	-761.2	542.6	615.0	-334.5	46.04	0.34	3.49	29.0
7.01	1523.4	1348.5	884.1	914.2	-892.7	701.1	663.2	-534.8	47.66	0.36	3.13	27.7
7.01	1499.6	1310.0	872.0	860.4	-896.2	688.0	636.0	-529.1	47.69	0.33	3.13	25.2
7.51	1719.8	1681.3	1024.4	1050.4	-1034.1	753.1	712.7	-568.1	50.21	0.36	2.84	34.2
7.51	1632.6	1665.7	979.9	1028.7	-1001.8	788.0	738.7	-601.1	50.13	0.34	2.84	31.8
8.00	1826.5	2105.9	1063.3	1133.5	-1143.5	945.6	755.9	-596.4	53.44	0.39	2.74	39.9

Table A.6 – Phase I Experimental Results: Model Weight 29.55 kg, Model LCG = 0.572 m

Model Speed [m/s]	PT1 (gauge) [Pa]	PT2 (gauge) [Pa]	PT3 (gauge) [Pa]	PT4 (gauge) [Pa]	PT6 (gauge) [Pa]	PT7 (gauge) [Pa]	PT8 (gauge) [Pa]	PT9 (gauge) [Pa]	Tow Force [N]	Trim Refer. [deg]	Trim Untared [deg]	Sinkage Tared [mm]
4.00	538.8	431.6	333.3	485.8	-175.5	224.7	426.9	-162.9	57.20	1.32	7.59	11.1
4.00	628.2	421.8	501.3	494.5	-185.2	238.0	402.2	-380.5	57.11	1.33	7.57	5.2
4.50	798.5	588.7	440.6	618.4	-302.5	245.5	430.8	-349.7	54.06	1.35	6.69	25.2
4.50	913.8	581.4	600.3	628.3	-306.5	260.2	414.5	-441.3	53.89	1.34	6.68	27.7
5.00	1231.0	770.9	706.7	766.9	-417.5	322.2	445.4	-556.1	51.60	1.33	5.83	31.3
5.01	1198.4	767.4	706.6	760.1	-430.8	319.9	440.2	-523.2	51.50	1.31	5.82	33.6
5.50	1508.5	969.9	800.7	874.9	-540.1	385.2	477.4	-610.9	49.86	1.29	5.09	35.6
5.50	1476.0	976.3	786.6	861.9	-549.3	380.3	465.7	-545.8	49.90	1.31	5.07	36.7
6.00	1633.2	1225.8	763.5	992.2	-659.2	457.5	527.3	-597.6	49.55	1.32	4.48	42.0
6.01	1781.1	1227.9	886.8	1003.9	-665.8	472.2	521.0	-604.7	49.74	1.31	4.50	43.0
6.51	2030.3	1375.8	667.4	1095.6	-819.8	558.4	233.8	-503.1	50.40	1.37	3.99	42.8
6.51	2121.2	1593.4	991.6	1142.3	-772.7	603.7	591.0	-635.1	50.17	1.30	4.03	38.7
7.01	2481.4	2113.1	1075.2	1364.2	-881.7	708.7	643.4	-721.5	51.76	1.28	3.61	44.5
7.01	2428.1	2127.9	1065.1	1347.3	-891.3	505.0	652.5	-649.8	51.71	1.32	3.60	41.5

Table A.7 – Phase I Experimental Results: Model Weight 33.91 kg, Model LCG = 0.535 m

APPENDIX B

Results from Physical Model Tests Boundary Layer Measurements

B.1 Results from Boundary Layer Measurements

The physical tests of the planing hull model were performed in two phases. The second phase of the experimental program was dedicated to determining velocity profiles in the boundary layer at two locations for four different model speeds in the design ballast condition. A discussion of these measurements, made using a laser Doppler velocimeter (LDV) fitted in the model, is given in Section 2.3.6.

This appendix gives the experimental results for the boundary layer velocity measurements using the LDV. The following four figures show the profiles for both the forward and aft profiles measured at the four model speeds (4.0 m/s, 5.0 m/s, 6.0 m/s and 6.5 m/s). All of the tests in this phase of experiments were conducted for the design ballast condition of the model with a displacement of 29.55 kg and an LCG of 0.53 m (referenced from the transom base).

The experimental data is also presented in Tables B.1 – B.4. The tables are divided into two sets of three columns each. The first set gives the data for the aft LDV location in the model, while the second set are for the forward LDV location. In each set, data is given for the measurement location (referenced perpendicular to the hull surface), the mean velocity, and the standard deviation of the data set for that measurement.

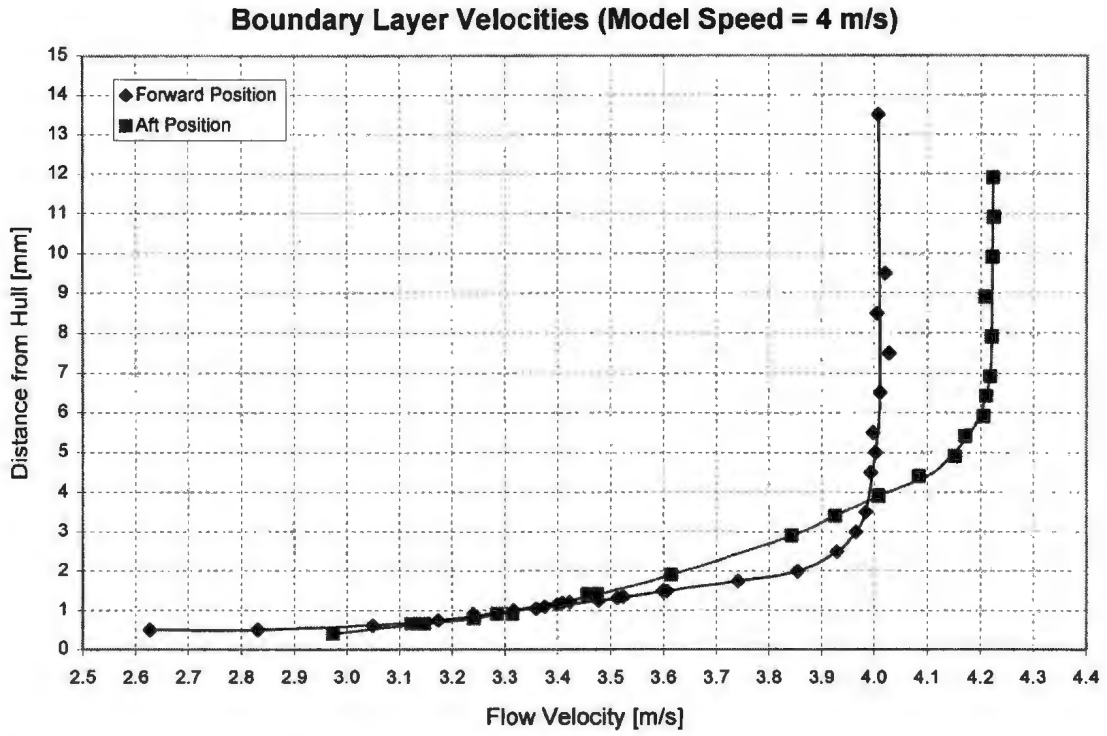


Figure B.1 – Boundary Layer Velocities (model speed = 4.0 m/s)

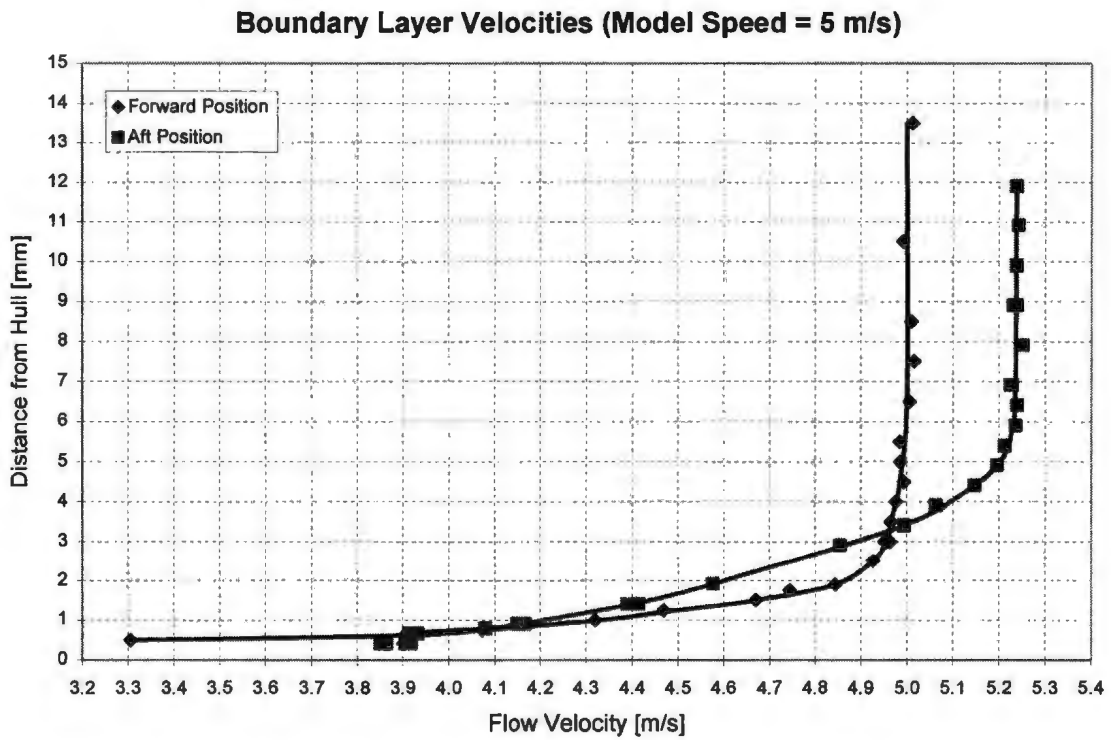


Figure B.2 – Boundary Layer Velocities (model speed = 5.0 m/s)

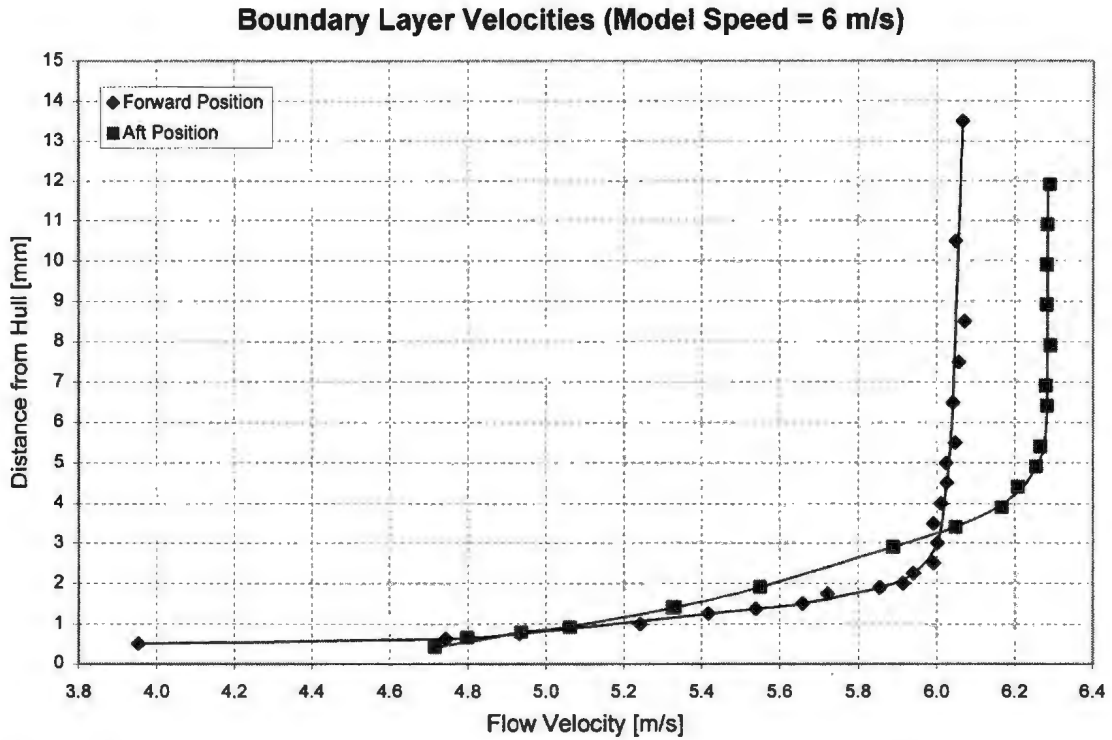


Figure B.3 – Boundary Layer Velocities (model speed = 6.0 m/s)

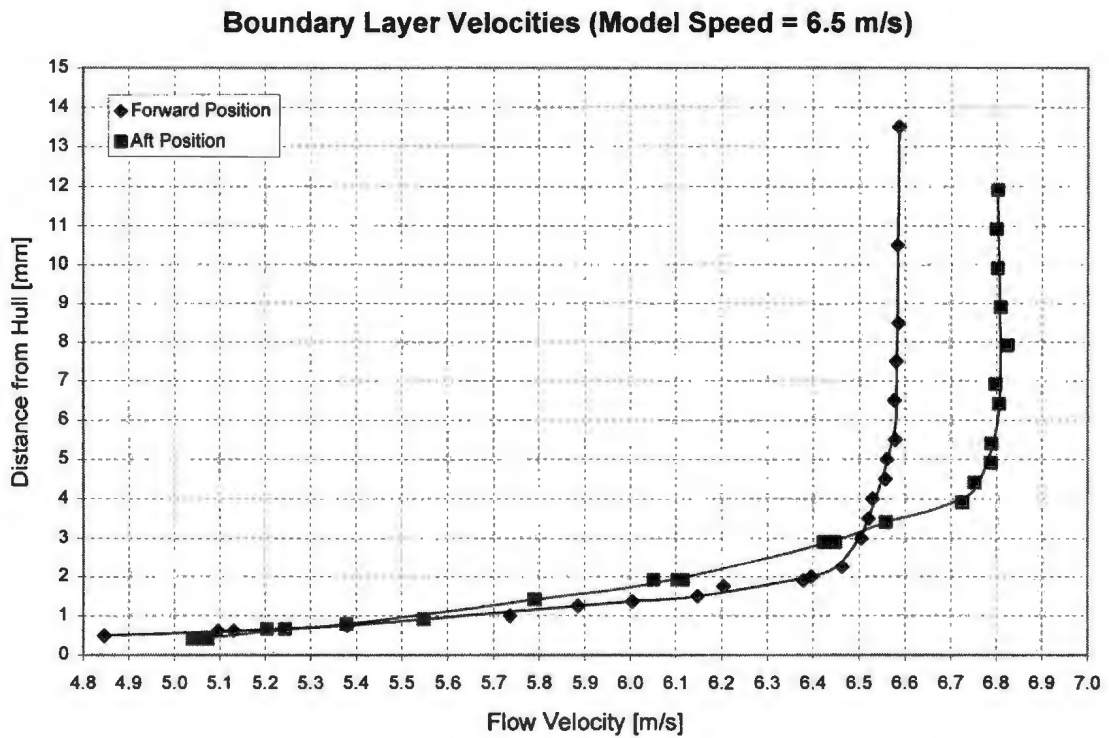


Figure B.4 – Boundary Layer Velocities (model speed = 6.5 m/s)

LDV Position (Aft) [mm]	Velocity (m/s)	Standard Deviation (m/s)	LDV Position (Forward) [mm]	Velocity (m/s)	Standard Deviation (m/s)
0.41	2.97	0.350	0.50	2.63	0.979
0.66	3.12	0.344	0.62	3.05	0.349
0.66	3.15	0.359	0.75	3.17	0.341
0.79	3.24	0.345	1.00	3.32	0.320
0.91	3.28	0.331	1.25	3.48	0.301
0.91	3.31	0.321	1.50	3.61	0.282
1.41	3.47	0.299	1.75	3.74	0.278
1.41	3.46	0.308	2.00	3.85	0.264
1.91	3.61	0.279	2.50	3.93	0.216
2.91	3.84	0.342	3.00	3.97	0.176
3.41	3.93	0.217	4.50	3.99	0.143
3.91	4.01	0.203	5.00	4.00	0.135
4.41	4.08	0.182	5.50	4.00	0.134
4.91	4.15	0.147	6.50	4.01	0.126
5.41	4.17	0.131	7.50	4.03	0.121
5.91	4.21	0.116	8.50	4.00	0.111
6.41	4.21	0.112	9.50	4.02	0.127
6.91	4.22	0.100			
7.91	4.22	0.087			
8.91	4.21	0.093			
9.91	4.22	0.092			
10.91	4.22	0.100			
11.91	4.22	0.096			

Table B.1 – LDV Results: Model Speed = 4.0 m/s

LDV Position (Aft) [mm]	Velocity (m/s)	Standard Deviation (m/s)	LDV Position (Forward) [mm]	Velocity (m/s)	Standard Deviation (m/s)
0.41	3.90	0.402	0.50	3.31	1.315
0.41	3.92	0.402	0.62	3.90	0.440
0.41	3.86	0.424	0.75	4.07	0.484
0.41	3.85	0.453	1.00	4.32	0.381
0.66	-0.02	0.058	1.25	4.47	0.361
0.66	3.93	0.366	1.50	4.67	0.316
0.66	0.00	0.000	1.75	4.74	0.346
0.66	3.91	0.445	1.90	4.84	0.323
0.79	4.08	0.401	2.50	4.93	0.234
0.91	4.15	0.374	3.00	4.96	0.191
0.91	4.17	0.385	3.00	4.96	0.194
1.41	4.41	0.363	3.00	4.95	0.188
1.41	4.39	0.368	3.50	4.96	0.171
1.91	4.58	0.323	4.00	4.98	0.163
2.91	4.85	0.562	4.50	4.99	0.154
3.41	4.99	0.240	5.00	4.99	0.143
3.91	5.06	0.223	5.50	4.98	0.150
4.41	5.15	0.174	6.50	5.01	0.128
4.91	5.20	0.161	7.50	5.02	0.134
5.41	5.21	0.127	8.50	5.01	0.125
5.91	5.24	0.128	10.50	4.99	0.174
6.41	5.24	0.119	13.50	5.01	0.143
6.91	5.22	0.113			
6.91	5.23	0.114			
7.91	5.25	0.099			
8.91	5.23	0.116			
8.91	5.24	0.109			
9.91	5.24	0.110			
10.91	5.24	0.107			
11.91	5.24	0.110			

Table B.2 – LDV Results: Model Speed = 5.0 m/s

LDV Position (Aft) [mm]	Velocity (m/s)	Standard Deviation (m/s)	LDV Position (Forward) [mm]	Velocity (m/s)	Standard Deviation (m/s)
0.41	4.72	0.472	0.50	3.95	1.811
0.66	4.80	0.495	0.62	4.74	0.521
0.79	4.94	0.465	0.75	4.93	0.507
0.91	5.06	0.467	1.00	5.24	0.479
1.41	5.33	0.410	1.25	5.42	0.458
1.41	5.33	0.403	1.37	5.54	0.428
1.91	5.55	0.359	1.50	5.66	0.384
2.91	5.89	0.570	1.75	5.72	0.421
3.41	6.05	0.260	1.90	5.85	0.389
3.91	6.17	0.209	2.00	5.91	0.333
4.41	6.21	0.180	2.25	5.94	0.369
4.91	6.25	0.148	2.50	5.99	0.295
5.41	6.27	0.135	3.00	6.00	0.234
6.41	6.28	0.133	3.50	5.99	0.210
6.91	6.28	0.121	4.00	6.01	0.180
7.91	6.29	0.104	4.50	6.02	0.178
8.91	6.28	0.119	5.00	6.02	0.158
9.91	6.28	0.118	5.50	6.05	0.138
10.91	6.28	0.119	6.50	6.04	0.135
11.91	6.29	0.122	7.50	6.06	0.126
			8.50	6.07	0.095
			10.50	6.05	0.147
			13.50	6.07	0.148

Table B.3 – LDV Results: Model Speed = 6.0 m/s

LDV Position (Aft) [mm]	Velocity (m/s)	Standard Deviation (m/s)	LDV Position (Forward) [mm]	Velocity (m/s)	Standard Deviation (m/s)
0.41	5.07	0.709	0.50	4.85	0.647
0.41	5.04	0.568	0.62	5.10	0.889
0.41	5.05	0.547	0.62	5.13	0.760
0.66	5.24	0.551	0.75	5.38	0.593
0.66	5.20	0.525	1.00	5.74	0.519
0.79	5.38	0.487	1.25	5.88	0.499
0.91	5.55	0.496	1.37	6.00	0.477
1.41	5.79	0.417	1.50	6.15	0.419
1.41	5.79	0.455	1.75	6.20	0.444
1.91	6.12	0.426	1.90	6.38	0.437
1.91	6.10	0.431	2.00	6.40	0.371
1.91	6.05	0.389	2.25	6.46	0.385
2.91	6.45	0.586	3.00	6.50	0.269
2.91	6.42	0.566	3.50	6.52	0.212
3.41	6.56	0.282	4.00	6.53	0.200
3.91	6.73	0.205	4.50	6.56	0.169
4.41	6.75	0.195	5.00	6.56	0.166
4.91	6.79	0.153	5.50	6.58	0.139
5.41	6.79	0.136	6.50	6.58	0.135
6.41	6.81	0.113	7.50	6.58	0.122
6.91	6.80	0.130	8.50	6.58	0.128
7.91	6.82	0.126	10.50	6.58	0.158
8.91	6.81	0.105	13.50	6.59	0.126
9.91	6.80	0.126			
10.91	6.80	0.126			
11.91	6.80	0.125			

Table B.4 – LDV Results: Model Speed = 6.5 m/s

APPENDIX C

Results from Physical Model Tests

Phase II

C.1 Results from Physical Model Tests: Phase II

The physical tests of the planing hull model were performed in two phases. The second phase was used to determine boundary layer velocity profiles at two locations on the hull for four model speeds. All of the tests in this phase were performed with the design ballast condition: displacement = 29.6 kg, LCG = 0.53m, resting trim = 1.1°, draft at tow point = 71.7mm. Although the purpose of the tests was to collect data using the LDV, (see Section 2.3.6), data was also acquired from the other instruments. This data was used to estimate the uncertainties associated with the measured quantities of tow force, trim, model speed, sinkage and hull pressure. For a given LDV configuration (aft or forward location), the model was run at essentially the same ballast condition for an average of about 20 runs for each model speed. The only changes from run to run were small vertical movements (a few millimeters) of the LDV probe as it measured the velocity in at different positions in the boundary layer. The data from these repeated runs gave an indication of the random error associated with each instrument. The procedure used to determine the instrument uncertainties with a discussion of the results is given in Section 2.4.

The following tables, C.1 – C.9, list the data collected from phase II of the physical experiments for: tow force, trim, model speed, sinkage and hull pressure. Descriptions of the various columns in each table can be found in Table A.2.

Model Speed [m/s]	PT1 (gauge) [Pa]	PT2 (gauge) [Pa]	PT3 (gauge) [Pa]	PT4 (gauge) [Pa]	PT6 (gauge) [Pa]	PT7 (gauge) [Pa]	PT8 (gauge) [Pa]	PT9 (gauge) [Pa]	Tow Force [N]	Trim Refer. [deg]	Trim Untared [deg]	Sinkage Tared [deg]
4.00	694.4	444.9	528.2	546.0	-157.2	236.7	422.6	-462.0	48.09	1.22	6.86	13.8
4.00	631.3	449.5	292.1	293.9	-124.7	206.0	18.8	-67.5	47.90	1.24	6.84	11.3
4.00	659.2	480.1	193.2	248.8	-356.7	8.4	27.5	-474.2	48.11	1.21	6.83	11.5
4.00	661.2	446.3	328.9	560.1	-176.0	208.5	399.1	-454.9	48.13	1.25	6.84	7.3
4.00	671.9	456.5	349.1	563.0	-170.7	213.2	443.1	-430.5	48.25	1.16	6.86	10.7
4.00	665.0	446.0	313.0	549.8	-208.0	236.2	412.1	-467.6	48.05	1.20	6.82	16.7
4.00	655.3	444.0	320.1	555.0	-198.1	213.5	408.6	-454.5	47.96	1.20	6.81	14.2
4.00	671.5	446.6	334.4	556.4	-198.8	236.0	429.0	-465.9	48.17	1.17	6.83	13.4
4.00	669.9	444.4	357.1	556.9	-172.8	223.0	400.0	-336.4	48.22	1.23	6.84	11.6
4.00	660.5	448.0	324.5	551.3	-182.2	228.3	413.5	-472.6	48.11	1.18	6.82	11.0
4.00	678.0	433.1	330.8	555.7	-174.1	254.5	434.6	-402.8	48.22	1.23	6.84	12.9
4.00	737.0	455.5	301.4	574.8	-112.4	242.9	443.2	-445.2	48.19	1.17	6.84	13.6
4.00	711.6	412.9	336.7	547.5	-131.3	246.4	437.8	-476.7	48.42	1.23	6.84	10.2
4.00	629.2	451.3	351.6	491.5	-159.2	200.2	403.0	-316.8	48.01	1.21	6.86	12.7
4.00	623.7	449.5	361.7	497.2	-152.8	217.9	392.2	-488.2	47.97	1.23	6.85	11.7
4.00	710.6	364.3	374.0	547.9	-123.5	248.0	428.1	-431.6	48.48	1.21	6.84	11.0
4.00	708.9	335.4	513.7	551.6	-122.6	226.4	421.3	-418.8	48.44	1.22	6.84	7.8
4.00	585.0	449.1	316.5	503.7	-204.0	192.5	406.3	-471.3	48.03	1.23	6.88	12.6
4.00	700.2	436.5	306.0	539.0	-187.7	205.2	415.0	-348.8	48.07	1.21	6.87	8.7
4.00	679.3	437.4	345.2	517.4	-165.5	138.4	429.7	-300.6	48.15	1.24	6.89	5.6
4.00	681.4	437.5	336.4	509.8	-176.7	52.6	402.8	-307.9	47.94	1.20	6.85	15.0
4.00	680.0	441.8	334.6	519.7	-203.7	75.4	408.6	-485.8	47.98	1.17	6.88	11.7
4.00	597.2	447.0	179.0	214.7	-152.7	29.7	124.6	-472.5	47.90	1.21	6.87	11.6
4.00	607.8	435.4	327.1	541.9	-188.8	181.6	393.9	-485.9	48.26	1.24	6.87	11.9
4.00	607.5	440.0	308.3	538.5	-197.5	179.4	398.9	-140.2	48.30	1.18	6.86	9.8
4.00	608.1	431.9	291.1	533.1	-209.9	170.7	385.8	-473.1	48.15	1.21	6.85	12.2
4.00	616.3	436.8	348.7	541.8	-169.5	190.9	398.7	-402.3	48.30	1.24	6.87	12.0
4.00	618.6	440.5	469.4	530.5	-163.5	157.0	402.2	-428.4	48.34	1.20	6.87	11.9
4.00	611.5	437.5	493.9	520.6	-147.6	123.8	406.3	-440.6	48.23	1.25	6.86	13.1
4.00	651.9	433.4	488.8	504.8	-204.3	174.4	399.0	-498.7	48.14	1.25	6.85	13.7

Table C.1 – Phase II Experimental Results: LDV Aft Position, Model Speed = 4.0 m/s

Model Speed [m/s]	PT1 (gauge) [Pa]	PT2 (gauge) [Pa]	PT3 (gauge) [Pa]	PT4 (gauge) [Pa]	PT6 (gauge) [Pa]	PT7 (gauge) [Pa]	PT8 (gauge) [Pa]	PT9 (gauge) [Pa]	Tow Force [N]	Trim Refer. [deg]	Trim Untared [deg]	Sinkage Tared [deg]
4.00	551.0	237.1	126.6	483.3	-156.9	63.9	372.1	-270.2	47.16	1.10	6.65	11.2
4.00	545.2	292.8	156.7	357.6	-349.5	-135.4	315.6	-375.3	47.29	1.07	6.63	16.8
4.00	540.4	294.8	99.3	345.0	-362.8	-149.9	292.6	-380.8	47.22	1.11	6.66	6.5
4.00	553.1	288.4	60.6	329.1	-407.4	-139.6	268.9	-371.2	47.26	1.12	6.66	11.7
4.00	553.2	297.2	59.9	325.0	-427.1	-111.6	276.6	-373.3	47.18	1.04	6.67	11.3
4.00	500.3	262.8	29.2	310.2	-463.5	-105.4	283.6	-278.0	47.28	1.05	6.65	9.8
4.00	524.1	225.4	-21.1	284.4	-559.6	-87.3	293.2	-326.5	47.50	1.09	6.65	7.7
4.00	515.4	241.4	-27.2	289.1	-551.7	-77.8	311.3	-324.2	47.59	1.03	6.64	10.0
4.00	498.4	218.9	-36.9	274.7	-596.1	-92.2	293.0	-325.6	47.51	1.12	6.63	10.9
4.00	494.3	236.8	-37.1	276.8	-573.9	-83.0	304.8	-327.7	47.70	1.08	6.64	12.9
4.00	671.1	266.2	272.2	435.6	-141.9	24.8	330.9	-356.8	47.04	1.09	6.63	12.2
4.00	490.1	243.2	-21.7	279.5	-544.6	-62.7	327.9	-291.1	47.74	1.04	6.65	11.9
4.00	476.7	250.9	-23.4	280.2	-523.4	-65.0	317.5	-314.2	47.76	1.08	6.66	10.4
4.00	447.4	272.9	-15.7	288.9	-486.3	-38.2	323.8	-341.7	47.53	1.14	6.65	11.1
4.00	655.5	271.0	249.6	394.5	-174.2	7.4	321.1	-361.7	47.07	1.09	6.63	13.5
4.00	633.5	265.8	233.2	367.1	-199.3	-18.0	306.2	-390.7	47.08	1.12	6.65	9.4
4.00	607.5	257.4	213.8	355.7	-236.1	-66.7	310.7	-380.7	47.01	1.12	6.63	12.2
4.00	599.4	258.8	231.3	349.5	-250.7	-90.1	306.5	-423.7	47.07	1.04	6.63	11.5
4.00	572.8	251.7	250.3	346.7	-283.3	-100.1	309.0	-429.3	46.74	1.06	6.65	11.5

Table C.2 – Phase II Experimental Results: LDV Forward Position, Model Speed = 4.0 m/s (Part 1)

Model Speed [m/s]	PT1 (gauge) [Pa]	PT2 (gauge) [Pa]	PT3 (gauge) [Pa]	PT4 (gauge) [Pa]	PT6 (gauge) [Pa]	PT7 (gauge) [Pa]	PT8 (gauge) [Pa]	PT9 (gauge) [Pa]	Tow Force [N]	Trim Refer. [deg]	Trim Untared [deg]	Sinkage Tared [deg]
4.00	578.5	246.7	232.7	334.5	-295.6	-102.8	301.5	-393.0	46.82	1.07	6.59	7.6
4.00	542.1	257.3	238.1	354.6	-316.4	-77.1	289.5	-267.8	47.07	1.05	6.66	10.5
4.00	509.8	271.6	349.5	353.2	-305.0	-125.5	288.4	-368.1	46.67	1.09	6.65	9.8
4.00	525.4	282.7	368.5	357.9	-294.4	-127.3	304.6	-366.2	47.33	1.02	6.67	10.0
4.00	546.7	284.9	193.3	347.6	-336.7	-136.3	290.9	-369.5	47.25	1.11	6.66	6.4
4.00	691.7	264.1	510.1	522.4	-128.8	161.5	410.5	-417.5	47.40	1.11	6.67	10.3
4.00	680.3	250.2	536.5	521.3	-122.5	199.2	406.0	-400.8	47.10	1.07	6.62	11.6
4.00	681.6	255.8	525.1	536.4	-122.3	155.3	395.4	-377.9	47.23	1.07	6.64	11.3
4.00	684.2	254.7	491.2	508.5	-124.7	122.2	388.0	-374.1	47.21	1.05	6.62	11.0
4.00	613.1	239.8	96.5	479.9	-119.3	96.3	382.4	-365.8	46.91	1.05	6.61	15.6
4.00	609.0	244.7	105.9	489.6	-134.9	125.1	373.5	-358.7	47.25	1.07	6.66	11.1
4.00	591.5	242.0	89.9	483.9	-142.0	116.0	365.9	-380.1	47.20	1.10	6.65	10.7
4.00	577.1	241.9	110.8	484.0	-157.9	109.8	371.6	-300.8	47.20	1.07	6.63	9.8
4.00	562.5	233.9	89.3	488.9	-167.2	68.4	360.3	-284.9	47.08	1.12	6.62	11.9
4.00	682.9	232.1	462.2	504.0	-138.6	105.1	370.0	-390.3	47.14	1.11	6.63	10.6
4.00	686.3	237.5	436.9	517.1	-130.6	138.9	378.3	-393.4	47.34	1.08	6.63	11.6
4.00	688.5	233.4	400.7	503.0	-143.7	122.4	370.4	-391.5	47.31	1.09	6.62	10.7
4.00	687.9	238.6	412.4	499.3	-134.0	114.4	376.8	-376.4	47.29	1.06	6.62	11.5
4.00	683.4	237.4	433.2	494.2	-123.2	102.8	377.6	-382.8	47.41	1.10	6.64	11.2
4.00	686.2	233.1	368.4	475.7	-128.6	121.7	358.9	-376.5	47.41	1.12	6.65	11.7
4.00	621.7	243.5	99.8	481.7	-114.6	-2.7	364.3	-365.0	47.08	1.09	6.63	10.9

Table C.3 – Phase II Experimental Results: LDV Forward Position, Model Speed = 4.0 m/s (Part 2)

Model Speed [m/s]	PT1 (gauge) [Pa]	PT2 (gauge) [Pa]	PT3 (gauge) [Pa]	PT4 (gauge) [Pa]	PT6 (gauge) [Pa]	PT7 (gauge) [Pa]	PT8 (gauge) [Pa]	PT9 (gauge) [Pa]	Tow Force [N]	Trim Refer. [deg]	Trim Untared [deg]	Sinkage Tared [deg]
5.00	1266.8	449.9	259.9	626.2	-663.2	132.4	141.9	-538.7	44.70	1.16	5.24	31.5
5.00	1285.2	797.9	706.2	817.6	-449.0	172.7	439.8	-531.2	45.29	1.22	5.26	29.7
5.00	1271.6	845.3	388.6	763.8	-641.7	154.8	507.9	-606.9	45.09	1.22	5.23	31.7
5.00	1269.0	811.0	506.6	900.9	-393.3	288.6	477.1	-525.2	45.20	1.17	5.23	29.8
5.00	1283.9	813.3	500.8	875.4	-416.4	288.3	510.4	-619.8	45.04	1.17	5.23	30.4
5.00	1283.5	793.9	469.4	877.8	-431.2	313.5	469.4	-458.1	45.10	1.22	5.22	33.6
5.00	1297.3	801.7	540.8	888.1	-428.8	320.4	492.5	-588.0	45.22	1.24	5.24	30.6
5.00	1316.4	812.2	508.6	887.9	-419.1	333.1	481.5	-528.8	45.27	1.20	5.24	29.8
5.00	1320.4	769.2	518.4	896.1	-355.1	358.6	522.3	-555.6	45.00	1.22	5.24	32.8
5.00	1321.9	795.3	481.3	920.9	-334.6	327.3	507.9	-544.7	45.41	1.22	5.24	32.4
5.00	1325.1	737.4	550.5	884.2	-346.9	334.0	496.5	-528.4	45.40	1.23	5.23	30.3
5.00	1221.4	772.6	549.6	790.4	-415.1	232.8	477.9	-414.6	44.73	1.24	5.26	33.1
5.00	1209.1	774.6	552.3	798.4	-387.5	287.3	490.7	-597.4	44.76	1.23	5.26	31.5
5.00	1196.0	775.8	531.1	819.6	-401.5	288.5	469.1	-530.0	44.83	1.23	5.27	32.6
5.00	1319.7	690.5	595.8	900.9	-347.4	333.9	493.0	-516.7	45.61	1.18	5.23	32.4
5.00	1325.4	654.9	768.5	903.1	-340.2	302.2	487.1	-518.5	45.55	1.18	5.22	27.7
5.00	1327.9	565.7	750.6	885.7	-353.1	285.4	460.2	-501.3	45.35	1.23	5.22	29.7
5.00	1165.8	781.7	512.8	807.1	-461.3	260.4	468.5	-468.8	44.74	1.21	5.26	28.8
5.00	1301.5	746.8	497.5	825.6	-421.4	258.7	456.5	-347.9	44.61	1.25	5.26	35.9
5.00	1316.7	748.6	504.5	799.5	-417.9	198.0	436.9	-470.1	44.67	1.23	5.27	27.2
5.00	1316.4	751.0	517.5	804.9	-435.3	82.0	440.8	-505.0	44.64	1.20	5.26	32.2
5.00	1190.4	770.2	298.4	652.4	-398.1	67.5	430.5	-560.3	44.55	1.26	5.26	31.6
5.00	1194.7	765.2	487.5	833.1	-396.7	253.6	466.0	-607.8	44.61	1.22	5.26	30.4
5.00	1209.1	797.0	558.3	871.6	-388.7	240.0	460.5	-604.5	45.40	1.23	5.27	30.4
5.00	1226.4	788.9	695.3	884.1	-406.8	182.6	458.2	-507.8	45.33	1.22	5.27	30.0
5.00	1252.1	784.3	734.4	865.3	-378.1	155.5	459.7	-513.4	45.20	1.23	5.26	30.8
5.00	1268.2	781.8	734.8	854.7	-438.6	217.7	464.7	-555.7	45.10	1.25	5.27	34.5

Table C.4 – Phase II Experimental Results: LDV Aft Position, Model Speed = 5.0 m/s

Model Speed [m/s]	PT1 (gauge) [Pa]	PT2 (gauge) [Pa]	PT3 (gauge) [Pa]	PT4 (gauge) [Pa]	PT6 (gauge) [Pa]	PT7 (gauge) [Pa]	PT8 (gauge) [Pa]	PT9 (gauge) [Pa]	Tow Force [N]	Trim Refer. [deg]	Trim Untared [deg]	Sinkage Tared [deg]
5.00	1144.5	508.5	281.1	735.9	-312.6	-107.4	389.5	-264.8	44.67	1.09	5.11	31.7
5.00	1011.2	571.0	205.9	587.3	-631.6	-280.8	312.9	-449.2	44.63	1.09	5.11	34.1
5.00	1018.3	561.0	124.4	596.9	-640.9	-292.2	295.4	-465.0	44.72	1.09	5.12	34.8
5.00	1028.0	579.6	73.6	570.4	-722.4	-276.0	269.6	-453.7	44.63	1.06	5.11	29.5
5.00	1024.4	560.2	36.3	555.2	-766.2	-265.9	239.8	-461.3	44.39	1.08	5.12	26.0
5.00	986.4	478.8	3.8	524.1	-826.0	-190.7	269.6	-310.5	44.57	1.11	5.12	29.8
5.00	1020.1	461.7	-24.0	499.2	-965.3	-186.1	286.2	-317.0	44.95	1.06	5.13	28.2
5.00	1007.6	475.9	-43.5	497.6	-947.0	-187.7	306.9	-332.5	44.91	1.04	5.12	27.9
5.00	1000.6	469.5	-34.8	500.5	-979.5	-183.5	314.0	-332.5	44.99	1.07	5.13	26.4
5.00	982.7	476.4	-42.3	489.9	-946.3	-185.0	309.3	-406.3	44.95	1.11	5.12	26.8
5.00	1256.4	533.8	445.5	686.1	-309.4	-46.8	353.3	-402.4	44.52	1.11	5.12	29.5
5.00	966.6	480.5	-38.5	491.0	-929.3	-162.9	328.0	-354.2	44.99	1.11	5.12	34.2
5.00	955.7	486.6	-35.0	488.6	-854.1	-169.1	324.4	-379.0	45.01	1.12	5.12	31.1
5.00	936.0	542.5	2.5	519.8	-749.4	-124.3	354.8	-242.1	44.94	1.07	5.12	29.7
5.00	1229.4	530.5	413.8	653.0	-390.2	-51.5	329.5	-398.6	44.55	1.11	5.11	28.8
5.00	1093.8	513.9	301.4	610.3	-543.4	-136.8	309.2	-258.7	44.62	1.05	5.13	29.8
5.00	1196.3	529.0	398.0	615.3	-377.0	-100.6	320.2	-426.2	44.49	1.12	5.11	26.8
5.00	1097.2	488.6	397.5	571.5	-518.4	-213.6	294.0	-505.7	44.71	1.08	5.12	32.7
5.00	1093.9	479.4	395.4	567.8	-532.0	-205.4	294.1	-495.3	43.86	1.08	5.10	32.3
5.00	983.7	546.6	24.8	533.5	-790.5	-257.0	244.4	-479.9	44.73	1.11	5.12	27.1
5.00	1167.3	510.6	368.9	609.0	-437.5	-162.9	320.5	-395.0	44.53	1.05	5.11	29.1
5.00	1003.0	566.4	41.5	551.4	-789.6	-250.6	250.9	-462.2	44.74	1.05	5.12	30.6
5.00	1134.5	506.5	449.1	594.2	-470.1	-212.6	299.2	-488.2	44.48	1.11	5.11	31.6
5.00	1073.6	477.4	386.6	563.8	-519.8	-191.6	292.5	-526.6	44.52	1.10	5.10	32.8
5.00	1083.7	521.8	360.4	598.6	-532.0	-184.3	317.0	-258.2	44.66	1.08	5.13	29.8
5.00	1074.3	510.4	398.1	589.9	-566.0	-158.5	293.4	-281.0	44.36	1.08	5.12	28.7
5.00	1006.1	550.3	458.4	600.6	-567.2	-277.2	289.2	-442.7	44.66	1.08	5.13	30.9
5.00	1022.8	575.3	304.6	593.5	-591.3	-270.3	319.5	-448.8	44.69	1.06	5.11	33.2

Table C.5 – Phase II Experimental Results: LDV Forward Position, Model Speed = 5.0 m/s

Model Speed [m/s]	PT1 (gauge) [Pa]	PT2 (gauge) [Pa]	PT3 (gauge) [Pa]	PT4 (gauge) [Pa]	PT6 (gauge) [Pa]	PT7 (gauge) [Pa]	PT8 (gauge) [Pa]	PT9 (gauge) [Pa]	Tow Force [N]	Trim Refer. [deg]	Trim Untared [deg]	Sinkage Tared [deg]
6.00	1896.3	1255.0	433.2	1151.3	-583.3	344.3	605.0	-604.6	44.71	1.12	4.02	36.9
6.00	2006.4	1195.8	949.6	1254.5	-647.4	479.9	577.8	-701.3	44.87	1.20	4.03	37.6
6.01	1923.3	1223.6	565.0	1180.3	-605.4	450.0	585.2	-506.2	44.70	1.21	4.02	40.1
6.01	1902.2	1288.9	974.8	1279.2	-646.5	272.2	547.9	-592.7	45.29	1.27	4.03	36.9
6.01	1937.4	1335.5	527.2	1307.4	-563.9	362.9	608.9	-698.3	45.21	1.20	4.00	38.6
6.01	1933.7	1323.8	687.1	1330.2	-599.9	451.4	581.9	-650.8	45.30	1.23	4.02	33.5
6.00	1937.4	1323.2	655.2	1339.5	-644.8	474.3	610.8	-610.2	45.28	1.17	4.00	35.0
6.01	1959.2	1322.8	680.9	1356.0	-617.5	482.5	640.3	-601.6	45.45	1.21	4.01	40.2
6.00	1955.3	1308.4	722.4	1327.3	-631.9	476.2	615.5	-654.4	45.26	1.23	4.00	36.6
6.01	1962.7	1333.1	729.0	1336.7	-625.5	515.2	630.7	-578.3	45.39	1.20	4.01	42.7
6.00	1975.3	1288.8	726.7	1321.6	-605.8	539.3	637.4	-619.7	45.22	1.22	4.00	39.4
6.00	1925.4	1313.9	460.4	1342.3	-590.1	447.9	345.4	-597.5	45.29	1.20	4.00	38.8
6.00	1955.5	1212.8	753.9	1352.7	-558.8	486.5	605.2	-598.6	45.63	1.20	4.00	38.0
6.01	1898.7	1193.1	716.3	1193.4	-639.9	370.4	595.9	-661.5	44.76	1.22	4.03	38.3
6.01	1868.2	1222.1	693.9	1172.0	-637.8	424.9	574.2	-622.5	44.73	1.22	4.04	38.1
6.01	1934.7	1179.8	850.5	1339.9	-550.6	470.9	606.6	-582.3	45.56	1.21	4.01	36.0
6.01	1933.8	1123.5	981.1	1335.8	-555.6	459.1	590.4	-545.5	45.54	1.22	3.99	38.0
6.01	2010.5	1195.4	699.0	1217.3	-654.9	288.8	580.1	-684.9	44.74	1.23	4.03	42.8
6.01	2036.3	1196.5	694.4	1200.7	-587.9	253.4	550.2	-524.1	44.63	1.22	4.03	34.6
6.00	1976.7	1167.7	719.1	1213.3	-700.1	193.5	548.3	-782.8	44.57	1.23	4.04	37.5
6.01	1958.3	1301.1	721.1	1322.6	-609.3	555.6	643.2	-616.9	45.18	1.18	3.99	38.3
6.00	1969.4	1201.5	748.3	1254.2	-630.5	549.5	652.1	-649.2	44.62	1.24	4.00	38.1
6.01	1850.1	1195.3	529.1	1262.3	-579.2	359.9	574.0	-237.3	44.58	1.25	4.03	37.7
6.00	1813.0	1200.3	662.3	1366.7	-614.4	388.4	565.5	-710.4	45.22	1.22	4.03	40.0
6.00	1836.4	1193.4	707.4	1240.6	-671.3	377.7	560.0	-563.2	44.65	1.19	4.03	38.1
6.00	1875.8	1308.9	704.5	1363.9	-608.9	315.3	567.0	-584.6	45.30	1.22	4.03	37.6
6.01	1839.3	1285.5	767.8	1361.9	-610.2	374.0	558.3	-631.3	45.39	1.24	4.03	38.0
6.01	1820.9	1238.5	956.3	1348.3	-610.3	259.3	569.3	-683.1	45.26	1.27	4.03	37.7
6.01	1836.4	1265.5	968.3	1343.6	-600.4	241.0	568.9	-566.1	45.39	1.27	4.04	37.4
6.01	1897.7	1286.1	974.4	1286.1	-659.4	362.7	589.6	-599.9	45.31	1.22	4.03	37.8

Table C.6 – Phase II Experimental Results: LDV Aft Position, Model Speed = 6.0 m/s

Model Speed [m/s]	PT1 (gauge) [Pa]	PT2 (gauge) [Pa]	PT3 (gauge) [Pa]	PT4 (gauge) [Pa]	PT6 (gauge) [Pa]	PT7 (gauge) [Pa]	PT8 (gauge) [Pa]	PT9 (gauge) [Pa]	Tow Force [N]	Trim Refer. [deg]	Trim Untared [deg]	Sinkage Tared [deg]
6.01	1821.7	949.9	771.8	1129.5	-523.0	-24.0	460.1	-348.3	44.78	1.08	3.93	34.0
6.00	1446.9	1005.2	253.8	905.6	-890.5	-406.4	358.0	-497.6	45.01	1.11	3.92	38.4
6.01	1440.2	1030.4	86.8	927.4	-958.7	-391.5	314.8	-490.5	44.85	1.08	3.92	37.3
6.01	1450.7	1024.1	71.2	906.1	-1055.6	-412.2	285.2	-493.1	44.89	1.06	3.93	34.2
6.01	1419.7	1054.1	60.1	884.5	-1087.5	-386.3	277.5	-507.6	45.36	1.05	3.92	37.9
6.00	1478.6	959.7	-65.4	973.0	-1058.1	-142.2	381.2	-417.4	44.99	1.11	3.92	39.0
6.01	1521.5	885.5	-49.2	844.5	-1206.0	-270.4	307.9	-267.2	44.94	1.13	3.92	37.1
6.01	1521.6	885.4	-49.1	844.1	-1206.0	-270.5	308.1	-266.9	44.95	1.13	3.92	37.1
6.00	1483.1	848.9	-71.7	788.6	-1385.2	-265.6	300.5	-326.4	45.29	1.10	3.93	41.5
6.00	1469.2	852.6	-77.4	793.3	-1371.2	-269.1	334.3	-382.2	45.34	1.05	3.93	33.8
6.01	1465.7	858.3	-64.5	796.8	-1398.4	-263.9	333.3	-364.0	45.42	1.08	3.93	41.3
6.01	1461.7	857.6	-67.4	798.0	-1315.4	-257.4	349.9	-422.1	45.20	1.10	3.94	35.1
6.00	1822.4	951.4	645.9	1058.5	-434.1	-65.1	426.0	-439.2	44.80	1.11	3.93	35.4
6.01	1438.5	862.7	-64.6	798.9	-1308.6	-248.2	357.2	-371.5	45.20	1.12	3.92	36.6
6.01	1468.1	895.9	-74.7	821.7	-1175.2	-234.9	382.3	-339.2	45.02	1.07	3.92	37.2
6.00	1458.5	943.5	-63.8	895.5	-1167.2	-200.0	381.4	-246.2	45.09	1.12	3.92	37.7
6.01	1841.6	989.7	-13.0	1052.8	-1058.2	-117.6	437.1	-452.8	45.07	1.13	3.94	38.5
6.01	1793.4	957.6	589.4	1018.0	-538.1	-81.1	377.1	-424.6	44.80	1.09	3.92	34.8
6.01	1753.5	944.0	610.1	986.9	-559.3	-141.7	375.0	-448.8	44.78	1.10	3.93	34.9
6.01	1720.1	930.9	595.2	974.1	-655.7	-239.6	342.0	-469.0	44.84	1.10	3.92	38.9
6.01	1414.9	1005.0	29.1	868.7	-1141.8	-369.5	283.2	-514.9	45.34	1.06	3.91	41.1
6.00	1674.2	922.2	640.5	955.4	-703.0	-286.0	336.4	-534.8	44.82	1.09	3.92	35.3
6.01	1607.5	1000.9	743.6	942.6	-882.3	-342.6	332.6	-385.9	44.89	1.07	3.92	36.4
6.00	1526.6	995.7	556.4	930.3	-823.0	-386.3	326.3	-500.3	44.96	1.05	3.93	36.7
6.01	1503.6	1044.6	363.7	942.7	-851.2	-387.5	363.9	-498.6	45.00	1.05	3.93	35.3

Table C.7 – Phase II Experimental Results: LDV Forward Position, Model Speed = 6.0 m/s

Model Speed [m/s]	PT1 (gauge) [Pa]	PT2 (gauge) [Pa]	PT3 (gauge) [Pa]	PT4 (gauge) [Pa]	PT6 (gauge) [Pa]	PT7 (gauge) [Pa]	PT8 (gauge) [Pa]	PT9 (gauge) [Pa]	Tow Force [N]	Trim Refer. [deg]	Trim Untared [deg]	Sinkage Tared [deg]
6.51	2228.3	1618.1	1091.6	1580.6	-736.5	364.5	631.4	-635.1	46.77	1.23	3.60	36.9
6.51	2258.9	1649.3	668.7	1640.0	-722.2	570.4	666.0	-889.8	46.69	1.20	3.55	40.6
6.51	2281.4	1693.5	827.0	1680.7	-735.2	554.2	690.0	-664.7	46.69	1.16	3.56	33.5
6.51	2285.1	1674.1	793.6	1686.2	-742.8	569.9	672.4	-687.8	46.61	1.24	3.54	39.7
6.51	2257.7	1629.3	876.9	1663.1	-748.9	580.8	712.1	-632.3	46.66	1.23	3.55	36.4
6.50	2299.5	1688.0	868.6	1688.7	-727.8	583.5	680.5	-713.0	46.71	1.23	3.57	36.9
6.51	2370.2	1775.7	928.4	1812.2	-713.4	639.1	728.8	-678.0	46.75	1.22	3.54	35.6
6.51	2270.4	1698.1	832.2	1683.2	-653.5	599.9	687.6	-648.4	46.91	1.19	3.56	39.6
6.51	2335.1	1657.7	918.9	1769.6	-635.7	579.0	679.4	-622.8	47.05	1.23	3.54	40.5
6.51	2303.2	1747.4	884.3	1699.8	-760.1	487.7	647.3	-718.5	46.22	1.23	3.59	39.2
6.51	2266.4	1533.9	1120.0	1652.0	-658.1	553.2	674.1	-613.1	46.88	1.21	3.54	37.2
6.50	2307.9	1569.2	1102.9	1746.0	-632.7	564.0	667.4	-593.8	47.03	1.17	3.52	42.4
6.51	2220.1	1442.8	1104.3	1644.3	-623.6	542.2	657.6	-574.7	46.97	1.16	3.55	37.1
6.51	2242.9	1436.4	1071.6	1652.7	-646.9	544.1	641.9	-584.0	46.88	1.23	3.53	42.3
6.51	2635.2	1830.7	920.2	2246.9	-754.7	543.3	653.7	-690.0	46.31	1.21	3.56	39.9
6.51	2398.6	1555.7	867.9	1582.5	-748.9	288.8	658.7	-669.1	46.12	1.22	3.60	39.4
6.50	2396.9	1573.6	852.1	1572.2	-739.2	174.4	638.6	-683.3	46.11	1.25	3.61	41.0
6.51	2324.0	1558.7	870.4	1570.7	-781.5	244.8	581.7	-766.5	46.11	1.23	3.59	35.8
6.50	2142.0	1534.3	784.1	1566.3	-695.9	364.1	645.2	-680.2	45.98	1.20	3.60	38.9
6.51	2203.0	1563.2	833.8	1608.5	-724.9	504.8	634.4	-495.5	46.04	1.24	3.59	35.4
6.51	2205.0	1678.5	927.2	1714.7	-697.2	466.1	635.3	-777.5	46.65	1.24	3.58	42.5
6.51	2300.2	1892.0	1004.3	1926.8	-696.6	465.3	647.4	-670.7	46.79	1.21	3.58	41.3
6.51	2152.0	1579.7	1084.8	1662.3	-724.1	264.1	634.1	-642.7	46.66	1.22	3.59	39.8
6.50	2256.2	1572.5	1125.7	1683.4	-726.1	472.0	647.0	-656.5	46.53	1.23	3.59	39.4
6.51	2272.9	1666.3	1115.5	1612.3	-745.2	446.5	633.6	-603.7	46.67	1.20	3.59	36.9

Table C.8 – Phase II Experimental Results: LDV Aft Position, Model Speed = 6.5 m/s

Model Speed [m/s]	PT1 (gauge) [Pa]	PT2 (gauge) [Pa]	PT3 (gauge) [Pa]	PT4 (gauge) [Pa]	PT6 (gauge) [Pa]	PT7 (gauge) [Pa]	PT8 (gauge) [Pa]	PT9 (gauge) [Pa]	Tow Force [N]	Trim Refer. [deg]	Trim Untared [deg]	Sinkage Tared [deg]
6.51	2128.3	1329.5	716.0	1383.5	-529.3	-8.1	486.6	-361.9	46.11	1.10	3.48	39.9
6.51	1677.1	1362.7	212.1	1147.5	-1031.6	-460.7	388.6	-489.4	46.55	1.05	3.49	34.1
6.51	1655.7	1359.5	73.2	1143.4	-1119.8	-445.4	326.0	-488.2	46.42	1.07	3.49	37.2
6.51	1643.5	1358.0	22.6	1112.2	-1207.5	-460.3	307.7	-487.0	46.45	1.04	3.50	37.2
6.51	1628.2	1408.3	23.2	1100.1	-1286.0	-423.4	289.6	-504.7	46.77	1.09	3.48	41.3
6.51	1605.9	1366.3	-14.2	1055.5	-1306.6	-436.5	280.4	-527.3	46.78	1.11	3.50	34.2
6.50	1738.5	1138.6	-50.7	1049.7	-1365.8	-328.8	360.8	-413.1	46.71	1.05	3.50	37.4
6.51	1748.6	1196.4	-111.2	1012.7	-1541.4	-302.4	345.1	-418.4	46.75	1.06	3.51	32.2
6.50	1726.9	1175.4	-118.6	1005.0	-1624.1	-308.8	346.3	-429.1	46.83	1.10	3.51	32.8
6.51	1705.7	1164.7	-94.7	1006.9	-1579.3	-308.9	353.3	-476.1	46.83	1.11	3.51	39.8
6.51	1729.0	1188.5	-110.6	1025.4	-1542.2	-292.8	373.2	-462.0	46.72	1.07	3.50	38.3
6.51	2132.1	1326.7	715.9	1326.7	-523.6	-55.3	470.9	-459.2	46.17	1.06	3.48	37.0
6.51	1727.9	1215.9	-105.0	1034.7	-1408.4	-291.3	383.1	-425.8	46.62	1.11	3.50	38.9
6.51	1736.4	1198.6	-105.1	1059.4	-1400.2	-246.8	417.7	-462.9	46.37	1.11	3.50	36.0
6.51	1708.1	1268.2	-86.5	1067.6	-1328.6	-239.2	420.2	-420.6	46.49	1.07	3.49	36.8
6.50	1752.4	1292.5	-99.8	1207.9	-1308.0	-199.2	408.4	-467.7	46.42	1.10	3.49	34.4
6.51	1823.2	1294.6	-66.8	1234.1	-1294.5	-157.5	446.0	-452.2	46.40	1.05	3.49	37.1
6.51	1928.3	1260.5	-78.1	1304.8	-1315.5	-149.6	443.3	-476.3	46.23	1.13	3.49	36.0
6.51	2064.1	1293.1	726.4	1260.5	-602.4	-84.1	412.0	-474.3	46.17	1.06	3.50	36.7
6.51	2013.3	1273.6	723.1	1219.4	-669.7	-170.5	399.7	-506.3	46.16	1.06	3.49	37.6
6.51	2003.4	1289.0	716.3	1214.7	-798.4	-267.3	367.8	-451.3	46.33	1.10	3.49	36.0
6.51	1623.0	1381.7	-1.6	1083.6	-1316.4	-417.4	301.1	-512.1	46.76	1.07	3.49	41.5
6.51	1934.7	1284.0	727.9	1210.7	-842.7	-337.1	370.9	-579.0	46.30	1.11	3.49	40.8
6.50	1876.6	1309.6	764.6	1189.9	-976.7	-342.6	361.2	-496.1	46.35	1.10	3.50	36.8
6.50	1786.2	1325.5	556.3	1190.4	-953.6	-442.7	350.6	-513.8	46.43	1.04	3.49	38.6
6.51	1751.4	1375.4	354.3	1192.6	-995.2	-440.2	398.5	-500.0	46.52	1.05	3.49	41.5

Table C.9 – Phase II Experimental Results: LDV Forward Position, Model Speed = 6.5 m/s

APPENDIX D

Results from Physical Model Tests: Wave Profiles

D.1 Results from Physical Model Tests: Wave Profiles

Waves profiles were measured during the physical model tests discussed in Chapter 2. A set of 23 capacitance probes were placed 177.8 mm (7 inches) apart in a transverse array at the side of the towing tank. The first probe was 177.8 mm from the side of the model, which had a beam of 533mm. A proximity switch triggered by the passing of the tow carriage determined the position of the wave profile relative to the model. The time the switch was triggered corresponded to the time when the model's bow (model had an overall length of 1.473m) was directly in line with the probe array. The wave profile data collected by the probes was in terms of wave height verses time of sampling (sampling rate was 100 Hz). This data was converted to wave height verses longitudinal position relative to the model by multiplying the sample time by the model speed. The data could then be plotted for visualization of the wave profiles at various model speeds (using Matlab® version 6, release 12).

The following figures, D.1 – D.13, show the wave profiles for the model in the design ballast condition (mass = 29.55 kg, LCG = 0.534m from transom) for model speeds from 1.0 – 7.0 m/s in 0.5 m/s intervals. The figures are color coded by elevation: blue represents a depression from the still wave surface, yellow for the still water surface, and red for a raised surface. Axes in the figures are position in meters. Froude numbers are only given in the captions for the tests where wetted lengths were determined.

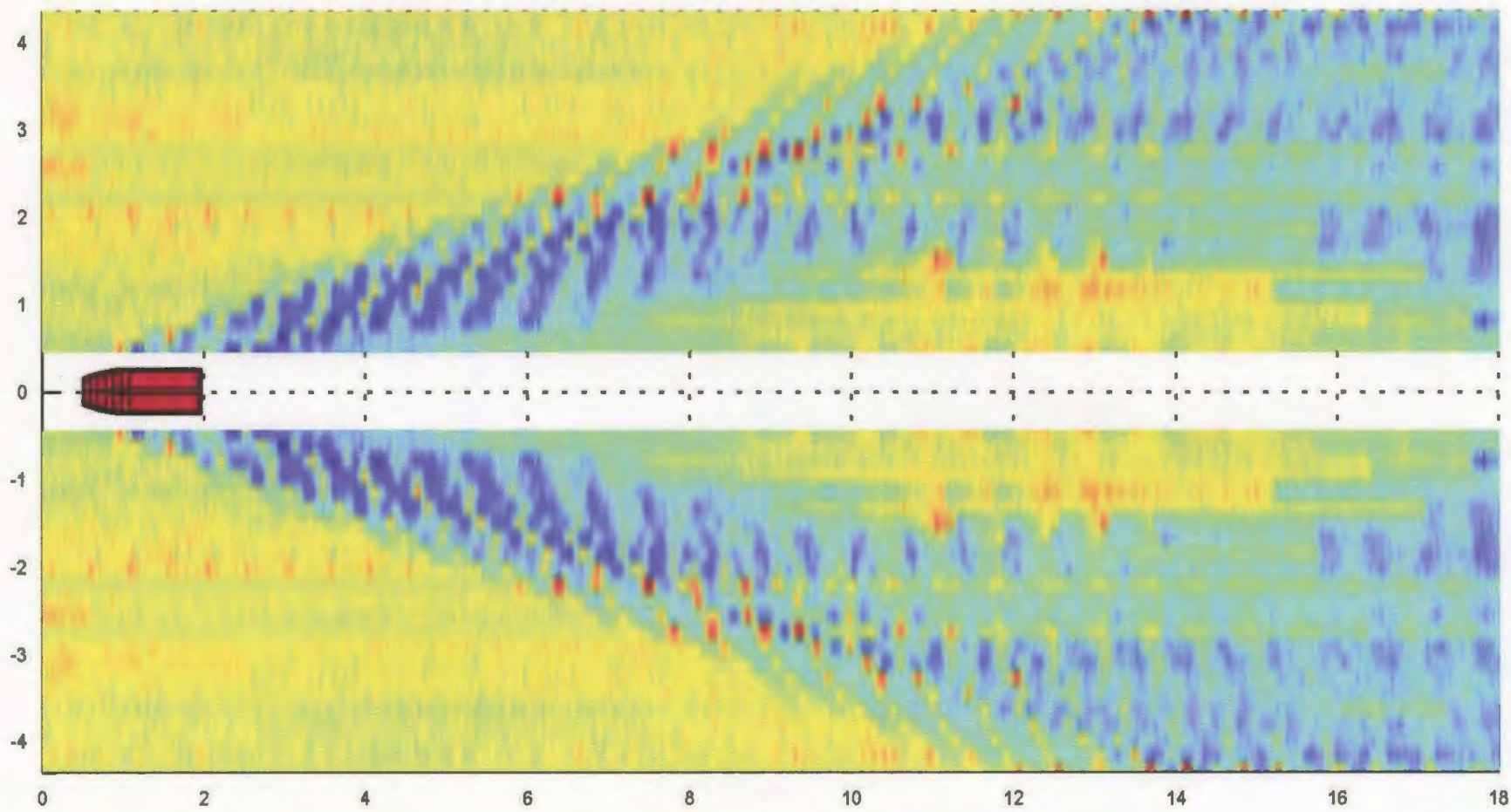


Figure D.1 – Wave Profile: 1.0 m/s

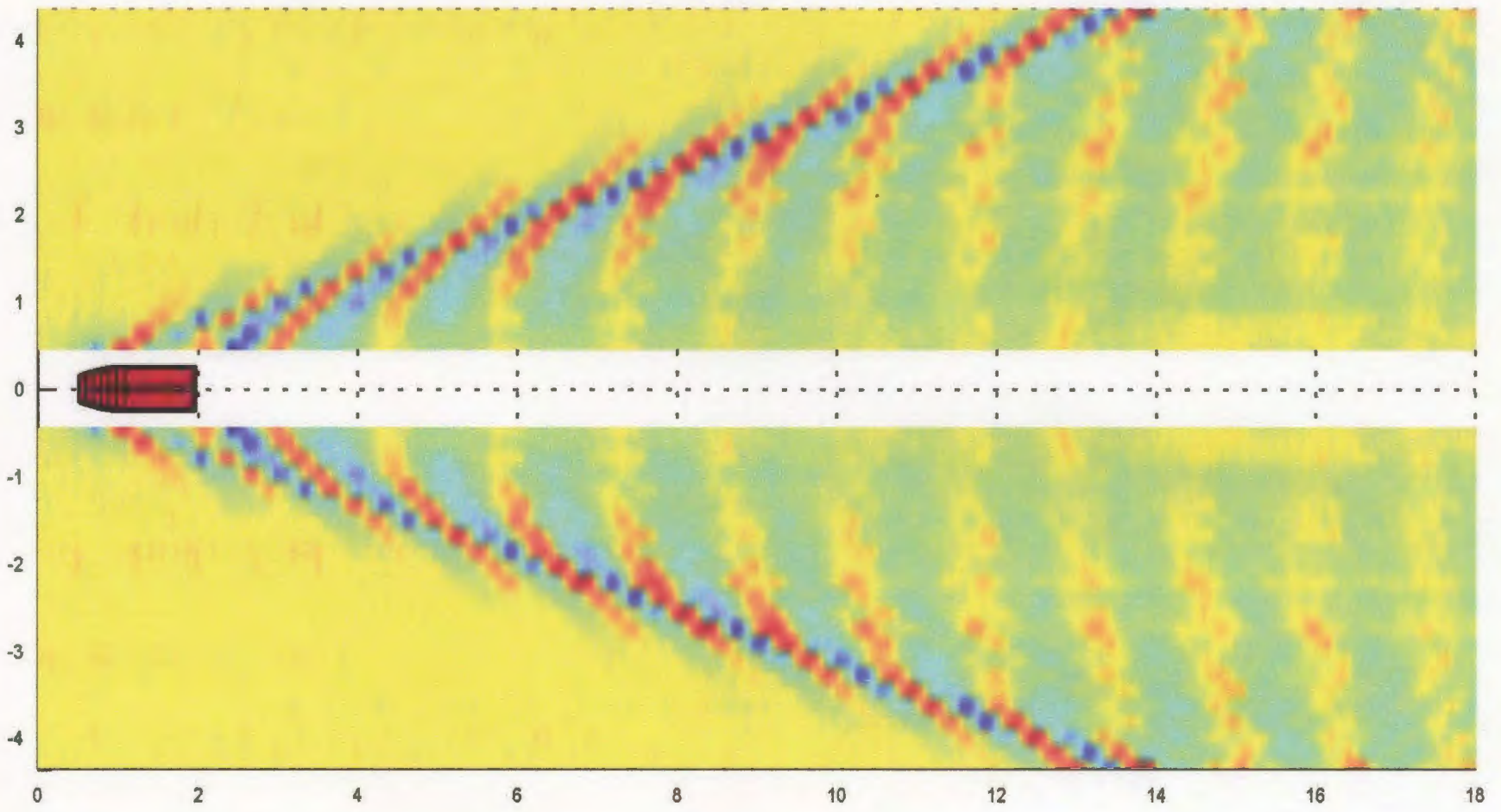


Figure D.2 – Wave Profile: 1.5 m/s

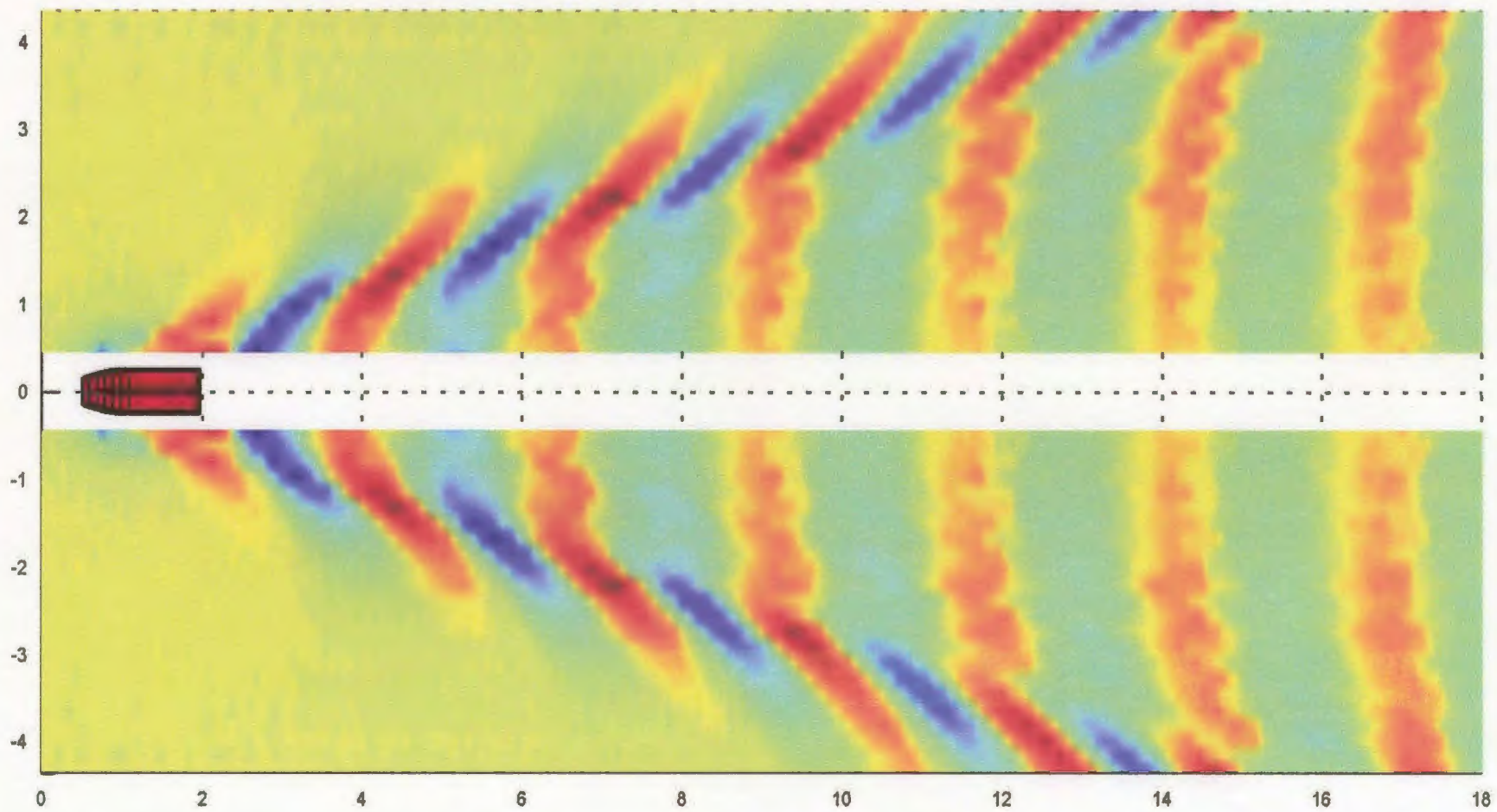


Figure D.3 – Wave Profile: 2.0 m/s ($F_n = 0.59$)

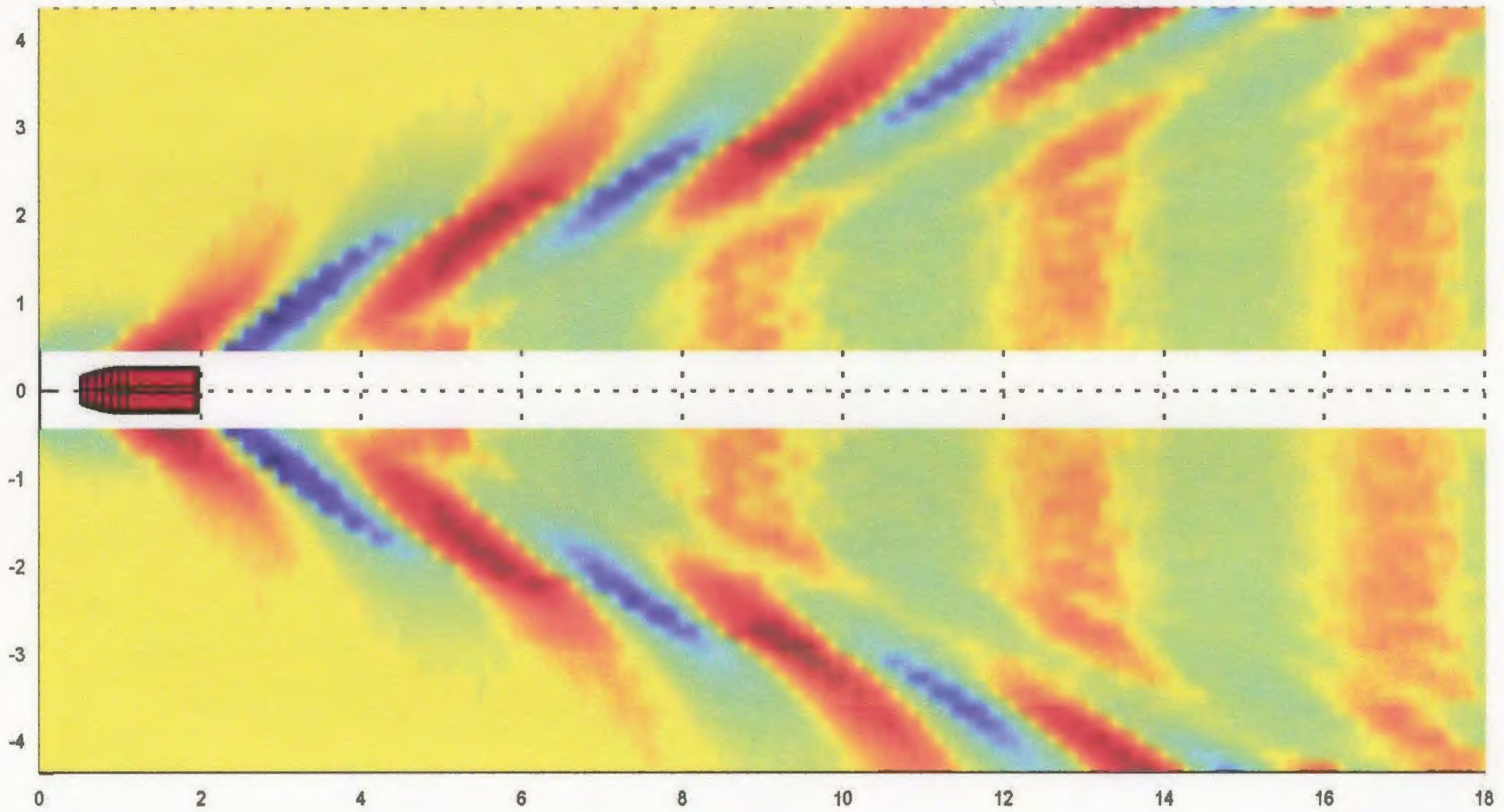


Figure D.4 – Wave Profile: 2.5 m/s ($Fn = 0.79$)

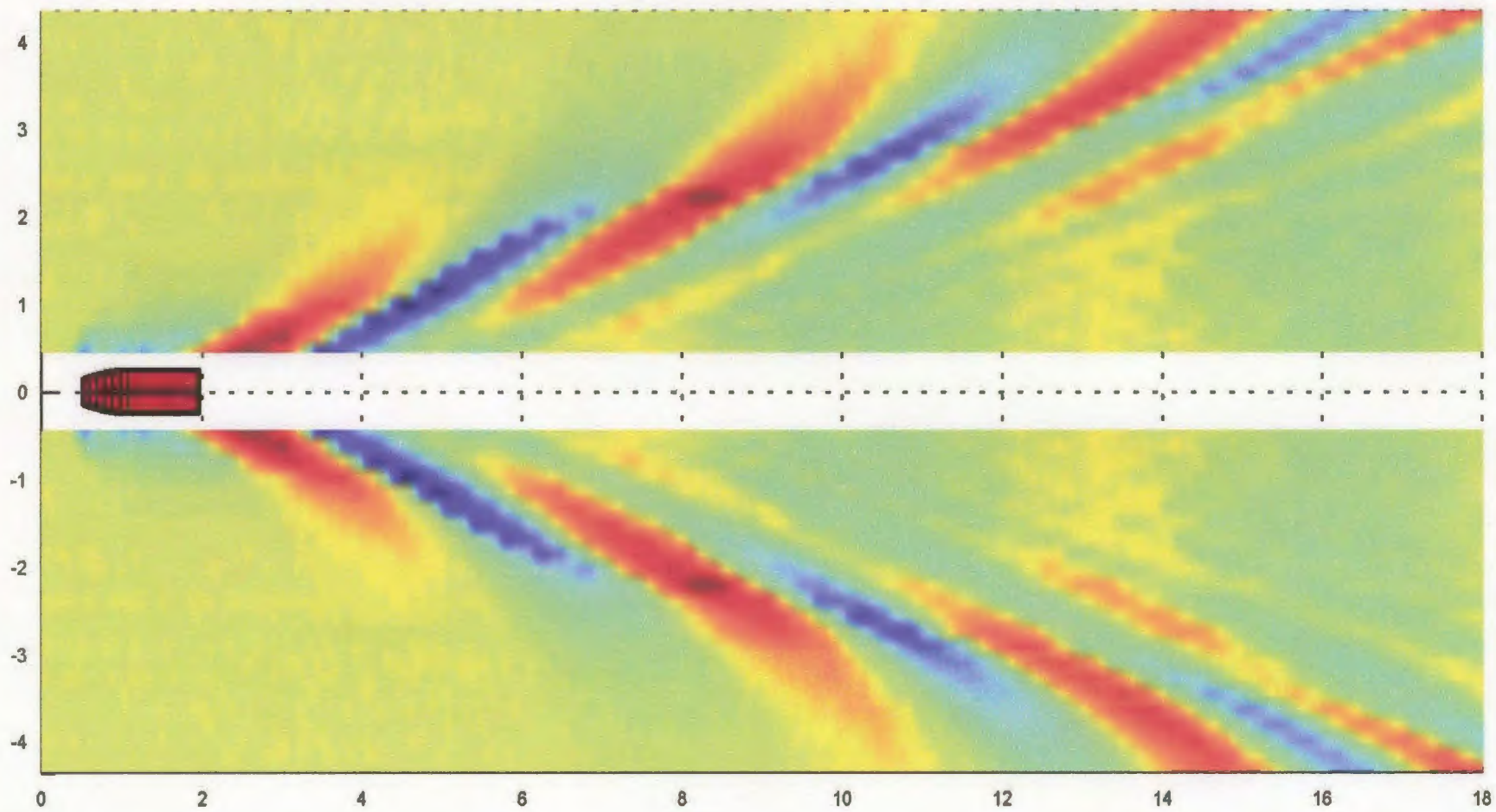


Figure D.5 – Wave Profile: 3.0 m/s ($Fn = 1.00$)

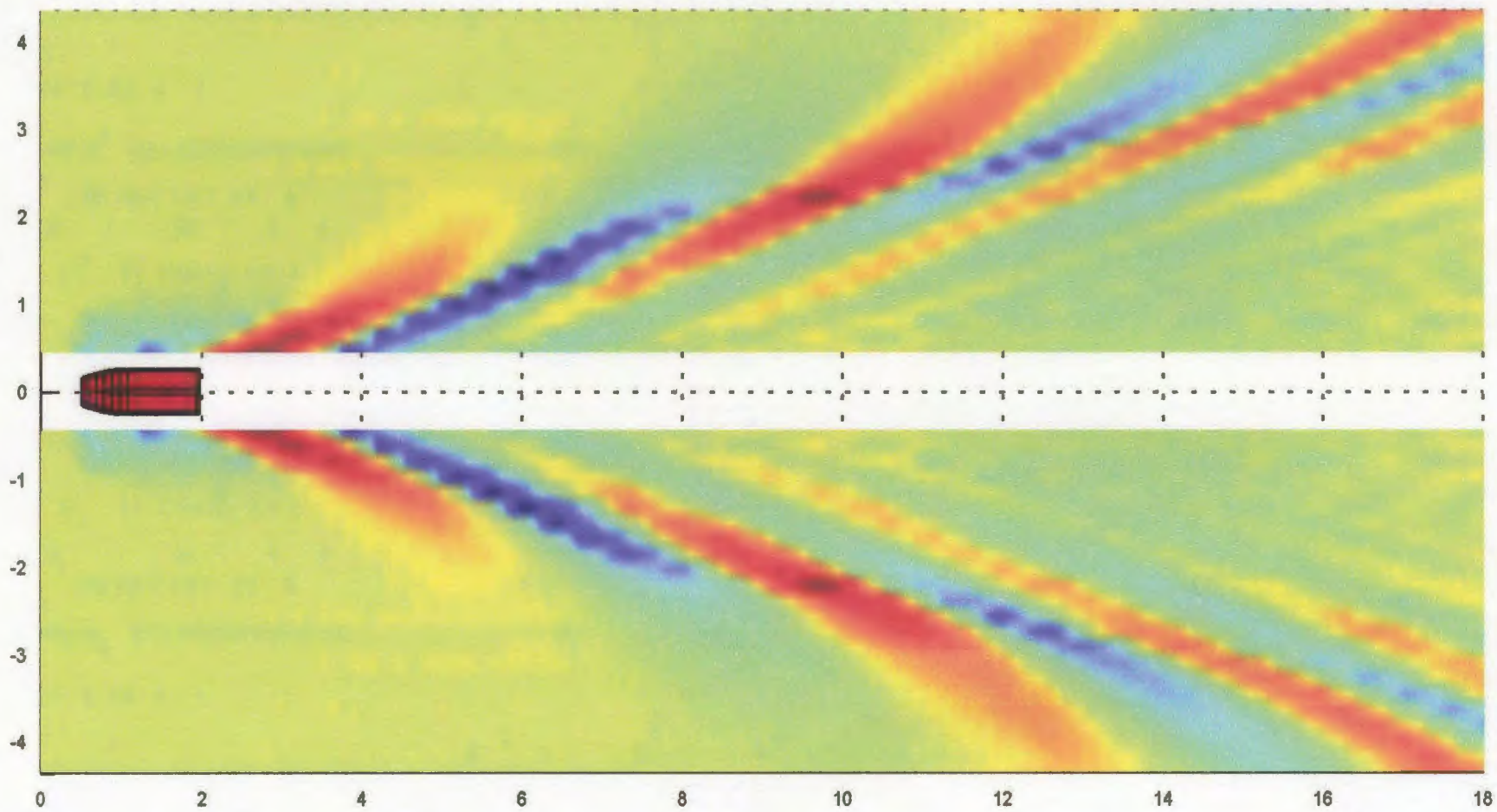


Figure D.6 – Wave Profile: 3.5 m/s ($Fn = 1.23$)

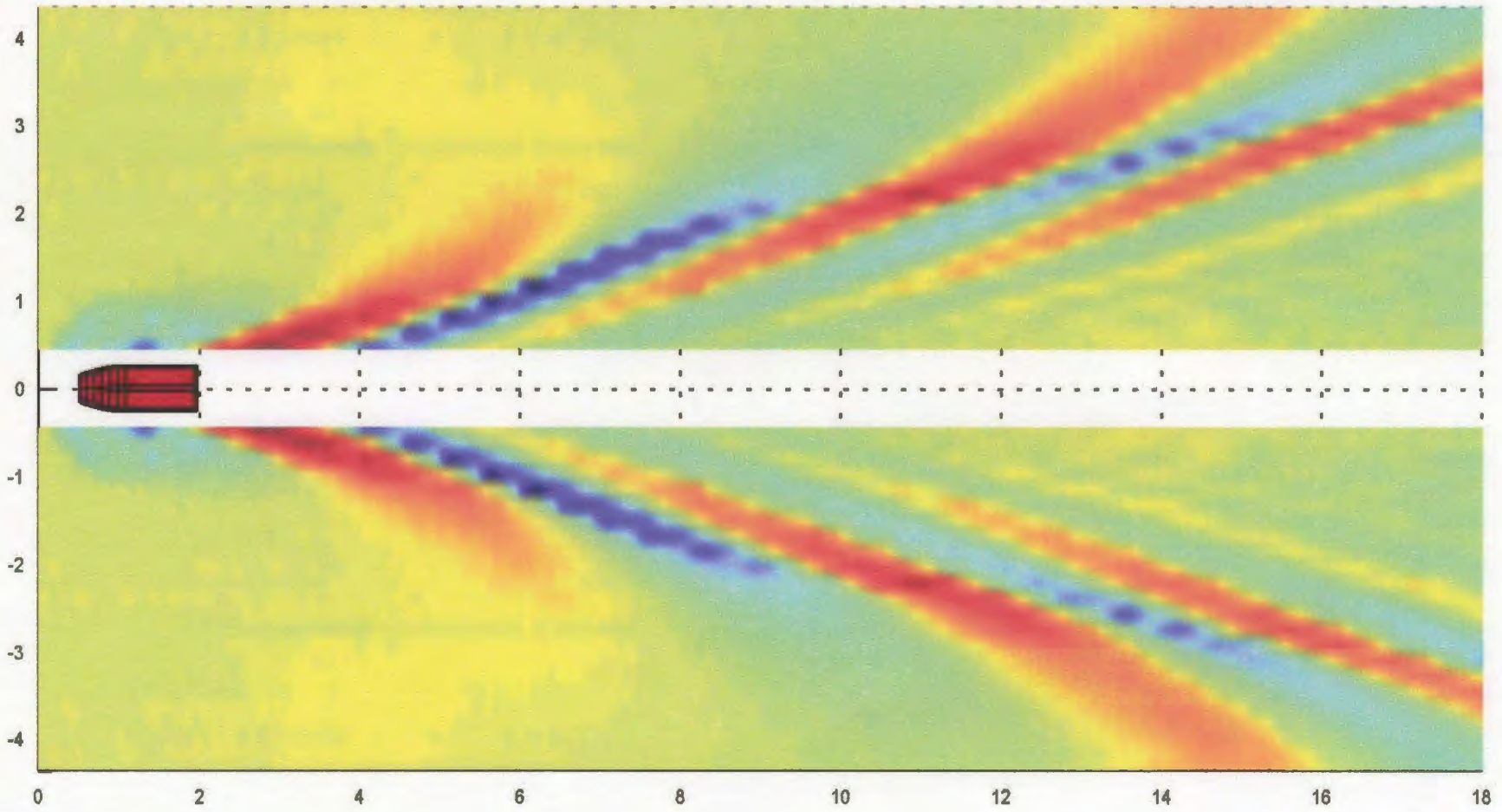


Figure D.7 – Wave Profile: 4.0 m/s ($Fn = 1.47$)

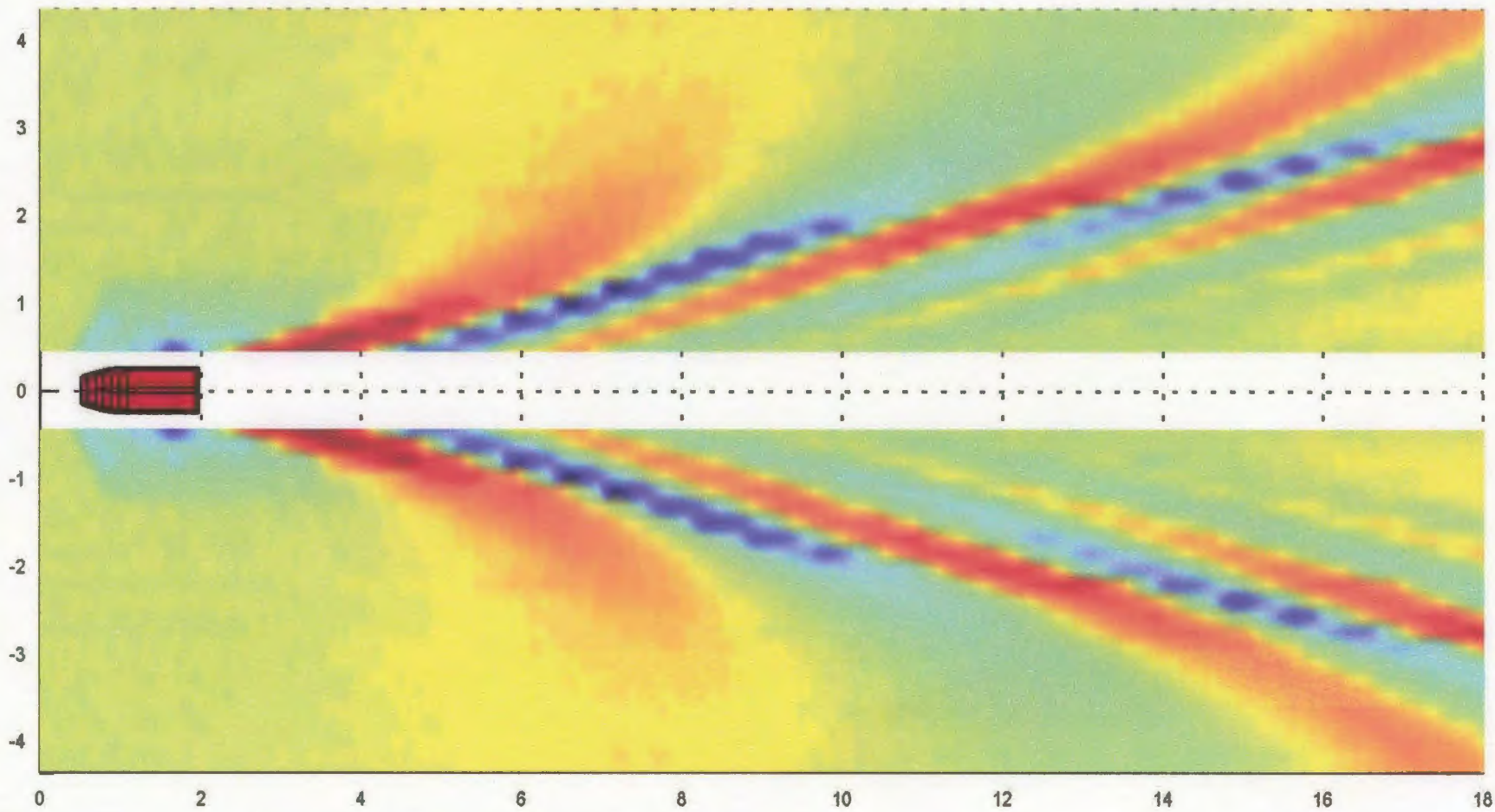


Figure D.8 – Wave Profile: 4.5 m/s ($Fn = 1.71$)

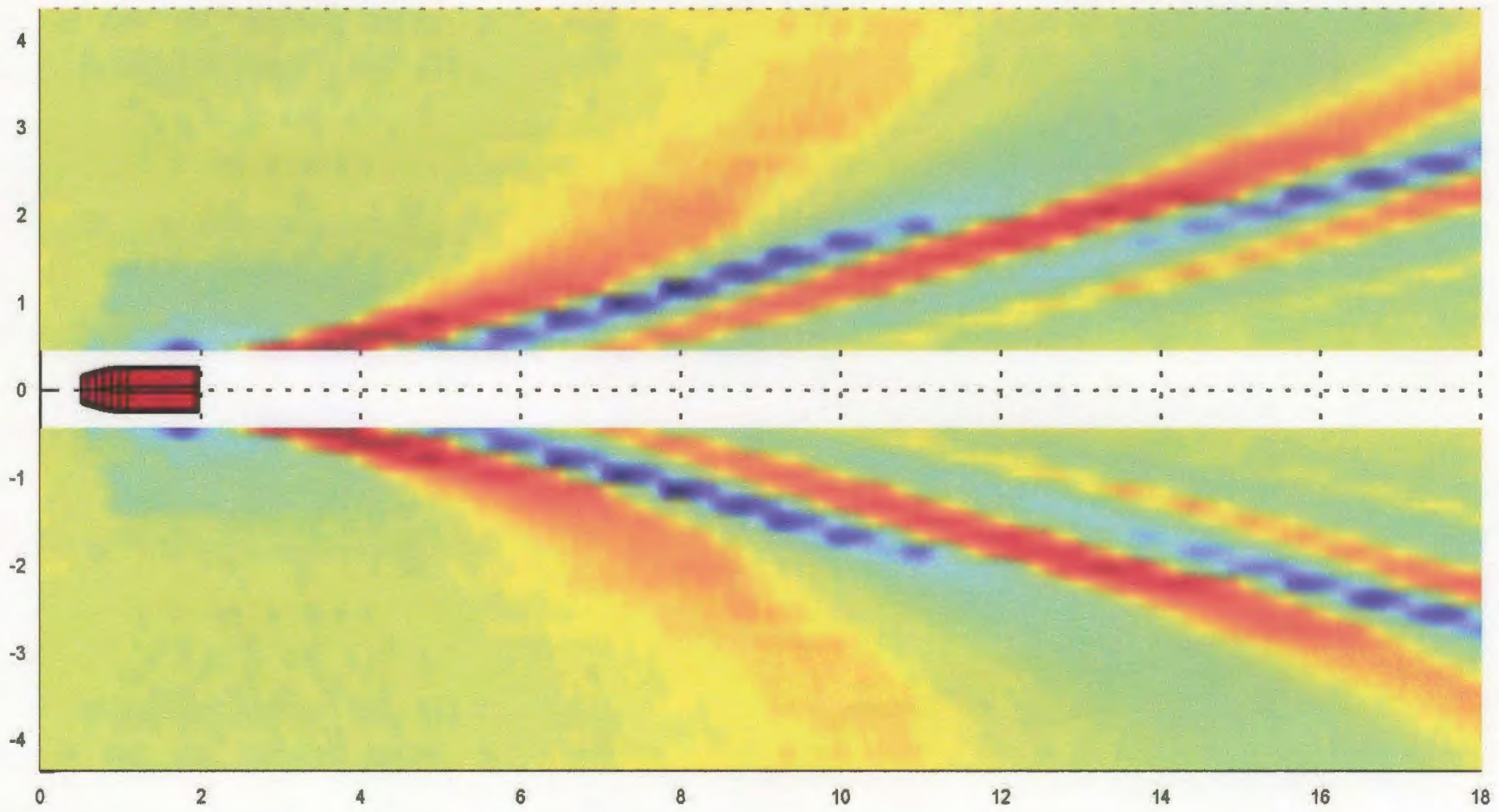


Figure D.9 – Wave Profile: 5.0 m/s ($F_n = 1.96$)

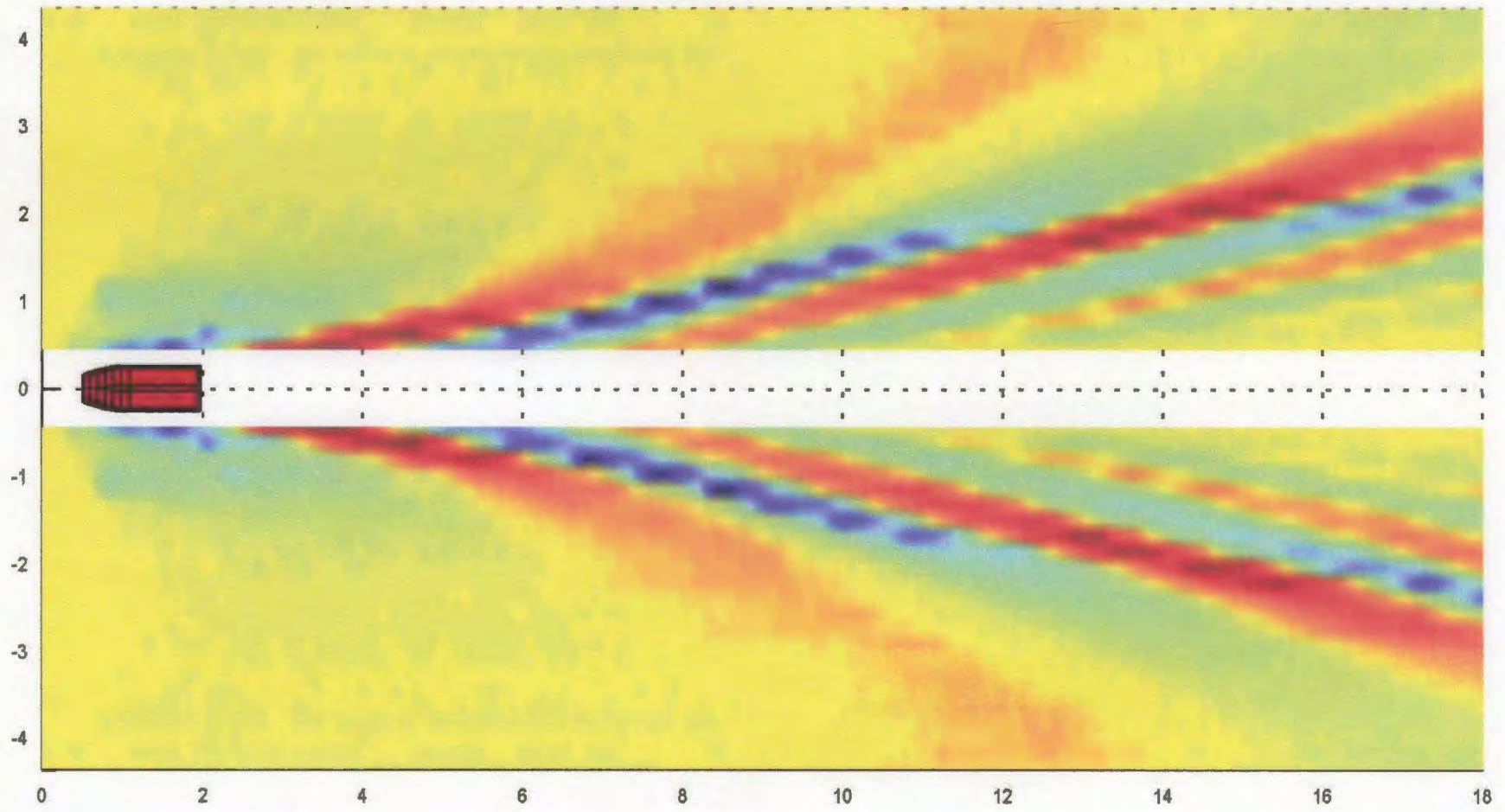


Figure D.10 – Wave Profile: 5.5 m/s ($F_n = 2.21$)

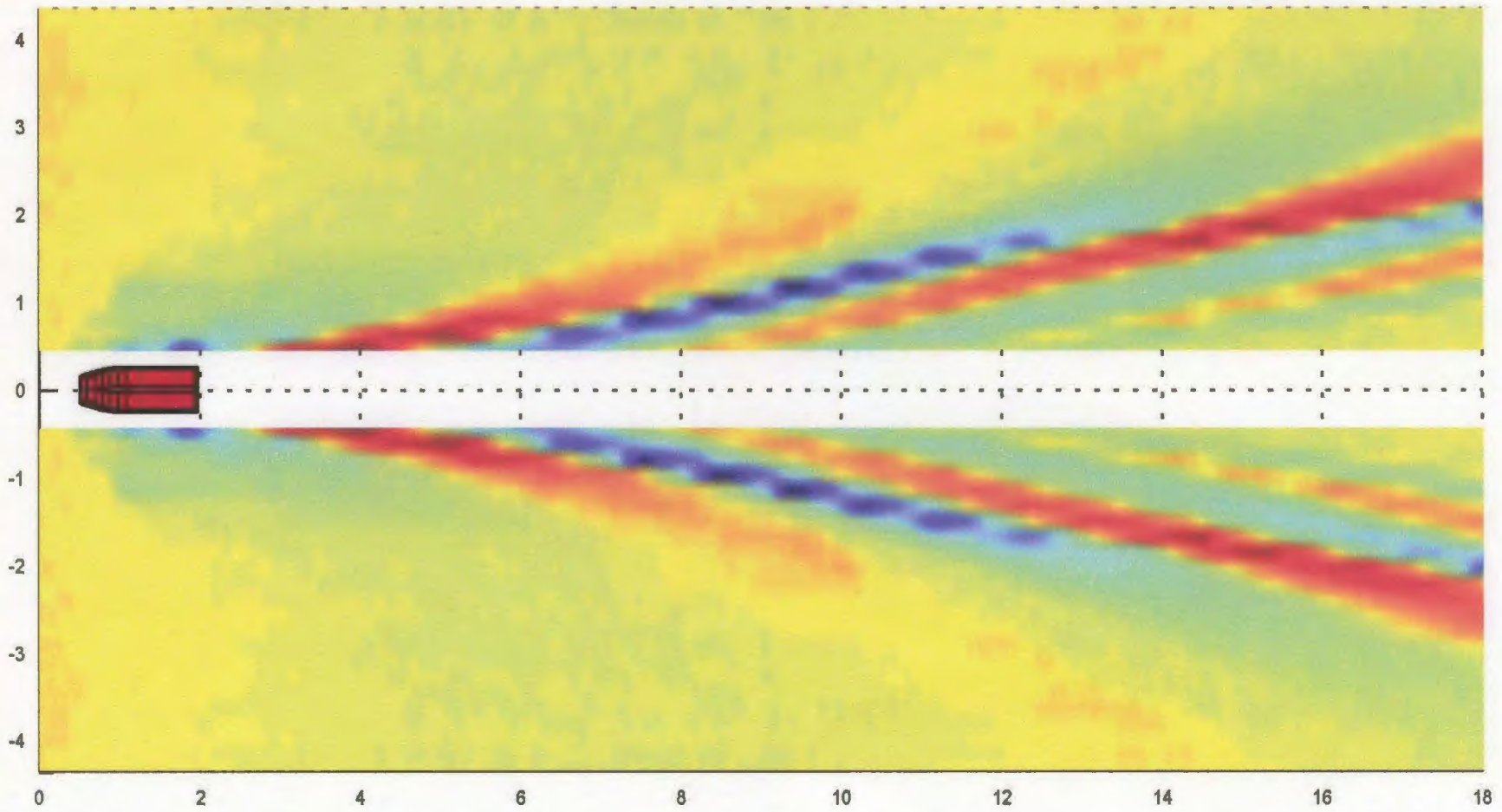


Figure D.11 – Wave Profile: 6.0 m/s ($F_n = 2.47$)

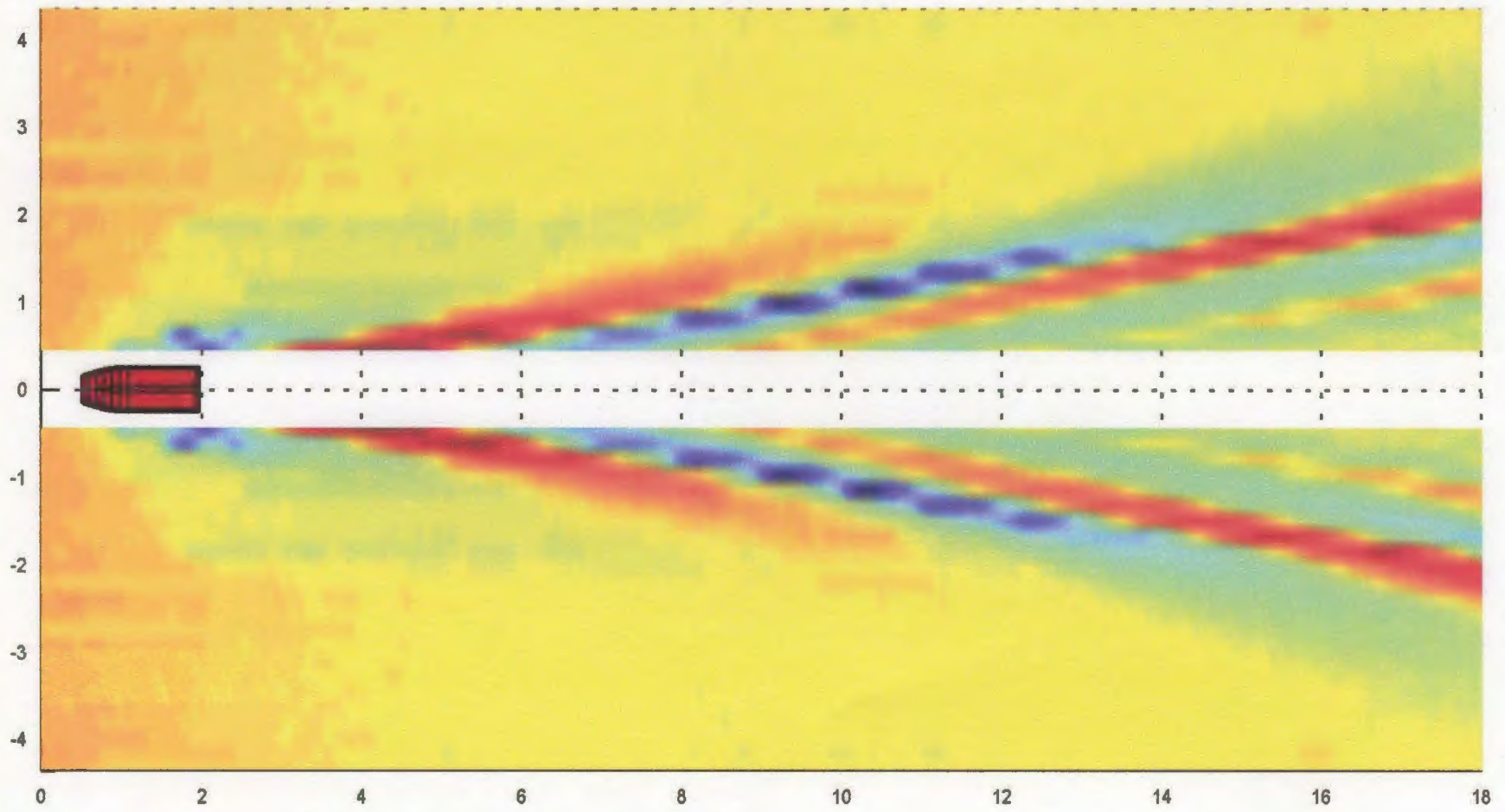


Figure D.12 – Wave Profile: 6.5 m/s ($F_n = 2.72$)

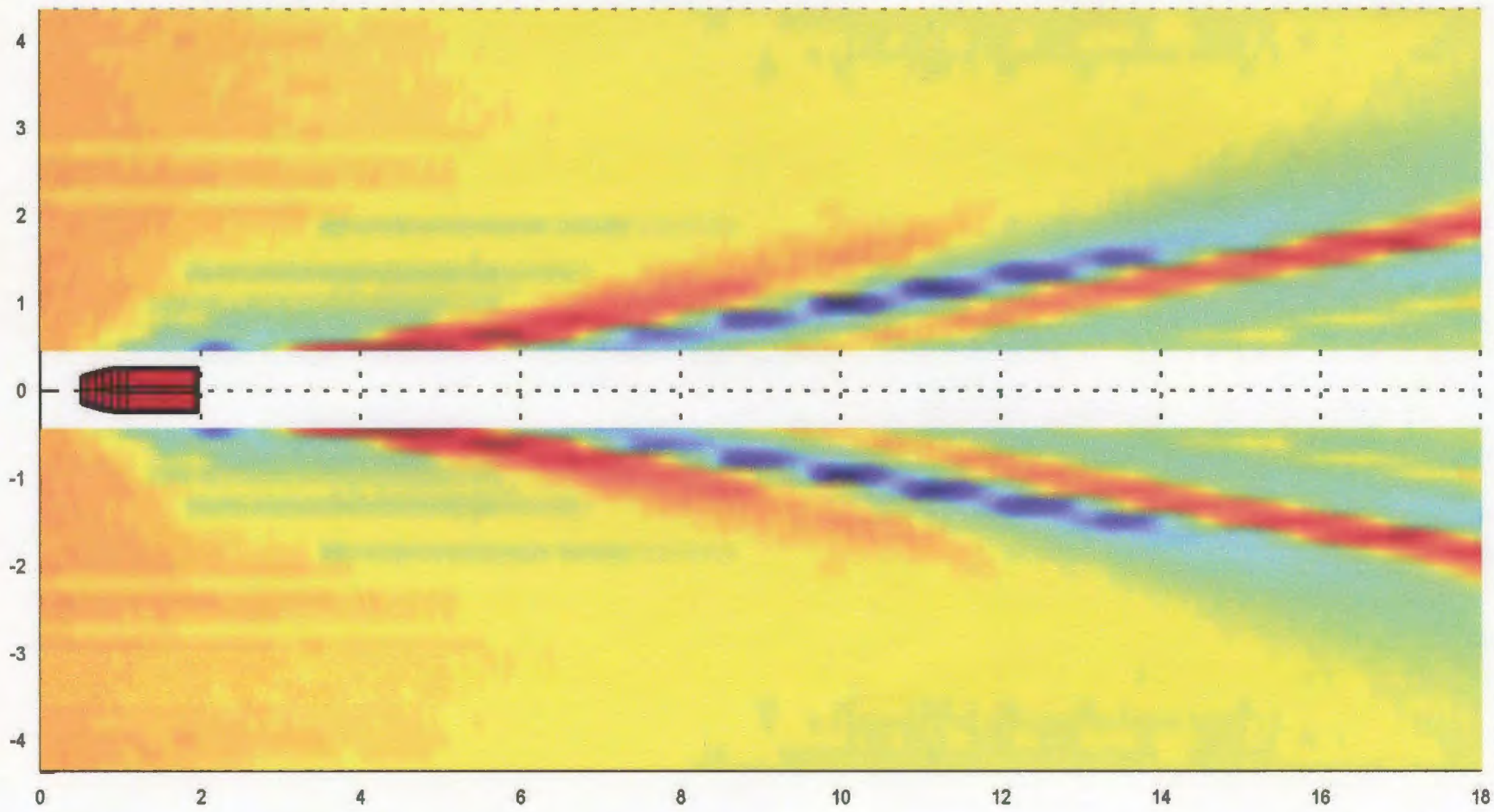


Figure D.13 – Wave Profile: 7.0 m/s (Fn = 2.98)

APPENDIX E

Results from Numerical Simulations

Model Speed [m/s]	Running Trim [deg]	Heave Post Delta [mm]	Total Resist. [N]	A_w Wetted Area [m ²]	L_k Wetted Center [m]	L_c Wetted Chine [m]	L_m Mean Length [m]	λ_w Length Ratio [-]	F_n [-]	Re [-]	ATTC C_f [-]	Frict. Resist. [N]	Pres. Resist. [N]
2.0	5.33	-33.1	38.97	0.675	1.267	1.059	1.163	2.182	0.59	2.32E+06	3.77E-03	5.08	33.89
2.5	6.53	-26.0	43.55	0.603	1.130	0.929	1.030	1.932	0.79	2.56E+06	3.71E-03	6.97	36.58
3.0	7.04	-14.6	46.57	0.543	1.020	0.820	0.920	1.726	1.00	2.75E+06	3.66E-03	8.93	37.64
3.5	7.10	-2.9	47.47	0.494	0.933	0.729	0.831	1.559	1.23	2.89E+06	3.63E-03	10.95	36.52
4.0	6.70	9.3	46.58	0.454	0.866	0.654	0.760	1.426	1.47	3.03E+06	3.60E-03	13.03	33.54
4.5	5.97	19.6	44.98	0.421	0.817	0.592	0.705	1.322	1.71	3.16E+06	3.57E-03	15.21	29.77
5.0	5.26	32.7	43.80	0.396	0.783	0.540	0.662	1.242	1.96	3.29E+06	3.54E-03	17.51	26.29
5.5	4.59	35.3	43.35	0.376	0.761	0.497	0.629	1.180	2.21	3.44E+06	3.52E-03	19.94	23.40
6.0	4.08	36.6	43.86	0.363	0.748	0.458	0.603	1.131	2.47	3.60E+06	3.49E-03	22.75	21.11
6.5	3.65	35.4	45.18	0.356	0.741	0.421	0.581	1.090	2.72	3.76E+06	3.46E-03	26.00	19.18
7.0	3.33	35.9	47.04	0.347	0.738	0.384	0.561	1.052	2.98	3.91E+06	3.44E-03	29.17	17.87

Table E.1 – Physical Experimental Results: Model Weight 25.2 kg, Model LCG = 0.528 m

Model Speed [m/s]	Running Trim [deg]	Total Resist. [N]	A_w Wetted Area [m ²]	L_m Mean Length [m]	λ_w Length Ratio [-]	Vm [m/s]	Fn [-]	Re [-]	ATTC Cf [-]	Frict. Resist. [N]	Pres. Resist. [N]
2.0	5.87	34.48	0.660	1.232	2.311	1.95	0.58	2.39E+06	3.75E-03	4.72	29.76
2.5	6.63	39.90	0.573	1.070	2.008	2.42	0.77	2.58E+06	3.70E-03	6.24	33.65
3.0	6.78	42.26	0.510	0.951	1.784	2.89	0.98	2.74E+06	3.66E-03	7.86	34.40
3.5	6.35	41.99	0.470	0.878	1.647	3.38	1.19	2.95E+06	3.61E-03	9.75	32.24
4.0	5.71	40.91	0.446	0.833	1.562	3.88	1.40	3.21E+06	3.56E-03	11.97	28.93
4.5	5.04	40.05	0.431	0.804	1.508	4.38	1.60	3.50E+06	3.51E-03	14.50	25.55
5.0	4.44	39.80	0.420	0.784	1.472	4.88	1.80	3.81E+06	3.45E-03	17.32	22.48
5.5	3.92	40.24	0.413	0.771	1.446	5.39	2.00	4.13E+06	3.41E-03	20.42	19.82
6.0	3.47	41.34	0.407	0.760	1.427	5.89	2.20	4.46E+06	3.36E-03	23.78	17.56
6.5	3.09	43.04	0.403	0.753	1.412	6.40	2.39	4.79E+06	3.32E-03	27.40	15.64
7.0	2.77	45.28	0.400	0.747	1.401	6.90	2.59	5.13E+06	3.28E-03	31.27	14.01

Table E.2 – Savitsky’s Method Results (Savitsky, 1964)

Model Speed [m/s]	Running Trim [deg]	Heave Post Delta [mm]	Total Resist. [N]	A _w Wetted Area [m ²]	L _k Wetted Center [m]	L _c Wetted Chine [m]	L _m Mean Length [m]	λ _w Length Ratio [-]	Fn [-]	Re [-]	ATTC Cf [-]	Frict. Resist. [N]	Pres. Resist. [N]
2.0	5.33	-33.1	43.14	0.712	1.369	1.307	1.338	1.338	0.55	2.66E+06	3.68E-03	5.21	37.93
3.0	7.04	-14.6	66.76	0.610	1.165	1.045	1.105	1.105	0.91	3.30E+06	3.54E-03	9.64	57.12
4.0	6.70	9.3	61.36	0.484	0.940	0.797	0.868	0.868	1.37	3.46E+06	3.51E-03	13.50	47.86
5.0	5.26	32.7	52.37	0.413	0.810	0.665	0.737	0.737	1.86	3.67E+06	3.48E-03	17.83	34.54
6.0	4.08	36.6	47.16	0.343	0.758	0.530	0.644	0.644	2.39	3.85E+06	3.45E-03	21.18	25.98
7.0	3.33	35.9	49.63	0.322	0.763	0.499	0.631	0.631	2.81	4.40E+06	3.37E-03	26.53	23.11

Table E.3 – Equilibrium Simulation Results: 0-Degree of Freedom

Model Speed [m/s]	Running Trim [deg]	Heave Post Delta [mm]	Total Resist. [N]	A _w Wetted Area [m ²]	L _k Wetted Center [m]	L _c Wetted Chine [m]	L _m Mean Length [m]	λ _w Length Ratio [-]	Fn [-]	Re [-]	ATTC Cf [-]	Frict. Resist. [N]	Pres. Resist. [N]
2.0	5.33	-27.1	39.45	0.705	1.280	1.232	1.256	1.256	0.57	2.50E+06	3.72E-03	5.21	34.24
3.0	7.04	9.8	42.94	0.483	0.925	0.782	0.853	0.853	1.04	2.55E+06	3.71E-03	7.99	34.95
4.0	6.70	33.4	44.91	0.358	0.703	0.554	0.628	0.628	1.61	2.50E+06	3.72E-03	10.56	34.34
5.0	5.26	43.6	41.33	0.310	0.624	0.461	0.542	0.542	2.17	2.70E+06	3.67E-03	14.16	27.17
6.0	4.08	48.7	40.00	0.286	0.598	0.347	0.472	0.472	2.79	2.82E+06	3.64E-03	18.66	21.33
7.0	3.33	50.0	42.51	0.288	0.625	0.344	0.484	0.484	3.21	3.38E+06	3.53E-03	24.82	17.69

Table E.4 – Equilibrium Simulation Results: 1-Degree of Freedom

Model Speed [m/s]	Running Trim [deg]	Heave Post Delta [mm]	Total Resist. [N]	A_w Wetted Area [m ²]	L_k Wetted Center [m]	L_c Wetted Chine [m]	L_m Mean Length [m]	λ_w Length Ratio [-]	Fn [-]	Re [-]	ATTC Cf [-]	Frict. Resist. [N]	Pres. Resist. [N]
2.0	5.6	-27.8	39.92	0.698	1.279	1.231	1.255	1.255	0.57	2.50E+06	3.72E-03	5.17	34.76
3.0	5.5	7.9	38.13	0.533	1.044	0.873	0.958	0.958	0.98	2.86E+06	3.63E-03	8.66	29.47
4.0	4.5	21.2	36.06	0.450	0.933	0.747	0.840	0.840	1.38	3.34E+06	3.53E-03	12.67	23.39
5.0	3.9	32.4	38.61	0.422	0.844	0.581	0.713	0.713	1.88	3.55E+06	3.49E-03	18.36	20.25
6.0	3.07	39.2	41.14	0.407	0.847	0.521	0.684	0.684	2.31	4.09E+06	3.41E-03	24.91	16.23
7.0	2.98	41.2	47.34	0.381	0.800	0.498	0.649	0.649	2.53	4.52E+06	3.27E-03	31.47	15.88

Table E.5 – Equilibrium Simulation Results: 2-Degree of Freedom

